Surface functionalization of silicon nanocrystals *via* a microwave reactor

zur Erlangung des akademischen Grades eines

Doktors der Naturwissenschaften
(Dr. rer. nat.)

von der KIT-Fakultät für Chemie und Biowissenschaften
des Karlsruher Instituts für Technologie (KIT)

genehmigte

Dissertation

von

Deski Beri

Aus Indonesien

Tag der mündlichen Prüfung: 8. Dezember 2020
Erster Gutachter: Prof. Dr. Frank Breitling
Zweiter Gutachter: Prof. Dr. Bryce S. Richards

Kurzfassung

Silizium-Nanokristalle (SiNCs) haben in den letzten Jahrzehnten aufgrund ihrer vielfältigen (potenziellen) Anwendungen in Forschung und Industrie großes Interesse geweckt. SiNCs könnten zum Beispiel für 1) In Licht-Energie-Umwandlungsprozesse wie photovoltaische Lichtabsorber, lumineszierende Solarkonzentratoren und SiNCs-Solarzellen, 2) in der Optoelektronik z. B. für Leuchtdioden und Laser mit Nahinfrarot-Emission, 3) in der Sensortechnik z. B. für kleine Temperatursensoren und 4) in der photodynamischen Therapie als chemische Sonden und als "Trojanisches Pferd" in der Theranostik und photodynamischen Therapie. Die kritischen Faktoren für solche Zwecke sind für SiNCs eine große Quantenausbeute, geringe Größenverteilung und hohe chemische Stabilität. Daher konzentriert sich diese Forschung auf die Herstellung von SiNCs mit großer Quantenausbeute und geringer Größenverteilung durch Optimierung der verschiedenen Schritte im Syntheseprozess: Glühen, Ätzen und Funktionalisierung.

Im ersten Teil dieser Arbeit wird die Rolle der Alkylkettenlängen als Passivierungsmittel untersucht. Der Einfluss der Alkylkettenlänge auf die photophysikalischen Eigenschaften und die Stabilität wurde durch Funktionalisierungsreaktionen verschiedener Alkylkettenlängen mit SiNCs untersucht. Diese Arbeit stellte die Hypothese auf, dass eine Verringerung der Alkylkettenlänge zu einer Verringerung der sterischen Behinderung führt, was sich auf die Oberflächenbedeckung, die photophysikalischen Eigenschaften und die Oxidation auswirkt. Die Funktionalisierungsreaktion von langen Alkylketten wird durch Dodecyl (C12), Tetradecyl (C14) und Hexadecyl (C16) dargestellt, während für die mittelkettige Hexyl- (C6), Octyl- (C8) und Decylkette (C10) und für die kurze Kette Allyl, Methylether (C3) und Pentyl (C5) verwendet werden. Alle funktionalisierten Alkyl-SiNCs zeigen starke Emission in Rot bis Nah-Infrarot (600-1000 nm). Der höchste photolumineszente Quantenausbeutewert (PLQY) wurde von (C3)-SiNCs mit nahezu ~ 41% erreicht. Es besteht die Tendenz, dass die PLQY mit zunehmender Anzahl von Kohlenstoffen in der Alkylkette abnimmt. Das photolumineszente (PL)-Emissionsmaximum aller funktionalisierten SiNCs liegt zwischen ~850 nm für (C5)-SiNCs und ~905 nm für (C16)-SiNCs. Mittlerweile zeigt die PL-Lebensdauer ~157 s für (C5)-SiNCs bei 820 nm PL-Emission und ~120 s für (C16)-SiNCs bei gleicher PL-Emission. Die Haltbarkeit aller synthetisierten Materialien wurde systematisch untersucht, um die Charakterisierung der SiNCs abzuschließen. Nach sechsmonatiger Lagerung unter dunklen Umgebungsbedingungen (PLQY/PLQY0 > 0,9) wurden keine signifikanten Veränderungen der Photolumineszenz-Emissionen beobachtet. Daher besitzen Alkyl-SiNCs, die mittels mikrowellenunterstützter Hydrosilylierungsreaktion funktionalisiert wurden, eine ausgezeichnete photophysikalische Stabilität.

Im zweiten Teil dieser Arbeit wurde die Funktionalisierung von SiNCs mit Farbstoffen zur Verbesserung der Lichtabsorption als Strategie zur Erhöhung der Helligkeit der SiNCs-Emission untersucht. Es wird erwartet, dass der konjugierte Farbstoff und SiNCs aufgrund der zusätzlichen

Absorption durch die Farbstoffmoleküle höhere PL-Emissionen aufweisen. Perylen- und Dipyrromethenbordifluorid-Farbstoffe (BODIPY) werden verwendet, um die Lichtabsorption im sichtbaren Bereich der elektromagnetischen Strahlung zu erhöhen. Perylen und BODIPY absorbieren Photonen im Bereich von ~350-500 nm bzw. ~450-600 nm. Aufgrund der Farbstoffanhaftung zeigten Perylen-SiNCs bei ~350-500 nm eine ~10-fache Verbesserung der Lichtabsorption, während BODIPY-SiNCs bei ~450-600 nm eine ~3-fache Verbesserung der Lichtabsorption zeigten. Hier beobachten wir den effizienten Energietransfer von Farbstoffen zu SiNCs, der zu einer PL-Emissionsverstärkung von SiNCs führt. Die Ergebnisse zeitaufgelöster photolumineszenter Spektroskopiemessungen zeigten, dass die Abklingzeiten von gebundenen Perylen- und BODIPY-Farbstoffen ~100-mal kürzer waren als die der ungebundenen Farbstoffe, was zu einer berechneten Effizienz von > 95% für den Energietransfer führte. Die effiziente Energieübertragung der Farbstoffmoleküle auf SiNCs führt zu einer Erhöhung der Emissionen von Perylen-SiNCs und BODIPY-SiNCs im nahen Infrarot (NIR) um ~ 270% bzw. ~ 140% bei Anregung bei 440 nm bzw. 515 nm. Trotz der Zunahme der absoluten Helligkeit der Emission (aufgrund der Absorptionsverstärkung) bewirkt die Rückenergieübertragung von den SiNCs auf den Farbstoff eine Abnahme der PLQY von perylenmodifizierten SiNCs im Vergleich zu unmodifizierten SiNCs. Wir gehen davon aus, dass eine effiziente Rückenergieübertragung von SiNCs auf Perylen über einen Perylen-Triplett-Zustand erfolgen muss. Der Perylen-Triplett-Zustand liegt im Bereich von ~800-850 nm und fällt mit der PL-Emission von SiNCs zusammen (~800-860 nm). Die Koinzidenz der Energiezustände könnte genutzt werden, um den Perylen-Triplett-Zustand zu bevölkern, und über Triplett-Triplett-Energieübertragung zur Bildung von Singulett-Sauerstoff ($^1O_2$) führen.

Im letzten Teil dieser Arbeit wurden die kovalent verankerten Perylen-SiNCs, die über eine mikrowellenunterstützte Hydrosilylierungsreaktion synthetisiert wurden, auf ihre Fähigkeit zur Erzeugung von 1O2 untersucht. Obwohl Alkyl-SiNCs keine intrinsische Fähigkeit besitzen, $^1O_2$ zu erzeugen, zeigt diese Arbeit, dass Perylen-SiNCs $^1O_2$ mit einer moderaten Quantenausbeute (Φ_Δ) von bis zu 27% in Cyclohexan erzeugen. Diese Ergebnisse wurden durch Messung der Singulett-Sauerstoff-Phosphoreszenz bei 1270 nm erzielt. SiNCs spielen eine wichtige Rolle bei der Erzeugung von $^1O_2$ mit Perylen-SiNCs-Konjugaten, da SiNCs UV- und blaue Strahlung ernten und die absorbierte Energie in einen Triplett-Zustand der angelagerten Farbstoffe übertragen können. Die Triplett-Zustandspopulation nimmt zu und führt zu einer Zunahme der $^1O_2$-Erzeugung. Gleichzeitig zeigten die SiNC-Farbstoffkonjugate NIR-Lumineszenz mit einer PLQY von bis zu 22%. Das Lumineszenzverhalten und die photosensibilisierenden Eigenschaften des SiNC-Farbstoffkonjugats könnten daher als neue multifunktionale Plattform im Bereich der Bioanwendungen von Interesse sein.

Abstract

Silicon nanocrystals (SiNCs) have attracted great interest in recent decades due to their diverse (potential) applications in research and industry. For example, SiNCs could be used for: 1) In light-to-energy conversion processes such as photovoltaic light absorbers, luminescent solar concentrators, and SiNCs solar cells. 2) In optoelectronics such as near-infrared emission light-emitting diodes and lasers. 3) In sensor technology such as small-scale temperature sensors. 4) In photodynamic therapy as chemical probes and as "Trojan horse" in theranostics and photodynamic therapy. For such purposes, the critical factors for SiNCs are high quantum yield, narrow size distribution, and high chemical stability. This research is focused on the production of high quantum yields SiNCs with a narrow-size distribution achieved through optimization of the various steps in the synthesis process: annealing, etching, and functionalization.

The first part of this thesis examines the role of alkyl chain lengths as a passivating agent. The effect of alkyl chain length on photophysical properties and stability was investigated through functionalization reactions of various alkyl lengths with SiNCs. This thesis hypothesized that a reduction of alkyl chain length results in a reduction in steric hindrance, which impacts surface coverage, photophysical properties, and oxidation. The functionalization reaction of long alkyl chains is represented by dodecyl (C12), tetradecyl (C14), and hexadecyl (C16), while for the medium-chain hexyl (C6), octyl (C8), and decyl (C10) and for the short-chain represented by allyl, methyl ether (C3), and pentyl (C5). All functionalized alkyl-SiNCs show strong emission in red to near-infrared (600-1000 nm). The highest photoluminescent quantum yield (PLQY) value was achieved by (C3)-SiNCs to be close to ~ 41%. There is a tendency of decreasing PLQY with increasing number of carbons in the alkyl chain. Photoluminescent (PL)-emission maximum of all functionalized SiNCs is located from ~850nm for (C5)-SiNCs to ~905 nm for (C16)-SiNCs. Meanwhile, PL-lifetimes shows ~157 μs for (C5)-SiNCs at 820 nm PL-emission and ~120 μs for (C16)-SiNCs at the same PL-emission. The shelf life of all synthesized materials was systematically investigated to complete the SiNCs characterization. No significant changes in photoluminescence emissions were observed after six months of storage in dark ambient conditions ($PLQY/PLQY_0 > 0.9$). Therefore, alkyl-SiNCs functionalized *via* microwave-assisted hydrosilylation reaction possess excellent photophysical stability.

In the second part of this thesis, the functionalization of SiNCs with dyes to enhance the light absorption was investigated as a strategy for increasing the brightness of SiNCs emission. The conjugate dye and SiNCs are expected to have higher PL-emissions due to the additional absorption from the dye molecules. Perylene and dipyrrometheneboron difluoride (BODIPY) dyes are used to enhance light absorption in the visible range of electromagnetic radiation. Perylene and BODIPY absorb photons in the range of ~350-500 nm and ~450-600 nm, respectively. Due to dye attachment, perylene-SiNCs at ~350-500 nm exhibited a ~10-fold enhancement in light absorption, whereas BODIPY-SiNCs at ~450-600 nm

exhibited ~3-fold enhancement in light absorption. Here, we observe the efficient energy transfer from dyes to SiNCs, which leads to PL-emission enhancement of SiNCs. The results of time-resolved photoluminescent spectroscopy measurements demonstrated that the decay times of bound perylene and BODIPY dyes were ~100 times shorter than the unbound dyes, which led to a calculated efficiency of > 95% for the energy transfer. The dye molecules' efficient energy transfer to SiNCs leads to an increase in emissions from perylene-SiNCs and BODIPY-SiNCs in the near-infrared (NIR) by ~ 270% and ~ 140% when excited at 440 nm and 515 nm, respectively. Despite the increase in the absolute brightness of the emission (due to absorption enhancement), back energy transfer from the SiNCs to the dye causes a decrease in the PLQY of perylene-modified SiNCs compared to unmodified SiNCs. We foresee that efficient back energy transfer from SiNCs to perylene must occur *via* a perylene triplet state. The perylene triplet state lies in the range of ~800-850 nm and coincides with SiNCs PL-emission (~800-860 nm). The coincidence of the energy states could be employed to populate the perylene triplet state, and *via* triplet-triplet energy-transfer could lead to the formation of singlet oxygen ($^1O_2$).

In the last part of this thesis, the covalently anchored perylene SiNCs, which were synthesized *via* a microwave-assisted hydrosilylation reaction have been examined for its ability to generate $^1O_2$. Although alkyl-SiNC does not possess an intrinsic ability to produce $^1O_2$, this thesis shows that perylene-SiNCs produce $^1O_2$ with a moderate quantum yield (Φ_Δ) of up to 27% in cyclohexane. These results were obtained by measuring singlet oxygen phosphorescence at 1270 nm. SiNCs play an important role in generating $^1O_2$ with perylene-SiNCs conjugates, as SiNCs can harvest UV and blue radiation and transfer the absorbed energy to a triplet state of the attached dyes. The triplet state population increases and leads to an increase in $^1O_2$ generation. At the same time, the SiNC-dye conjugates demonstrated NIR luminescence with PLQY up to 22%. The luminescence behaviour and photosensitizing properties of the SiNC-dye conjugate could therefore attract interest as a new multifunctional platform in the field of bio-applications.

Table of Content

List of Figures

List of Tables

List of Publications

I. Beri, D., D. Busko, A. Mazilkin, I.A. Howard, BS. Richards, and A. Turshatov, *Highly photoluminescent and stable silicon nanocrystals functionalized via microwave-assisted hydrosilylation.* RSC Advances, 2018. **8**(18): p. 9979-9984.

II. Beri, D., M. Jakoby, I.A. Howard, D. Busko, BS. Richards, and A. Turshatov, *Improved photon absorption in dye-functionalized silicon nanocrystals synthesized via microwave-assisted hydrosilylation.* Dalton Transactions, 2020. **49**(7): p. 2290-2299.

III. Beri, D., M. Jakoby, D. Busko, BS. Richards, and A. Turshatov, *Enhancing Singlet Oxygen Generation in Conjugates of Silicon Nanocrystals and Organic Photosensitizers.* Frontiers in Chemistry, 2020. **8**(567).

Abbreviations

Φ_{Δ}	Singlet oxygen quantum yield
$^1O_2$	Singlet oxygen
AFM	Atomic force microscopy
ATR-IR	Attenuated total-reflectance infrared spectroscopy
AU	Absorbance unit
CB	Conduction band
CTH	Conventional thermal hydrosilylation
DLS	Dynamic light scattering
DET	Dexter energy transfer
EMA	Effective mass approximation
FTIR	Fourier-transform infrared
FWHM	Full width at half maximum
HF	Hydrofluoric acid
HOMO	Highest occupied molecular orbital
HSQ	Hydrogen silsesquioxane
LED	Light emitting diode
LUMO	Lowest unoccupied molecular orbital
MW	Microwave
MWH	Microwave-assisted hydrosilylation
N4E	Nanophotonic for energy
NCs	Nanocrystals
NIR	Near-infrared
PDT	Photodynamic therapy
PL	Photoluminescent
PLE	Photoluminescent excitation
PLQY	Photoluminescent quantum yield
PS	Photosensitizer
QC	Quantum confinement
QD	Quantum dots
RT	Reverse energy transfer
SiNCs	Silicon nanocrystals
SLS	Static light scattering
TEM	Transmission electron microscope
TTA-UC	Triplet-triplet annihilation up-conversion
UV	Ultraviolet
VB	Valence band
Vis	Visible
XRD	X-ray diffraction

Preamble

First of all, a big thanks to my supervisor Prof. Bryce S. Richards, who has provided guidance and direction in completing this thesis. I also give a huge thanks to my mentor, Dr. Andrey Turshatov, who has been patiently guiding me to find a passion for scientific research. It might be challenging to find someone else like you, and it will be a debt of gratitude for my entire life. I am deeply grateful to Prof. Frank Breitling for being willing to be my "Doktorvater" and allowing me to be graduated from the Faculty of Chemistry and Biosciences. I also thank my co-authors Dr. Ian A. Howard, Dr. Dmitry Busko, Dr. Andrey Mazilkin, and Marius Jakoby, for their support and patience in many discussions and sharing ideas, photoluminescent (PL) and singlet oxygen QY measurements, TEM measurements, time-resolved lifetimes, and PL-temperature dependent measurements.

Friends have become family in the past five years of doing this Ph.D. and have stood by me in the time I spent here. I would like to thank you for all of the moral support and advice through all of the rough times I have been through, especially to my colleagues and office mates Dr. Stephan Dottermusch and Dr. Michael Oldenburg, to my lab mates and colleagues Natalia Kiseleva, Roman Lyubimenko, Dr. Damien Hudry, Tobias Berger, Dr. Hossein B. Nasrabadi, Dr. Wengsheng Yan, Dr. Lwitiko Mwakyusa, Vu Hong Lee, Dr. Nicolö Beroni, Dr. Michael Adams, Sheying Li, Reetu Joseph, Aiman Roslizar, Vinay Kumar, Ngei Katumo, Dr. Aditya Chauhan and Milian Kaiser for their support and fruitful discussions in nanocrystals silicon and measurements.

I would like to thank all of the IMT members (past and present), mostly to Dr. Holger Moritz, Dr. Mathias Heckele, Dr. Klaus Bade, Dr. Markus Guttmann, Dr. Uwe Köhler, Siegfried Roth, Giraud Nina, Jürgen Benz, Heinz Dinglreiter, Matthias Gramlich, Birgit Hübner, and Alexandra Möritz for helping me with any difficulties that I came across. I would like to thank Hartmut Speck and Oliver Kaas from International Affairs (INTL) at KIT, and Dr. Martin Lauer from KSOP, who have provided much supports during my stay here. I wish to express my sincere gratitude to Prof. Ganefri and Prof. Ali Amran from UNP and Ditjen Kemristek Dikti for Scholarships and valuable guidance during my journey in KIT.

I would like to thank my family, my lovely wife Okriyeni Sudiar, my handsome boys Asby R. Beri, and Dziad F. Beri and my lovely little girl Jasmine S. Beri. Last but not least, my dad M.Akmal, my mom Rismawati, my lovely sisters Arleni M. Deli and Ratmeli Storina, my dear brothers Taufik Hidayat and Mazwir Ramon for always being there for me throughout my entire life with encouragement, love, and support.

Karlsruhe, December 2020

Deski Beri

1 Introduction

1.1 Research evolution on silicon nanocrystals

The history of quantum dots (QDs) or nanocrystals (NCs) based on semiconductors (group IIB, IIIA, IVA, VA, and VIA) can be traced back to the invention of diffused CuCl and CdSe nanocrystals in a glass substrate by Ekimov in the 1980s [1, 2]. Although a comprehensive theory about the properties of these QDs came out later, the impacts of this invention were remarkable [3]. Indeed, for more than 30 years, people have tried to understand the physical properties of QDs and exploit those in a large variety of devices, such as solar cells, light-emitting diodes (LEDs), television light-emitting displays, sensors, bioimaging, and photodynamic therapy [4]. The primary feature of QDs is size-induced tuneable emissions, spanning from ultraviolet to a near-infrared spectrum with a relatively narrow distribution and relatively high photoluminescent quantum yields (PLQY). QDs demonstrate a broad absorption spectrum, with larger cross-sections compared to fluorescent dyes (chromophores) [5].

The use of QDs in solar cell technology has long been one of the most significant research and development concerns [6]. QD's solar cells are expected to surpass the Shockley–Queisser power conversion efficiency of 33% for silicon-based solar cells [7]. QDs such as PbSe show the ability to generate multiple excitons [8] from a single photon [9]. In 2016, Lan *et al.* [10] reported that solar cells made from PbS provided a power energy conversion of 9.9% [10]. This record was then broken two years later by Xu *et al.* [11], who modified the distance between the QDs using the inorganic matrix and attained a power conversion efficiency of up to 12%, the highest record reported to date [11]. There is still a lot of work and improvement that needs to be done in the technological and scientific approach to surpass the Shockley–Queisser power conversion efficiency.

In light-emitting diodes (LED), QDs are used as a luminescent centre. Metal-based QDs [12] have been used to generate electroluminescence at various wavelengths of visible light, such as the ZnCdS quantum dot for blue luminescent (~ 440 nm), combinations of ZnSe / CdSe / ZnS quantum dot for green light luminescent (~ 550 nm) and ZnCdSe QDs for red light emission (~ 630 nm) [13]. The biggest challenge in quantum dot-based LEDs is relatively low PLQY [13]. Bozyigit *et al.* [14] proposed that the main reason is the high luminescent quenching due to Auger recombination. Thus, it takes a compelling material design to suppress this Auger process as much as possible [14].

Another potential application of semiconductor QDs is in photoluminescent (PL)-based sensors technology [15]. Among the fluorophore materials – e.g., organic dyes, transition metal complexes, and semiconductor QDs –semiconductor QDs offer an advantage over other materials (e.g. luminol and ruthenium bipyridine $Ru(bpy)_3^{2+}$) in sensors technology due to their broad absorbance band in the ultraviolet and visible range, longer PL-lifetimes (in microseconds), good stability, and relatively low production cost [16]. Therefore, there is a high degree of freedom to choose the excitation wavelength to

get a relatively narrow emission [17]. An optical [18, 19] and smart temperature sensors [19, 20] made of QDs could be used to detect a rise in temperature [21] at the first state precautions of contagious/infectious diseases [22]. Semiconductor QD based sensors are expected to contribute substantially to modern sensing technology because of the device's effectivity and reliability [23]. However, some problems arise in fabricating QDs based sensors, including low solubility of QDs materials, amplifying photoluminescent properties, and improving PL-sensing [16].

Due to the chemical stability [24, 25], sensitivity [26, 27], and minimal invasiveness [28] of QDs, it is ideal to be used as a fluorescent probe in bioimaging [29], including optical imaging [30, 31], and magnetic imaging [32]. Fluorescent QDs with significant quantum yields could benefit optical imaging (e.g., $CuInS_2$ QDs with high PLQY synthesized in a microwave reactor) [33]. In addition, the magnetic resonance from unpaired electrons distributed in *f*-orbitals could be used to synthesize a magnetic imaging probe quantum dot (e.g., in Gd-doped CuInS2/ZnS, synthesized in microwave reactor) [34]. Finally, some semiconductor QDs such as CdSe, CdTe, CdS, PbS, PbSe, and PbTe have become a topic of interest over the last decades, as photothermal probes in photodynamic therapy [35-37].

However, toxicity becomes one of the main drawbacks of those semiconductors (group IIB, IIIA, IVA, VA, and VIA) QDs [38]. Some elements in (IIB, IIIA, IVA, VA, and VIA) groups are known hazardous for humans, and there are many reported cases about Cd [39]and Pb-poisoning [40-42]. On the other hand, silicon is a non-toxic element that is also very abundant in nature [43, 44]. However, due to its indirect bandgap, silicon has limited emission properties. Therefore, excited electrons need another pathway (phonon mediated) to recombine with holes [45-47]. Such a recombination pathway does not emit photons effectively (see Figure 1-1). In photonic and optoelectronic applications, the potential of bulk silicon is less exposed until the luminescence of porous silicon is observed [45, 46], proposing that porous silicon's luminescence are due to the so-called quantum confinement effect [47]. In addition to porous silicon, quantum confinement could also be achieved by silicon particles having spatial dimensions in a few nanometres, nearly at the range of the Bohr radius (≤ 5 nm) [48, 49]. The spatial dimension of a silicon particle in the Bohr radius range is called silicon nanocrystals (SiNCs). This breakthrough invention opens up a new era of silicon chemistry into a vicinity dimension, related only in two aspects of interest, either by tuning the particle size or ligands modification by functionalization [50].

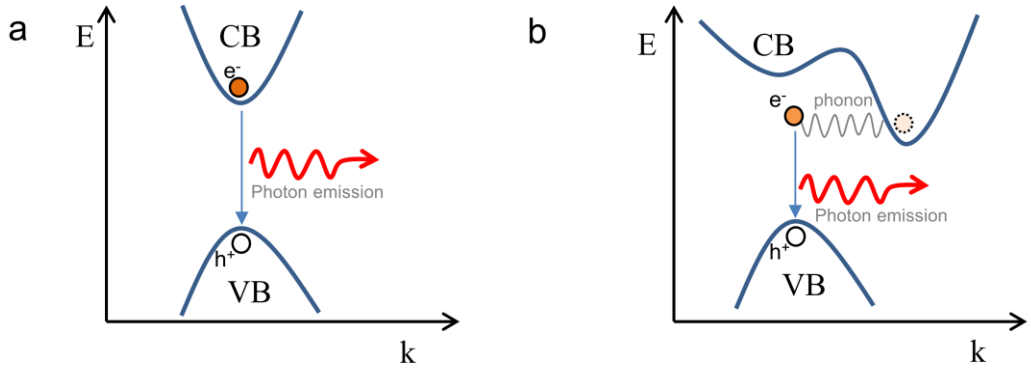

Figure 1-1. Schematic illustration of (a) direct bandgap and (b) indirect bandgap semiconductor

The emission from SiNCs of different sizes has been intensively studied for more than 30 years, and as well as in direct bandgap semiconductor QDs, the emission of SiNCs could also be tuned from orange-red (~590-800 nm) at particle size ~1-3.5 nm into Near Infrared (NIR) at ~800-1,100 nm at particle size ~3.6 – 12 nm. In Google Scholars©, the number of publications in luminescence SiNCs is astonishing. Our data present a positive trend since 1990, and the peak shows 12,000 articles published in 2017 (Figure 1-2a). When we specify our search only for photodynamic therapy, which is one of the potential applications in the future of luminescence SiNCs, the data shows sharp increases since 2000, from ~0 to ~6000 articles in 2019 (Figure 1-2b).

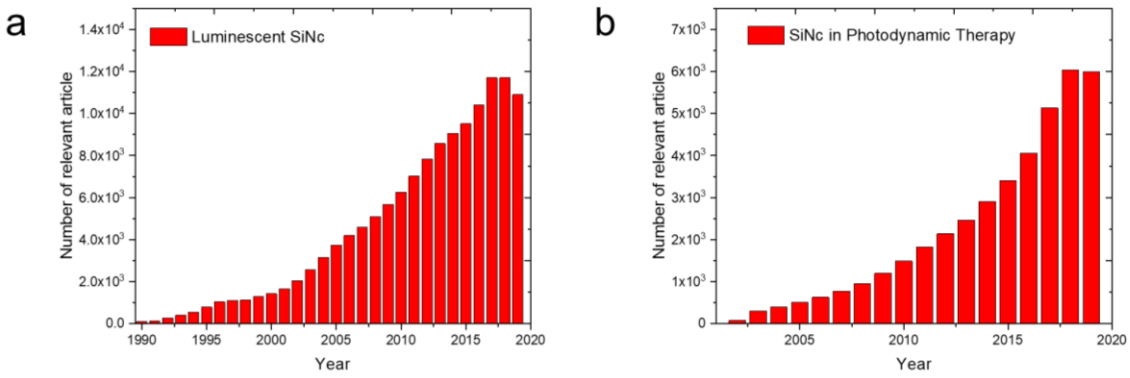

Figure 1-2. The number of articles describing luminescent SiNCs published since 1991 retrieved using Google Scholar search engine with the keywords: (a) "luminescence of SiNCs"; and (b) "SiNCs in photodynamic therapy".

In this thesis, I seek to answer the following research questions relating to SiNCs research:

(1) How surface passivation with different alkyl chain length has affected the photophysical and stability of SiNCs,

(2) How surface passivation with chromophores/dyes could be used as an alternative to enhance the luminescent properties of SiNCs, and

(3) How energy transfer from SiNCs could be used to enhance singlet oxygen production of chromophores/dyes.

There may be some other challenges in the SiNCs research that is not covered in this thesis. Nevertheless, the challenges will be discussed in more detail in the following chapters.

In Chapter 1, semiconductor QD research's evolution has been discussed briefly—the essential and potential application of semiconductor QDs in daily life. Furthermore, SiNCs, as part of semiconductor QDs, were described as advance than others in toxicity. Therefore, SiNCs research demonstrated a positive trend in the last few decades. In the closing section, our small contribution was described to the future of SiNCs research.

Chapter 2 will describe the literature study, including the luminescent origin of SiNCs, an overview of various chemical and physical methods for fabrication of hydride functionalized (H-SiNCs), an overview of functionalization reactions for surface modification of H-SiNCs, and an overview of efficient energy transfer. Herein, the luminescence properties are described both using quantum confinement and surface modification. Whereas the synthetic method of hydrogen-terminated SiNCs is described by using top-down and bottom-up approaches. The functionalization reaction is described based on the existing literature methods, including thermal and radical initiated functionalization reactions. Indeed, the reference work on dye functionalization and the ligands' vital role in passivation is described herein. The literature review on efficient energy transfer of dye modified QDs (CdTe), and SiNCs is described in the final section.

Chapter 3 will describe the methodology, covering the experimental section of the SiNCs synthesis, characterization methods, and measurements of photophysical properties. The synthesis starts from hydrogen functionalized SiNCs, followed by the functionalization reaction using alkyl and chromophore/dyes. Resulting in materials which are then cleaned and purified and ready for structural and optical characterization. The structural characterization is conducted using ultra-violet-visible (UV-Vis) spectroscopy, fourier-transform infrared (FTIR) spectroscopy, X-ray diffraction (XRD), transmission electron microscope (TEM), and dynamic light scattering (DLS). Whereas the optical characterization is performed using PL-excitation and emission, PLQY, and PL-lifetimes measurements. In chapter 3, PLQY measurements are described using comparative and absolute methods. Additionally, singlet oxygen yield measurements are described using the chemical and phosphorescent methods. Finally, a brief description of the uncertainty in computation is discussed.

Chapter 4 will present the results of the synthesis and characterization of alkyl functionalized SiNCs. Herein, the functionalization reaction with different alkyl chain lengths is described in the discussion. The effect of different alkyl chain lengths passivation on PLQY and stability is well described in PLQY *vs*. alkyl chain length and PLQY *vs*. time. TEM and DLS data describe the effect of functionalization on the particle size. In addition, FT-IR analysis presents the oxidation level of different alkyl chain length functionalization SiNCs.

Chapter 5 will present the results on dye functionalized SiNCs. The dye has an essential role as a light antenna to absorb light at the visible region of electromagnetic radiation. The fact is that alkyl-SiNCs' have minimum absorption at 400 to 600 nm. Therefore, dyes are expected to enhance the absorption and donate their energy to SiNCs *via* efficient energy transfer. Here, two different dyes are using namely perylene and BODIPY. The results demonstrate that due to functionalization with dyes, the absorption of SiNCs increases significantly, leading to the emission's enhancement at the near-infrared region *via* efficient energy transfer. Overall, the brightness of dye functionalized SiNCs demonstrates significant enhancement (up to~2.8x) compare with the corresponding alkyl functionalized SiNCs.

Chapter 6 will present the results on perylene-SiNCs as a photosensitizer for singlet oxygen. The results of singlet oxygen quantum yields using chemical and phosphorescent methods are presented here. Although alkyl functionalized SiNCs do not possess the intrinsic ability to generate singlet oxygen. Perylene functionalized SiNCs demonstrate an ability to generate singlet oxygen. Therefore, the luminescent and photosensitizing properties of dye functionalized SiNCs could be attractive for future bio-applications.

Finally, Chapter 7 will present the conclusions and outlook of the thesis. Essential results on SiNCs synthesis are outlined in the conclusion, as well as significant results regarding the structural characterization and photophysical properties also described for alkyl-SiNCs and dye-SiNCs synthesized in microwave reactors. This chapter will conclude with possible efforts to develop research on SiNCs and correct any weaknesses that may exist at this time.

2 Literature Review

2.1 The luminescent origin of SiNCs

The luminescence origins of SiNCs have long been debated. The emission from the core of SiNCs is well defined in quantum confinement (QC) theory [51-53]. When the particle size of semiconductor material is finely divided close to Bohr's theoretical radius (~5 nm for Si), the core of the material could be assumed as a centre of mass surrounded by the swarm of electrons, and the electrons on the surface behaving as the trajectory of an electron in the hydrogen atom [54]. The electronic behaviour around nano-size particles could be approximated by the particle in the box or quantum well theories [55]. Basically, NCs or QDs has been described as a zero-dimensional quantum well, characterized by discrete energy levels [56]. Very sharp lines have been observed in silicon as well as in other materials investigated by PL spectroscopy of single SiNCs [56-58]. This energy level (leads to bandgap) is particle size-dependent, and the boundary condition is the theoretical Bohr radius. The smaller particle size leads to the wider in the band gap, while the more extensive particle size leads to the narrowing of the band gap[59]. The band gap is proportional to the emission energy of photons. Thus, the electronic transition from the wider band gap results in to the emission of higher energy photons, whereas the electronic transition from the narrow band gap results in to the emission of lower energy photons.

The band gap insight could be revealed by discussing the energy band of the bulk semiconductor materials (see Figure 1-1). Although it is a bit vague because SiNCs do not have a genuine energy band (e.g., valence or conduction), the terminology is still valid to some extent in order to simplify the problems [54, 60]. Luminescence is expected due to electron-hole pairs' radiative recombination from the lowest exciton states [61-64]. The lowest energy of electrons and holes is called the ground state, whereas the higher energy level of an electron and hole is called an excited state. Electrostatically couple of electrons and holes consisted of excitons [65] and will play the primary role in the QDs and nanocrystals' photophysical properties. Using the Heisenberg uncertainty principle, the electron is distributing at any possible state/wave function. In quantum mechanics, the shortest distance an electron has to move around the nucleus is called Bohr radius (a_0). Holes and electrons in particular energy levels are bonded by Coulomb attraction [66]. In nanocrystals or QDs, the expression of Bohr radius (a_0) is formulated using Equation (2.1).

$$\boldsymbol{a_0 = \frac{h^2 e_r}{\pi e^2}\left[\frac{1}{m_e^*} + \frac{1}{m_H^*}\right]} \tag{2.1}$$

Where e_r is the permittivity of material in a vacuum, m_e^* is electron reduced mass and m_H^* is reduced mass of the hole, and *h* is Planck constant.

The Brus model uses the bandgap approximation to determine the Coulomb-correlation effect for semiconductor QDs [67]. The model could predict quantum dot size based on PL-energy emission, as formulated in Equation 2.2 [68-70].

$$\boldsymbol{E_{PL} = E_g + \frac{h^2\pi^2}{2R^2}\left(\frac{1}{m_e^*}+\frac{1}{m_H^*}\right) - \frac{1.786e^2}{e_r R}} \qquad (2.2)$$

Where $\boldsymbol{E_{PL}}$ is emission energy (eV), the E_g is the energy gap of silicon (1.17 eV), R is quantum dot/nanocrystal radius, e_r is relative permittivity in a vacuum (11.68), m_e^* and m_H^* is the effective mass of electron and hole equal to $0.19m_0$ and $0.286m_0$, respectively. Equation 2.2 is a so-called effective mass approximation (EMA) because it only considers the effective mass ratio of holes and electrons [52, 71, 72].

The peak maximum of PL-spectra in Figure 2-1a was re-plotted in Figure 2-1b. PL- spectra demonstrate strong relationships with particle size. The solid line in Figure 2-1b demonstrates the EMA calculation and is compared against the experimental data taken from Yu *et al.* [73]. In this work, the particle size was obtained using a transmission electron microscope (TEM) and small-angle x-ray scattering (SAXS). Data in Figure 2-1b shown that EMA calculation is working correctly to predict PL- spectra of SiNCs, in size diameter above 4.3 nm. However, for a diameter too below 4.3 nm, the plot deviates from the experimental values (overestimation). Therefore, to have an acceptable combination of theoretical and experimental data, another approach used the so-called semi empirical approximation [74].

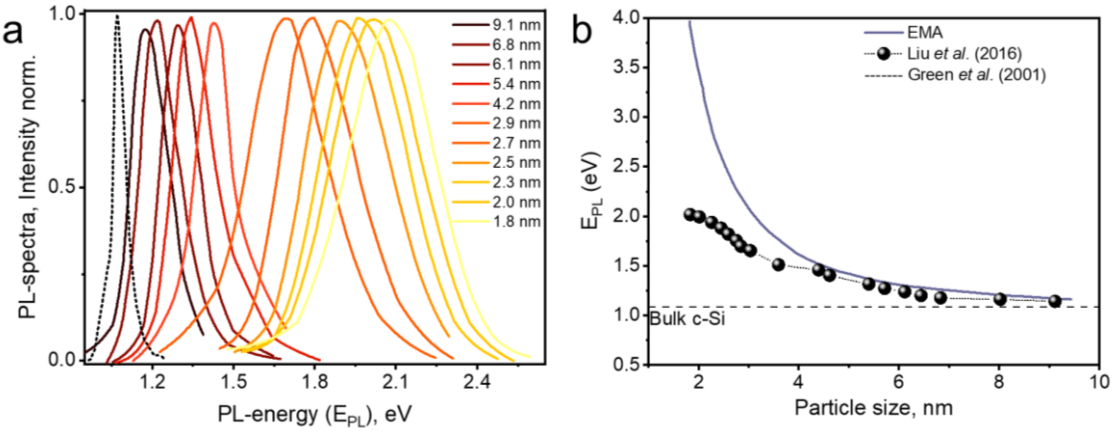

Figure 2-1. (a) PL-spectra spectra of SiNCs with various average diameters and maximum intensity normalized. Adapted with permission from Yu *et al.* [73] Copyright © 2017, American Chemical Society. PL-spectra of bulk crystalline silicon [75] presented in dash line. (b) Peak PL-spectra energy plotted versus the average nanocrystal size, and the plot determined using Equation 2.4. The dotted line provides a reference for the bulk bandgap of Si (1.12 eV), and (●) is experimental data from [73]. Adapted with permission from Yu *et al.* [73] Copyright © 2017, American Chemical Society.

The early semi-empirical approximation quantum confinement theory for SiNCs was developed by Proot *et al.* [76]. The calculation was made based on the suitability of experimental PL to the linear combination of atomic orbital theory (LCAO). The calculation was performed for various numbers of Si atoms, up to 2058. The result was that PL-emission energy was inversely proportional to particle diameter

and could be formulated as, $E_{PL} \propto {}^{1}/_{d^{1.39}}$. Then, Delerue *et al.* [64] formulated the corresponding Equation (2.3) by considering the dangling bonds on the surface of SiNCs [77].

$$\boldsymbol{E_{PL} = E_0 + \frac{3.73}{d^{1.39}}} \tag{2.3}$$

Where, E_{PL} is PL-emission energy (eV), E_g is the energy gap of bulk silicon ($E_g = 1.17eV$), and d is particle diameter (in nanometre). Next, Ledoux *et al.* [78] made some corrections by considering the lattice parameter of SiNCs, rather than using bulk silicon lattice, and the corrected formula is presented as Equation 2.4 [78].

$$\boldsymbol{E_{PL}^{corr} = E_0 + \frac{3.73}{d^{1.39}} + \frac{0.881}{d} - 0.245} \tag{2.4}$$

However, the resulting calculation using Equation 2.4 still deviated when determining particle sizes below 3.5 nm. Likewise, many other theories were proposed to explain the relation between PL-emission energy and particle size, including the tight-binding band theory [79, 80] and ab-initio density functional theory [74]. So far, there is no single theory that could satisfactorily explain the experimental data [81]. Figure 2-2 depicted the re-plotted data of some experimental and theoretical relationships between PL-emission energy and particle size of SiNCs.

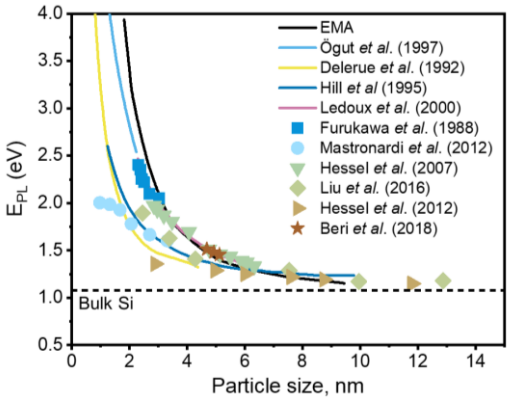

Figure 2-2. Size dependence of photoluminescence SiNC, comparing theoretical and semi empirical approximations (lines) against experimental values (symbols) [10, 64, 70, 72, 74, 76, 78, 79, 82-85].

2.2 Photoluminescent quantum yields and photoluminescent lifetimes of SiNCs

Sun *et al.* [86] demonstrated the relationship between size and PLQY. When particle size decreases gradually from ~13 nm to at least ~1 nm, the PLQY value of particles exhibits unique behaviour [74]. Quantum yields will gradually increase if the particle size is decreased from ~ 13 nm to ~ 3.5 nm; here, quantum yield reaches a maximum and then slowly decreases if particle size continues to decrease from ~3.0 nm to ~1 nm (Figure 2-3a). The PLQY as a function of particle size resembles the shape of a volcano or pyramid, so it is known as the volcano or pyramid behaviour of quantum yield [87-90].

Firstly, the smaller the particle size of SiNCs, the better the optical quality is due to the bandgap changing from an indirect bandgap to a direct bandgap [91]. The lifetime's measurement in Figure 2-3b well supports this phenomenon. Ultra-small particle size (~1 to ~3 nm) have a nanosecond to a few microsecond lifetimes (resembling the direct semiconductor QDs), whereas a slightly bigger particle size (~3.5 to ~13 nm) have hundreds of microseconds and up to a millisecond of lifetime (resembling the indirect semiconductor QDs). Secondly, when the confinement effect strengthens, the emission is also increased, explaining the volcano's maximum point. [79, 81, 92].

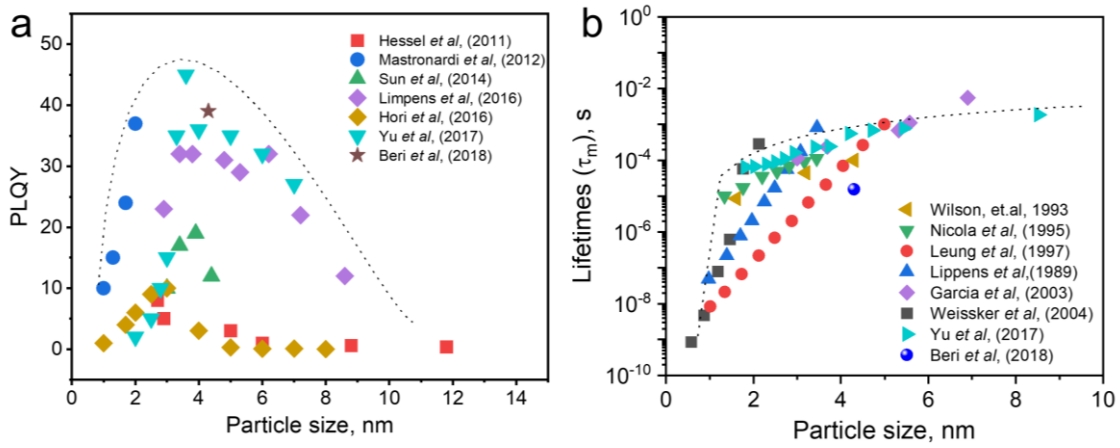

Figure 2-3. (a) PLQY of alkyl functionalized SiNCs as a particle size function from some reports (■)[72], (●) [90], (▲) [86], (♦) [93], (♦) [94], (▼) [73], and (★)[85]. (b) Radiative lifetimes in μs were measured at PL peak wavelengths of different size of SiNCs, (■)[95], (●)[96], (▲)[97], (▼) [79], (◄)[98], (►) [73], (●) [85]. The dash line is the eye-guide to accentuate the optimum reported PLQY.

The relationship between PL-lifetimes and the diameter of SiNCs is demonstrated in Figure 2-3b. Radiative lifetimes increased monotonically with increasing particle size, and the relationship between PLQY and PL-lifetimes can be formulated as in Equation (2.5).

$$PLQY = \frac{k_r}{k_r + k_{nr}} = k_r \tau_m = \frac{\tau_m}{\tau_r} \tag{2.5}$$

$$\tau_m = \frac{1}{k_r + k_{nr}} \tag{2.6}$$

Where k_r and k_{nr}, are radiative and non-radiative recombination rates, τ_m, is measured lifetimes, which is the sum of radiative lifetimes - τ_r, and non-radiative lifetimes - τ_{nr} [83]. The high PLQY can occur because the radiative recombination contribution rate is dominating the rate of non-radiative recombination contributions. Nevertheless, from the data presented in Figure 2-3 and Equations 2.5 and 2.6, it can be seen that for particle size from 1 to 4 nm, radiative lifetimes significantly enhanced from sub-nanosecond to microseconds and then gradually flattened when particle size increased from 4 up to 9 nm. The explanation for this phenomenon could be referred to as the behaviour change of the bandgap in [99-101]. When the particle size was reduced to below 4.0 nm, the bandgap behaves as a direct-like bandgap

semiconductor. Herein, the emission emerges phononless, whereas radiative lifetimes were in the nanosecond to microsecond ranges.

2.3 Synthesis of hydrogen-terminated SiNCs

SiNCs could be synthesized in various ways [102-104]. A standard method to synthesize SiNCs is carried out using two approaches: the bottom-up synthesis, where particles in angstrom size are enriched in the condensation process to become more extensive in size. In contrast, the second approach is the so-called top-down approach, where large particles (bulk material) are breaking down into nano-sized particles. The first approach is ubiquitous for synthetic chemists to synthesize nanoparticles from elements/compounds [105]. Typically in the bottom-up approach, nanocrystals are built atom-by-atom, molecule-by-molecule to form cluster-by-cluster of SiNCs [106]. The bottom-up approach promises a better chance to obtain fewer nano-structural defects, more homogeneous chemical compositions, and better long-range ordering. This is mostly driven by the reduction of Gibbs free energy into a thermodynamically equilibrium state [106]. Among many synthesis steps, the nucleation is crucial for succeeding in the synthesis process [107]. In the following paragraph, the bottom-up approach is described briefly, based on the precursors' ambient state.

The precursors for bottom-up reactions could be in gas, liquids, and solids states. The report from Jurbergs *et al.* [108] surprised many researchers by claiming an ensemble of alkyl functionalized SiNCs exhibited ~60% PLQY, synthesized in the non-thermal plasma reactor. However, the report was somewhat inconsistent with others [109, 110], and the reproducibility of the results has remained in question[111]. The non-thermal plasma synthesis is one method to synthesize SiNCs using a bottom-up approach and a silane gas is used as a precursor. To my knowledge, the first work on SiNCs synthesis by using plasma synthesis was conducted by the group of Roca I Carbaroccas, which demonstrated the deposition of an amorphous matrix mixture of polymorph silicon consisting of SiNCs with ~2-5 nm in diameter [112-115]. The formation of SiNCs was unexpected at the beginning and treated as contamination by the Carbaroccas group. However, the research shifted when SiNCs become the main product [116]. Further outstanding work on developing synthetic methods of using a non-thermal plasma reactor in SiNCs synthesis could be attributed to the group of Kortshagen [117]. In a non-thermal plasma reactor, silane (SiH_4) gas was used as precursors. The reactor consists of a glass tube with copper rings wrapped around it, functioning as high voltage electrodes. The precursor (SiH_4) and argon gas mixture were fed continuously into the discharge, and at the bottom, SiNCs were collected continuously [118]. By adjusting the precursor's flow rate in the reaction zone, the size of the produced SiNCs can be tuned. The functionalization of the produced SiNCs was performed as post-reaction treatment *via* thermal or radical functionalization reaction. The synthetic materials functionalized with dodecene (C12) and a particle size ~5nm, which exhibited tremendous quantum yield (~60%) [85].

The advantage of using non-thermal plasma synthesis are that non-thermal plasma is capable of converting gas precursors, such as silane (and silicon tetrachloride) into high-quality nanocrystals, it has a high production rate, and tight control over the average particle. Additionally, non-thermal plasma is a promising tool to produce high-quality silicon QDs that show excellent optoelectronic properties after the proper surface functionalization. However, this technique's possible drawbacks are the result of reasonably broadband size distributions observed at the end of synthesis. So the post-processing techniques are developed to separate the ensemble into narrow size distributions samples [118].

Liquid phase precursors could be used to synthesize SiNCs in the bottom-up approach. The group of Kauzlarich [119-124] has been actively developing a synthetic method in this area. The synthesis's reaction route was developed using Zintl salt [123], such as SiK and SiNa [120], as precursors. The precursors were further reacted with tetrachloro silane ($SiCl_4$) to form chloride-terminated SiNCs [124]. Chloride-terminated SiNCs were then treated with alcohol or siloxane to functionalize the surface and produce dispersible functionalized SiNCs in solvents [122]. In general, the reaction could be performed in a reflux reactor integrated with the Schlenk line and could also be conducted in the microwave reactor [119]. The main advantage of this process was that this work proved to yield a relatively narrow size distribution. Relatively narrow size distribution ~2-3 nm were produced using this method with microwave-assisted hydrosilylation [119]. However, the synthesis required expert users because very reactive reagents were used in reactions. Due to low reaction temperature and limited solvents, longer reaction times are required to perform synthesis. The advances in microwave synthesis could reduce the drawback and be considered a promising candidate to produce a reasonable amount of SiNCs [118].

Pressurized liquid precursors were developed by the Körgel [73, 125-127] group to synthesize SiNCs. In the synthesis, the supercritical reactor was designed for the critical point of solvents (e.g., 500°C, 345 bar). The precursor diphenyl silane was decomposed at a supercritical point to produce nanocrystal silicon [126]. The development of this method could produce tuneable emission SiNCs. The main advantage of using this technique is the relatively narrow distribution of particle size; however, to run a reaction at such a high temperature and pressure requires advanced knowledge and skills in chemical synthesis [125].

Another method to synthesize SiNCs from liquid precursors is the microwave-assisted synthesis and hydrothermal synthesis from 3-aminopropyl trimethoxysilane (APTMS). The silane conversion into SiNCs is carried out in water using citrate groups as reducing agents in the microwave (MW) or hydrothermal reactor. Ddungu *et al.* [128] conducted a study to compare the yield of MW-assisted and hydrothermal synthesis on fabricating SiNCs from APTMS precursors. The results showed that hydrothermal synthesis produced SiNCs with particle size 2.9 ± 1.0 nm, whereas MW synthesis produced SiNCs with particle size 3.7 ± 1.5 nm. The particle sizes were measured by TEM. Both synthetic methods result in a mixture of amorphous and crystalline, as confirmed by XRD and electron diffraction. PL-spectra shows emissions in the blue region of electromagnetic radiations (PL-max at 450 nm). A relatively similar result was reported previously by He *et al.* group [129], and the group even claimed super high PLQY value

(~90%) for blue emissions [109], which were scientifically thrilling. However, Shen *et al.* [130] wrote a critical review, describing the misleading interpretation of the organic contaminant in the TEM-grid as SiNCs. Therefore, super high PLQY of blue emissions remains a question until now, because the photoluminescent origin is very closely similar to the carbon quantum dot emission [46].

SiNCs could be synthesized from silicon embedded in a solid matrix, namely silicon oxide, silicon nitride, and silicon carbide matrices. Sub-stoichiometric silicon oxide (SiO_x, $x<2$) has been used as a precursor to synthesize luminescent SiNCs since the early 1990s [118]. Annealed silicon monoxide in an argon atmosphere and at a high temperature range of 800-1300°C, produces SiNCs embedded in SiO_2 matrix. Various annealing temperatures could vary the PL-spectra and particle size [85, 88, 89, 131-136]. The synthesis of SiNC embedded in a silicon dioxide matrix will be described in more detail in the next section. Beside silicon monoxide, silicon nitride could also be used as a precursor to synthesize SiNCs. The work from Park *et al*. (2000) and co-workers proved that amorphous SiNCs were growing in silicon nitride film by using plasma-enhanced chemical vapour deposition. Interestingly, photoluminescent of the result in SiNCs could be tuned from blue to near-infrared radiation. In the explanation, the author claimed that the emission properties of the SiNCs produced by this method followed the existing quantum confinement theory, where the emission spectra correspond with the size of the particle [137]. Compared to the oxide embedded SiNCs, nitrogen embedded SiNCs demonstrate the emission in the full range of visible in electromagnetic radiation [138]. However, the full detail on emission properties and fabrication needs to be understood more [118]. There is a slight similarity with the silicon nitride; silicon carbide can also be used as a precursor to synthesize SiNCs by using plasma chemical vapour deposition. SiNCs were developed by modifying an inductively coupled plasma system to produce high crystalline silicon film. In principle, the process was interrupted by introducing methane gas to the gas mixture to obtain some degree of carbon atom in the thin layer of amorphous film. The final yield is the formation of ~5 nm SiNCs embedded in the silicon carbide matrix investigated by TEM [118, 139]. Generally, synthesis of SiNCs embedded in oxide and nitride seems to be applicable for large scale synthesis, whereas SiNCs embedded in carbide limits the formation of side nucleation of silicon carbide. The main drawback of the synthesis using oxide, nitride, and carbide precursors are that is so hard to control the homogeneity of the particle size (narrow size distribution) [118].

The second approach is so-called top-down synthesis, where large particles (bulk material) break down into nano-sized particles. The process of breaking down large particles can be performed chemically or physically. Chemically, large particles are etched in a controlled environment using corrosive chemicals, so the corrosive substances dissolve the particles gradually from the surface. The process is conducted within a period until the desired particle size is obtained. SiNCs could be synthesized by etching the bulk silicon gradually into nano-size silicon. The mixture of HNO_3 and HF was used to etch bulk silicon produced by silane pyrolysis into ~5 nm diameter of SiNCs [140]. The wavelength of PL-spectra was controlled by controlling the etching concentration and time. The particle size and crystallinity were monitored using TEM and XRD and demonstrated that wet etching was gradually digging from the edge of the material without affecting the core of SiNCs [141]. Heinrich *et al.* [142] performed an

electrochemical etching to produce a colloidal suspension of SiNCs. Porous silicon or silicon wafer was electrochemically etched in electrolytic HF batch. The resulting material was claimed to be hydrogen-terminated SiNCs (**H**-SiNCs) and SiO_2 free and ready to be re-dispersed in the solvent. PL-spectra of H-SiNCs was in visible to a near-infrared range of electromagnetic radiation (500-800 nm). Broad size distribution in the range of below 10 nm was obtained using TEM. The XRD analysis shows that SiNCs have polycrystalline structures. Compared to the pyrolysis of silane gas, electrochemical etching from porous silicon has an advantage regarding the purity of the SiNCs, as the pyrolysis method might result in some other trace elements being contained in the reaction product. However, the main drawback of this method is that it is very challenging to control the narrow size distributions [142].

The physical method could also be performed by blasting porous or crystalline silicon into ~1 to ~20 nm particle size. In application, the physical and chemical methods were used complementarily to get the desired result. One example of silicon blasting is laser ablation synthesis. Abderrafi *et al.* [143] used a pulsed nanosecond Nd: YAG laser (355 nm, 40 ns pulse duration, 5 kHz repetition rate) to irradiate the dipped silicon wafer in the chloroform solvent. The excavated SiNCs were dispersed in the solvent and collected after evaporation in a vacuum. In the TEM image, the particle size of the sample after laser ablation showed wide distribution from ~20-120 nm and did not show any luminescent properties. Therefore, the author proposed post-treatment with HF etching. After being etched chemically, the particle size was down to 3.8 ± 2.5 nm, and Raman spectra proved a wideband peak at 521 cm^{-1} as the signature of SiNCs. PL-spectra of the hydrogen-terminated SiNCs shows a broad luminescent from 400-900 nm. A similar report on the laser ablation synthesis method could be found in [144-149]. The advantage of using laser ablation is that it produces a high amount of SiNCs in a relatively brief period. However, the size distribution of non-etched samples could be anywhere from 20-150 nm, far above quantum confinement. The post-treatment needs to be done to target the particle in 2-10 nm. Hence, the combination of laser ablation and the wet chemical etching method could potentially be an alternative synthesis for large-scale narrow distribution of SiNCs [145, 150-152].

The other method could be performed by fine-grasping large particles to become particle sizes in the nanometre range using the ball miller or crusher [153]. Technically this work is very straightforward, where the large particles are crushed in the crusher or ball miller to produce a few nanometre particles [154]. This physical method's essential parameters are the number of beads that determine the frequency of collisions among beads and the walls, the dimensions of the cylinder (container); the rotation rates (rotation-per-minutes) cylinder; and the processing time [133, 134]. English *et al.* [125], [155, 156] performed ball-milled synthesis to produce SiNCs. The high quality powder silicon (99.999%, <20 µm) precursor was crushed in the high energy ball mill to produce ~5 nm particle size, confirmed both using TEM and AFM. The XRD spectra confirmed the crystallinity of the resulting in SiNCs. However, iron (Fe) and cobalt (Co) contaminant originated from the chamber, and the grinding balls were confirmed using energy-dispersive X-ray spectroscopy (EDX). PL-spectra demonstrated a luminescent maximum at~450nm, PL-lifetimes in ns-ranges, and independent to quantum confinement. Metal contaminations were proposed as being responsible for causing the blue emission origin[128]. Ball-milled synthesis could be used to produce a

high quantity and environmentally friendly SiNCs. However, contamination from the chamber and balls materials could cause unexpected and challenging issues [157-163].

2.3.1 Disproportionation reactions of silicon monoxides

In this research, the synthesis is tailored by the combination of bottom-up and top-down approaches. The synthesis started from the annealing of silicon atoms embedded in the silica (SiO_2) matrix. At high-temperatures, the silicon monoxide is performing the so-called disproportionation reaction [118]. The disproportionation reaction is nothing but a reduction-oxidation reaction, which means the reaction causes the product to have different oxidation numbers from the starting material [149]. The precursor in this reaction is SiO powder; with the oxidation number of Si in SiO is +2; after synthesis, the product is nanocrystals Si with an oxidation number of 0.

The proposed reaction is $2Si^{+} \rightarrow Si^{0} + Si^{4+}$, where the silicon atom in SiO diffuses in the solid matrix and recombine at the nucleation point together with another silicon and form bigger particles of SiNCs [46]. This diffusion process is slow, and temperature accelerates the process. Therefore, the size of nanocrystals can be controlled by the annealing temperature and time. Figure 2-4 depicted the formation of embedded SiNCs inside the SiO_2 matrix.

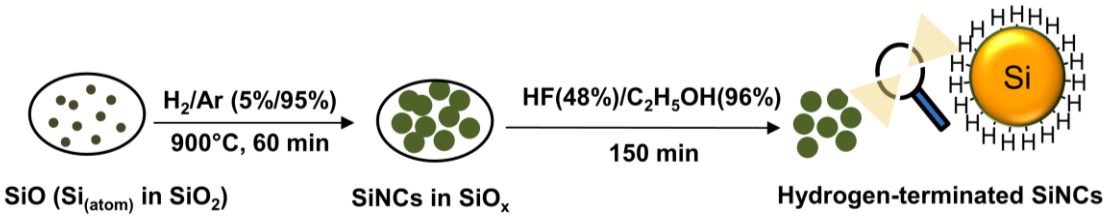

Figure 2-4. A schematic representation of H-SiNCs synthesis from silicon monoxide precursor.

In general, the temperature and time are directly proportional to the particle size [164]. An illustration of the relationship of annealing temperature and annealing time to the diameter of SiNCs is depicted in Figure 2-5a and Figure 2-5b. Mamiya *et al.* [136] screened annealing temperature for silicon monoxide from 800°, 900°, 1,000°, 1,100°, 1,200°, 1,300° and 1,400 °C, respectively [136]. X-ray diffraction analysis and transmission electron microscopy showed that annealing temperatures lower than 900 °C did not show a clear diffraction pattern. Annealing at temperatures of 1,000 °C to 1,400 °C shows the crystoballite silicon crystalline structure pattern. Annealing at 900 °C and 1,000 °C shows the broadband at $2\theta = 15–32°$, the peak at $2\theta = 28°$ is the lattice diffraction pattern (111) for Si. Annealing at temperatures of 1,000°C and above shows that this broadband is shrinking, and the intensity of the silicon crystal diffraction pattern is increasing. Using Scherrer approximation to determine particle size, it is estimated that the result from 900°C to 1,000°C annealing, is a particle size of ~4 nm. The increase in annealing

temperature shows a significant increase in particle size. Annealing at temperatures from 1,300-1,400 °C produces particles with a size of ~16-20 nm [136].

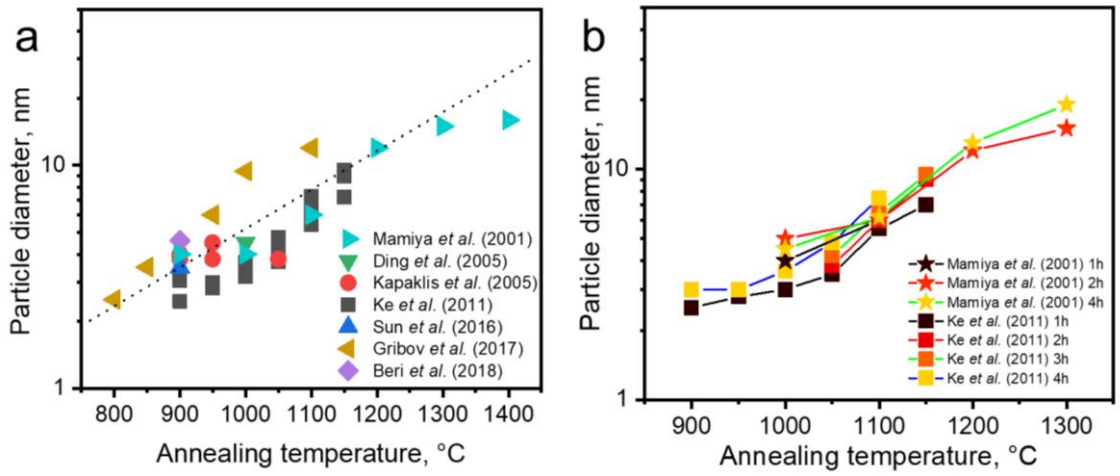

Figure 2-5. (a) Annealing temperature versus particle size of silicon monoxide, (►) [136], (▼)[131], (●)[133], (■) [135], (▲)[88] ,(◄)[132], (♦)[85] , (b) Annealing temperature and time versus particle size of silicon monoxide (*)[136], (■) [135]. The dashed line in (a) is the eye guide to help the reader.

Ke *et al.* [135] conducted a similar study with the temperature increased gradually from 900°; 950°; 1,000°; 1,050°; 1,100°; and 1,150°C [135]. By using XRD and TEM, it could be seen that particle size was increased from ~ 4 nm to ~ 7.5 nm when annealing time increased from 1 hour to 4 hours at a constant annealing temperature of 1,050 °C [135]. An illustration of the relationship of annealing temperature and annealing time to the diameter of SiNCs is depicted in Figure 2-5a and Figure 2-5b. Sun *et al.* [88] studied the formation of SiNCs in the annealing temperature range from 850-1,100 °C. The results found that disproportionation reactions started to occur in the temperature range from 900-950°C. In these temperature ranges, the resulting materials show emission at ~820-830 nm, which corresponds to the particle ~3.5-4.0 nm in diameter [88].

2.3.2 Wet chemical etching of SiNCs

After the annealing/reduction process, the SiNCs in 3.5-5.0 nm are embedded in the SiO_2 matrix. The silica matrix protects the silicon nanoparticles from further oxidation. The protective silica has an amorphous phase structure, and by using XRD diffraction, the broadband at $2\theta = 15\text{-}32°$ is attributed to the amorphous silica. Photoluminescent measurement of annealing products did not show any emissions when excited with $\lambda = 405$ nm because there were allegedly many trap sites found on the surface of SiNCs. Therefore, this SiO_2 matrix needs to be removed by etching[165]. The SiO_2 is reactive towards HF and its sibling's compounds such as NH_4F, SF_6, CHF_3, and CF4 [166-169]. Among these compounds, concentrated HF (48-49% v/v) is one of the most durable etching agents and works very efficiently on the silica surface.

In atmospheric conditions, the liquid HF behaves calmly and is easy to handle. However, HF is one of the most toxic compounds in chemistry, when someone is exposed to HF vapour or liquid, the fluoride ion will penetrate through the body. Because of many similarities, the fluoride ions will surrogate the chloride ion in the body and behaves like a fake-chloride ion. The fake-chloride or fluoride will cause massive damage to the body [170, 171]. This fluoride works to damage the cells, glands, and bonds structure by diluting essential minerals and calcium in the metabolism process [172-174]. Therefore, HF handling needs to be done professionally, under strict protocols and supervision.

A high concentration HF (48-49% v/v) works very efficiently to etch silica (SiO_2), and to increase the etching power, sometimes concentrated HCl and HNO_3 is added to the solution. The acid is added to increase the affinity of silicon to absorb oxygen during the etching process. The hydrogen ion (H^+) from the acid activates the oxygen atom in the SiO_2 to become more acidic ($Si\text{-}O\text{-}O^-\text{---}H^+$). Activated $SiOOH^+$ reacts more vigorously with fluoride ions rather than SiO_2 [175]. Sato *et al.* [175] synthesized nanocrystalline silicon from a commercial silicon powder precursor. The etching was performed with a given proportion of HF (46%v/v) and HNO_3 (60% v/v) mixture to etch ~50 nm in diameter of Si to become ~5 nm in diameter SiNCs. The result shows that by increasing the concentration of the etching solutions (HF), blue shift of the SiNCs luminescence is observed. Also, increasing the etching times results in reducing the yields of SiNCs [175]. Miyano *et al.* [176] conducted a synthesis of styrene functionalized SiNCs from silicon-rich oxide. In the process, the SiNCs emission was controlled by the etching times. Prolonging etching times tends to blue shift the emission from ~800 nm to ~550nm. The etching solutions were a mixture of 10ml HF 48%(w/w) and 2ml HNO_3 65%(v/v), the etching times were conducted from 20 to 112 seconds [176]. Relationships between etching time and PL-spectra maximum is depicted in Figure 2-6. The measurement demonstrates the reciprocal relation between PL-spectra maximum and etching time. Longer etching time shows all PL-maximum blue shifts towards shorter wavelengths.

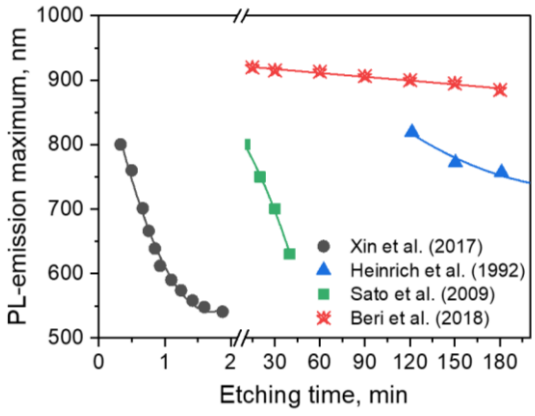

Figure 2-6. Photoluminescent maximum and etching times of SiNCs (■) [175], (●) [177], (▲) [142], and (*) my work [85]. All precursors used were annealed silicon-rich oxide; the etching solution used in the experiment was the mixture of HF 48/49% (v/v) and HNO_3 65% (v/v) at a given concentration, except for our work was conducted using HF 48% (v/v) and absolute ethanol (98 %+).

Tay *et al.* [178] Performed experiments to study the effect of different HF concentrations on the etching ability on annealed and non-annealed silicon dioxide. The results found that by increasing the concentration of HF solutions and annealing the SiO_2, the etching rate is higher than annealing the SiO_2, the etching rate is higher than that of low concentration non-annealed samples [178]. The proposed mechanism of dissolution of SiO_2 in the HF solution was proposed by Knotter [179]. The kinetics of the etching reaction was investigated in-situ using a patented home-build reactor. There are two key parameters in etching SiO_2, both hydrogen ion (H+) and the concentration of hydrophile HF_2^- or H_2F_2. The possible mechanism is substitution nucleophilic, where the reaction is initiated by protonation of the oxygen atom at the surface using the following equation Si-O-X $+H^+ \rightarrow$ Si-(O)H^+ - X (X=Si or H). The next step is nucleophilic attack of HF_2^- (or H_2F_2) on the electrophilic silicon atom: Si-O(H)$^+$ - X + HF_2- $\rightarrow$ SiF + HO-X +HF, where HO-X is a stable leaving group [179].

Figure 2-7 depicted proposed reaction mechanism of silicon dioxide etching, firstly oxygen on the surface of silicon dioxide acidified by the hydrogen ions of hydrogen fluoride (HF) (**1**). The nucleophile approaching one or two protons from the HF solution to form ≡Si-OH or ≡$SiOH_2^+$ (**2**). Next, the ≡SiO bonding cleavage and leaving the ≡Si^+ species (**3**). The ≡Si^+ species is attracting a fluoride ion to form ≡Si-F (**4**). Due to F's strong electron affinity in ≡Si-F species, the silicon becomes partially positive and pushing the electron towards another oxygen (**5**). The oxygen attracts one hydrogen atom to form silanol (**6**) and the silicon fluoride as leaving group (Si-F_2) (**7**).

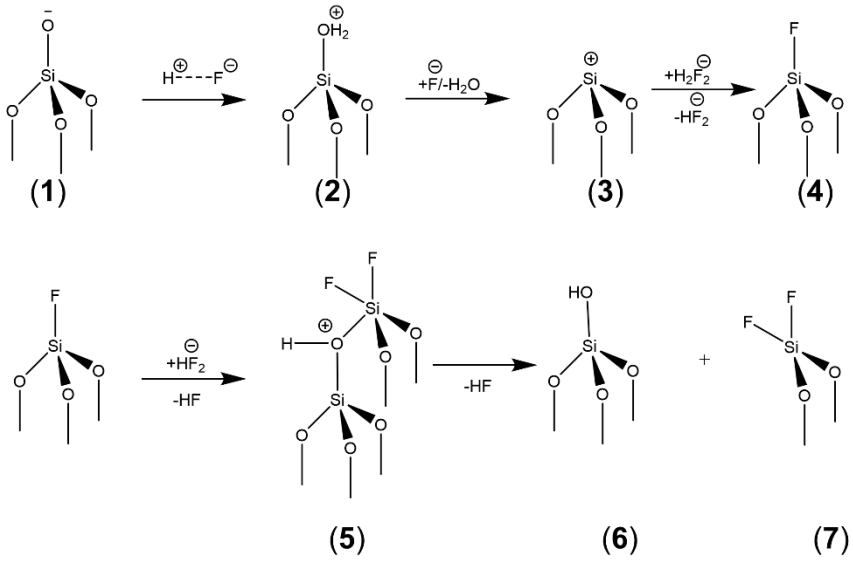

Figure 2-7. Proposed reaction mechanism of wet HF etching on silicon dioxide surface[179]

2.4 Synthesis of alkyl functionalized SiNCs

2.4.1 Photostability of hydrogen-terminated SiNCs

The silicon core of H-SiNCs must be protected because it is very reactive towards oxygen molecules. At atmospheric conditions, silicon reacts with oxygen to form a thin layer of silicon dioxide and behaves as a protective layer against further oxidation [180]. This passivation is not always beneficial for silicon because the protective layer (SiO_2) behaves as an electron trap or the energy absorber. The silicon dioxide layer has a large energy gap, and the electron needs tremendous energy to surmount it. Therefore, a reaction with oxygen creates a bad influence on the luminescence and must be avoided. Figure 2-8a depicted the oxidation level of hydrogen-terminated SiNCs after etching [181, 182]. The Si-O stretching peaks represented in the vibrational bands in 950-1250 $cm^{-1,}$ and 2250 cm^{-1} were gradually enhanced when H-SiNCs were stored in the atmosphere. Simultaneously SiH_x vibration at 2100 cm^{-1} decreases [181, 183]. It is assumed that Si-OH, Si-O-Si, and Si=O substituted hydrogen in $Si-H_2$ (on the surface of SiNCs). Figure 2-8b depicted the emission quenching due to oxidation. Freshly hydrogen-terminated SiNCs show high PL-spectra and gradually decreased by oxidation. In the insert, normalized PL-spectra also shows blue shift due to oxidation [184].

In Figure 2-8c, PLQY of six samples in ensemble of allylphenylsulfide-SiNCs demonstrated quenching after storage in an ambient atmosphere. PLQY measurements for ensembles were performed at PL-spectra maximum. After aging, every ensemble demonstrated trends: blue shift and quenching [184]. The blue shift and PL-spectra quenching were explained in a cartoon representation in Figure 2-8d. Hydrogen terminated SiNCs reacted with oxygen and water in the atmosphere to form Si-O, bonding on the surface. Long term oxidation strained the SiNCs core due to the formation of a SiO_2 shell. Reduced SiNCs due to straining could explain the blue shift, whereas the SiO_2 shell formation explains PL-spectra reduction [155].

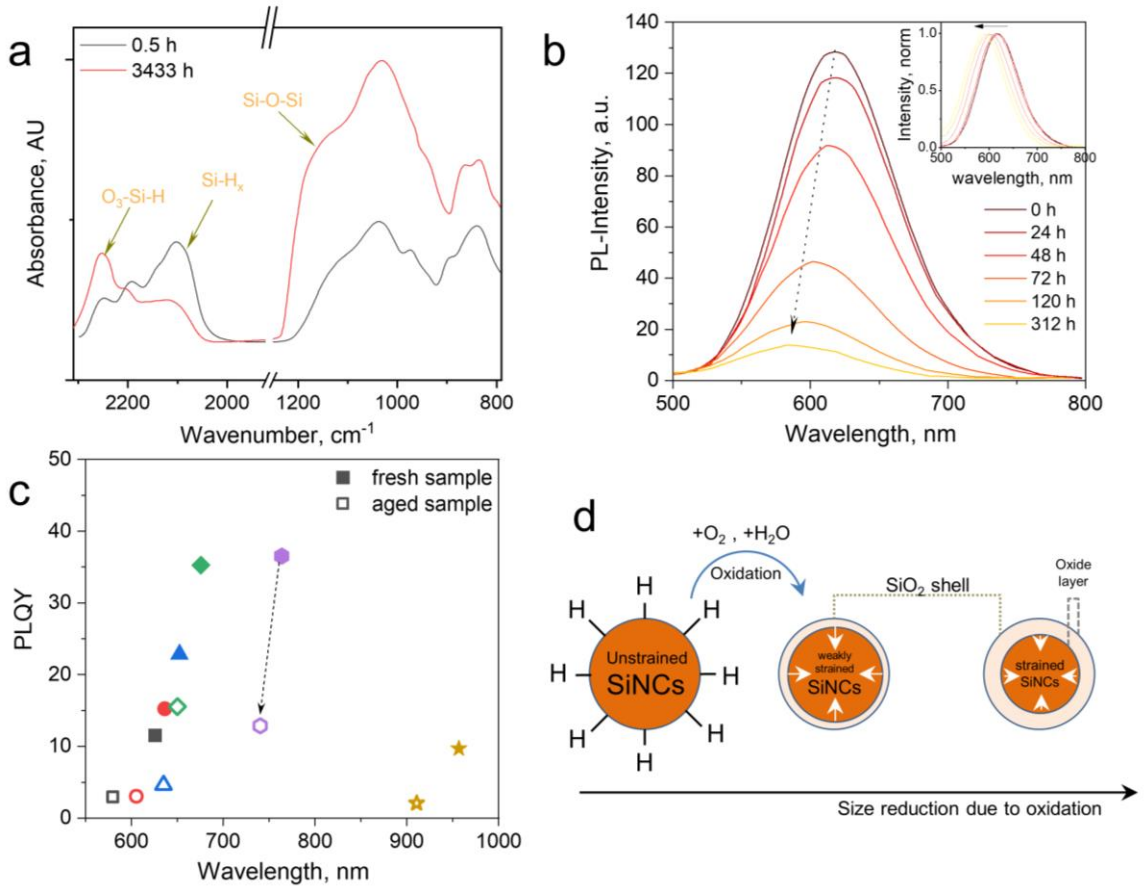

Figure 2-8. (a) FT-IR spectra of long exposure of hydrogen functionalized SiNCs in the air. Adapted with permission from Falcão *et al.* [181], © 2019 American Physical Society (b) PL-emission of long-time exposure H-SiNCs in the air, in the insert: normalized PL-spectra *vs.* wavelength. Adapted with permission from Rinck *et al.* [184], © 2014 WILEY-VCH Verlag GmbH & Co. KGaA, Weinheim (c) PLQY *vs.* PL-spectra maximum of fresh and aged sample of allyl phenyl sulphide-SiNCs. Adapted with permission from Rinck *et al.* [184], © 2014 WILEY-VCH Verlag GmbH & Co. KGaA, Weinheim, and (d) cartoon representation of SiO_2 shell formation after the oxidation process, Adapted with permission from Falcão *et al.* [181], © 2019 American Physical Society.

2.4.2 Tuning SiNCs' emission by varying ligand

In general, there are two domains of photoluminescent emerging from SiNCs, namely near-infrared PL-emission (600-1,100 nm) or so-called the slow (S)-band and blue PL-emission (350-500nm) or so-called the fast (F)-band. The S-band of PL-emission has PL-lifetimes in the microsecond range, whereas the F-band of PL-emission has PL-lifetimes in the nanosecond range. The S-band of SiNCs comes from the material properties under confinement, as widely explained in the quantum confinement section. The emission behaviour is similar to the other semiconductor QDs such as CdSe, CdTe, CdS, PbS, and PbSe. On the other hand, the F-band of PL-emission is coming from the surface defect of SiNCs. The best

demonstration of the F-band origin can be traced back to the experiments by Gupta *et al.* [185]. Freshly etched SiNCs (H-SiNCs) demonstrated the S-band of PL-emission and gradually, due to oxidation, the F-band was popping up, and after 24 hours stored in the ambient atmosphere, the PL-spectra of H-SiNCs shifted from near-infrared to blue region of electromagnetic radiation [185].

There are many possibilities for the luminescent origin of the blue emission. The electronic transition of direct bandgap silicon from the ultra-small SiNCs (1.0-1.4 nm) could lead to blue emission. Finely divided particles make it possible for excitons to achieve phononless transition similar to the other direct semiconductor QDs. For ultra-small particles, quantum confinement theory explains that the origin of blue emission is nothing, but the continuity of bandgap tuning due to size [186-189]. However, quantum confinement was not only the primary source of blue emission. Ulusoy Ghobadi *et al.* [190] demonstrated that blue emission was strongly related to oxide surface defects of SiNCs. When the surface of SiNCs was partially oxidized, the emission was blue shifted, compared with the relevant non-oxidized one [176, 190]. Indeed, fully oxidized H-SiNCs could lead to blue emission [191]. Furthermore, Dasog *et al.* [121] demonstrated that blue emission was also related to the nitrogen functionalized SiNCs. Trace element of oxygen and nitrogen contamination induced surface defects that leads to blue emission [121, 192]. The intense blue emission was also claimed to stem from surface engineered SiNCs. Next, Nilssen *et al.* [156] proposed how to tune PL-emission by anchoring different ligands (e.g., alkyl, amine, phosphine, and acetal) on SiNCs with a particle size of 3-4 nm. The emission could be tuned from blue, green, yellow, orange, and red under ultraviolet excitation. However, there was no clear separation between PL-emission stemming from the surface defect and PL-emission stemming from surface modification. In particular, by introducing halide and phosphine, many trap states were introduced to the surface of SiNCs, and PL-emission might stem from defects and passivation. Therefore, the origin of blue and green emission with high PLQY in this method is questionable [193].

Later, Carroll *et al.* [194] conducted a systematic study on the effect of surface chemistry/functionalization on to PL-emission. The experiment was performed on two distinct sizes of SiNCs; 3.5 nm and 6.5 nm. The synthetic condition of two different sizes was controlled similarly, except for functionalized ligands. Both SiNCs were functionalized with three different ligands, namely alkyls, amides, and alkoxides. Time-resolved PL and transient absorption measurements were performed to study the dynamic of the excitons. The results demonstrated that PL-emission of amide and alkoxides functionalized SiNCs were blue shifted compared with alkyl functionalized SiNCs for the same particle size [194, 195]. The emission shift was more pronounced when the particle size was smaller. So, surface chemistry plays an essential role in PL-emission.

In 2010, the highly luminescent quantum yield of blue emission SiNCs was reported for carbazole functionalized SiNCs [196]. Next, the same group was claiming that SiNCs with 90% of PLQY were synthesized using one-pot synthesis at low temperatures. In the explanation, the main difference between a very high PLQY with traditional SiNCs was surface functionalization [197]. However, this claim was doubtful because the resulting blue emissions were very similar to carbon quantum dot and organic

dye emissions. Therefore, Canham [46], in a published lecture on SiNCs, disagreed that the luminescent origin of exotic blue emissions (with extremely high PLQY) were coming from SiNCs synthesized at a lower temperature [46]. Nevertheless, the blue emission in SiNCs could be stemmed from direct bandgap emission of silicon, and it could explain the emission from tiny SiNCs (~1 nm). Besides, blue emission could also stem from oxygen or nitrogen related surface defects, contaminations, and oxidations. Similarly, it could stem primarily from surface-functionalization [46].

In my research, the discussion is focused on the S-band of PL-emission. The S-band of PL-emission is located at the red to near-infrared electromagnetic radiation (~600-1200 nm). The emission behaviour obeys quantum confinement theory and surface chemistry. A previous report on alkyl functionalized SiNCs produced suspensions of SiNCs with maximum PLQY of 20-35%, with emission in the near-infrared region [71, 180]. Figure 2-9 depicted PLQY values as a function of ligand tuning for SiNCs, with a diameter of 2.5-6.0 nm. The PLQY values were determined at PL-emissions of red to near-infrared, and functionalizations were specified for Si-C bonding. The random value is due to the quantum confinement (particle size), and the surface chemistry effects are not separated well.

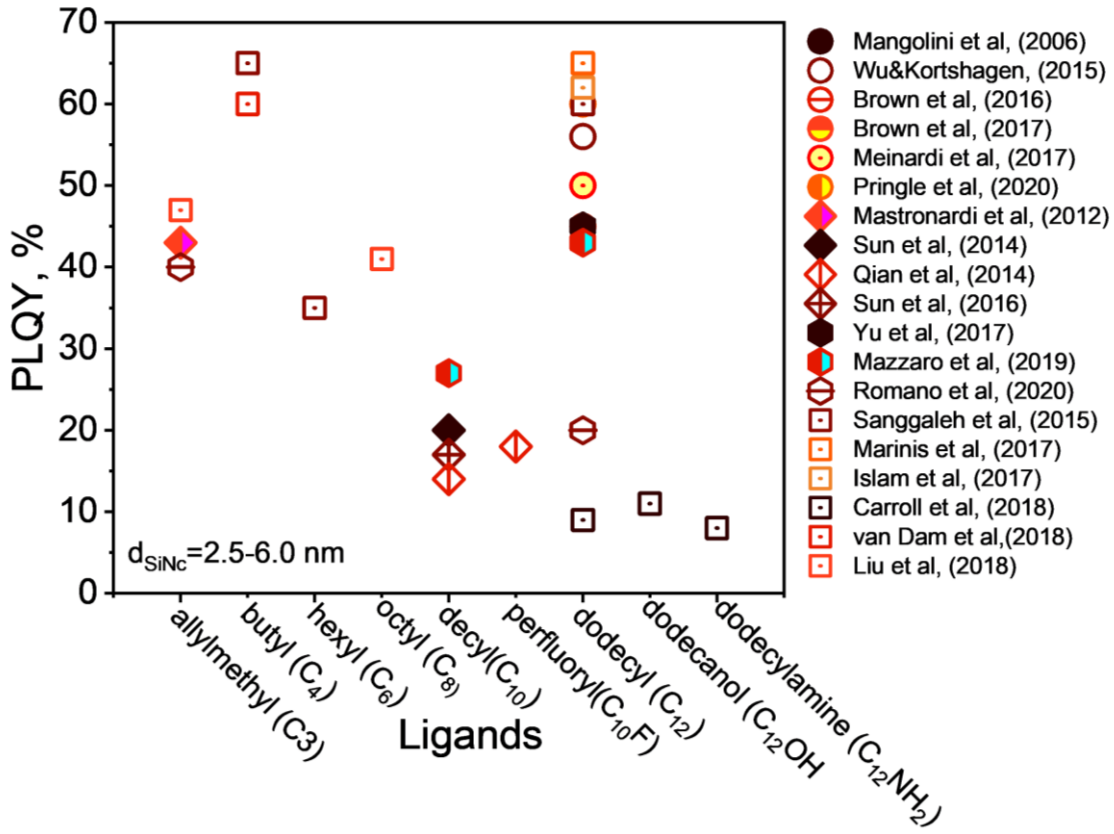

Figure 2-9. PLQY values *vs.* ligands of alkyl functionalized SiNCs determined by previous reports. (○) Kortshagen group [198-203]; (◇) Ozin group [83, 88, 89, 204], (△) Körgel group [73, 205, 206], (□) Veinot and other groups [194, 207-209].

There are some reports on improving photophysical properties due to ligand tuning. For instance, the PLQY value of dodecyl functionalized SiNCs in toluene was reported at 50-60% [111, 201]. This PLQY value was higher compared with the reported PLQY value by Mastronardi *et al.* [83] on decyl functionalized SiNCs (~45%) [90]. Meanwhile, by using another synthetic method, namely PCl_5 precursor, Islam *et al.* [102] claimed to get PLQY ~ 62% and long shelf-life (60 days) with dodecyl-SiNCs [102]. Sangghaleh *et al*. [208] also claimed the high PLQY value (~60%) for butyl and undecanoic functionalized SiNCs synthesized with radical functionalized hydrosilylation [208]. So far, there is no systematic study on the effect of the length of carbon in ligands on the photophysical properties of SiNCs yet. Apart from improving photoluminescent properties, ligand passivation has another function to maintain environmental and photo stabilities. The second term is strongly related to oxygen, water (hydrolytic), thermal, and photochemical reactions.

Sieval *et al.* [210] demonstrated that monolayer alkyl functionalized SiNCs have adequate protection against oxidation for four months [210]. The x-ray photoelectron spectroscopy (XPS) measurement was performed to investigate the formation of SiO_2 on the surface of alkyl-SiNCs. The results show that under ambient atmospheric storage conditions, proper alkyl functionalized SiNCs demonstrated almost no-signature of SiO_2 formation [210]. Bhairamadgi *et al.* [211]conducted a systematic study on hydrolytic (pH resistant) and thermal stability for the monolayer functionalization of alkyl chain length ligands with 6 different set of functional groups, namely -alkene, -alkyne, -chloro-silane, -thiol, -amine, and -phosphine (=C-R, ≡C-R, -$SiCl_3$, -SO_3, -NH3, and PO_2^-) on to the surface of Si (111) and Si (100) [211]. Hydrolytic stability was monitored using a static contact angle and XPS measurement. Silicon functionalized with alkene and alkyne demonstrated good stability against acid (pH=3.0) and base (pH=11) for at least 30 days. In addition, thermal stability was conducted with XPS at elevated temperature from room temperature (25°C), up to 600°C. The result shows that covalent bonding of alkene and alkyne functionalized Si demonstrated good stability from room temperature until Si-C bonding was degraded at 260°C [211].

Finally, Wu *et al.* [203] studied the photostability of SiNCs after functionalization with alkyl (dodecyl). The result demonstrated that PLQY of SiNCs was degraded by ~20% (from original ~60%) after 4 h illumination using 365 nm of UV-light (power density similar to AM 1.5G sun) [203]. PLQY degradation is caused by dangling bonds in formation after the Si—H bond was cleavaged due to illumination. The formation of dangling bonds created the trap state and led to reduced emissions. Re-functionalization of photo-degraded PLQY SiNCs using thermal functionalization can fully recover PLQY value [203].

Nevertheless, alkyl functionalized SiNCs produced tunable PL-emission at red to the near-infrared region and obeyed the quantum confinement theory. The highest reported PLQY for alkyl functionalized SiNCs was butyl –SiNCs ensemble at ~65% [208], dodecyl-SiNCs ensemble at ~62% [180], and decyl SiNCs ensemble at ~45% [83]. Adequate functionalized SiNCs with aliphatic alkyl (alkene and

alkyne) demonstrated good stability against oxidation, acid, or base (hydrolysis), thermal, and photodegradation (photolysis).

2.4.3 Hydrosilylation reaction

Surface engineered/modification nanocrystals/QDs is a critical feature in the development of chemically based nanotechnology. Surface modifications have become available *via* the covalent attachment of functionalized monolayers on silicon surfaces [210]. The hydrosilylation reaction could be tailored to create the functionalized monolayer. Hydrosilylation reaction is an additional reaction of the unsaturated chemical group to the hydrosilane. Its reaction could be performed through thermal inducement or using photochemical. Thermally induced hydrosilylation is performed at elevated temperature under a controlled atmosphere, whereas photochemical at low temperatures use high energy photon[212]. The energy consumption and time of thermally induced hydrosilylation are relatively higher compared with photochemical hydrosilylations. Additionally, it requires advanced chemistry and knowledgeable scientists to experiment with relatively high temperatures and pressure. Therefore, another approach was developed to overcome the limitations. Catalytic hydrosilylation using the metal-complex catalyst and radical-initiated hydrosilylation using radical initiators were developed to reduce energy consumption [213]. Although the microwave-assisted hydrosilylation (MWH) reaction is performed even at a higher temperature, the process's speed could save energy and time. Also, the design of a bench-top reactor could be another benefit for less experienced chemists [85, 127, 214-216]. Figure 2-10 depicted the hydrosilylation reaction of SiNCs and alkene.

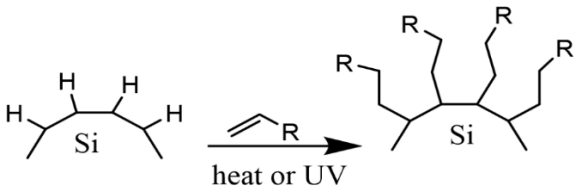

Figure 2-10. Proposed mechanism of functionalization reaction of SiNCs under thermal and radical hydrosilylations. Successful hydrosilylation marked by substitution of hydrogen terminated SiNCs demonstrated with alkyl terminated SiNCs. Adapted from ref [217]

The first work on thermally induced hydrosilylation was performed with pyrolysis of diacyl peroxide in the presence of hydride-terminated Si film. Introducing alkene in the presence of radical diacyl peroxide results in the formation of monolayer alkyl terminated silicon [217]. The proposed mechanism was initiated by the formation of alkyl radicals from the homolytic cleavage of diacyl peroxide. The alkyl radical then abstracts $H^{\bullet}$ from a surface Si−H group, to produce a silicon radical. Silyl radicals react very rapidly with the olefins and perform a chain reaction on the propagation step. The termination step was performed when carbon-based radicals then abstract a hydrogen atom, either from a neighbouring Si−H

group or from an unreacted olefin's allylic position [218]. The proposed mechanism of hydrosilylation reaction of alkyl functionalized SiNCs by pyrolysis of diacyl peroxide is illustrated in Figure 2-11.

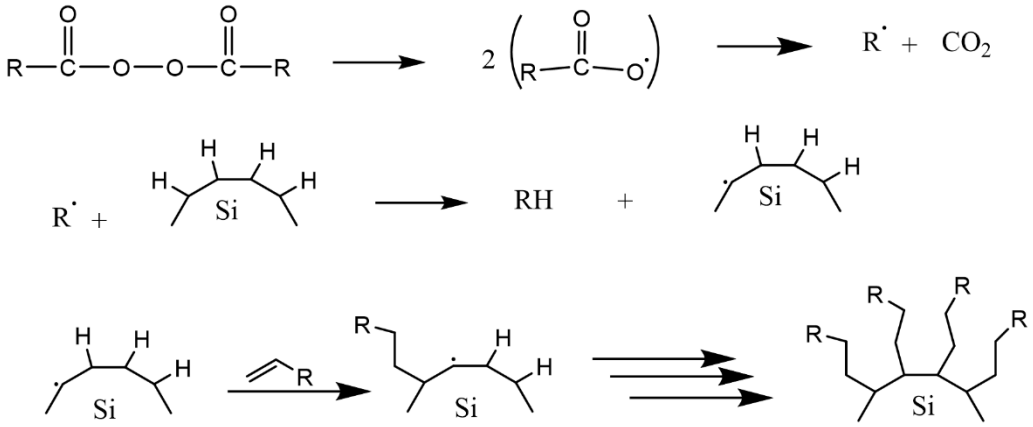

Figure 2-11. Proposed mechanism of thermal functionalization reaction of alkyl functionalized SiNCs. Adapted from ref [218]

The hydrosilylation reaction could also be tailored endothermically via thermal decomposition in the absence of a diacyl peroxide initiator at a temperature above 150°C. At this temperature condition, the homolytic cleavage of Si—H takes place independently according to reaction mechanism Si—H → Si• + H•[218]. The yields of silicon radicals reacting with alkene correspond with the mechanism presented in Figure 2-12, to yield monolayer surface functionalization [218]. Based on the thermodynamical calculation, the bond-formation of Si—H is thermodynamically stable with bond energy 80-90kcal/mol; therefore, this reaction will take place very slowly at a temperature of 150°C [219]. However, in the experiment, the functionalization reaction at that temperature runs much quicker. So, there must be another mechanism that promotes the reaction. Coletti *et al.* [219] proposed a new reaction mechanism that explains the reactions that can happen at a high rate [219]. The idea is the remaining fluoride molecules from the etching step act as promotor - in reaction, the F^- working on acidifying the silicon by creating intermediate compounds called Si --- F. These intermediate compounds are helping Si to capture alkene or alkyne molecules. The reaction mechanism resembles nucleophilic substitution, and thermodynamically this reaction can occur at a significant rate at temperatures below 200°C [219]. The description of the hydrosilylation reaction is presented in the schematic in Figure 2-12.

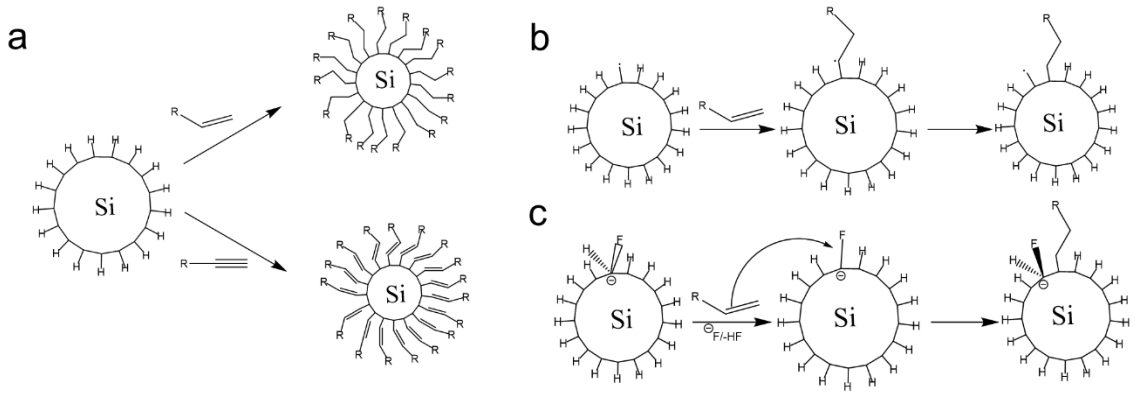

Figure 2-12. Schematic of (a). 1-alkene and 1-alkyne hydrosilylation reaction of hydrogen terminated SiNCs, (b). Radical based hydrosilylation reaction, and (c). A fluoride assisted hydrosilylation reaction mechanism [219].

The second reaction is called photochemical hydrosilylation. In a particular case, high thermal exposure should be avoided in the reaction. Photochemical hydrosilylation is developed to minimize the input of thermal energy. High energy UV light was used to create a homolytic cleavage of Si—H bonding to form a silyl radical and hydrogen radical. Silyl radicals can react with alkene or alkyne to form alkyl functionalized silicon [218]. The brief mechanism of photochemical hydrosilylation is presented schematically in Figure 2-13.

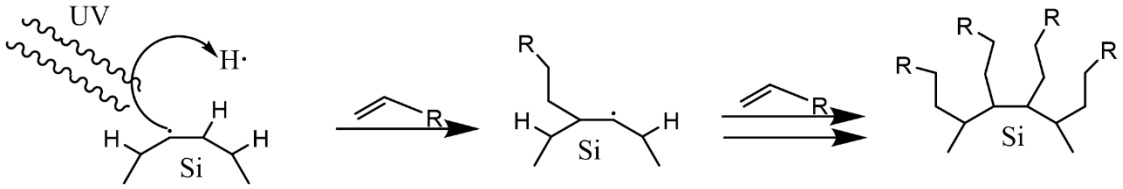

Figure 2-13. Proposed mechanism of photochemical hydrosilylation of alkyl functionalized SiNCs. Adapted from ref [218]

Apart from thermal efficiency, photochemical hydrosilylation could also benefit in terms of the monolayer surface functionalization [220-222]. The drawback of the photochemical method is high energy photons (UV) create many dangling bonds on the surface of SiNCs. The dangling bonds create many trap states on the surface and reduce the photoluminescence of materials.

Catalytic hydrosilylation could be performed using metal-complex catalysts such as platinum (Pt) [223], rhodium (Rh) [218], palladium (Pd) [218], copper (Cu) [224], boron (B) [225], phosphor(P) [102], and aluminium (Al) [225-228]. The main advantage of using metal-complex catalysts significantly reduces the temperature reactions. However, the deposit metal-complex on the surface of

silicon is the main problematic issue so far. The catalyst deposit tends to reduce luminescent properties, and the metal spot is highly pronounced to absorb oxygen [218].

There is another method to functionalize SiNCs called radical initiated hydrosilylation. The reaction could be performed at relatively low temperatures by with assistance of materials called radical initiators. Moran *et al.* [229] conducted a functionalization reaction of hydride-terminated silicon using 2,2′-azobis(2-methylpropionitrile) (AIBN) as a radical precursor [229]. The reactions were completed after 24 h at 60°C and 30 minutes at 90°C. The graft polymer layer formed on the surface of the silicon was investigated using XPS and contact angle measurements. The polymer layer was intended to guarantee surface passivation and coverage[229]. Yang *et al.* [230] conducted a systematic study on the functionalization reaction of hydride-terminated SiNCs using radical AIBN initiators and benzoyl peroxide (BP) [230]. The significant results were that the hydrosilylation reaction could be performed at a slightly lower temperature of 60°C for AIBN and 85°C for BP. A radical initiator for differing functional groups (i.e., alkene, alkyne, carboxylic acid, and ester), and the result of functionalization, was the formation of monolayer surface passivation [180, 194, 230]. Yu *et al.* [127] used undecanoic acid as a radical initiator to produce alkyl functionalized SiNCs [127]. The main advantage of using undecanoic acid is that the reaction could be tailored at room temperature with promising results [127]. The luminescent properties of undecanoic acid-promoted hydrosilylation of styrene functionalized SiNCs were comparable to classical decyl functionalized SiNCs [127]. Figure 2-14 depicted the proposed mechanism of a radical initiated hydrosilylation reaction.

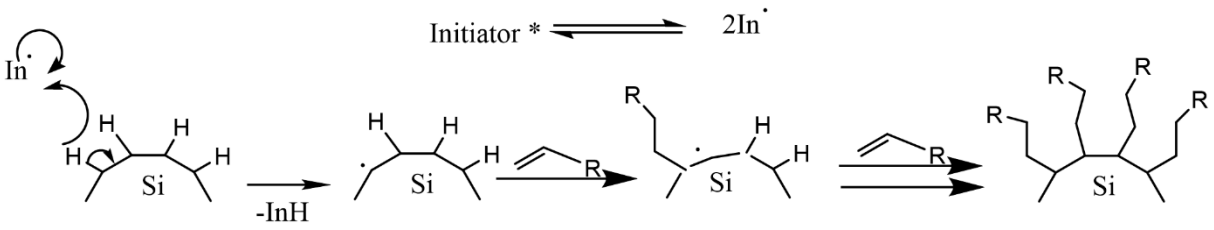

Figure 2-14. Proposed mechanism of radical initiated hydrosilylation of alkyl functionalized SiNCs. Adapted from ref [230]

In my research, the reaction is conducted using microwave-assisted hydrosilylation (MWH). In principle, the reaction could be categorized as thermally induced hydrosilylation. The reactant is radiated using microwave radiation to stimulate vibration at the molecular level. The heat is created by dipolar polarization and ionic conduction, where the first term is attributed to molecules having dipoles gradient (permanent or induced dipoles), and the second term is mainly attributed to charged particles (ions) [231]. When microwave frequency is applied, the samples' dipoles align themselves in the applied field direction—the oscillation frequency of microwave radiation forces the molecule to oscillate to compensate for the applied frequency. Molecular re-alignment across the applied field creates friction and dielectric loss and leads to elevated temperature (dielectric heating). The amount of heat created by this method is dependent on the ability of the molecule to re-align itself against the frequency of the applied field. If

molecules enable themselves to align quicker than the applied field, no heating is occurs [231]. Similarly, ionic particles oscillate to a microwave frequency. Oscillation causes a collision with neighbour particles and agitates a chaotic system to produce heat [232].

Boukherroub *et al.* [233] described the functionalization reaction of hydrogen-terminated porous silicon with 1-alkene under microwave irradiation to give monolayer alkyl functionalized porous silicon [233]. The hydrosilylation process's reaction rate was increased significantly, and the result was monolayer alkyl functionalized porous silicon. Furthermore, by using MWH, there are opportunities to perform functionalization using a wide range of functional group materials. The functionalized product was robust, highly stable, and has higher surface coverage [233]. The proposed mechanism of MWH is depicted in Figure 2-15.

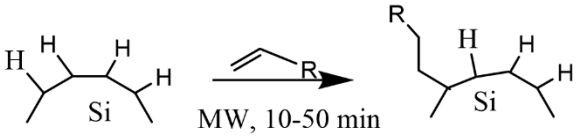

Figure 2-15. Proposed mechanism of microwave hydrosilylation reaction of alkyl functionalized SiNCs. Adapted from [233]

There is a dispute regarding the role of microwave radiation on hydrosilylation. Some people believe that the increase of reaction rate is due to a microwave energy stimulate reaction process, whereas the others believe that microwave radiation does not have any role in the reaction process. The second opinion argues that the reaction rate increase is just because it proceeds at a higher temperature. To study the effect of microwave radiation on a hydrosilylation reaction, Sun *et al.* [234] conducted a kinetic study comparing the rate and extent of reaction [234]. Both reactions were tailored in the same reaction condition, except for hydrosilylation methods. One sample was functionalized using conventional thermal hydrosilylation, and the other one was functionalized using MWH. However, the temperature and time were adjusted similarly at 170°C for 60 minutes. The extent of the reaction was monitored by FT-infrared spectroscopy to see the number of Si-C formation as a function of time. The rate constant for both hydrosilylation methods was deduced from the quantitative measurement of Si—H replacement during the functionalization of decyl-SiNCs as a function of time, relative to the original Si—H hydrogen-terminated SiNCs. In the result, both functionalization methods presented relatively similar rate constants: $k = (15 \pm 1) \times 10^{-3}$ minutes^{-1} for conventional thermal functionalization, and $k = (12.3 \pm 0.6) \times 10^{-3}$ minutes^{-1} for MWH. Hence, there is no influence of microwave radiation on a hydrosilylation reaction [234]. The advantage of microwave hydrosilylation is the homogeneity of the internal heat, as the heating is caused by molecular resonance towards microwave frequency intramolecularly, the heat efficiency is maximum, and heat loss is minimum. Which also results in surface coverage of alkyl functionalization being higher because every bond is affected by vibrations and tends to be involved in the reaction [235]. Because some reactions must be conducted for hours with conventional thermal hydrosilylation, this could be compressed

into minutes in MWH at higher temperature, the reaction in MWH is therefore time-efficient [231, 232]. Reactions in the MW reactor could proceed above the reactants' boiling point under so called solvatothermal condition, so the reactants' volatility is not an issue. Likewise, the reaction is easy to handle because it is performed in the safety proof bench-top reactor. Last but not least, monolayer alkyl functionalized SiNCs are possible to achieve by strictly controlling the reaction conditions. However, the main drawback of using a microwave reactor so much depends on a relatively expensive instrument. Also, since the reaction is tailored at a slightly higher temperature ~200-270°C, the grafted polymer layer is most likely to form outside the surface of SiNCs. Multilayer (corona) guarantees the ligand to surface ratio, but it also enhances the hydrodynamic ratio of individual SiNCs.

Nevertheless, the hydrosilylation reaction is tailored to perform surface modification. The reaction could be performed using thermally induced hydrosilylation and photochemical hydrosilylation. Thermally induced hydrosilylation could be performed above 150°C. Some methods to lower thermal-induced hydrosilylation include using metal-complex catalysts or introducing material called the initiators. In the wet chemical method, the leftover fluorine ion acts as a catalyst to promote reactions at relatively low temperatures. Metal ion complex could also be used as a catalyst and initiator, but the deposit of metal ion on the surface of SiNCs could create another problem. Radical initiators such as AIBN, AIBCN, BP, and undecanoic acid could be used as promising candidates for room temperature thermal-initiated hydrosilylation.

2.5 Synthesis of dye functionalized SiNCs

2.5.1 Chromophore-assisted photoluminescent SiNCs

One of the simple chromophores functionalized SiNCs is styrene terminated SiNCs, which was synthesized by Marinins *et al.* [180] . The synthesis started from the annealing of silicon-rich oxide (Fox-16 from Dow Corning) under an inert atmosphere and was followed by wet chemical etching using hydrogen fluoride to form hydrogen-terminated SiNCs. Functionalization with styrene was performed by radical-initiated hydrosilylation at room temperature using undecanoic acids as a catalyst. The result was a monolayer surface styrene passivation with photophysical properties similar to the common alkyl passivation of SiNCs. PL-spectra demonstrated typical broadband emission with a maximum at 615 nm under 295 nm λ-excitation. A measurement of PLQY gives a result of 12% for PL-emissions in the 500-900 nm range. Compared with typical alkyl functionalized SiNCs – for example decyl-SiNCs – the absorption and the emission spectra have similar shapes, but the PL-maximum of styrene-SiNCs underwent a slight blue shift of ~20 nm. Indeed, the slight blue shift was because room temperature hydrosilylation was more efficient in forming a monolayer, whereas thermal-induced hydrosilylation tends to embed SiNCs in the polystyrene layer, resulting in the enlargement of particle size. PL-lifetimes measurement of styrene-SiNCs was an agreement with PL-lifetimes of typical decyl or dodecyl-SiNCs. Hence, covalent attachment

of styrene molecules to the surface of SiNCs did not change the photophysical properties of SiNCs compared with the corresponding alkyl functionalized SiNCs [127].

However, conjugated organic dye and SiNCs might be used to enhance light absorption and PL-emission [195, 236, 237]. The dye molecule's strong light absorption was expected to donate the excitons to the SiNCs core acceptor *via* energy transfer [110, 238-241]. The result was that light absorption of SiNCs was enhanced because of additional absorption from dye ligand, and also PL-emission of SiNCs was increased due to exciton transfer from dye-to-SiNCs. Locritani *et al.* [242] functionalized SiNCs with a pyrene group to enhance the light-harvesting devices' absorption [242]. The synthesis was conducted using thermal decomposition of the hydrogen silsesquioxane (HSQ) under an inert atmosphere and following by wet chemical etching using hydrofluoric acid to produce H-SiNCs. Functionalization was conducted thermally at 170°C using a given mixture of 1-(allylmethoxy) pyrene (py) and 1-dodecene (C12) to two class particle sizes of H-SiNCs (2.6 and 5.0 nm). The resulting materials were 2.6 nm (**C12**)-py-SiNCs with PL-spectra of 600-900 nm and 5.0 nm (**C12**)-py-SiNCs PL-spectra of 700-1200 nm. The absorption spectra demonstrated significant enhancement at 300-400 nm due to 3-fold absorption of light from pyrene groups. PL-emission shows both carbon emissions at PL-maximum 400 nm and SiNCs at PL-maximum 680 nm for 2.6 nm particle size and 970 nm for 5.0 nm. Meanwhile, (C12)-SiNCs exhibited PL-maximum at 635 nm for 2.6 nm and 970 nm for 5.0 nm. So, the pyrene molecule's attachment was redshifted PL-maximum of (C12)-SiNCs by ~45 nm for 2.6 nm particle size, but none for 5.0 nm particle size. PLQY of 2.6 nm of (C12)-SiNCs at PL-maximum of 635 nm was 11%, whereas (C12)-py-SiNCs PL-maximum of 680 nm was 8%. While PLQY of 5.0 nm of (C12)-SiNCs at PL-maximum of 970 nm was 45%, and (C12)-py-SiNCs PL-maximum 970 nm was 40%. Comparing the PLQY values of attached and non-attached pyrene on (C12)-SiNCs, authors claimed ~95% energy transfer from pyrene moieties to 2.6 nm particle size of SiNCs that led to significant brightness enhancement by 300% in the visible range and an additional 78% in the near-infrared [242].

Hence, the experiment demonstrated that pyrene (a chromophore) could enhance the light absorption and PL-emission of SiNCs. The light absorption enhancement was performed by additional strong absorption from the pyrene molecule at 300-400 nm, whereas PL-emission enhancement was performed by energy transfer from the pyrene molecule to the core of SiNCs. Overall, the brightness of conjugate materials was enhanced by a factor of 300% due to the contributions of pyrene and (C12)-SiNCs. However, selecting pyrene as a chromophore to increase light absorption in the ultraviolet range was not a perfect choice because the light absorption of SiNCs at 300-400 nm could be enhanced by increased concentration of SiNCs. Also, the strong emission of pyrene molecule at 350-500 nm might destroy the original goal of focusing only on near-infrared emission. For example, in the luminescence-solar concentrator (LSC), the unwanted PL-emission from the pyrene molecule might produce unwanted colours and reduce transparency in the solar window. Hence, the pyrene molecule caused a limitation in the applications of chromophore functionalized SiNCs.

A slightly similar experiment was conducted by Fermi *et al.* [243] in an attempt to enhance the absorption of SiNCs at a visible range of electromagnetic radiation [243]. The chromophore of tetraphenylporphyrin Zn (II) (TPP-Zn) was used because it has a strong absorption at 426 nm and 560 nm. The SiNCs were synthesized using thermal decomposition of the hydrogen silsesquioxane (HSQ) and followed by wet chemical etching using hydrofluoric acid to yield two classes of H-SiNCs materials having particle sizes of 3nm and 5nm. The functionalization reactions were performed under thermal hydrosilylation by adding the given mixture of dodecene (C12) and tetraphenylporphyrin Zn (II) (TPP-Zn) to the dispersion of H-SiNCs at a temperature of 170°C. The resulting materials of 3 nm size (C12)-(TPP-Zn)-SiNCs exhibited two sorts of PL-emission maximum; at 605 nm attributed to TPP-Zn emissions, and 670 nm attributed to (C12)-SiNCs and some energy transfer from TPP-Zn. Whereas, the resulting materials of 5 nm size (C12)-(TPP-Zn)-SiNCs also exhibited two sorts of PL-emission maximum at 608 nm attributed to TPP-Zn emissions, and PL-emission maximum at 905 nm attributed to (C12)-SiNCs and some energy transfer from TPP-Zn. PLQY of 3 nm size (C12)-(TPP-Zn)-SiNCs exhibited 7%, a reduction of 6% from the original 13% from (C12)-SiNCs. Whereas PLQY of 5 nm size (C12)-(TPP-Zn)-SiNCs exhibited 8%, which was significantly reduced from the original 42% of (C12)-SiNCs. Nanosecond lifetimes of dye molecule were quenched from 2.3 ns to 1.2 ns. Likewise, microsecond lifetimes of chromophore TPP-Zn attached to SiNCs were quenched from 110 μs to 70 μs for 3 nm particle size and from 140 μs to 100 μs for 5 nm particle size. Quenching PLQY and PL-lifetimes demonstrated energy transfer from TPP-Zn to SiNCs. The calculation of efficient energy transfer leads to a 50% light synthesized process from TPP-Zn to SiNCs [243].

Hence, Fermi *et al.* [243] experimented with overcoming the drawback of previous research [243]. However, TPP-Zn might work poorly as a transmitter, as demonstrated in the experiment, efficient energy transfer of 50% could be improved by covalently anchoring other chromophores such as perylene, phenanthrene, and other organic chromophores.

Abdelhameed *et al.* [238] conducted a systematic study on conjugate dyes (9-vinylphenanthrene (**ph**), 1-vinylpyrene (**py**), and 3-vinylperylene (**pl**)) functionalized ultra-small (1.7-2.1 nm) SiNCs on the PL-quantum yields [230]. Tilley's synthesis was conducted using precursor silicon tetrachloride ($SiCl_4$) and tetraoctylammonium bromide (TOAB). Hydride-functionalized SiNCs were synthesized by precursors' reaction with an excess lithium aluminium hydride ($LiAlH_4$). The functionalization reactions of dyes were conducted using catalytic hydrosilylation using platinum (Pt) as a catalyst. The resulting materials were ultra-small (1.7-2.1 nm) dyes (**ph**, **py**, and **pl**) with functionalized SiNCs, as confirmed by TEM. The results demonstrated that PL-emission of SiNCs functionalized by **ph**, **py**, and **pl**, dyes were redshifted compared with the corresponding non-conjugated dyes. Dye functionalized **ph**-SiNCs, **py**-SiNCs, and **pl**-SiNCs exhibited PLQY values were18, 11, and 8%, respectively. These PLQY values were higher than the corresponding alkyl functionalized SiNCs for the same particle size (i.e., PLQY = 8% for heptyl (C7)-SiNCs). PL-lifetime measurements show that there were energy transfers from the dye to SiNCs. However, the magnitude of efficiency energy transfer did not present in this research [244].

Nevertheless, it is possible to enhance light absorption and PL-emission of SiNCs with the aid of energy transfer from chromophores (dyes) to SiNCs. The synthetic method could be started from H-SiNCs synthesis and was followed by the functionalization of chromophores *via* hydrosilylations. H-SiNCs synthesis could be performed by the thermal annealing of silicon-rich oxide and followed by wet chemical etching, or Tilley's method, using precursors $SiCl_4$ and TOAB reaction with reducing agent $LiAlH_4$. Subsequently, hydrosilylation could be performed using thermal hydrosilylation at 170°C, radical-initiated hydrosilylation, and catalytic hydrosilylation. The resulting materials demonstrated the redshift of PL-spectra after functionalization with chromophores, except for an experiment conducted for styrene-SiNCs. PLQY after chromophore attachments demonstrated reductions, except for experiments conducted by Abdelhameed *et al.* [238] which shows enhancement and an experiment by Yu *et al.* [127], where PLQY value remain constant. The kinetic energy transfers were studied by PLQY and PL-lifetimes measurements. Energy transfers from chromophore molecules to the core of SiNCs, which led to PL-emission enhancement at the near-infrared region of electromagnetic radiation.

2.5.2 The mechanism of energy transfer in dye functionalized SiNCs

As demonstrated by Mongin *et al.* [245], the possibility of exciton transfer might open up new opportunities in physical and chemical science[245]. The authors demonstrated Dexter-like energy transfer from CdSe nanocrystals to the surface anchored organic dyes using transient absorption spectroscopy. Further investigation shows that triplet-triplet energy transfer in the aerated solution also occurred from surface acceptor to freely organic dyes (solutes). The experimental evidence demonstrated that a surface anchored or covalent anchored nanocrystal could be used as an effective substitute for the available organic sensitizers. The sensitization process might lead to the triplet-triplet annihilation upconversion (TTA-UC) process and singlet oxygen generation[245]. In the next report, Mongin *et al.* [246] demonstrated substantial decreases in PL-emission of air saturated covalent anchored 1-pyrenecarboxylic acid (PCA) CdSe nanocrystals due to the formation of singlet oxygen. Strong PL-spectra appearance at 1,270 nm confirmed the claim of triplet energy transfer from ^{3}PCA* to the ground state oxygen ($^3O_2$) and generated singlet oxygen ($^1O_2$) [246]. Whereas the existence of triplet energy transfers was investigated using temperature-dependent PL-measurement, time-resolved PL-spectroscopy, and transient absorption spectroscopy. Herein, the formation of ^{3}PCA excited state was confirmed using transient absorption spectroscopy experiments. Energy transfer from PCA to CdSe nanocrystals was observed through time-resolved temperature-dependent experiments (at -80 to +20°C) [246]. However, the materials' main drawback was the potential toxicity of CdSe nanocrystals, and the singlet oxygen quantum yields ($^1O_2$) of this material remained low. Therefore, for biological applications such as in photoimaging and phototherapy, CdSe nanocrystals were not suitable. The mechanism of singlet oxygen generation from CdSe nanocrystals is depicted in Figure 2-16a.

Recently, Xia *et al.* [247] demonstrated that conjugated 9-ethylanthracene (9EA) functionalized SiNCs performed TTA-UC mechanism when dispersed in 9,10-diphenylanthracene (DPA). The experiment

was conducted under an inert nitrogen atmosphere using (9-EA)-SiNCs as a sensitizer and DPA as an emitter. The efficient Dexter-energy transfer was investigated by femtosecond transient absorption spectroscopy. Photoexciting sensitizer materials drove spin-triplet exciton transfer from silicon-to-anthracene through Dexter-like energy transfer with nearly 50% efficiency. With an excess of DPA molecules, these particles readily upconverted 488-640 nm photons to 420 nm photons with TTA-UC quantum yields exceeding ~7%. The schematic is depicted in Figure 2-16b. The upconverting process occurred for (9EA)-SiNCs sensitizer only, whereas octadecene (C18)-SiNCs sensitizer with similar treatment did not show any upconverting phenomenon. The plotting of upconversion intensity as a function of excitation rate demonstrated that excitation rate threshold power fell from 0.95 Wcm^{-2} for 488 nm excitation, to 2 Wcm^{-2} for 532 nm excitation. It was because the absorption of low energy photons was significantly lower than the high energy photons. Another significant result was that the upconversion process depended on the particle size of SiNCs, since upconversion quantum yields were increasing from 0 to 7% as the particle size decreases from 3.6 to 3.1 nm. Authors described it as being due to decreasing particle size, the bandgap energy laid above 9EA triplet state (~1.8 eV), and the energy barrier was reduced for nanocrystals to molecule energy transfer and led to increasing upconversion quantum yields.

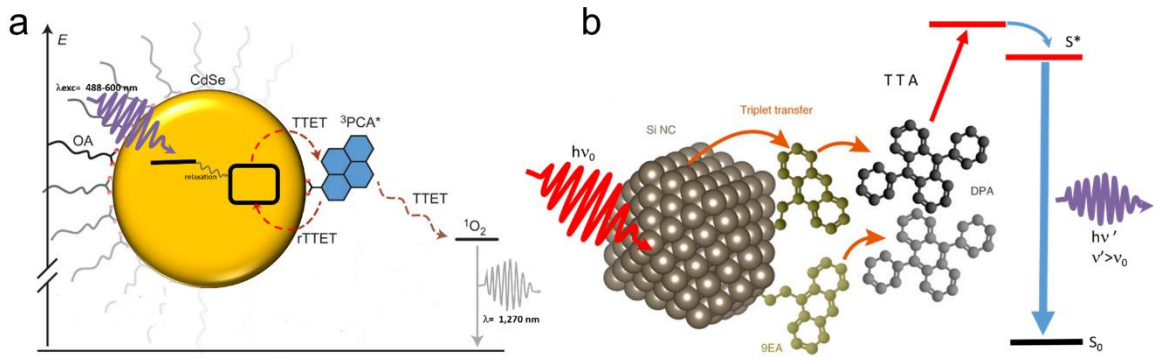

Figure 2-16. (a). Singlet oxygen generation mechanism of dye functionalized CdSe nanocrystals. Adapted with permission from Mongin *et al.* [246] Copyright © 2017, Springer Nature. (b). Triplet-triplet annihilation upconversion schematics tailored by dye functionalized SiNCs immersed in the dye solvents. Adapted with permission from Xia *et al.* [247] Copyright © 2017, Springer Nature.

2.6 Applications of dye functionalized SiNCs

2.6.1 As light-harvesting antenna

Locritani *et al.* [242] attached chromophore (pyrene) to functionalized SiNCs. The pyrene group is tethered by (-C_3H_6-O-CH_2-) to guarantee the long distance between SiNCs-core and pyrene groups. The authors investigated efficient energy transfers from chromophore to the SiNCs that have two distinct particle sizes, namely 2.6 nm and 5.0 nm. The actual results of this experiment are efficient energy transfer

from chromophore, for 2.6 nm particle size it was ~95%, which led to 300% brightness enhancement in the visible range, whereas for 5.0 nm particle size was ~65%, which led to 78% brightness enhancement in near-infrared ranges. Nevertheless, this experiment demonstrated that SiNCs could be used as a viable scaffold in light-harvesting antenna because chromophore enables the enhancement of molar absorption of SiNCs and leads to PL-emission or brightness enhancement [242, 248]. Beside pyrene, other chromophores could also be attached to SiNCs to get strong absorption at visible ranges. Ruthenium (II) bipyridine and Zinc (II) tetraphenylporphyrin were synthesized to manipulated SiNCs with strong absorption at visible ranges [206, 249, 250].

2.6.1.1 In bioimaging

As light-harvesting materials, dye functionalized SiNCs could be used as probe materials in photoimaging. Owing to the UV-excitation potentially damaging the biological tissues, other excitation methods need to be developed in SiNCs probe-based bioimaging. One attractive method was using a near-infrared photoexcitation *via* two-photon excitation (2P). Herein, 2P excitation was done by exciting dye-SiNCs using near-infrared radiation to produce emission at a PL-emission of SiNCs. Ravotto *et al.* [237] conducted a systematic study on two-photon excitations of dye-SiNCs. SiNCs with particle size ~5.0 nm was functionalized with 4,7-di(2-thienyl)-2,1,3-benzothiadiazole chromophores (**TBT**) and dodecyl chains exhibited PL-emission at near-infrared radiation (900 nm). The authors claimed that PL-emission could be obtained from 2P absorption by 960 nm excitations. The resulting emission could be differentiated from the excitation wavelength by measuring PL-lifetimes of photoluminescences. The resulting emission was the characteristics of that long-lived photoluminescence of SiNCs and completely different from the excitation wavelength. This breakthrough invention might be useful when it is used as a probe in photoimaging [237]. The resulting PL-emission exhibited from 2P absorption demonstrated that dye functionalized SiNCs could be used as a bioimaging probe [244, 251, 252].

2.6.1.2 In luminescent solar concentrator

In luminescence properties, SiNCs show similar behaviour compare with other direct semiconductors nanocrystals, since the emission is size dependent. In fact, SiNCs demonstrate some advantages in toxicity, and large Stoke-shift compared to other semiconductor nanocrystals. The large Stoke-shift makes it possible to design a semi-transparent solar luminescence concentrator (LSC) that is aesthetically attractive [253]. However, the main drawback is the absorption of SiNCs in the ultraviolet-A (UVA) (315-400 nm) region is relatively low. Meinardi *et al.* [201] demonstrated that an LCS device fabricated using alkyl functionalized SiNCs could exhibit power conversion efficiencies as high as 2.85% and 70% transmittance [201]. In order to enhance the absorption in the UVA range, Mazzaro *et al.* [205] used 9,10-diphenylanthracene (DPA) functionalized SiNCs embedded in methyl methacrylate (MMA) polymer. The authors found that LSC's absorption was significantly enhanced due to dye attachment, and optical efficiency was enhanced as high as 4.25%, almost without losing transparency [205]. This remarkable result shows the possibility of dye functionalized SiNCs as a lumiphore in LSC.

2.6.1.3 In biosensors

Terbium-amine functionalized SiNCs were used as a biomarker to detect dipicolinic acid (DPA) as one constituent in *Bacillus anthracis* spores. By using a biomarker made of terbium-amine-functionalized SiNCs, the detection of anthrax disease could be performed much more efficiently compared with polymerase chain reaction, which was used as a standard detection method today. The detection method was done by comparing the fluorescent intensity of terbium-amine functionalized SiNCs in the interaction with DPA and fluorescent intensity, without interaction with DPA. This method's detection limit was about 24 nM, four orders of magnitude lower than the spores' infectious dosage (6×10^{-5} M required)[254].

2.6.2 As photosensitizer

2.6.2.1 In triplet-triplet annihilation upconversion (TTA-UC)

Surface anchored 9-anthracene carboxylic acid-functionalized CdSe nanocrystals demonstrated the ability to sensitize triplet-triplet annihilation on emitter molecule of diphenylanthracene. The resulted upconverting was 432 nm emission wavelength from 532 nm excitation wavelength. Using rhodamine-6G as a standard, 9-anthracene carboxylic acid-functionalized CdSe nanocrystals exhibit ~9% UC-quantum yields [255]. The same authors demonstrated the kinetics of energy transfer from the CdSe exciton state to the anthracene ligands' triplet state in the next publication [256]. The highest UC-quantum yield was reported from the same group, for the same system, which exhibits 17% for upconverting green (488 nm) to blue (430 nm) light [257-259]. Nevertheless, the SiNCs-analogue system could exhibit UC-quantum yield at such a high value is remarkable, and similar work theoretically could also be done for dye functionalized SiNCs [260, 261].

As described in the previous section, 9-ethyl anthracene functionalized SiNCs in the dispersion of 9,10-diphenyl anthracene as solvent, demonstrated TTA-UC quantum yields exceeding ~7% at a given particle size and excitation energy. Although the quantum yields are threefold lower than the comparative CdSe nanocrystals system, the breakthrough invention could open up new prospects for dye functionalized SiNCs in light-to-energy conversion, biological imaging, photovoltaic, and photocatalysis.

2.6.2.2 In singlet oxygen generation ($^1O_2$)

Singlet oxygen ($^1O_2$) is one of the key ingredients for photodynamic therapy (PDT) to treat oncological disease. A suitable photosensitizer could be applied to form $^1O_2$, if the following requirements are fulfilled: (1) having low toxicity in the absence of irradiation, (2) working specifically to the target cancer cells, (3) having relatively high efficient energy transfer, (4) short retention time in the body, (5) having stability against coagulations/aggregation, and (6) exhibiting excellent photostability [262]. Owing to the excellent behaviour of SiNCs as PS, it has potential to be developed for nano-theranostics. Nano-theranostics is a term introduced for the comprehensive effort that integrates diagnostics and therapy in a single platform using nanomaterials. Dye functionalized SiNCs is one of the potential nano-theranostics

agents which could be applied in this platform. Applying dye functionalized SiNCs as PS in-vivo, the image of cancer and another diseases could be resolved (photoimaging), simultaneously $^1O_2$ is released to cure and heal [263-265].

Samia *et al.* [266] demonstrated that the CdSe quantum dot could be used as a photosensitizer for $^1O_2$. Generating reactive oxygen species were tailored by triplet-triplet energy transfer (TTET) from the quantum dot to oxygen [266]. The emission spectra of resulting radiative relaxation of $^1O_2$ were investigated at 1270 nm using laser-flash photolysis with liquid-nitrogen Ge detector. Singlet oxygen quantum yields ($\Phi_{^1O_2}$) of oxygen saturated CdSe quantum dot exhibited ~5%, relative to the reference phenalenone $\Phi_{^1O_2}$ (~1.0%) [266]. As a result, the authors claimed that the CdSe quantum dot could be used as an agent for photodynamic therapy.

As previously described, Mongin *et al.* [245] demonstrated the formation of singlet oxygen due to efficient triplet-triplet energy transfer from dye functionalized CdSe to ground-state oxygen in the atmosphere [245]. In the relaxation process, $^1O_2$ was emitting fluorescent at 1270 nm radiation wavelength. Therefore, dye functionalized CdSe materials appear to be promising candidates for oxygen sensing [245, 246, 260].

3 Methodology

3.1 Functionalization with linear alkyl ligands

3.1.1 Materials

Silicon monoxide (99.9%, 325 mesh) purchased from Sigma-Aldrich, Fox 16 purchased from Dow Corning, hydrofluoric acid (HF) (48%) obtained from Fisher Scientific, ethanol absolute, methanol (MeOH) (98%++), potassium hydroxide (KOH) HPLC grade, toluene (99%), pentene-1 (98%), dodecene-1 (94%), tetradecene-1 (96%), hexadecene-1 (98%), allyl methyl ether (97%), and octadecene-1 (96%) purchased from Merck, hexene-1 (99%) and octane-1 (99%) purchased from Acros, decene-1 (96%) and n-hexane spectroscopic grade obtained from Alfa-Aesar and α-lipoic acids purchased from VWR.

3.1.2 Synthetic procedures

3.1.3 Synthesis of hydrogen-terminated Si-NCs

A 1.0 g SiOx (x<2) was transferred to a quartz boat (Figure 3-1a) and reduced thermally under flowing forming gasH_2 (5%) in Ar (95%) at 900°C for 60 minutes in the quartz tube furnace (Figure 3-1b). Experiments were performed at different annealing temperatures; 900; 1,000; 1,100; 1,200; 1,300; and 1,400°C. After annealing, the products were cooling down to room temperature and grounded using an agate mortar. Since the IMT laboratory is equipped with a dedicated fume hood and neutralisation system for handling concentrated HF, etching with concentrated HF was possible in my work.

The fine powder was transferred to 100 ml Teflon (PTFE) flask and 20 ml of absolute ethanol and 20 ml of HF solution 48% v/v was added. The solution was stirred for 150 minutes to etch the SiO_x matrix. Since working with highly concentrated HF poses severe chemical hazards, experiments using low concentration HF (12.5% v/v) were also performed to reduce the risk of using high HF concentration. However, from our observation, using the acid with low concentration significantly increases reaction time. Our experiments indicated that to get comparable results with 150 minute etching time, with 48% v/v HF, the process needs approximately~750 minutes (12-13 hours) if 12.5% v/v HF was used. Furthermore ammonium fluoride (NH_4F) was also performed as an alternative etching agent. A 17.8 g NH_4F was diluted in water to make 20 mL solution NH_4F (aq). The fluoride (F^-) concentration in the solution is comparable with 48% v/v HF. In this case, H-terminated SiNCs' products were produced after 150 minutes etching with the yield comparable to the experimental protocol with 48% v/v HF [267-269].

The brown dispersion obtained after etching was transferred to a Teflon separatory funnel and extracted with 20 ml of the corresponding alkene. Allyl, methyl ether was used to produce allyl, methyl (**C3**), pentene-1 was used to produce pentyl (**C5**), hexene-1 was used to produce hexyl (**C6**), octene-1 was

used to produce octyl (**C8**), decene-1 was used to produce decyl (**C10**), dodecene-1 was used to produce dodecyl (**C12**), tetradecene-1 was used to produce tetradecyl (**C14**) and hexadecane-1 was used to produce hexadecyl (**C16**)-SiNCs. The top layer (non-polar organic part) was transferred to the round bottom flask or G30 microwave flask for argon purging.

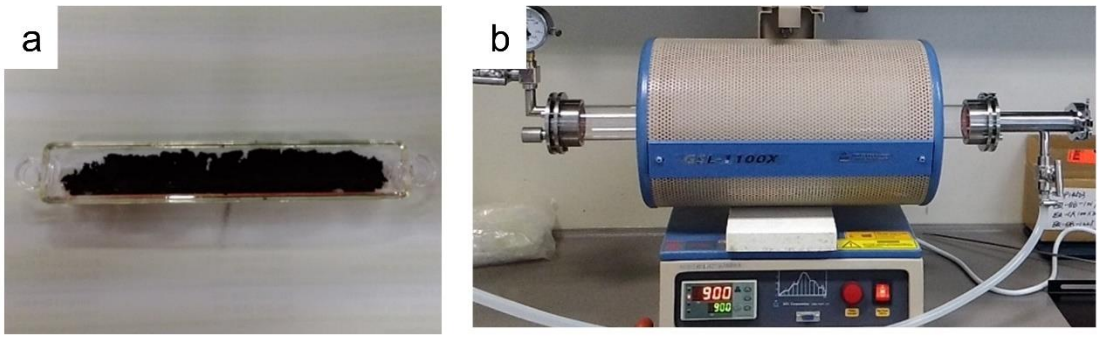

Figure 3-1. (a) Black powder of silicon monoxide (SiOx(x<2)) in the quartz boat, and (b) High-temperature tube furnace for the synthesis of SiNCs. A silicon rubber-sealed quartz tube makes it possible to deliver forming gas (H_2/Ar, 5%/95%) during the annealing process.

Fox-16 from Dow Corning & Co was also used in the annealing process as a reference from the previous reports [127, 270, 271]. A 5 ml of liquid was transferred to a 10 ml rotary evaporator flask to evaporate solvent under low temperature. A 5-hour evaporation process was used to get the white precipitate powder, at the bottom of the container, transferred to the quartz boat. The same reduction process was performed at 1,000°C for 60 minutes. The brown glassy chunk material was collected and grounded in an agate mortar. The fine powder was treated similarly to the above procedure. Our experiment produces (**C10**)-SiNCs with particle size ~3.8nm on average, and batch PLQY is ~15%, which is ~50% lower than our SiO precursors.

In an etching process, a strong base (e.g., KOH) is also attempted to etch annealed SiO using. 10 grams of KOH was diluted in 20 mL of absolute methanol (98%+ v/v) with vigorous stirring, the KOH gradually became soluble to form a viscous solution. A 0.3 g annealed SiO was transferred to the solution and stirred for 3-5h. Orange viscous solution was spooned out and diluted with methanol (MeOH) and observed with a 405 nm laser pointer to see the emission. A strong emission at 450 nm indicated the blue emission SiNCs that were previously reported by several authors [192, 272, 273].

3.1.4 Hydrosilylation reaction

In my project, there were two reactions used, namely, conventional thermal hydrosilylation reaction (CTH) [274] and microwave-assisted hydrosilylation reaction (MWH). Our first attempt used a reflux reactor in order to replicate previous results reported by other groups [275, 276]. Our approach was to get the same declared value of SiNCs PLQYs, learn from it, and develop a method to optimize the yields

and photophysical properties. In reflux reactor, only 1-decene as passivating agent was used as reference work because Ozin's group widely reported the results [83, 86-90, 234, 275-282].

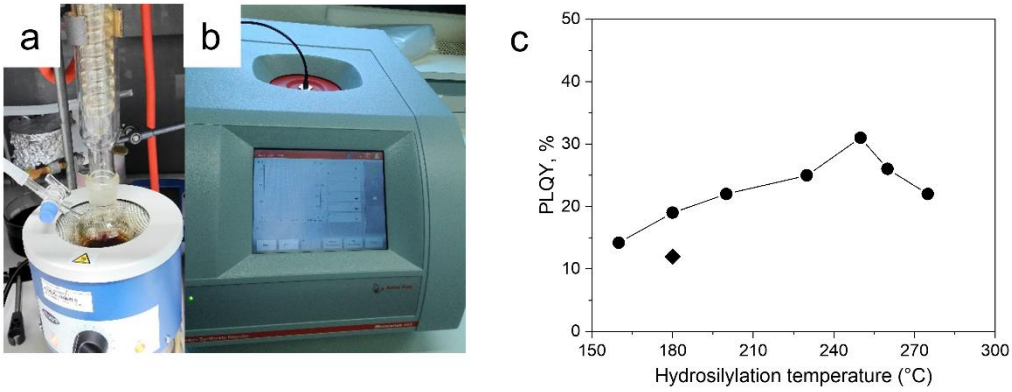

Figure 3-2. (a) Reflux reactor and (b) microwave reactor (Monowave 400®) for hydrosilylation reaction functionalization in SiNCs synthesis. (c) PLQY values of hexyl (C10) functionalized SiNCs using conventional hydrosilylation methods in reflux reactor (♦) and microwave-assisted hydrosilylation reaction in a microwave reactor (●). PLQY values were attributed to batch products right after the synthesis.

Conventional thermal hydrosilylation (CTH) was performed using a reflux reactor. Two-neck round-bottom flasks were placed in the electric heating mantle, and the top neck was mounted to the condenser or reflux that was filled with spiral pipe water-cooling to let the vapour from the solvent re-condensate back to the bottom of the flask. Another neck was mounted to the argon gas inlet, allowing argon gas to flow on top of the solvent and exit at the top of the condenser. The condenser's height is long enough to prevent the solvent's evaporation while introducing argon gas (Figure 3-2a). The reaction proceeds at the boiling point of the solvent. There is only one possibility of doing a hydrosilylation reaction in conventional thermal reflux at the solvent's boiling point of ligands. If the reaction works above the solvent's boiling point, it must be done using another approach, such as solvatothermal synthesis/reaction. The generic name attributed to the reaction above the liquid's boiling point was named as a hydrothermal reaction. This term has been used since the mid-19th-century when geologists first simulated the formation of rocks and minerals[19]. In solvatothermal synthesis, the reaction proceeds at a very high temperature as long as the chamber can hold the extreme confine pressure inside [283, 284].

The heating method can be fire, melting metals, steam, electricity, and microwave. One way to do solvatothermal reaction is by using microwave-assisted hydrosilylation. My experiment uses the Monowave 400® microwave reactor produced by Anton Paar GmbH (Figure 3-2b). The device consists of an 850W magnetron to generate microwave radiation. The sample holder is located in the round cylinder shape in the middle and is 10 cm in diameter. At the bottom is a hole for the exhaust and in the wall at 90° respective to each other are windows, one is directly facing the infrared sensor (which is simultaneously measuring reaction temperature), and one is facing to the front camera lens (which simultaneously monitors the progress of the reaction).

The cylinder is equipped with a white PTFE cavity holder that is screwed to the metal cylinder and equipped with silicone rubber as protection. This PTFE cavity is designed as a protective and cooking chamber for this instrument. Sometimes an accident might happen (for example, vial rupture or electric sparks), this chamber (cavity) should hold the debris and fire to prevent further damage to the instrument (vial ruptures are our collective experiences when performing reactions). Because the device can work at high pressure (max 30 bar) and relatively high temperature (max 300°C), the unique holder and vial are designed for it. The vials for this instrument are G30 and G10, and the index refers to the maximum volume of the vials. G30 means that this vial has a maximum volume of 30 ml, but in the reaction it must be filled to a maximum of 20 ml to anticipate the thermal volume expansion, whereas G10 means this vial has a maximum volume of 10ml, but must be filled to a maximum of 5 ml for the same reason. The vials are made of thick quartz glass and can hold up to 30 bar pressure. However, by request, there is also a vial made of silicon carbide for a particular purpose. The vials are capped with Teflon® coated silicon septum and tightened with a heat resistant plastic/polymer cap. There is a hole in the middle of the septum to mount a small glass pipe for a ruby thermometer. This ruby thermometer is used to measure reaction temperature in real-time and with high accuracy. The sample holder is attached to a rotating hydraulic-lid operating with pressured air. Pressured air is used as a coolant for the hydraulics. Finally, the instrument works with factory-developed software equipped with a full touch-screen display for users' convenience. The brief photophysical properties of conventional thermal hydrosilylation and microwave-assisted hydrosilylation are presented in Figure 3-2c for comparison**.**

3.1.5 Conventional thermal *vs.* microwave-assisted hydrosilylation

3.1.5.1 Conventional thermal hydrosilylation (CTH)

The brown dispersion obtained after etching process was transferred to a Teflon® separatory funnel and extracted with 20 ml of hexene-1. The polar part was discarded, and the non-polar part was collected in a 100 ml two-neck round bottom flask. The condenser is assembled, argon gas was delivered, and the mantle's temperature was adjusted to reach boiling temperature. The temperature was maintained by fixing the knob of the mantle to boiling temperature. At boiling temperature, the reaction was maintained at this condition for at least 15-18h to complete the hydrosilylation reaction. When the reaction was completed, the dark orange solution was formed, and under 405 nm laser excitation, it was easy to see the red fluorescent light as an indicator for the successful formation of decyl (**C10**)-SiNCs. A small quantity of solution was pipetted and re-dispersed in n-hexane for PLQY measurement of the batch solution. The solution was then transferred to a centrifuge tube, rotating at 2,500 rpm for 5 minutes to remove the big particles. The dispersion was transferred to a new tube, and dropwise of ethanol/methanol (1:2) mixture was added to the solution until the milk solution formed and the centrifuge began at 2,500 rpm. The precipitate was collected and re-dispersed in n-hexane and labelled as fraction number one (F1). The solution was transferred to the new centrifuge tube, and again dropwise of the mixture was re-added until homogeneous milk was formed. Other consecutive centrifugation processes were carried out similarly with

the above procedure with the speed being increased gradually from 2,500 rpm to 3,000; 3,500; 4,000; 4,500; 5,000; 6,000; 7,000; 8,000 and 9,000 rpm. The time is increased from 5, 10, 15, and 20 minutes until a precipitate was formed. Collected precipitate were named as fraction number 2, 3, 4…14 (F2, F3, F4, F5, F6, F7, F8, F9, F10, F11, F12, F13, and F14). F14 is bright reddish SiNCs in hexane solution having bright red emission when illuminated with a 405nm laser. Whereas F1 is dark black-reddish SiNCs dispersed in hexane solution, having dim red emission when illuminated with 405 nm laser. The precipitation process was stopped when the solution is water-clear and showing no-red-emission when illuminated with a 405 nm laser (see Figure 3-3).

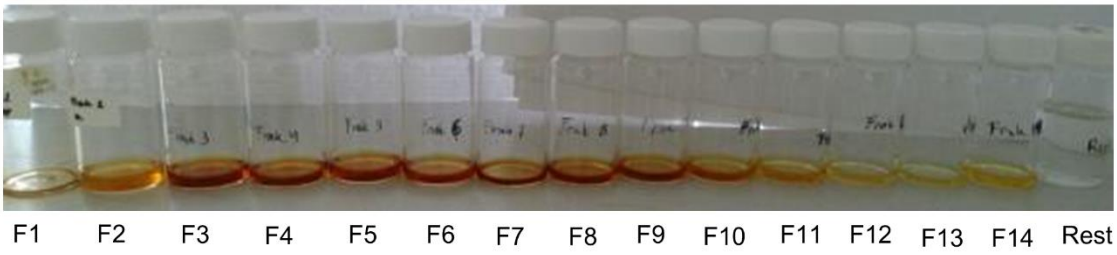

Figure 3-3. Size-separation with centrifugation by using a dropwise MeOH/EtOH (1:2) mixture. F represents the separated fraction due to the amount of mixture (dropwise), the speed of centrifuge rotation (increased gradually from 2500-9000 rpm), and rotation time (increased gradually from 5-20 minutes).

3.1.5.2 Microwave-assisted hydrosilylation

The brown dispersion was transferred to a Teflon® separatory funnel and extracted with 20 ml of hexene-1 (**C6**), octene-1 (**C8**), decene-1 (**C10**), dodecene-1 (**C12**), tetradecene-1 (**C14**), hexadecane-1 (**C14**), allyl-methyl ether (**C3**), and pentene-1 (**C5**). The polar solution was discarded, and the non-polar at the top was collected in a G30 microwave vial and sealed with silicone septum. Argon gas was delivered into the solution through a needle. The resulting dispersion was purged for 20 minutes before being placed in a microwave reactor (Figure 3-4a, b, c). Sample **C8, C10, C12, C14**, and **C16** were thermally heated at 250°C for 20 minutes and 600 rpm stirring, whereas sample **C6** was heated at 230°C for 20 minutes and 600 rpm, and sample **C3** and **C5** were mixed with 5ml p-xylene and heated at 230°C for 20 minutes and 600 rpm. The temperature was monitored in real-time using a ruby thermometer, which was dipped in solution. Afterwards, the products were transferred to a centrifuge tube and rotated for 5 minutes to discard large particles. A small quantity of solution was pipetted and re-dispersed in 5 ml n-hexane for PLQY measurement of batch solution. The batch synthesis was repeated four times for every alkene and seven times for hexene-1 (**C6**) to get confident statistics of reproducibility/repeatability and the procedure's reliability. Size separation was not performed because hexyl (**C6**)-SiNCs tended to precipitate under an ambient atmosphere. Once the synthesis was completed and the solution temperature was cooled down to room temperature, many tiny yellow particles started to precipitate at the bottom of G30. The non-precipitate (yellow solution) was collected for PLQY measurement. These yellow solutions were not

precipitated when a methanol/ethanol mixture was dropped, and even ultra-centrifuge (15,000 rpm) was applied to the solution (Figure 3-4d, e).

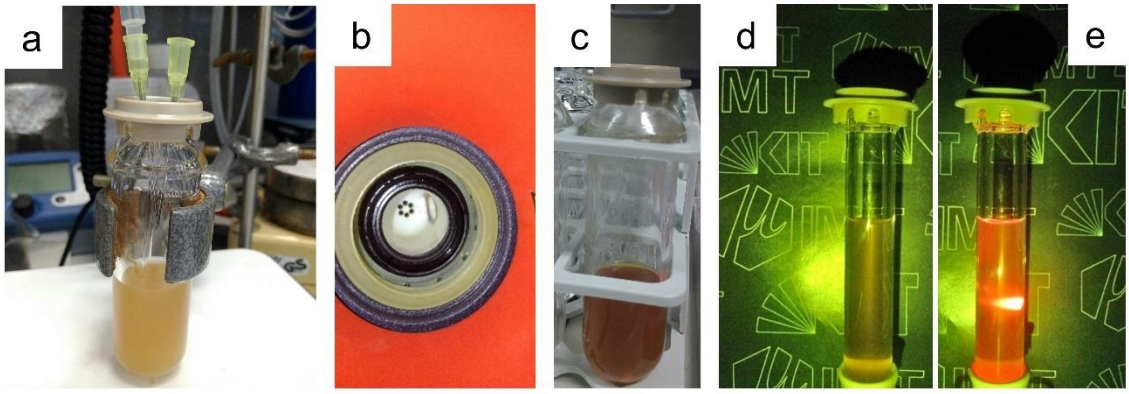

Figure 3-4. (a) H-SiNCs dispersed in alkene-1 is purged with argon for 20 minutes, (b) cavity in microwave reactor the place for vials during hydrosilylation reaction, (c) reaction produced under room fluorescent light, (d) reaction produced under 365 nm ultraviolet lamp, and (e) reaction produced under 405 nm laser excitations (0.2 mW).

3.1.5.3 Radical functionalization reaction

For compounds having a carbon chain lower than **C5**, namely, ethylene (**C2**), propene-1 (**C3**), and butene-1 (**C4**), their room temperature phases were usually a vapour or a gas. Since working with the gas phase is inconvenient, the radical functionalization reaction method is thus one way to do it. To commence, this work wants to functionalize **H**-SiNCs with butene-1 (**C4**). The procedure was that the brown dispersion was transferred to a Teflon® separatory funnel and extracted with 20 ml of hexane. The polar solution was then discarded, and the non-polar solution was collected in 100ml two-neck round-bottom flasks. The valve neck was closed, and the central neck was closed with a rubber stopper. The container is then connected with a rotary evaporator to evaporate n-hexane and end up with dry precipitate **H**-SiNCs at the bottom of the flask.

The quantity of black precipitate was approximate 1-5 mg. The procedure was continued by unmounting the flask from the rotary evaporator and closed with a rubber stopper. The flask was placed in a 500ml Dewar filled with liquid nitrogen. Once the expected temperature was achieved, butene-1 (**C4**) was delivered to the container. The regulator at the butene-1 bottle needs to be adjusted carefully to control the flow. Gradually clear transparent **C4** liquid started to form at the bottom of the flask, and the process was maintained for about 5-10 minutes until the significant liquid was formed. A 0.1 mg 2,2-azobis(2-methylpropionitrile), in short AIBN, was added to the solution as a radical precursor. The dispersion was shaken gently inside the Dewar for 10-15 minutes. The flask was lifted, and the solution gradually disappears, leaving behind black powder. When attempted to re-disperse it in 5 ml n-hexane the powder was no longer soluble in the hexane. When the powder illuminated with UV-light, there was no red emission coming from the powder as a sign of (**C4**)-SiNCs formation. From the appearance of the powder, it

resembled a pristine silicon monoxide. Based on the observation, it concluded that the experiment was failed, and the result was negative. It was not worth trying to dig any more profoundly into this research because finding a suitable precursor for the radical reaction that works at very low temperatures was time-consuming, and the objective was beyond our target.

3.1.6 Characterization

3.1.7 Structural and optical characterization

3.1.7.1 Ultraviolet-visible spectroscopy

Absorption spectra were taken with a UV-Vis-NIR spectrophotometer (Perkin Elmer Lambda 950) with a 2 nm resolution. Both sample and reference cuvettes (3.5 ml, path length 1 cm from Starna®) were filled with n-hexane to take a baseline. The SiNCs sample (dispersed in n-hexane) was dropwise to the sample cuvette using 20µl pipette and its spectra was collected. The absorbance/optical density was determined using the Lamber-Beer relation. All absorbance in this thesis is measured using a Perkin Elmer Lambda 950 instrument, resulting in the direct conversion of transmittance to absorbance. The device recorded only the number of photons transmitted through particles to the detector, and the absorbance was determined as transmittance-absorbance relation in the Lamber-Beer equation. In this thesis, the unit for absorbance is written as AU, to distinguish it from the arbitrary unit (a.u) the capital A and U are used instead.

3.1.7.2 Photoluminescent excitation (PLE)

PLE was taken with a spectrofluorometer (Varian Cary Eclipse®), equipped with a build-in Xenon lamp as an excitation source and photomultiplier tube (PMT) as the detector. The instrument can scan from 250-1,000 nm with the slits for excitation, and emission can be adjusted at 1.5, 2.5, 5, 10, and 20 nm. The device is also equipped with built-in filters for excitation and emission, and the detector's sensitivity can be increased by adjusting the detector's current/power. In SiNCs, rapid emission scanning was conducted to briefly locate the emission peak under excitation at 350 nm, at which SiNCs have significant absorption. Experiments showed that maximum emission peaks for our SiNCs sample were located around 800-890 nm. Therefore, PLE was acquired at 800 nm emission, and the excitation was scanned from 300-550 nm. Since alkyl functionalized SiNCs is considered a typical indirect bandgap semiconductor, the PLE is coinciding perfectly with UV-Vis spectra.

3.1.7.3 Attenuated-total reflectance fourier-transform-infrared spectroscopy (ATR-FTIR)

Infrared spectra were taken with Bruker Vertex 70 with a platinum ATR module. A diamond crystal was used as ATR crystals, and spectra were taken from 4000 cm^{-1} to 600 cm^{-1} with 2 cm^{-1} resolution. No specific sample preparation was required. SiNCs (dispersed in n-hexane) were drop-casted using micropipette on the top of the crystals, and the measurement can proceed. For SiNCs, determining Si-H

peaks at 2100 cm^{-1} is the most arduous task, since measuring this peak is quite tricky because signals at 2100 cm^{-1} are often buried in a loud noise floor due to the strong IR absorption of the diamond crystals. However, the signal-to-noise ratio was enhanced by carefully collecting the background signal for subtraction and thus successfully made this measurement possible at the cost of a long measurement time.

Moreover, ambient CO_2 and H_2O might disturb the measurement, but maintaining nitrogen flow at 140 (squared-cubic-centimeter) sccm/min and setting-up CO_2/H_2O calibration is very helpful. Most SiNCs peak and alkyl chain peaks are distinguishable, except for wide-band at 980-1,200 cm^{-1}, but overall measurement can be performed at ambient temperature and pressure with reasonable accuracy. The peaks acquired with ATR-methods were compared with the controlled atmosphere of potassium bromide (KBR)-pellet transmittance methods as references.

3.1.7.4 Photoluminescent (PL) emission

PL-emission spectra were measured with calibrated CCS200 spectrometer (Thorlabs) using 1 mW light emitting diode (LED) with $\lambda = 375$ nm for excitation. The LED beam was focused with a lens and directed into an integrating sphere (Labsphere) with 15 cm diameter. An optical 1mm fibre (FP1000URT, Thorlabs) was used to collect the emission from the integrating sphere and transfer it to the spectrometer (CCS200, Thorlabs). Short integration times, usually 20–50 times shorter than for UC detection, were utilized. All raw detected spectra were recalculated to give power spectra using an integration time value. The linearity of the signal versus integration time of CCD was proven experimentally. The whole detection system's spectral response was calibrated using a calibration lamp (HL-3plus-INT-CAL, Ocean Optics), and the correction was further applied to the power spectra.

3.1.8 Particle size characterization

3.1.8.1 Dynamic light scattering (DLS)

A particle size analyser, Litesizer 500^{TM,} was used to measure particle size. This instrument can determine the particle size of nanoparticle and microparticles in dispersion or solution (the measurement result is comparable with scanning electron microscope (SEM), transmission electron microscope (TEM), and atomic force microscopy (AFM)). In principle, the particle size is determined by simulating the number of scattering lights caused by the particle in random motion. There are two kinds of possible scattering measurements: static light scattering and dynamic light scattering. In static light scattering (SLS), every single particle in the system scattered light once in time in any direction; thus, by putting many calibrated detectors at all possible scattering points (half-sphere), and correlating the light interferences (constructive interferences) with a simulated cross-section of the theoretical particle, the hydrodynamic size (simply globular size for polymer) can be determined. However, confining single scattering light in one direction is not easy; thus, multiple scattering seems likely for photons by increasing the concentration. Therefore, the autocorrelation function was applied in dynamic light scattering (DLS).

In principle, DLS works based on fluctuation change in monochromatic scattering light due to time, caused by Brownian motion of tiny (nano-or micro size) particle or molecule. Two layers of polarizers were located at a given position, and slightly moving one polarizer, creating a fluctuating intensity of the scattering pattern. The dynamic of scattering intensity overtime is fitted to the auto-correlation function to get the particle information. This information was acquired to predict the particle properties, such as hydrodynamic diameter, size distribution, and monodispersity index using a series of mathematical approximations. In our project, Litesizer 500™ was used; this instrument is developed and fabricated by Anton Paar GmbH.

Alkyl-SiNCs samples were diluted in toluene or n-hexane and filtered through 0.02µm PTFE filter to a fluorescent cuvette (3.5 ml, path length 1 cm from Starna®), and closed with the cap. The cuvette was placed in the cuvette holder, and the lid was closed. Measurement was done using specific adjustments: the cuvette was quartz glass, the solvent was n-hexane, measurement temperature was at 20°C, and the measurement angle was optimum, meaning that the instrument will adjust to all possible measurement angles; 30°, 90°, and 127°. Every measurement was repeated at least three times, and every single analysis was done in 60 cycles to get a reliable result.

3.1.8.2 Transmission electron microscope (TEM)

Transmission electron microscope (TEM) investigations were carried out on a TITAN 60-300 microscope, at accelerating voltage 300 kV. The measurements were conducted in the institute of nanotechnology (INT), North Campus, Karlsruhe Institute of Technology (KIT).

3.1.9 Photoluminescent quantum yield (PLQY) and PL-lifetimes

3.1.9.1 PLQY

PLQY was determined using two methods: relative/comparative method and absolute method. In the relative method, one compares the gradient of integrated fluorescence/absorbance of the sample $[grad_x]$ and the reference $[grad_R]$ relative to the reference PLQY data retrieved from literature (Φ_{f_R}) according to Equation3.7.

$$\boldsymbol{\Phi_{f_x} = \Phi_{f_R} \frac{[grad_x]}{[grad_R]} \frac{n_x^2}{n_R^2}} \tag{3.7}$$

Where n_x^2 and n_R^2 is refractive index of sample and reference. In our research, zinc phthalocyanine (Zn-Pc) (Φ_f =23% in THF at 20°C) were used as standard [218]. Comparing the gradient of the integrated intensity of the SiNCs sample and the integrated intensity of the reference (Zn-Pc) material, the sample's quantum yield can be determined using Equation 3.7**.** In Figure 3-5 there is an example of PLQY determination for decyl (**C10**)-SiNCs fraction number-10 (F10) and PLQY (Φ_f =18.5%).

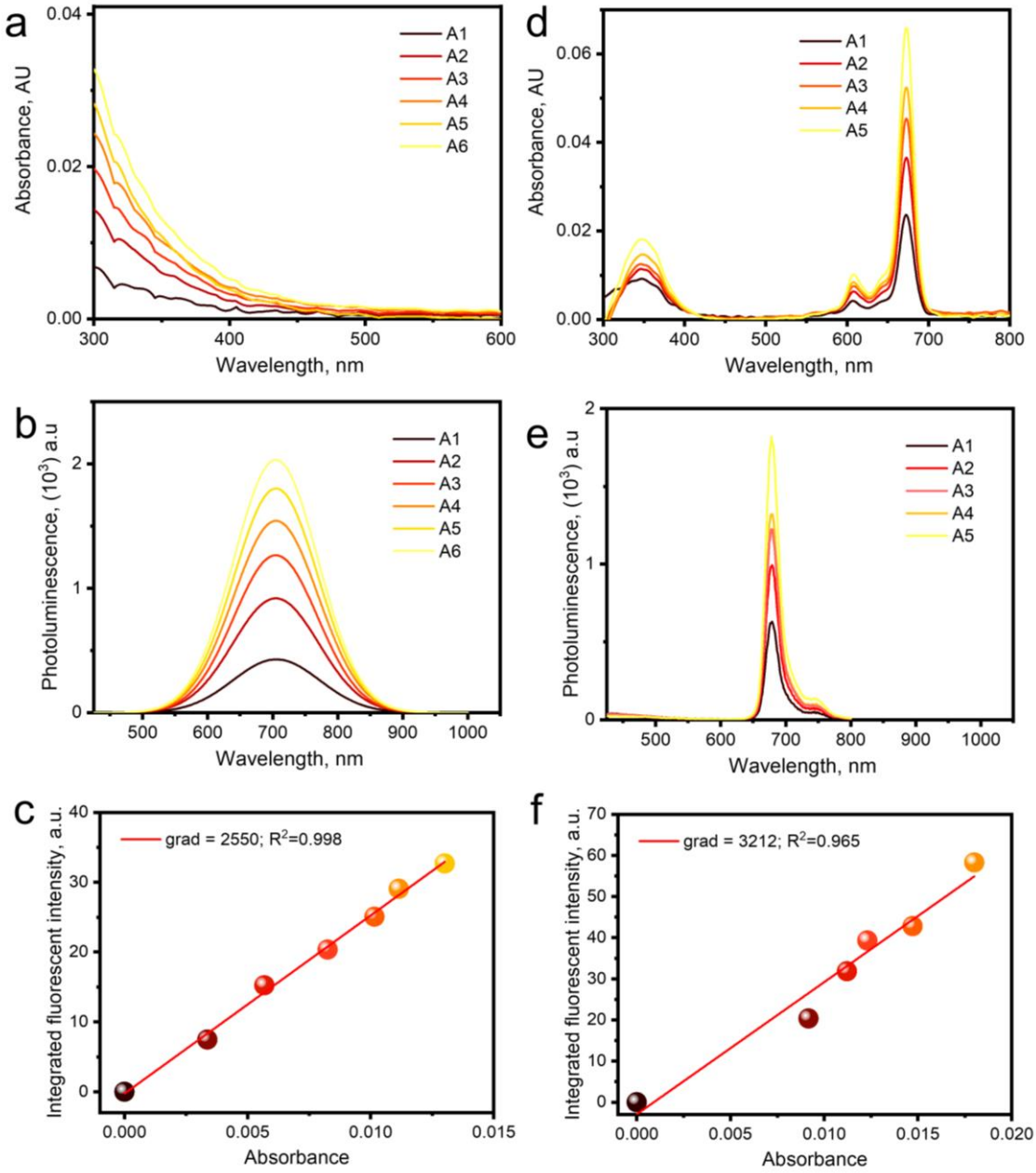

Figure 3-5. (a) Absorbance, (b) PL-emission excited at 350 nm, and (c) integrated fluorescent intensity vs. absorbance for decyl (C10)-SiNCs fraction-10 (F10) from the conventional heating hydrosilylation reaction. (d) Absorbance, (e) PL-emission excited at 350 nm, and (f) integrated fluorescent intensity vs. absorbance of Zn-phthalocyanine

The slit of UV-vis-NIR spectrophotometer (Perkin Elmer Lambda 950) and spectrofluorometer (Varian Cary Eclipse) are adjusted to achieve the same spectral bandwidth of 5 nm. Fluorescent cuvettes filled with 2 ml n-hexane (blank) were placed in the sample holder of the UV-vis-NIR spectrometer to take a baseline. A 10 µl (**C10**)-SiNCs (dispersed in n-hexane) attributed as sample F10 was dropped to one cuvette, and spectra were taken (bear in mind that gradual addition of the sample should be around optical density (OD) OD=0.01 or OD=0.02 to prevent reabsorption). The same fluorescent cuvette was moved to

the Varian Cary spectrofluorometer cuvette holder, and emission was collected at 350 nm excitation and 5 nm slit bandwidth. Next, a 10 µl (**C10**)-SiNCs was re-dropped into the cuvette, and absorption and emission spectra were collected. The addition of (**C10**)-SiNCs sample was continued 4 or 5 times to get an excellent square plot. The same principle was applied for reference Zn-Pc; instead of using an unknown concentration, in Zn-Pc, a stock 10^{-3} M solution was used as a starter. The solution of Zn-Pc in tetrahydrofuran (THF) were used because PLQY data was available from the literature[218]. Similar procedures were realized with Zn-Pc, and our plot demonstrated gradient was 3212 for linear plot integrated fluorescent intensity *versus* absorbance (see Figure 3-5f). Overall, the procedure was reliable except that the PMT detector in our spectrofluorometer is not sensitive at NIR emission (800-1,200nm). For a sample fraction-1 (F1) of (**C10**)-SiNCs, the emission was cutting off at 860nm, and the shape of emission was a truncated bell-shape. Due to the problem, this method was decided not to be used any further. However, as a learning process, the PLQY of fractionated (ensemble) of (**C10**)-SiNCs can be determined for samples (F1, F2, F3…F14). Apart from the accuracy, our work demonstrates good agreement with the previous report (pyramid shape of PLQY trend).

Another technique called an absolute method is used to solve a problem with the relative/comparative method. Instead of measuring PLQY sample-x relative to reference-y, all incoming emission photons were collected from the sample and divided by the absorbed photons from the sample (coming from the sources). Careful measurement in the integrating sphere and avoiding all possible loss due to reflections, refractions, et cetera, an absolute PLQY was attained. The home-build PLQY apparatus illustrated schematically in Figure 3-6a.

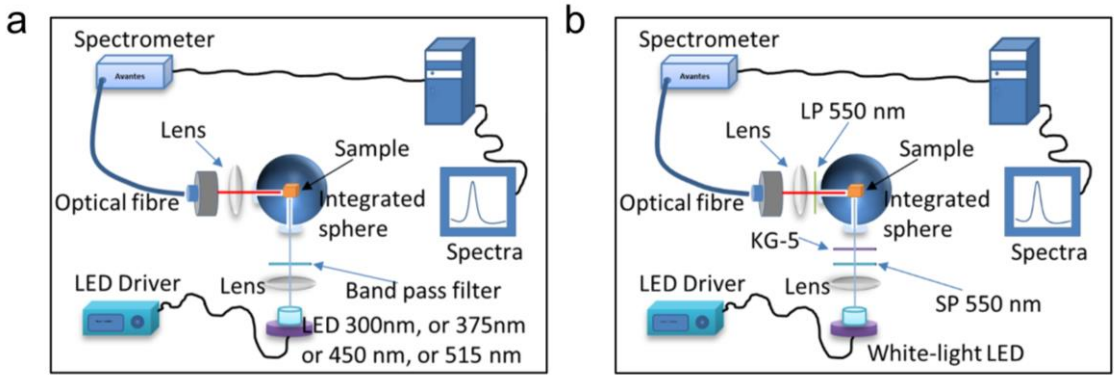

Figure 3-6. Schematic of (a) home built PLQY and (b) broadband excitation setup

The spectra of emission and photoluminescent quantum yield (PLQY) of the materials were measured in a home-built optical system. As an excitation source, a 375 nm LED with a glass lens (LED375L, Thorlabs GmbH) is driven by the laser diode controller (ITC4001, Thorlabs GmbH) was used. For the PLQY measurements, the LED emission was directed through a small opening (5mm) straight into the integrating sphere (IS) (Labsphere), having a diameter of 15 cm. A sample was placed in the middle of the integrating sphere on the rotatable holding adapter. Optical fibre with a diameter of 1 mm (FP1000URT, Thorlabs) was collecting an emission from the integrating sphere and transferred the light to the CCD

spectrometer (AvaSpec-2048x64-TEC, Avantes BV). The detection system's spectral correction was done using a certified halogen calibration lamp (HL-3plus, Ocean Optics). The correction factors include spectral sensitivity of the CCD of the spectrometer, spectral transmittance of the optical fibre, and spectra changes caused by other reasons like non-ideality of the scattering coating of IS. The spectra necessary for an absolute PLQY value determination were measured and analysed according to the published procedure [278, 285]. The schematics of our home-build PLQY setup and broadband excitation setup is illustrated in Figure 3-6b.

3.1.9.2 PL lifetimes

For PL lifetime measurements, time-correlated single-photon counting (TCSPC) and a multichannel scaling (MCS) card (Timeharp 260, Pico Quant) were used. The diode laser (Thorlabs 405 nm) was performed via a built-in function generator in the laser diode driver. To detect UC emission, the TTL signal from the laser diode controller was delayed using a delay generator (DG645, Stanford Research Systems). The spectral separation of the photoluminescence was achieved via a double monochromator (DTMS300, Bentham), and the emission at a specific wavelength was detected via a photomultiplier tune (R928P, Hamamatsu), mounted in a temperature-cooled housing (Cool One, Horiba).

3.1.10 Stability measurement

Alkyl (**C6**, **C8**, **C10**, **C12**, **C13**, **C14**, and **C16**) functionalized-SiNCs samples were stored in separate vials, one was stored in a screw cap vial at ambient oxygen atmosphere, and the other one was stored in the glovebox. The sample stored in ambient oxygen was investigated daily for the emission and PLQY, whereas the glovebox sample was examined at the end of the experiment.

3.2 Dye functionalized SiNCs

3.2.1 Materials

Silicon monoxide (99.9%, 325 mesh) was purchased from Sigma-Aldrich®, hydrochloric acid (48%) was purchased from Fisher Scientific®, ethanol 98%, methanol (HPLC grade) and toluene (99%+) were purchased from Merck®, 1-hexene (99%) was purchased from Acros®, n-hexane spectroscopic grade was purchased from Alfa Aesar®, 3-ethenylperylene was purchased from Fluorochem®. Ltd, UK, and 3-ethynylperylene were obtained from Lumiprobe GmbH, Germany. All chemicals were used without further purification. Ethylene-m-phenyl BODIPY (MS (APCI): m/z (%) 406.3(99.2) M-) was synthesized in agreement with Clark *et al.* [220] using 3-vinylbenzaldehyde (Sigma-Aldrich®) as a precursor[286].

3.2.2 Synthetic Procedures

3.2.3 Synthesis of hydrogen terminated SiNCs

1.0 g SiO(x<2) was transferred to a quartz boat and reduced thermally under flowing H_2 (5%) in Ar (95%) at 900°C for 60 minutes in a tube furnace. After annealing, the product was cooled down to room temperature and ground using an agate mortar. The fine powder was transferred to 100 ml Teflon® vessel, and 15 ml of absolute ethanol and 15 ml of HF acid solution 48% v/v were added and stirred for 150 minutes to remove the SiO_2 matrix. The resulting brown dispersion was transferred to a Teflon® separatory funnel, and SiNCs were extracted with 15 ml toluene or n-hexane.

3.2.4 Hydrosilylation of dye molecules and SiNCs in MW reactor

A 3-step optimization method was done to the sample to get an effective dye functionalization. Our first approach is based on the alkyl functionalization, and then the procedure were developed afterward to get an expected materials. For the first method, the dispersion of **H**-SiNCs in toluene was transferred to G30 MW glass tube, 2 mg of the dye molecule was added and the solution stirred under argon atmosphere for 30 minutes before the reaction in the MW reactor. The MW reactor (Anton Paar Monowave 400®) was performed at 230°C for 120 minutes. The second method, **H**-SiNCs in hexene-1 was transferred to G30 MW vial, and 2 mg of the dye molecule was added to the solution while stirring under the argon atmosphere for 30 minutes before conducting the reaction in the MW reactor. The reaction in the MW reactor was performed at 230°C for 120 minutes. Finally the third method, 5 ml of hexene-1 was injected into the solution obtained in the first method, and additional heating at 230°C was performed for 120 minutes.

3.2.5 Purification of SiNCs

After the hydrosilylation reaction, the product was centrifuged (centrifuge Sigma 2-16P®) at 2000 rpm for 10 minutes to discard the massive particles. A mixture of ethanol: methanol (2:1) was used to precipitate SiNCs with the attached dyes. The resulting cloudy solution was centrifuged at 10,000 rpm for 20 minutes; the precipitate was collected, washed three times with methanol, and re-dispersed in n-hexane. The dye attachment was controlled using thin-layer chromatography (TLC). The bright spot (with Rf = 0.6 - 0.9) was observed in the control experiment with the unreacted dyes. Under UV-excitation, the TLC plate with dye functionalized SiNCs did not demonstrate any bright spots that might correspond to the unreacted dyes.

3.2.6 Characterization

A Bruker Vertex 70 with platinum attenuated total reflection (ATR) module was used for the IR absorption measurements. Anton Paar Litesizer 500™ was used for the particle size distribution

measurements. A UV-VIS-NIR spectrophotometer (Perkin Elmer Lambda 950) was used for the optical absorption measurements.

3.2.7 Measurements of the extinction coefficient

A stock solution 0.1 % w/w SiNCs in n-hexane was prepared via dissolution of 0.655 mg dried SiNCs powder in n-hexane (1 ml). The stock solution 20 µl (13.1 µg) was then diluted in the n-hexane (2 ml) in 3 ml cuvette resulting in dispersion with a concentration of 1 x 10^{-3} % w/w. The stock solution (20 µl) was gradually added to the cuvette to prepare the least-square plot. Least-square-plot of absorbance as a function of concentrations were used to calculate the value of the extinction coefficient.

3.2.8 Measurements of the PL and PLE spectra

Varian Cary Eclipse 50® spectrometer was used for measurements of PLE spectra. The PL-emission at excitation wavelengths λ_{ex} = 300 nm, 375 nm, 405 nm, 440 nm, and 515 nm were measured during PLQY measurements using a calibrated spectrometer (AS 5216 DLL, Avantes). The absolute PLQY is defined as the procedure described previously in section **3.2.3.1**.

3.2.8.1 Broadband excitation

In the experiment with broad excitation via a white-light LED, a short-pass filter with a cut-off edge at 550 nm was used to block the incoming light. A long-pass filter with a cut-off edge of 550 nm was used in the detector's front to block the dyes luminescent. All measurements were performed for dispersions with the same optical density at λ 300nm = 0.3 absorbance unit (AU). The brightness enhancement ($\Delta_{brightness}$) is determined with Equation 3.8.

$$\Delta_{brightness} = \frac{\int I_{corr_s}(\lambda)d\lambda}{\int I_{corr_R}(\lambda)d\lambda} \tag{3.8}$$

Where $\left(I_{corr_s}\right)the$ corrected intensity of the measured sample, $\left(I_{corr_R}\right)$is the corrected intensity of reference (**C6)**-SiNCs. The home-build setup for broadband excitation measurement is illustrated schematically in Figure 3-6b.

3.2.8.2 PL-lifetimes

For the NIR PL lifetimes measurements, multichannel scaling (Time Harp 260, Pico Quant) was used. A modulated 405 nm, 80mW DL-7146-1012S lasers diode from Roithner Laser Technique is used to excite samples in the four edges of the polished cuvette. The TTL signal from the laser diode was controlled with a delay generator (DG645, Stanford Research Systems). A double monochromator (DTMS300, Bentham) was used to collect photoluminescence at the specific 810 nm wavelength. The emission was detected by a PMT (R928P, Hamamatsu), mounted in cooled housing (Cool One, Horiba).

Nanosecond PL lifetimes were measured using a steak camera (Hamamatsu C10910) coupled to a spectrometer (Acton SpectraPro SP2300) with an instrument response function of 320 ps. For the excitation, a mode-locked Ti: sapphire laser (Coherent, Chameleon Ultra) with a pulse width of 140 fs and a repetition rate of 80 MHz was used.

3.3 Singlet Oxygen Generation

3.3.1 Materials

Silicon monoxide (99.9 %, 325 mesh) and phenalenone (**phen**) (also known as perinaphtenone, 97 %) were purchased from Sigma-Aldrich®. Hydrofluoric acid (48 %) was purchased from Fisher Scientific®. Ethanol (98%), methanol (HPLC grade), and toluene (99 %+) were purchased from Merck®. 1-hexene (**C6**) (99 %) was purchased from Acros®. Cyclohexane (spectroscopic grade) was purchased from Alfa Aesar®. 3-ethynylperylene (dye-1) was obtained from Lumiprobe GmbH, Germany, and 3-ethenylperylene (dye-2) was purchased from Fluorochem. Ltd, UK All chemicals were used without further purification.

3.3.2 Singlet Oxygen Quantum Yields (Φ_Δ)

In this experiment, singlet oxygen quantum yield (Φ_Δ) were determined using two approaches, namely chemical method and phosphorescent method. The chemical method is conducted by quantifying the number of the product (i.e. peroxide molecules from probe molecules such as 9, 10-dimethylanthracene (**dma**) and rubrene (**rubrene**), due to the photochemical reaction of singlet oxygen and probe molecules divided by the number of absorbed photons. In contrast, the phosphorescent method is conducted by quantifying the singlet oxygen phosphorescent at 1270 nm relative to the number of absorbed photons.

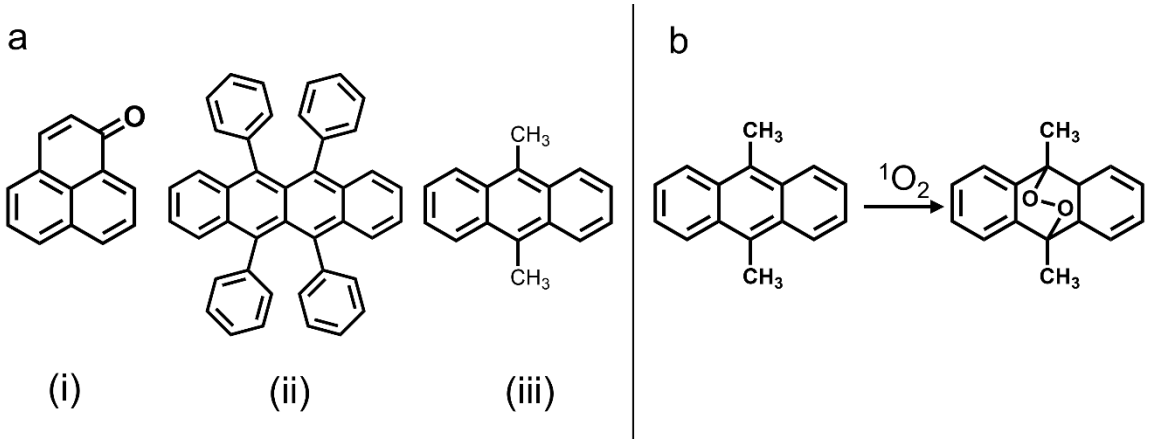

Figure 3-7. (a) Molecular structure (i) phenalenone, (ii) rubrene, (iii) 9,10-dimethyl anthracene. (b) Proposed chemical reaction between 9,10-dimethyl anthracene and singlet oxygen.

3.3.2.1 Chemical Method

Probe molecule, i.e., 9,10-dimethylanthracene (**dma**) and rubrene (**rubrene**)-are optically active molecules with an excess of delocalized π-bonds inside their structure that allow transition nπ* and ππ*. The transition is optically active, involving electronic transition from the ground state to the excited state. Thus, the delocalization electron is also a weak point of the molecule because it absorbs reactive species and reacts to saturate the bonding. Since the singlet oxygen molecule is a reactive species, it reacts simultaneously with a delocalized electron to form endoperoxide, and after the reaction, the molecule is no longer active optically. The reaction works correctly as one oxygen molecule depletes one probe molecule. Generating single singlet oxygen will shut down one probe molecule. In chemical kinetics, the reaction can be represented as per Equation 3.9.

$$\frac{d[\,{}^1O_2]}{dt} = k_{1O_2}[\,{}^1O_2] = \frac{d[dma - O_2]}{dt} = k_{dma-O_2}[dma - O_2] \tag{3.9}$$

Where $\frac{d[\,{}^1O_2]}{dt}$ is the formation rate of ($^1O_2$), $k_{1O_2}$the rate constant of ($^1O_2$), $\frac{d[dma-O_2]}{dt}$ is the disappearance rate of the **dma** probe and k_{DMA-O_2} is rate constant of the disappearance of **dma**. By taking the disappearance rate of **dma** at various sensitizers, singlet oxygen quantum yields of the sample could be determined using Equation 3.10.

$$\Phi_\Delta^{\mathrm{x}} = \Phi_\Delta^{\mathrm{R}} \frac{k^x}{k^R} \frac{(I_{abs}^R)}{(I_{abs}^x)} \tag{3.10}$$

Where Φ_Δ^{x} is singlet oxygen quantum yield of an unknown sample, Φ_Δ^{R} is singlet oxygen quantum yield a reference phenalenone molecule (**phen**), k^x is the rate constant of disappearance **dma/rubrene** molecule mixed with the sample, k^R is the rate constant of disappearance **dma/rubrene** molecule mixed with reference phenalenone (**phen**), (I_{abs}^R) and (I_{abs}^x) is the number of absorbed photons reference and for the sample. The representative molecular structure and the working mechanism is displayed in Figure 3-7**.**

A given concentration of the sample and **dma/rubrene** (2.5ml in 1 cm fluorescence cuvette) was illuminated with λ: 300nm, λ: 405nm, and λ: 450nm (LED from Thorlabs®) for 60 minutes inside the home build illumination box. The sample was then placed in the UV-vis-NIR spectrometer to take the spectra, and baseline was taken for non-illuminated samples. The illumination and measurement were done continuously for 60 minutes illumination. A similar procedure was done for reference phenalenone (**phen**). The schematic for the illumination box and emission profile of the LED and laser is illustrated in Figure 3-8.

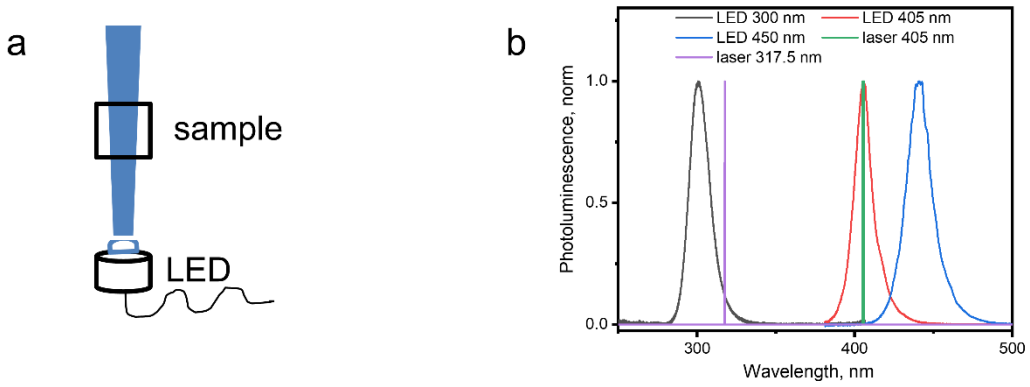

Figure 3-8. (a) Schematic of home-build illumination box, (b) emission profiles of LEDs and lasers used for excitations

3.3.2.2 Phosphorescent method

The samples (2.5 ml) dispersed in cyclohexane were placed in a quartz cuvette (Starna) with a path length of 1 cm and were irradiated with 405 nm diode lasers (75 mW, DL-7146-1012S, Roithner Laser Technique GmbH) or with a narrow-linewidth Ti: Sa laser (45 mW, SolsTiS, EMM-532, M-Squared Lasers) for the 317.5 nm excitations. The PL of $^1O_2$ was measured with irradiance calibrated NIR spectrometer (NIRQuest 512-1.7 Ocean Optics) operating in a 900 – 1,700 nm range. The integration time of 100 seconds was used for the collection of the $^1O_2$ phosphorescence spectra. The quantum yield of singlet $^1O_2$ generation (Φ_Δ) was calculated in agreement with Equation 3.11 using the **phen** as quantum yield standard.

$$\Phi_\Delta^x = \Phi_\Delta^R \frac{[S_{em}^x]}{[S_{em}^R]} \frac{[I_{abs}^R]}{[I_{abs}^x]} \tag{3.11}$$

Where $\boldsymbol{\Phi_\Delta^x}$ and $\boldsymbol{\Phi_\Delta^R}$ are singlet oxygen quantum yields of the sample and the reference, respectively. $[\boldsymbol{S_{em}^x}]$ and $[\boldsymbol{S_{em}^R}]$ are the integrated area of $^1O_2$ PL generated by the sample and the reference, while $[\boldsymbol{I_{abs}^x}]$ and $[\boldsymbol{I_{abs}^R}]$ are the number of absorbed photons by the sample and the reference. In the case of the excitation with monochromatic light, absorption (% of absorbed light $[\boldsymbol{A_\%^x}]$ and $[\boldsymbol{A_\%^R}]$ at the excitation wavelength) of the sample and the reference can be used instead of $[\boldsymbol{I_{abs}^x}]$ and $[\boldsymbol{I_{abs}^R}]$.

The reported value of Φ_Δ^R for **phen** in cyclohexane is 92 ± 0.5 % [287]. The concentrations of two sets of **phen**, dye-**p1**, dye-**p2**, (**C6**)-(**p1**)-SiNCs, and (**C6**)-(**p2**)-SiNCs solutions were adjusted to have roughly similar absorbance at 405 nm and 317.5 nm.

3.3.3 Temperature-dependent photoluminescence measurements

Dye molecules are dispersed in cyclohexane and placed in a quartz cuvette with a path length of 2 mm and purged with argon gas for 30 minutes. Subsequently, the cuvette was clamped to the cryostat

sample holder (Cryospares A7-103) and placed inside the sample chamber of the closed cycle cryostat (Oxford Instruments, Optistat Dry TLEX). After evacuating the sample chamber to ~10-5hPa, the chamber was flooded with helium (purity >99.999 mol %) to improve thermal coupling between the sample and the heat exchanger of the cryostat. PL emission spectra were measured at 20K for both dye-1 and dye-2 samples. For the excitation, a mode-locked ytterbium laser (Light Conversion, Pharos) with a pulse width of 190 fs and a repetition rate of 20 kHz was used. The laser's 1028 nm output was converted to 440 nm using an optical parametric amplifier (Light Conversion, Orpheus) and second harmonic generator (Light Conversion, Lyra). The steady-state photoluminescence spectra were recorded by a fibre-coupled UV/VIS spectrometer (Avantes, AvaSpec-2048L).

3.3.4 Uncertainty of singlet oxygen quantum yield

The uncertainty of $\Delta\Phi_\Delta$ comprised the uncertainties from the following experimental steps:

- $\Delta\Phi_\Delta^R$ = 0.5 % from the value of SO quantum yield of the reference PS
- Possible photobleaching of the reference PS (ΔS = 12 %)
- UV/Vis measurements ($\Delta UV/Vis$ = 0.1%)
- Luminescence detection (ΔDet = from 1% for strong luminescence up to 19 % for weak luminescence)

Thus, $\Delta\Phi_\Delta$ was calculated using Equation 3.12.

$$\Delta\Phi_\Delta = \sqrt{[\Delta\Phi_\Delta^R]^2 + [\Delta S]^2 + [\Delta UV/Vis]^2 + [\Delta Det]^2} \quad (3.12)$$

The results of the calculations are presented in Table 2 and Table 3 in Chapter 6.

4 Linear alkyl functionalized SiNCs

Some of the results present in Chapter 4 were published in Beri et al. [85]. The author did all the syntheses and performed all the characterization experiments in this chapter. Except for PL-lifetime measurements were performed by author and co-author Dr. Dmitry Busko, and TEM measurements were performed by co-author Dr. Andrey Mazilkin from the Institute of Nanotechnology (INT), KIT. The original idea was brainstormed with co-authors Prof. Bryce S. Richards, Dr. Andrey Turshatov, and Dr. Ian A. Howard. The main goal of this chapter was to study the photophysical properties and stability of alkyl functionalized SiNCs. To achieve this goal, the reduction of silicon monoxide at various heating temperatures were studied to produce various particle sizes of SiNCs. Then various etching techniques were also studied to obtain the desired particle size of hydrogen-SiNCs. Furthermore, hydrosilylation techniques were studied for various alkyl chain lengths to obtain alkyl-SiNCs whose surface area was optimally covered and producing maximum PLQY and high stability.

4.1 Synthesis of hydrogen-terminated SiNCs

As a preliminary study, the formation of SiNCs during the annealing process of silicon monoxide is monitored by employing two reciprocal techniques: FTIR and XRD. The results are shown in Figure 4-1, unveiling the insidious phase transformation of silicon monoxide at the different annealing temperatures.

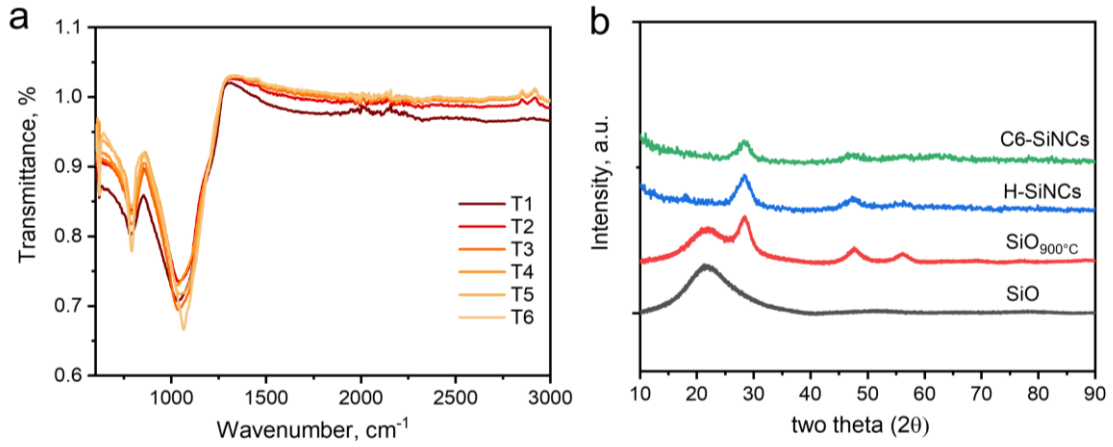

Figure 4-1. (a) FTIR spectroscopy of silicon monoxide at different annealing temperatures in H_2/Ar atmosphere, (T1, T2, T3, T4, T5, and T6 are attributed for thermal annealing at 900, 1,000; 1,100; 1,200; 1,300; and 1,400°C, respectively) (b) XRD spectra of silicon monoxide (black), annealed silicon monoxide (red), HF-etched silicon monoxide (blue) and hexyl (C6) functionalized SiNCs (green).

As annealing temperature increases from 900-1,400°C, changes in the stretching and bending modes of Si-O become more and more apparent, see Figure 4-1a [197, 288]. There are two recognizable absorption bands of a Si-O chemical bond: at 1,000 $cm^{-1,}$ attributing to stretching vibration mode, and at 760 cm^{-1} attributing to bending vibration mode. The shifting of resonance frequency at 1,000 cm^{-1} and 760 cm^{-1} manifests the decomposition process of amorphous silicon monoxide to crystalline Si-nano size

nucleates, according to SiO→ SiO_2 + Si chemical equation [289-291]. Moreover, the evolution of vibration amplitude at 760 cm^{-1}, implying the decrease of damping in the vibration spectra, conveys a piece of new information. This resonance frequency is attributed to the vibration mode of the Si-O bond of atoms constituting the surface of SiNCs [225]. Herein, the shift at 1,000 cm^{-1} is attributed to the boundary state of phase separation of SiNCs from the SiO_2 matrix.

As seen in Figure 4-1b, XRD of pristine precursor SiO shows no-signature of Si crystalline structure (leads to SiNCs). The wideband intensity at 2θ = 10° - 40° is attributed to the amorphous phase of the SiO. Annealed SiO at 900°C for 60 minutes shows the formation of nanocrystalline Si, due to the observation of peaks in the XRD at 2θ=28°, 48°, and 56°, which correspond to diamond cubic silicon. However, the remaining wideband background at 2θ =10-40° stands because the amorphous phase of SiO still exists at this annealing temperature. It also obtained that etched and alkyl functionalized samples no-longer have a broad background peak (amorphous phase), which is assumed to be diluted during the etching process. Hence, this amorphous phase is proposed belongs to the amorphous silica matrix, and it functions as a binder for nanocrystals [72].

4.2 Etching with HF (48% v/v), NH_4F, and KOH

To study the effectivity of HF etching, series of experiments are carried out to achieve the optimal duration of HF etching process. The optimal duration of the HF etching process is determined through the maximum photophysical property revealing in the samples' PLQY measurement. The experiments had been repeated at least three times to get more precise statistics. The samples are collected from the same etching batch using a 5 ml syringe every 15, 30, 60, 90, 120, 150, and 180 minutes, respectively, followed by adding 5 ml decene-1. After fractionation (described in Chapter3) it is transferred to a G10 microwave (MW) reactor vial and functionalized in the MW reactor for 20 minutes at 250°C. The PLQY of each sample is collected for the batch, and the results are presented in Figure 4-2a. Quite surprisingly, after 15 minutes of etching, SiNCs have formed by a considerable amount inside the sample as demonstrated by the appearance of PL peaks at 950 nm. The longer the etching duration is, the higher the PL peak intensity, and the more pronounced the PL peak blue-shifts (see Figure 4-2b). This phenomenon might be related to the decrease in the size of SiNCs.

Nonetheless, the increase in PLQY has no longer been obtained for the sample undergoing the etching process for more than 150 min. One of the rational explanations for this observation is that the absorbance enhancement might cause this. One can also answer this phenomenon based on the enhancement in the absorbance cross-section of a nano object, which possesses a higher surface area due to its small size of SiNCs in this case.

To compare the HF etching with other etching substances, a reaction with NH_4F was performed in 150 minutes of etching time (maximum point for HF). The sample undergoing the NH_4F etching process in 150 minutes exhibit PLQY = ~25%. This yield is in good agreement with the uncertainty range of HF

etching in a similar etching period (see Figure 4-2a). Nevertheless, the absorption and emission spectra for (**C10**)-SiNCs using NH_4F etching are precisely similar to (**C10**)-SiNCs using HF etching (Figure 4-3a) [269].

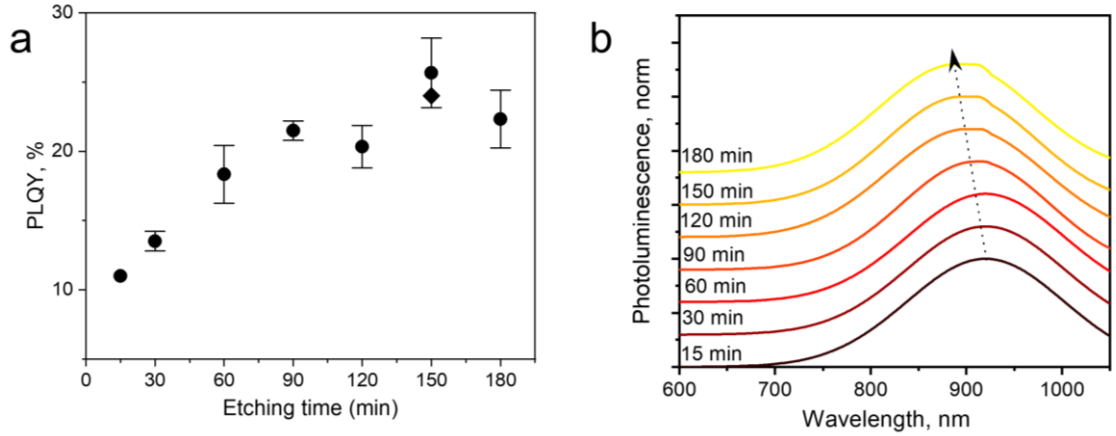

Figure 4-2. (a) Optimization of etching time with HF (●) and NH_4F (♦) of free-standing (C10)-SiNCs; functionalized in MW reactor for 20 minutes at 250 °C; PLQY was measured using LED excitation at 375 nm. Error bars were derived from the uncertainty of the three-times repeated etching process. (b) PL-emission's blue shift for free-standing (C10)-SiNCs functionalized in MW reactor for 20 minutes at 250°C

Experiment with base-solution etching is performed to study etching chemistry. Strong base solution (e.g., NaOH and KOH) have an ability to react with silica. In this experiment solution of KOH and MeOH was used as etching solution. The mixture of KOH/MeOH and annealed SiO exhibits a blue emission at ~440 nm when it was excited by a 350 nm xenon lamp in a Cary Eclipse fluorimeter (Figure 4-3c). Moreover, its absorption spectra are identical to the one of typical porous silicon. A meticulous examination of the absorption spectra reveals a signature of the indirect transition in the absorption of electrons under the excitation. Also, its PL-emission spectra are comprised of one of the saturated oxides, and hydroxide functionalized SiNCs, reported elsewhere [292].

Since MeOH/KOH also emits light in the same spectrum range, quantitative estimating this emission's contribution to the sample's total emission spectrum is worth doing. As a reference, the reaction carried out just using MeOH/KOH and without adding annealed SiO. The emission spectra of such a sample are collected afterwards. Excitation and PL-emission spectra for MeOH/KOH mixture present as a mirror image of each other where the peak of PLE is at ~275 nm (maximum) and the PL-emission is at ~330 nm (maximum) (Figure 4-3b). The PLE and PL-Emission spectrum coincide at 300nm creating internal absorption. The spectra look very similar to typical organic chromophore spectra and slightly different from the sample containing annealed and etched SiO in the mixture of MeOH/KOH [272]. However, this result was abandoned because there was no-option for further functionalized oxide functionalized SiNCs.

After optimizing the MW reactor's hydrosilylation reaction, the experiments are also performed to many possible functionalized ligands, and one of the possible ligands is ethylene glycol. The goal is to prepare crown-alike SiNCs' surface by reacting H- SiNCs with ethylene glycol. This crown-alike SiNCs' surface was expected to have a higher solubility in water and at the same time, maintaining its PLQY. It also targets biomedical applications related to water-soluble SiNCs. This research direction is appealing due to the lack of publications on literature about water-soluble ligand functionalized SiNCs that emit in 600-1,000 nm emission. It has been proved that the reaction between SiO and ethylene glycol could be performed using MW hydrosilylation reaction. Indeed, the SiO reacted adequately with ethylene glycol and created a bright yellow viscous solution and also soluble in water. The solution shows a bright blue emission peak at 440nm, under 405 nm excitation. This emission was a good match with the emission of KOH etching SiNCs.

The physicochemical properties of KOH-etched SiNCs are the same as **EG**-SiNCs. It has emission at 440 nm, is soluble in water to form a slightly yellow solution, and insoluble in organic solvents (Figure 4-3d). From our critical literature review, this blue emission of SiNCs may come from the oxide defect functionalization [293-299].

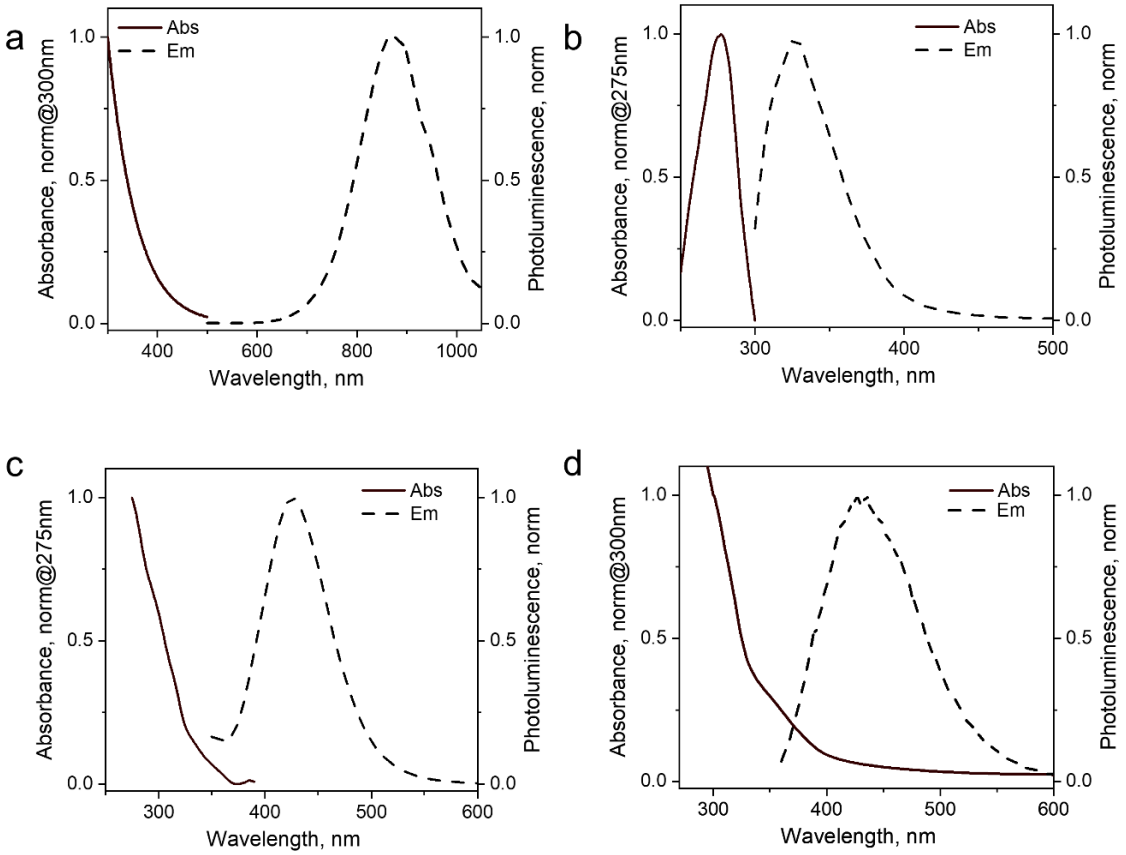

Figure 4-3. (a) Absorbance and PL-emission spectra of (C10)-SiNCs functionalized in MW reactor for 20 minutes at 250 °C (etched in NH_4F solution). (b) Absorbance and PL-emission spectra of the MeOH/KOH mixture without SiNCs. (c) Absorbance and PL-emission spectra of annealed SiO (etched in KOH/MeOH solution). (d) Absorbance and PL-emission spectra of ethylene glycol functionalized SiNCs. PL-emission spectrum for (a)

was taken at 375 nm LED excitation, whereas (b) (c), and (d) were taken at 350 nm excitation using a build-in xenon lamp inside the Cary Eclipse spectrofluorometer. All absorbance spectra were normalized at 275 nm and 300 nm to highlight the maximum peak position.

Although the blue emission's origin could deserve future punctilious research, our experiences stated that the emission remains constant at ~450 nm and is not prone to size tuning. In my opinion, one of the milestones of such a study should be the synthesizing of the crown-like hemisphere (glycolate bidentate ligands) surrounding SiNCs. However, in our project, this molecule has not been considered yet [300-303].

4.3 Conventional thermal hydrosilylation (CTH)

PLQY of the sample containing decyl functionalized SiNCs ((**C10**)-SiNCs) can be further enhanced up to ~26% after fractionation with centrifugation (briefly described in 4.2). As being shown, the PLQY before fractionation (batch) is ~5% but gradually increases thanks to precipitation with centrifugation (batch PLQY is in agreement with Mastronardi *et al.* [83]). Systematic precipitations were done, and optical properties of ensembles were determined using a Cary Eclipse spectrofluorometer. Despite the limitation of the PMT detector, its sensitivity drops sharply after 850nm; however, our measurements are still able to monitor emission shift when particle size gradually changes from ~10.0 nm to 3.0 nm

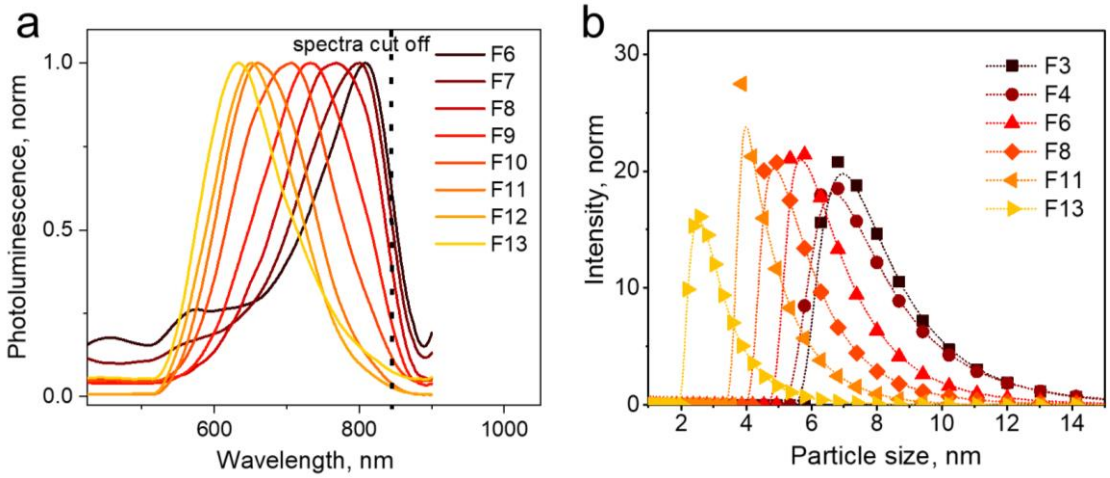

Figure 4-4. (a) Emission profile of fractionated (C10)-SiNCs samples precipitated using centrifugation. (b) Gradual decrement of particle size of (C10)-SiNCs due to fractionation monitored by DLS.

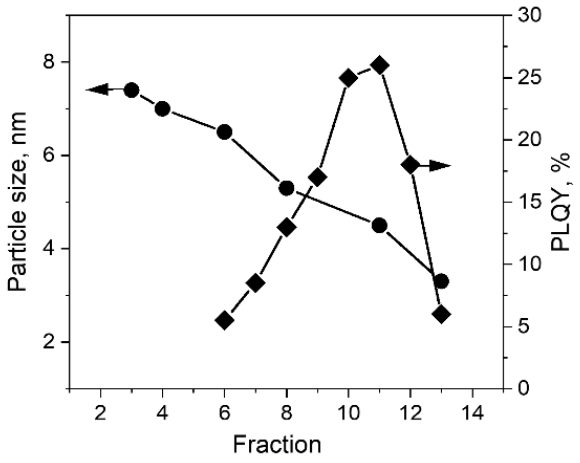

Figure 4-5. Particle size (●) and PLQY values (♦) as a function of fractionation by centrifugation of free-standing (C10)-SiNCs dispersion. PLQY values were measured using the comparative method described in section 3.1.9.

As seen in Figure 4-4a, the emission profile is cut-off somewhere at 850 nm. Therefore, for sample F6 and F7, the spectrum is cut off almost by a half, so it is impossible to retrieve information about this fraction. PL spectra of sample F1-F5 are also undetectable because the maximum peak is located at above 1,000 nm. Moreover, the emission tail below 850nm is too weak and wholly buried in the instrument's noise floor. In conjunction with PL emission data, DLS data presents the reduction of the particle size due to precipitation (Figure 4-4b). Two data sets were plotted in the same graph to identify the correlation between the number of precipitation and particle size reduction. The curves in Figure 4-5 demonstrated the effect of size reduction on the PLQY value. Herein, the measurements were conducted using the comparative method, and zinc-phthalocyanine (Zn-Pc) was used as standard with the reported PLQY value of ~23% in tetrahydrofuran (THF) [304]. Overall, the curve of PLQY data increases when fractionation increases (particle size decrease). After passing the maximum point ~26%, PLQY goes down. This pyramid trend is previously observed by [89, 92, 93, 305, 306]. PLQY measurement using this method has some weaknesses; (i) the sample's emission is not fully calibrated if the wavelength goes above 620 nm. The instrument issue causes this. Although the instrument is recording the spectra above 620nm, the spectra's wavelength is no longer calibrated. It is obtained that the spectra's exact location was blue-shifting about 7-20 nm from the spectra recorded using the lab-sphere-integrating-sphere. This mismatching may cause a slight decrease in the accuracy of the method. (ii) As mentioned above, the PMT sensitivity reduces rapidly in the spectrum range above 850 nm. So, it makes PLQY could be determined until 850 nm only, whereas PL-emission of these SiNCs could go above 1000 nm. It is the case for samples having an average diameter is ~8 to20 nm, e.g., fraction F1-F5. (iii) PL spectrum of the standard Zn-Pc used in this experiment is collected at 675 nm while the excitation is at 610 nm. In our measurement, the sample was excited at 350 nm, and the PL-emission band was located at 675 nm. Roughly, at 350 nm, ZnPc absorbs only ~10% of light as compared with 610 nm. The estimated error was suspected because using 350nm absorbance in

the gradient calculations is also higher than the one using 610nm absorbance. The estimated error will also be much higher when the PL spectra of SiNCs were estimated using this method. The main reason is that the emission peak of these SiNCs varies from 600-1,200 nm [304, 307]. Therefore, due to doubts in the accuracy, the comparative method was no longer being used in our measurements for future work. Finally, further discussion on the conventional thermal hydrosilylation (CTH) method will not be held. For the rest of this thesis, microwave-assisted hydrosilylation (MWH) will be used as a hydrosilylation method.

4.4 Microwave-assisted hydrosilylation (MWH)

The CTH method was practically considered a time-consuming hydrosilylation process, lasting around 14-20 hours of hydrosilylation time [235]. In recent work, the critical impacts of organic ligands were investigated on the luminescent properties of the SiNCs. In literature, SiNCs functionalized with organic ligands gave a strong emission over a broadband of electromagnetic radiation, from 630 nm to 1,200 nm. Moreover, its optical properties can be tailored in a very well controlled manner using particle size tuning [87]. There were some sporadic PLQY values on dodecyl (**C12**), decyl (**C10**), and octyl (**C8**) functionalized SiNCs (see Figure 2-9). The highest record of PLQY value was ~60% on (**C12**)-SiNCs [108], while for (**C10**)-SiNCs it was ~20%, and finally, for (**C8**)-SiNCs it was 30%[127]. Therefore, the dependence of PLQY of SiNCs on the length of alkyl as ligands aims to shed more light on this research. Linear alkyl such as (allyl, methyl)-ether (**C3**), pentene-1 (**C5**), hexene-1(**C6**), octene-1(**C8**), decene-1(**C10**), dodecene-1(**C12**), tetradecene-1(**C14**), and hexadecene-1(**C16**) were the materials of choice. In fact, during the hydrosilylation reaction, the competitor, such as oxygen, might react differently and lead to the difference in PLQY and stability of the products. Each reaction was carried out with 4 or 5 repetitions with the same experimental conditions to ensure genuinely reliable results. Even for samples with very high PLQY (e.g., (C6)-SiNCs), the experiments were carried out up to seven times. All of these were done to produce reliable and convincing results. Overall, 8 alkyl chains that must be paired with SiNCs, the total number of reaction needs was at least 32 times (4×8). If only the reactions were tailored using CTH, the amount of time for hydrosilylation was a minimum of ~580 hours in total, plus the annealing process (32 days) and purification works (32 days). So it will take roughly more than 12 months. Therefore, the hydrosilylation reaction in CTH was assumed time-consuming. The MW reactor was employed for the hydrosilylation process instead of using CTH to accelerate the hydrosilylation process. Using MWH, the reaction time was considerably shortened from 14-20 hours down to a couple of minutes. In our optimization process, functionalization with decene-1 to form (**C10**)-SiNCs lasts for only 20 minutes at 250°C, and the PLQY of this sample was ~30%. This PLQY was for batch solutions, and whereas functionalization with hexene-1 to form (**C6**)-SiNCs proceeded in 20 minutes at 230°C and yielded a sample whose PLQY was ~35%. The functionalization reaction and the luminescent (PLQY) of alkyl functionalized SiNCs versus the reaction time were presented in Figure 4-6.

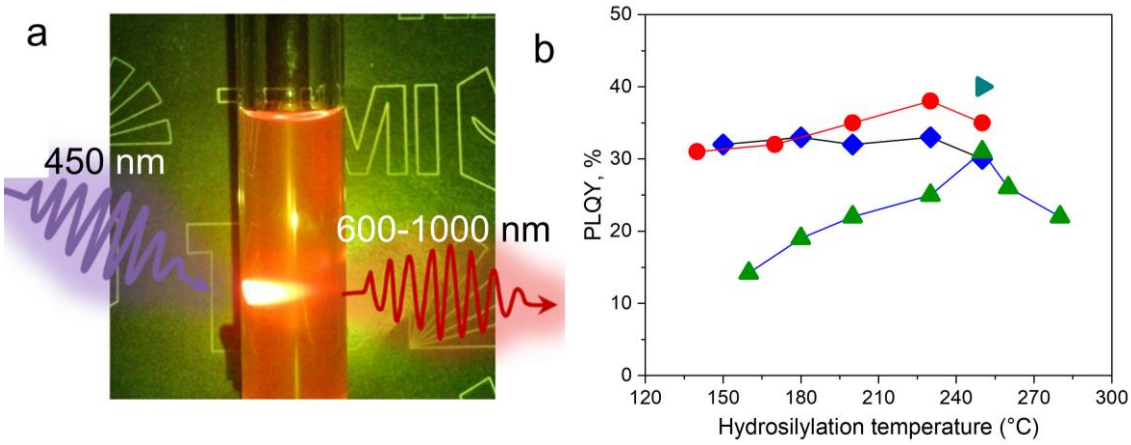

Figure 4-6. (a) The emission of (C6)-SiNCs functionalized using MW-assisted hydrosilylation illuminated by a 405 nm laser pointer. (b) Optimization hydrosilylation reaction of SiNCs with pentene-1 (♦), hexene-1 (●), decene-1 (▲), and allyl methyl ether (►). Reaction with pentene-1 (C5) was carried out with a mixture of pentene-1/p-xylene (2:1), as well as reaction with hexene-1 at 250 °C [85].

Figure 4-6a depicted the emission of (C6)-SiNCs functionalized using MWH reaction under the 405 nm laser pointer's illumination. The intense red emission can even be observed by the naked eye because the emission tail expands from ~600-1000 nm. Figure 4-6b depicted the optimization process to determine the best reaction condition in MWH. All the reactions were performed in a similar duration (20 minutes) with slightly modified procedures. A known quantity of p-xylene was added to the solution to reduce the vapour pressure. The addition process was introduced to observe PLQY value when the reaction was conducted at higher temperatures.

(i) For pentene-1, the reaction above 180°C cannot be carried out because at this temperature, the reaction pressure was too high (~28 bar), while the limited pressure the MW-reactor could safely handle was around 30 bar. To overcome the issue, p-xylene was added for the reaction above 180°C to reduce the pressure. As demonstrated in Figure 4-6b, the PLQY value was slightly reduced from ~31 % to ~30 % after p-xylene addition at 200°C. Afterward, PLQY bounced back to ~31 % at ~225°C before it went down to ~28 % at 250°C. The reaction could not be performed at any further higher temperature because, at 250°C, the MW chamber pressure had reached ~30 bar.

(ii) For hexene-1, the PLQY value was increased gradually from ~30% at reaction temperature 145°C to ~38% at reaction temperature 230°C. The reaction cannot be performed at any further higher temperature because, at 230°C, the reaction pressure reached 29 bar. Similarly, p-xylene was added to reduce the solution's vapour pressure and carried out the reaction at 250°C. However, p-xylene's addition deteriorated PLQY value, as previously demonstrated in pentene-1 observation. After addition, PLQY value went down approximately 3% from ~38% to ~34-35%. The reaction could not be performed at a temperature higher than 250°C because the pressure at this point reached ~30 bar.

(iii) For decene-1, PLQY value was increased sharply from ~15% at reaction temperature 160°C to ~29-30% at reaction temperature 250°C. The reaction cannot be performed at any further higher

temperature because, at 250°C, the reaction pressure reached ~30 bar. Similarly, p-xylene was added to reduce the vapour pressure and carried out reactions at 260°C and 275°C. The observation shows similar trends after p-xylene addition; PLQY values went down from 29-30% at reaction temperature 250°C to ~25% at reaction temperature 260°C and ~20% at reaction temperature 275°C. The reaction could not be performed at any further higher temperature because the pressure reached maximum MW-reactor could handle.

(iv) Herein PLQY from allyl-methyl ether was presented to show that 41% value was acquired from reaction conducted with allyl-methyl ether/p-xylene mixture at 250°C. This reaction condition was chosen based on the maximum PLQY value from decene-1. Optimization could not be performed for p-xylene because the available quantity was limited, and it was not enough to perform multiple reactions.

Thus, p-xylene can be added to reduce the reactant's vapour pressure so that the hydrosilylation reaction could be performed at higher temperatures. However, the downside of adding p-xylene was PLQY value of the products was reduced.

The highest PLQY value of ~41% was observed for capping with the shortest ligand – (allyl, methyl) ether or (C3)-SiNCs. Notably, the reported PLQY in this chapter were determined for the batch solution. To my knowledge, the reported PLQY of (C10)-SiNCs for batch solutions synthesized in CTH from Ozin's group was 5%[275]. The error bar of PLQY values was derived at least seven times for (C6)-SiNCs, five times for (C8) -SiNCs, (C10)-SiNCs, (C12)-SiNCs, (C14)-SiNCs, (C16) -SiNCs, four times for (C5)-SiNCs, and three times for allyl, methyl ether (C3)-SiNCs were performed (Figure 4-7). The overall trend indicates that the longer the ligand is, the lower the PLQY value can be achieved. One also can see the lowest PLQY of ~18% was obtained for hexadecene-1. Our first hypothesis was that the partial surface oxidation of the Si-NCs is responsible for decreasing the PLQY in ligands with longer carbon chains.

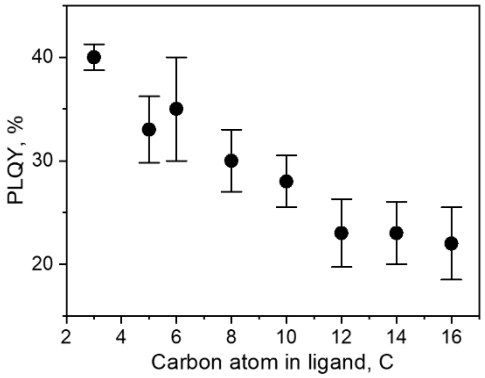

Figure 4-7. PLQY as a function of carbon atom in the ligand. Carbon atoms represent a linear aliphatic chain capping the surface of SiNCs. Error bars represent the uncertainty of synthesis for every batch of SiNCs, and every corresponding alkyl was synthesized at least seven times for hexene-1 (C6), five times for octene-1 (C8), decene-1 (C10), dodecene-1 (C12), tetradecene-1 (C12), hexadecane-1 (C16), four times for pentene-1(C5), and three times for allyl, methyl ether (C3) [85].

4.5 Size distributions

Figure 4-8 depicted the PL-spectra of the synthesized SiNCs. Under ultraviolet (UV-LED, 375 nm) excitation, all nanocrystals demonstrate a strong emission at 600-1,000nm of the electromagnetic spectrum. The effective mass approximation (EMA) model in Equation 2.2. gave particle size prediction of ~4 nm to ~5 nm based on PL-energy calculation.

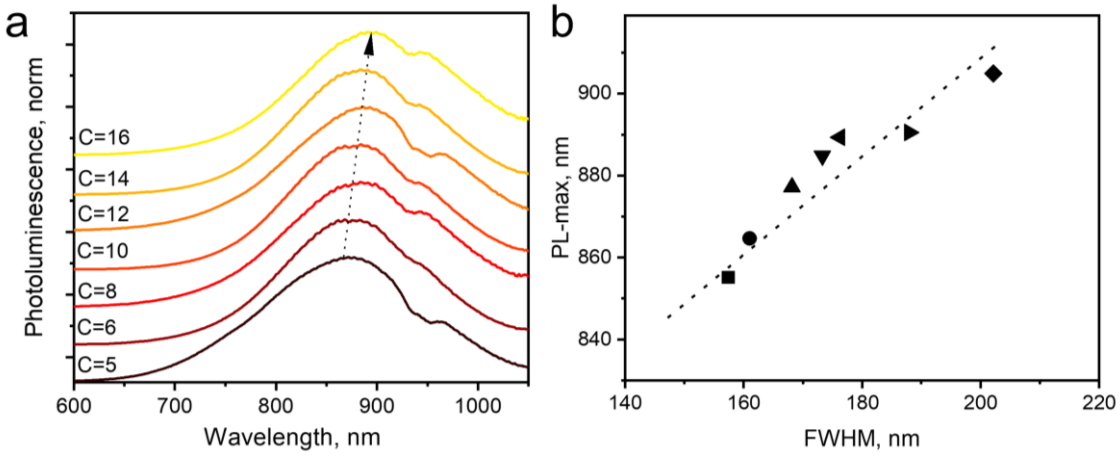

Figure 4-8. (a) Normalized fluorescent spectra of Si-NCs with different capping ligands (C=5, 6, 8, 10, 12, 14, and 16 represent pentyl, hexyl, octyl, decyl, dodecyl, tetradecyl, and hexadecyl functionalized SiNCs, respectively). Samples were excited with LED 375nm (b) Position of luminescence maximum as a function of the full width at half maximum (FWHM) derived for (■) (C5) Si-NCs, (●) (C6) Si-NCs, (▲) (C8) Si-NCs, (▼) (C10) Si-NCs, (◄) (C12) Si-NCs, (►) (C14) Si-NCs, (♦) (C16) Si-NCs luminescence peaks.

Also, redshift was observed in the position of PL- maximum (PL-max = 850–905 nm) for all ligands, as shown in Figure 4-8a (it should be noted that the local minimum at 920 nm can be explained by the absorption of the solvent associated with the overtone of C–H stretching vibration). At the same time, the polydispersity of the SiNCs fractions can explain the shift. A broad sized distribution results in the redshift in a position of an emission maximum compared to the theoretical prediction for monodisperse Si-NCs, as it has been recently described by Yu *et al.* [73]. Furthermore, the apparent correlation was observed between the FWHM of the emission peak and the position of PL-maximum (Figure 4-8b). The broader emission peaks, with the more red-shifted peaks, are observed.

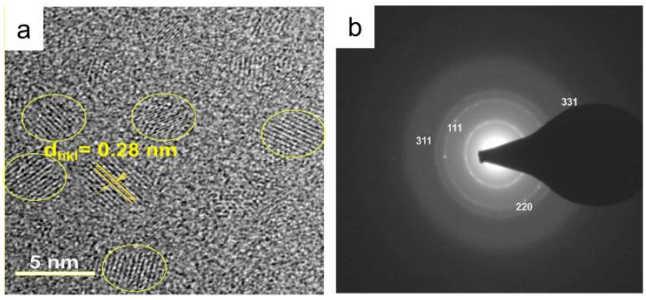

Figure 4-9. (a) HRTEM image of free standing C10-SiNCs. (c) Electron diffraction data for freestanding C10-SiNCs [85]

The XRD pattern for (**C6**)-SiNCs shows that most of the amorphous matrix was successfully removed during the etching process. As presented in Figure 4-1, the amorphous phase's broadband at 14-26° completely vanished after etching to form crystalline **H**-SiNCs. The crystalline peak at 28°, 47.8°, 56°, 69°, and 77° corresponds to diamond cubic phase silicon (JCPDS no. 027-1402) [72, 84, 85, 308]. The electron diffraction pattern shows the bright stars, which represent crystalline silicon in the lattice plane (see Figure 4-9). The Miller indices, which correspond to the peaks, were (111), (220), (311), (400), and (331), respectively. By using the Scherrer equation, it was estimated that the particle size of the nanocrystallite in the matrix based on the peak broadening (Equation 4.14).

$$D = \frac{K\lambda}{B\cos\theta} \tag{4.13}$$

Where D was approximated size diameter, K was a constant, which depends on the particle's shape. It assumed that the particle was spherical and attributed the value to $0.9B$, its full-width-half-maximum peaks at 28°. The crystallite size was 3.8-4.0 nm (closed to the predicted value using PL-energy). The average size of Si-NCs realized in this work was ~4.6 ± 0.3 nm (sum of six independent etching processes), as deduced from transmission electron microscopy (TEM) images (Figure 4-10). High-resolution transmission electron microscopy (HRTEM) (Figure 4-9) confirmed the crystal structure of Si-NCs with an interplanar distance of 0.32 nm (0.28 nm) corresponding to the distance (111) in c-Si. Importantly, TEM results indicate that the average size of the Si-NCs core remains the same after surface passivation with all investigated ligands (Figure 4-11).

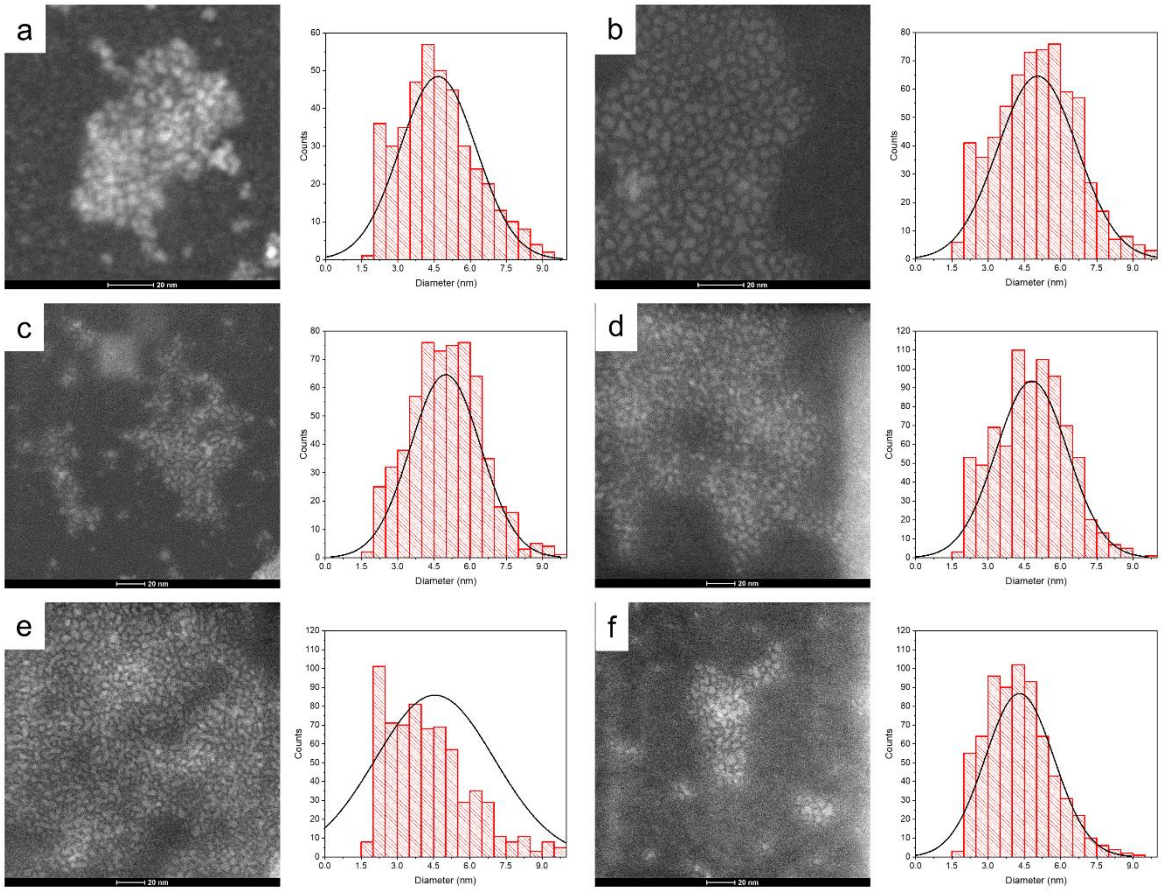

Figure 4-10. TEM images and particle distribution of free-standing SiNCs functionalized with (a) hexene-1, (b) octene-1, (c) decene-1, (d) dodecene-1, (e) teteradecene-1 and (f) hexadecene-1 [85].

In contrast, the results of DLS measurements (Figure 4-11a) indicated an increase of the hydrodynamic diameter in surface passivation with dodecene-1 and longer hydrocarbons. Previously, Yang *et al.* [309] reported a polymer corona formation around the Si-NCs core during the hydrosilylation process. They found that oxygen, high ligand concentration, and increased temperature were promoted chain propagation in oligomerization reactions and led to an organic corona formation. In our experiment, the nanocrystals' size and hydrodynamic diameter were consistent in the case of capping with relatively short ligands, *e.g.*, hexene-1, octene-1, and decene-1. In contrast, the use of the long ligands (with $C \geq 12$) leads to the growth of a thick organic shell surrounding the silicon core and a discrepancy between the particle size measured by TEM (seeing only the Si-NCs core) and DLS (seeing the Si-NCs core plus organic corona), see Figure 4-11b.

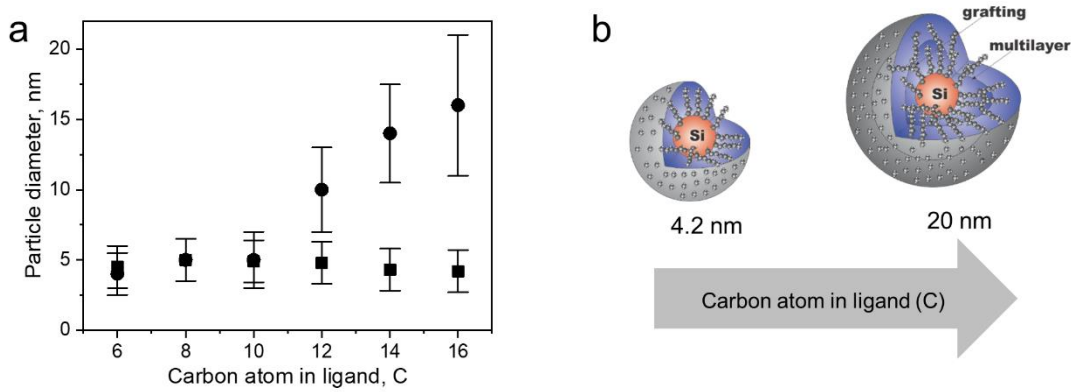

Figure 4-11. (a) The average diameter of Si-NCs estimated with TEM (■) and DLS (●) as a function of the number of carbon atoms in the linear aliphatic chain of the capping ligand (C). (b) Cartoon picture to illustrate the formation of multiple layers (corona) on the surface of alkyl functionalized SiNCs [85].

4.6 Oxidation reaction and reducing the oxygen content

As mentioned in the previous section, the position of PL-maximum was redshifted gradually from 850 nm to 905 nm when the alkyl chain as a ligand was substituted from C6 to C16 (see Figure 4-8). The shift was suspected from the side reaction between SiNCs and oxygen. Oxygen could be the biggest competitor since the reaction was conducted at ambient room condition, and the MW chamber was not vacuum sealed. The effort to reduce oxygen content before the reaction was performed by purging the sample with argon for 30 minutes before performing the reaction. However, in the other experiments, purging with argon for periods of time was not enough to eradicate oxygen. To study the oxidation rate of SiNCs, FTIR measurement was performed on the samples. Figure 4-12a depicted the selected region of the FTIR spectra measured for Si-NCs capped with different ligands. The peak at 800 cm^{-1} is attributed to Si–C $_{(stretching)}$ vibration, whereas the broadband at 960–1140 cm^{-1} is attributed to Si–O $_{(stretching)}$ vibration. The Si–C $_{(stretching)}$ vibration can overlap with Si–O $_{(bending)}$ peak (observed at 797–830 cm^{-1}). However, the Si–O$_{(bending)}$ peak has a much low intensity typically than Si–C$_{(stretching)}$ and, thus, has a minor impact in further calculations [232]. The absence of a characteristic peak at 900 cm^{-1} indicated almost complete substitution of Si–H bonds due to oxidation and hydrosilylation. It was expected that Equation (4.14) could provide qualitative information about surface oxidation of Si-NCs or *R*-value. The results were normalized in a way that the integral $A_{\bar{\nu}(Si-C)}$ equivalent to 1, so the value of the integral $A_{\bar{\nu}(Si-O)}$ reflected relative amount of oxidation occurring at the Si-NCs surface. The large $A_{\bar{\nu}(Si-O)}$ was the stronger oxidation and occurs at the surface.

$$R = \frac{A_{\bar{\nu}(Si-O)}}{A_{\bar{\nu}(Si-C)}} = \frac{\int_{960cm^{-1}}^{1140cm^{-1}} \bar{\nu}_{(1140-960cm^{-1})}\, d\bar{\nu}}{\int_{760cm^{-1}}^{830cm^{-1}} \bar{\nu}_{(830-760cm^{-1})}\, d\bar{\nu}} \tag{4.14}$$

There was a tiny increase in A_ν(Si–O) with an increase in the hydrocarbon chain length. Thus, surface oxidation was not a critical phenomenon responsible for the PLQY decreased. Surprisingly, washing the Si-NCs several times with hexane did not eliminate dodecene-1, tetradecene-1, and hexadecene-1 from Si-NCs. FTIR spectrums of Si-NCs capped with the long-chain ligands displayed additional peaks corresponding to the –C=C– and =C–H bonds. The FTIR spectrums (Figure 4-12a) also displayed a band at 1259 cm^{-1} that could be attributed to longitudinal phonons relating to Si–O–Si bond with the deformed bond angle ~142°. This peak was well separated from the other Si–O–Si peak at 960–1140 cm^{-1}, and its intensity did not change for different capping ligands. Though the existence of such a preferential configuration of Si–O–Si bond was unclear, it was assumed that this peak represented oxidation sites of the Si-NCs surface originating from the nature of SiO_x material because a similar peak was not observed in Si-NCs prepared from silsesquioxanes[102, 195, 220, 310].

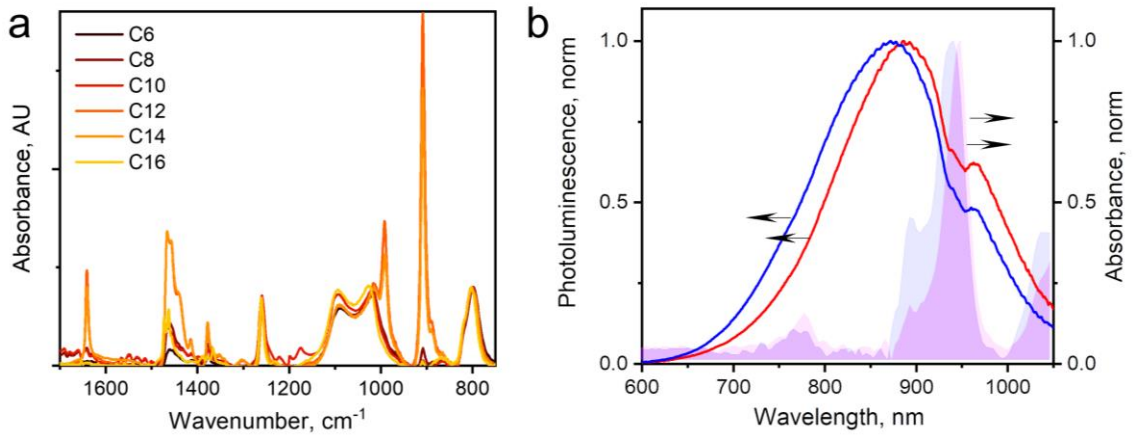

Figure 4-12. (a) Attenuated total reflectance infrared (ATR-FTIR) spectrum of Si-NCs with different capping ligands. (b) PL-emission of Si-NCs functionalized with hexene-1 (blue) and hexadecene-1 (red) dispersed in hexene-1 and hexadecene-1, correspondingly. NIR absorption (absorbance, norm) of hexene-1 (blue) and hexadecene-1 (red) [85].

An alternative explanation for the changes in PLQY, with the length of the capping ligands, can be proposed using the work of Aharoni *et al.* [311]. They described long-range electronic-to-vibrational energy transfer from excited QDs to matrix vibrational overtones. Figure 4-12b depicted emission spectrums of Si-NCs capped with hexene-1 and hexadecene-1 and absorption spectrums of solvents (hexene-1 and hexadecene-1). The alkenes' absorption spectrums (similar for all investigated alkenes) demonstrated C–H vibrational overtones with the absorption maximums peaking at 923–930 nm that perfectly match emission spectrums of Si-NCs. The matching was better for Si-NCs with long capping ligands. Experiments with α-lipoic acid show no-effect on the further addition of α-lipoic acid to the photophysical properties of alkyl-SiNCs. PL-emission demonstrates a similar peak maximum compared with non-lipoic addition, and PLQY value is in the range of error bar (~30%) of (**C6**)-SiNCs (Figure 4-13).

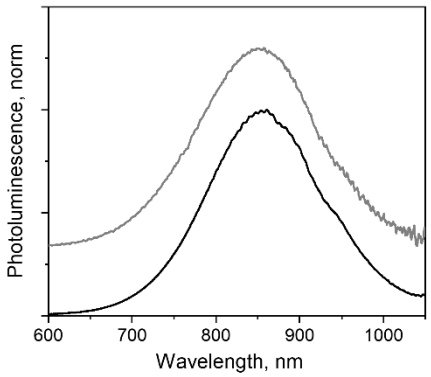

Figure 4-13. The PL-emission intensity of free-standing (C6)-SiNCs after reaction with α-lipoic acid addition, resulting in PLQY is ~31% (grey) and free-standing (C6)-SiNCs without α-lipoic acid addition, the resulting PLQY is ~33 % (black).

Thus, both solvent and capping ligands (forming the polymer corona) can act as an efficient quencher of excited Si-NCs. Indeed, Figure 4-14a displays a decrease of the radiative lifetime in range $C = 6 \rightarrow C = 16$ from 156 µs to 125 µs as presented in Figure 4-14b. The decrease of the lifetime signalizes an increase of non-radiative deactivation and is in good agreement with the observed decrease of PLQY.

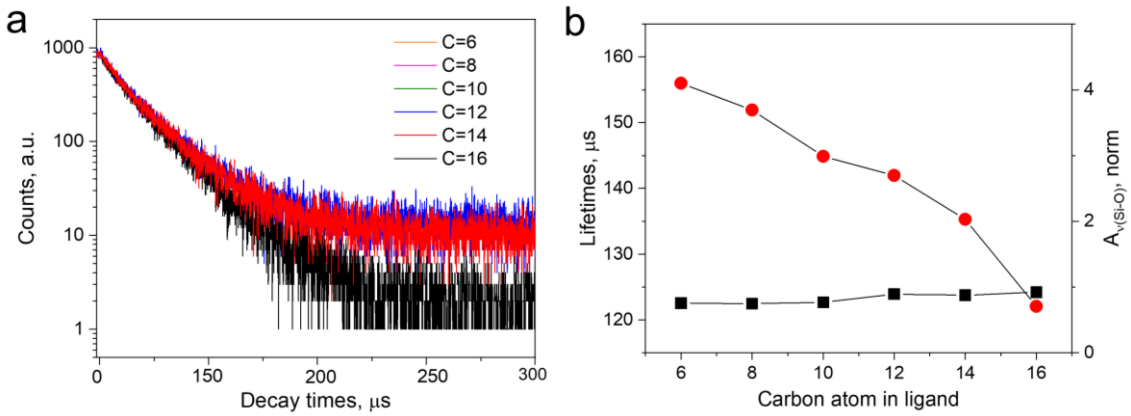

Figure 4-14. (a) Position of luminescence maximum as the full width function at half maximum (FWHM) derived for the Si-NCs luminescence peaks. (b) Plot A_ν (Si−O) (■) and luminescence lifetime (●) as function of carbon atoms in the capping ligand [85].

The presence of oxidized surface sites related to Si–O–Si bonds (from FTIR data) can also reduce the PLQY of SiNCs. It is observed that oxidation independently from used alkenes and methods of deoxygenation to prevent the oxidation. These types of surface defects limit the highest achievable PLQY to 39% – or an average value of ~34% calculated from six independent syntheses – achievable by the method used in the current work.

4.7 Photophysical stability

To complete the characterization of the Si-NCs, the shelf life of the synthesized materials were investigated systematically. Figure 4-15 displays the PLQY values taken for six months. Significant altering of photoluminescence emission was not observed after six months of storage in dark ambient conditions ($PLQY/PLQY_0 > 0.9$). The samples stored in a glovebox display PLQY comparable with PLQY of samples stored under ambient conditions. FTIR spectrums of samples stored in a glovebox also indicate a constant ratio between Si–C, and Si–O bonds. These experimental observations confirm the high stability of Si-NCs functionalized *via* microwave-assisted hydrosilylation (MWH).

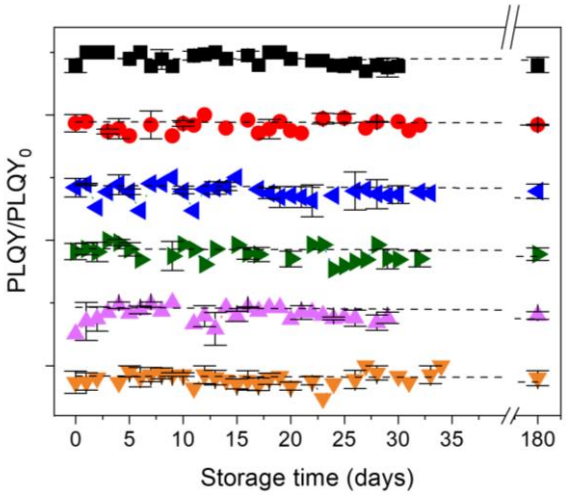

Figure 4-15. PLQY of Si-NCs stored in ambient as function shelf-life time for Si-NCs with different capping ligands. The symbols representing (■) for (C16)-SiNCs, (●) for (C14)-SiNCs, (◀), for (C12)-SiNCs, (▶) for (C10)-SiNCs, (▲) for (C8)-SiNCs, and (▼) for (C6)-SiNCs, respectively.

5 Dye functionalized SiNCs

Some of the results present in Chapter 5 were published in Beri et al. [236]. The author did all the syntheses and performed all the characterization experiments in this chapter. Except for PL-lifetime measurements were performed by author and co-authors, Dr. Dmitry Busko and Marius Jakoby, whereas TEM measurements were performed by Dr. Andrey Mazilkin from the Institute of Nanotechnology (INT), KIT. The original idea was brainstormed with co-authors Dr. Andrey Turshatov and Prof. Bryce S. Richards. This chapter's main goal was to study the functionalization reaction and photophysical properties of dye functionalized SiNCs. To achieve this goal, the functionalization reaction of H-SiNCs with perylene and BODIPY were performed in the MW-reactor. The characterization of resulting dyes functionalized SiNCs was studied by FTIR, UV-Vis-NIR spectroscopy, PL-excitation, PL-emissions, and PL-lifetimes. Conjugate dye and SiNCs were expected to have higher PL-emission due to extra absorption from dye molecules. The details about efficient energy transfer from dye molecules to SiNCs were studied by quenching of PLQY and PL-lifetimes. This research could be used, for example, to enhance the absorption of SiNCs fluorophore in the luminescent solar concentrator and also in visible-NIR excited SiNCs based photoimaging.

5.1 Synthesis of perylene and phenyl-BODIPY functionalized SiNCs

The synthesis of hydrogen-terminated SiNCs (**H**-SiNCs) was performed with the method described previously in **Chapter 3**. Briefly, **H**-SiNCs produced by the annealing of sub-stoichiometric SiO-x (x<2) precursors at 900°C (under an argon-hydrogen gas mixture). The phase separation triggered by thermal annealing resulted in SiNCs encapsulated in the SiO_2 matrix. The SiO_2 matrix was etched chemically using concentrated hydrofluoric acid (HF) acid (48% v/v) and ethanol. Toluene was used to extract **H**-SiNCs from the polar etching solution. Approximately fifty successful H-SiNCs were used to synthesize SiNCs, and the same conditions for thermal annealing and etching were always used. The functionalization with 1-hexene **(C6)** and 3-ethenyl perylene **(p1)**; 3-ethynyl perylene **(p2)**, and ethylene-m-phenyl BODIPY **(pb)** (as shown in Figure 5-1) was performed by microwave-assisted hydrosilylation (s).

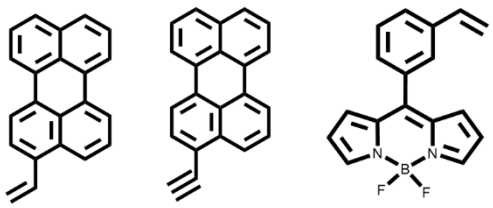

(p1) **(p2)** **(pb)**

Figure 5-1. Molecular structure of the reactive dyes used in the surface modification of SiNCs: 3-ethenyl perylene (p1); 3-ethynyl perylene (p2); and ethylene-m-phenyl BODIPY (pb) [236].

The UV/VIS absorption, PL, and PLE spectra for dye **(p1)**, **(p2),** and **(pb)** dissolved in hexane are presented in Figure 5-2. Dye (**p1**) and dye (**p2**) demonstrate strong light absorption between 400 and 460 nm. Dye (**pb**) absorbs between 490 and 540 nm. The dye (**p1**) and dye (**p2**) show similar PL spectra with PL maximum of 462 nm and 456 nm, respectively. Dye (**pb**) demonstrates green emission with a maximum of 537 nm. UV/VIS measurements were performed for all dyes to investigate the photophysical properties of the possible ligands. The objective was to determine whether the excitation wavelength correctly worked either for the core (SiNCs) or the ligands and to help us with data interpretations. The measurements demonstrated that all dyes exhibit local absorption minimum at 300 nm. Whereas **(C6)**-SiNCs show strong absorption at the wavelength of 300 nm and gradually decreases at a longer wavelength (approaching zero in the wavelength longer than 450nm, explained in detail in **Chapter 4**). It was expected that when excitation was performed at 300 nm, the emission should appear from SiNCs only. Likewise, when it was performed at 450nm or 515nm, the emission should emerge from the dyes **(p1)**, **(p2)**, and **(pb)**.

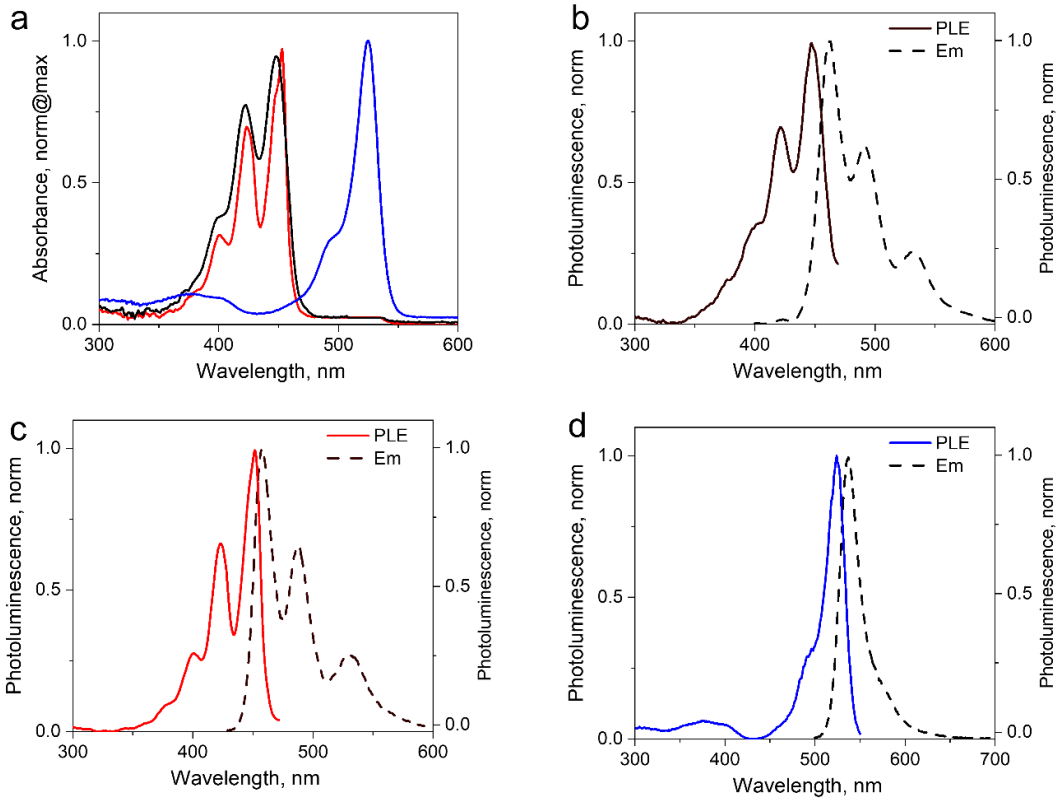

Figure 5-2. (a) Absorption spectra of solutions of 3-ethenylperylene (p1) (black), 3-ethynylperylene (p2) (blue) and ethenyl-m-phenyl-BODIPY (pb) (red) in hexane. (b), (c) and (d): PLE and PL emission of corresponding dyes [236].

As preliminary research, the stability of the dyes upon MWH reactions was performed in the experiment using MW-reactor. The experiment aim to investigate whether the dyes as ligands could stand

upon extreme heat and pressure (230°C, ~28 bar, and 2 x 120 minutes). The solutions of dyes (**p1**), (**p2**), and (**pb**) in toluene was treated in the microwave reactor for 240 minutes at 230 °C. The absorption spectra were measured before and after the treatments in MW-reactor and the results indicate that dyes are relatively stable. Only 6 % degradation was observed for the dye (**p1**), whereas for dye (**p2**) it remained unchanged during the hydrosilylation process. Eventually, the dye (**pb**) shows the fastest degradation rate. Degradation of 36% of the dye (**pb**) was seen after the 240-minute treatment at 230 °C. The absorption spectra before and after the reaction in the MW reactor are depicted in Figure 5-3**.**

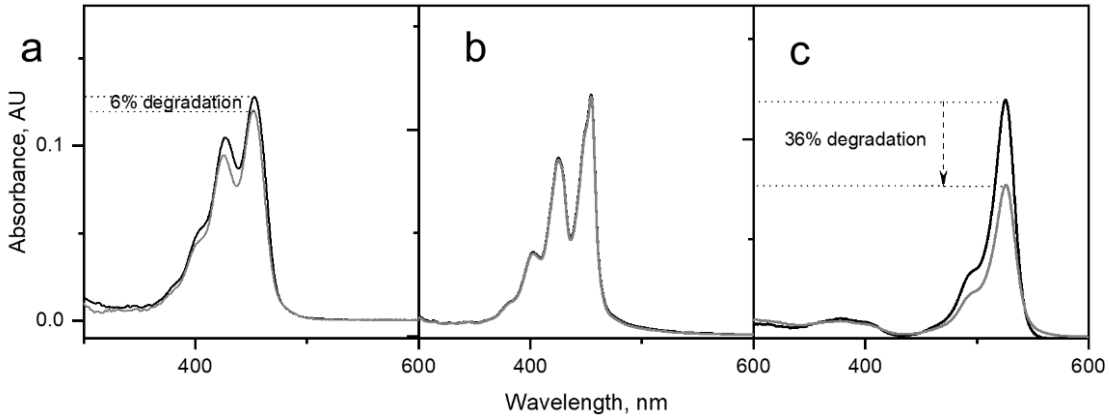

Figure 5-3. (a): Absorption spectra of dye (p1) in toluene before (black) and after (grey) the treatment in the microwave reactor. (b): Absorption spectra of dye (p2) in toluene before (black) and after (grey) the treatment in the microwave reactor. (c): Absorption spectra of dye (pb) in toluene before (black) and after (grey) the treatment in the microwave reactor. The treatment conditions: 240 minutes at 230 °C [236].

Figure 5-4 summarizes the effect of the reaction temperature and reaction time on the PLQY of (**C6**)-SiNCs performed in the microwave reactor. The results in Figure 5-4 indicate that the optimal reaction temperature was at 230°C and 120 minute reaction times (at 230°C reaction temperature) to obtain the highest PLQY values (in this optimization experiment) ~35%. Longer reaction time tends to reduce the PLQY value, and it might be caused by the crosslinking reaction among the ligands (dye, hexene-1, and between dye and hexene-1) to form corona (previously described in **Chapter 4**). The hydrosilylation reaction for dye functionalized SiNCs was performed at a temperature of 230°C, and the reaction time of 120 minutes to dyes (**p1**), (**p2**), and (**pb**). The hydrosilylation reaction products were organic-capped SiNCs dispersed in non-polar organic solvents (hexane, for instance). A vacuum evaporator was used to remove the left-over hexene-1 while rinsing at least three times with methanol removed the left-over dye.

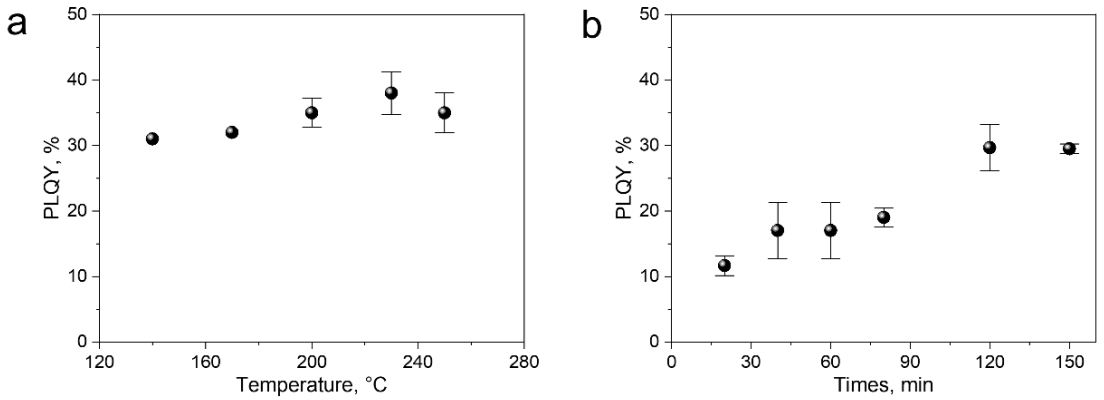

Figure 5-4. (a): PLQY of (C6) -SiNCs as a function of the temperature of hydrosilylation reaction performed in the MW reactor; (b): PLQY of (C6)-SiNCs as a function of the reaction time of hydrosilylation reaction performed in a microwave reactor. The error bars represent the uncertainty of five times experiments (for several chosen conditions).

Mazzaro *et al.* [312] described thermal hydrosilylation reaction between pyrene dye and **H**-SiNCs utilized a significant excess of a reactive dye (> 100 mg of a dye per 5 ml of the reaction mixture). This large amount of dye guaranteed high surface density of the attached dyes and led to inefficient dye consumption as the reaction yield was meagre. Using MWH, the amount of dye consumption was tried to minimize to gain optimum functionalization. In the optimization process, three different approaches to attach the dye chemically to the SiNCs were investigated as presented in Figure 5-5: firstly, (i) 2.0 mg of dye **(p1)** was dissolved in 5 ml dispersion of **H**-SiNCs in toluene and performed in the MW reactor at 230°C for 120 minutes. However, the resulting product displayed only weak NIR emission from the SiNCs. It was assumed that dye molecules could be afforded only a partial surface coverage of the SiNCs, and the weakly protected SiNCs were oxidized by oxygen that led to the reduced PL intensity of SiNCs. The second approach was (ii) 2.0 mg of dye **(p1)** dissolved in 5 ml dispersion of the mixture of **H**-SiNCs in hexene-1 **(C6)** and performed in the MW reactor for 120 minutes at 230°C. The product has shown that only a minimal amount of **p1** is attached to SiNCs. The UV/VIS measurement indicated that minimal dyes are attached to the surface of SiNCs. Our result demonstrated that the dye could not compete with the excess of **(C6)** in the reaction process and, thus, only a limited amount of dye reacted with the surface of **H**-SiNCs. Finally, (iii) in order to overcome the limitations of the approaches in (i) and (ii), 2.0 mg of dye **(p1)** was initially reacted with **H**-SiNCs in toluene for 120 minutes at 230°C. Then, 5.0 ml of **(C6)** was injected into the solution before the second hydrosilylation reaction performed for another 120 minutes at 230°C. Approach (iii) allows us to synthesis SiNCs with dye molecules covalently attached to the surface that exhibited strong NIR PL successfully.

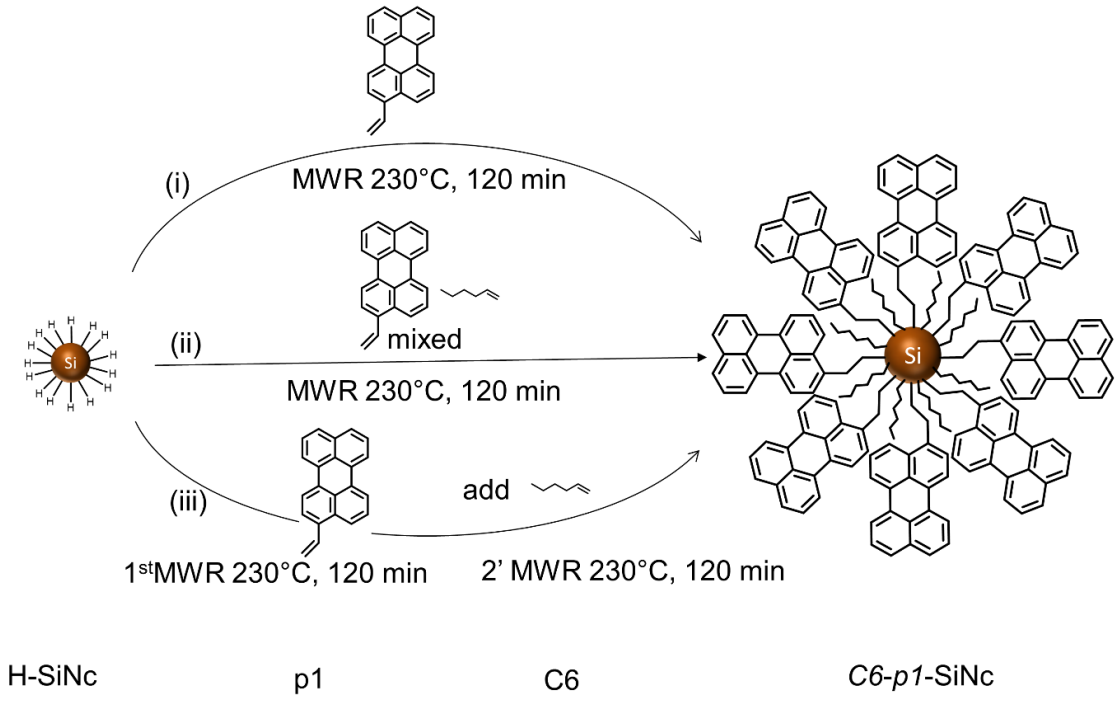

Figure 5-5. Functionalization reaction of hydrogen-terminated SiNCs (H-SiNCs) with hexene-1 (C6) and dye (p1). (i) Direct hydrosilylation reaction with the dye (p1); (ii) reaction H-SiNCs with the solution of the dye (p1) in (C6), and (iii) two-step process: reaction of H-SiNCs with dye (p1) within the step-1 and with (C6) within step-2.

To investigate the change in particle size during the reaction, TEM and DLS were performed to the yield of the hydrosilylation process. Under the TEM image, the core of SiNCs remains at the same size ~4-6 nm (Figure 5-6). Likewise, the crystallinity and the lattice parameter agreed with the alkyl functionalized SiNCs described previously in **Chapter 4**. All obtained dispersions under DLS measurement demonstrated that the particles' size distribution coincides with our previous report. The DLS data depicted in Figure 5-7 describes the average hydrodynamic diameter of 4.2 nm for (**C6**)-SiNCs), 5.2 nm for (**C6**)-(**p1**)-SiNCs), 4.6 nm for (**C6**)-(**p2**)-SiNCs) and 6.5 nm for (**C6**)-(**pb**)-SiNCs), respectively. The size distribution for (**C6**)-(**pb**)-SiNCs is slightly broader because the ligand's molecular size is also more prominent than the dye **p1** and **p2**.

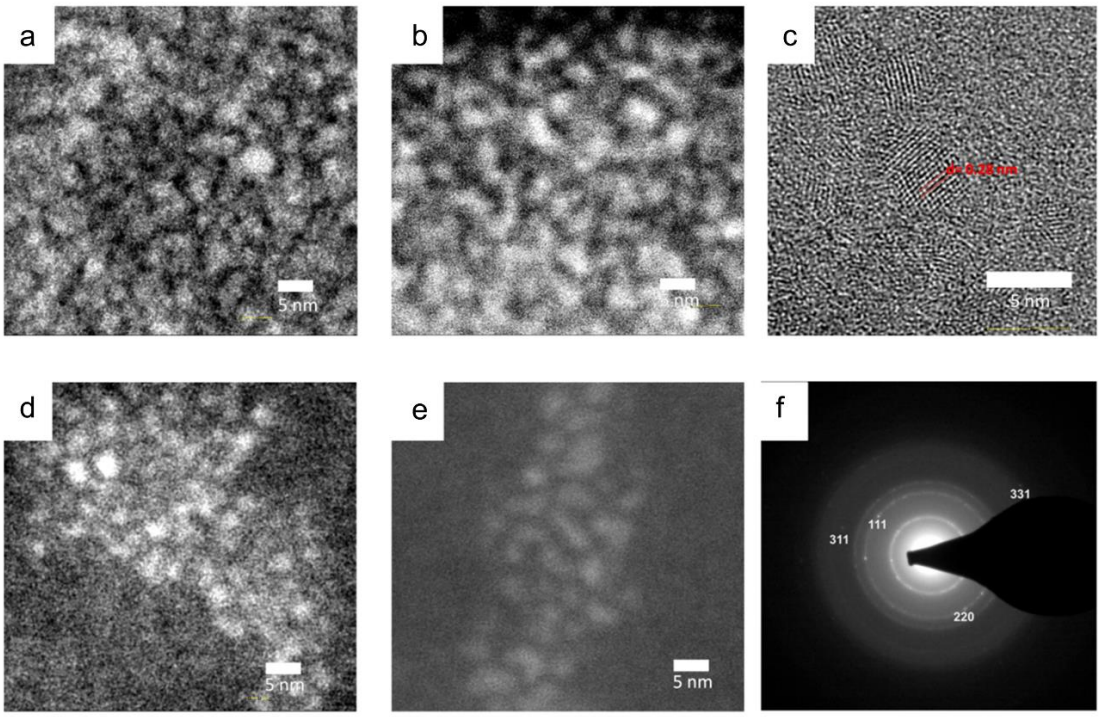

Figure 5-6. TEM image of (a). (C6)-SiNCs, (b). (C6) -(p1)-SiNCs, (c). (C6)-p2-SiNCs, (d). (C6) -(pb)-SiNCs, (e) HRTEM (C6)-SiNCs, and (f) electron diffraction of (C6)-SiNCs [236].

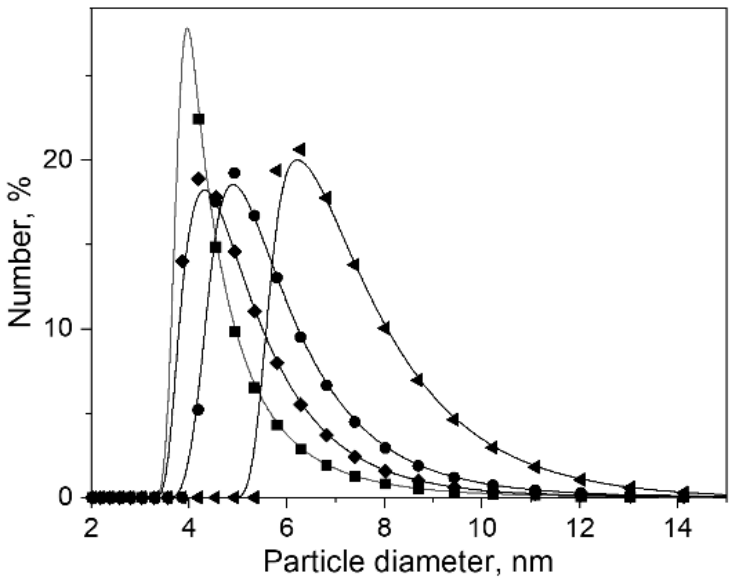

Figure 5-7. Particle size distribution measured with dynamic light scattering after functionalization in the MW reactor (■): (C6)-SiNCs; (●): (C6)-(p1)-SiNCs; (♦): (C6)-(p2)-SiNCs; and (◄): (C6)-(pb)-SiNCs.

Absorbance enhancement can be observed by increasing the extinction coefficient of the dye functionalized SiNCs, compared with compatible alkyl functionalized SiNCs. At a local minimum of 300

nm, the absorbance of the ligands approach zero; therefore, for quantification of the experimental results, all absorption spectra were normalized using the A_{300nm} absorbance, and extinction coefficients expressed in Equation 5.15.

$$\varepsilon_\lambda = \frac{A_\lambda}{l \,.\, C} \tag{5.15}$$

Where A_λ - absorbance at a particular wavelength (300 nm, 375nm, 405nm, 450nm, and 515nm), $\boldsymbol{\varepsilon_\lambda}$ - extinction coefficient (cm^{-1}), l - optical path length (in this experiment: 1 cm), and c - dimensionless weight fraction of SiNCs ($m_{SiNCs}/m_{dispersion}$). The extinction coefficient values for all investigated products under five different excitation wavelengths are summarized in Table 1, whereas the absorbance's corresponding concentration dependences are plotted in Figure 5-8**.**

Table 1. The extinction coefficient of (C6)-SiNCs, (C6)-(p1)-SiNCs, (C6)-(p2)-SiNCs and (C6)-(pb)-SiNCs solutions in hexane at different wavelengths.

Excitation *(λ,nm)*	*(C6)*[≠] *ε, (×10⁻⁴) cm⁻¹*	*(C6) -(p1)* *ε, (×10⁻⁴) cm⁻¹*	*(C6) -(p2)* *ε, (×10⁻⁴) cm⁻¹*	*(C6)-(pb)* *ε, (×10⁻⁴) cm⁻¹*
300[§]	0.72	0.73	0.75	0.71
375	0.17	0.26	0.36	0.17
405	0.09	0.34	0.47	0.09
440[†]	0.05	0.49	0.65	0.04
515[‡]	0.01	0.03	0.07	0.03

[†] Excitation wavelength dedicated for perylene dyes, and [‡] Excitation wavelength dedicated for BODIPY. [§]Reference excitation wavelength dedicated for SiNCs or limited absorbed by dyes. [≠](C6)-SiNCs is used as reference alkyl functionalized SiNCs where all absorbance-from dyes modified-should compared with.

Data in Table 1 demonstrate that the extinction coefficients of dye functionalized SiNCs were enhanced by factor 10 and 13 at 440 excitations for (**C6**)-(**p1**)-SiNCs and (**C6**)-(**p2**)-SiNCs, and by factor 3 at 515nm excitation for (**C6**)-(**pb**)-SiNCs, respectively. The enhancement factors came from the absorption of the dyes. One might argue that a homogeneously physical mixture of dyes and **C6**-SiNCs could produce similar enhancement factors. To answer this, UV/VIS and PLE measurements were performed to physical mixtures, and the results are shown in Figure 5-9. The UV/VIS spectra demonstrated that the absorbance of physical mixtures was similar in shape and position to chemically bonded dye functionalized SiNCs. However, the PLE spectra demonstrate that the physical mixture exhibited no sign of dyes at 860 nm. This information indicates the main difference between physical and chemical bonding of the core and the ligand. On the other hand, the experiments demonstrated that the absorption enhancements were led by bonded dyes instead of free dyes.

The UV/VIS absorption and photoluminescence excitation (PLE) measurements of **(C6)-**SiNCs dispersion in hexane displayed the characteristic behaviour of SiNCs with a gradual decrease of the optical density at a longer wavelength (Figure 5-10). Excitation of (**C6**)-SiNCs with different wavelengths led to PL spectra with a similar shape, full width half maximum (FWHM) of 170 nm, and position of the PL maximum of 840 nm (Figure 5-10b). The measured PLE spectrum (Figure 5-10c) also proved the possibility

of obtaining SiNC NIR PL via dye excitation. The PLE spectrum's shape corresponded to the (C6) absorption spectrum -(**p1)**-SiNCs conjugate with a clear contribution of dye absorption to the PLE spectrum. The NIR PL spectra of **(C6)** -(**p1)**-SiNCs (Figure 5-10d) excited with different excitation wavelengths displayed the same shape with an FWHM of 175 nm and the PL maximum lying at 848 nm. Strong NIR luminescence under blue excitation light (440 nm) was observed in agreement with our expectations. This observation highlighted the feasibility of the sensitization with the blue-absorbing dye attached to the nanocrystals' surface.

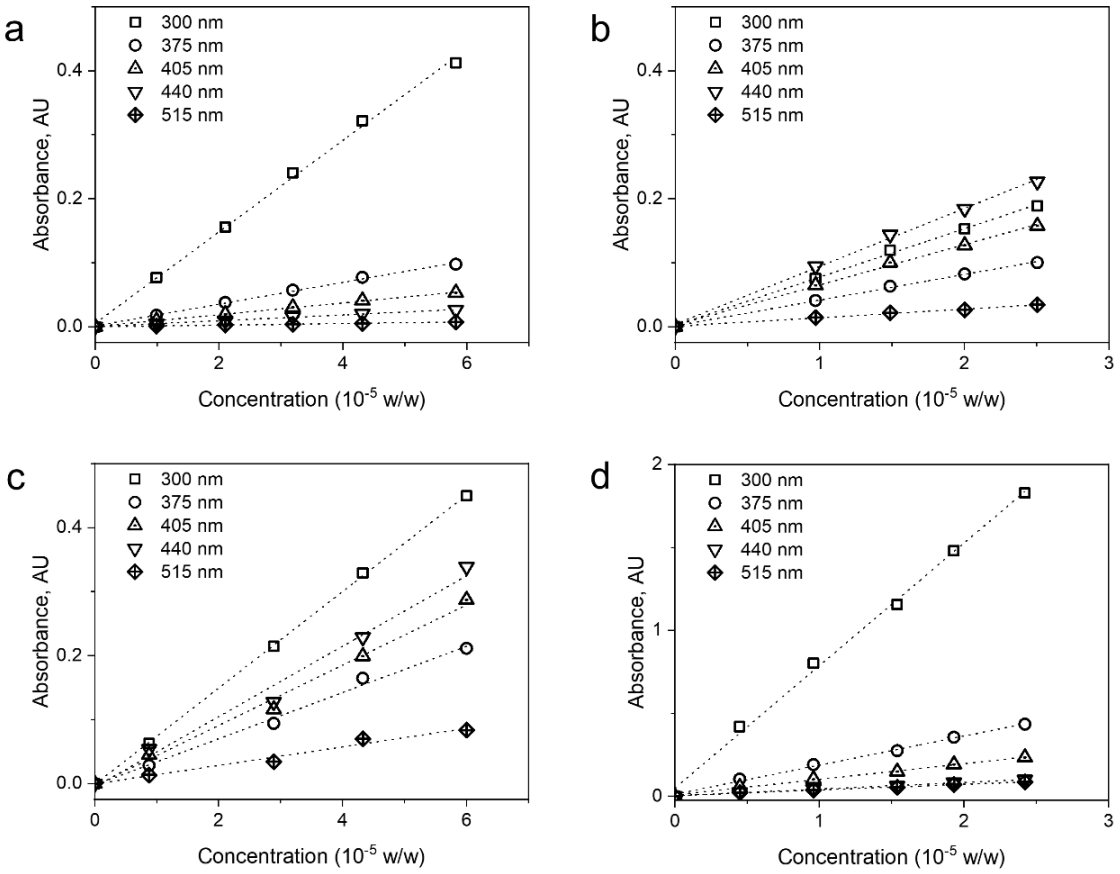

Figure 5-8. Estimation of the absorption coefficients at different wavelengths for solutions of (a): (C6)-SiNCs;(b): (C6)-(p1)-SiNCs;(c): (C6)-(p2)-SiNCs and (d): (C6)-(pb)-SiNCs in hexane [236].

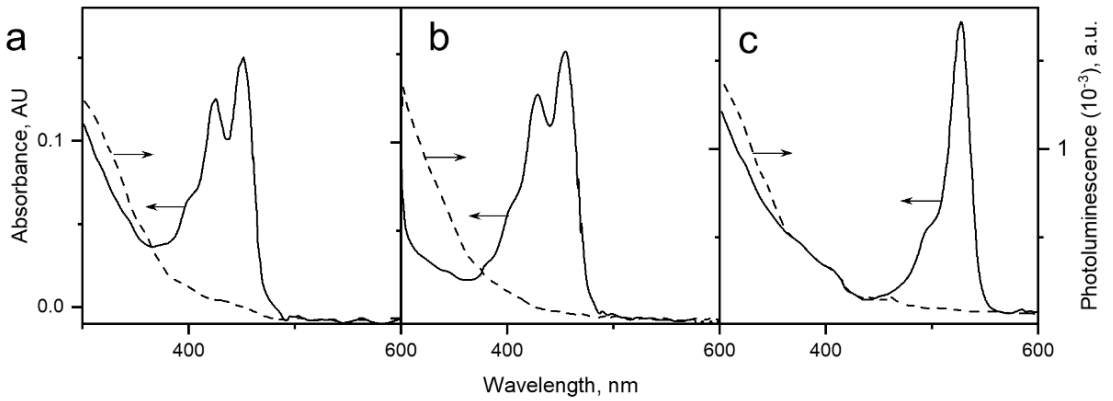

Figure 5-9. Absorption (solid lines) and PLE (dash lines) spectra of physical mixture of (C6)-SiNCs and dye (p1) - (a), dye (p2) - (b), dye (pb) – (c). PLE spectra were measured at a fixed luminescence wavelength of 830 nm.

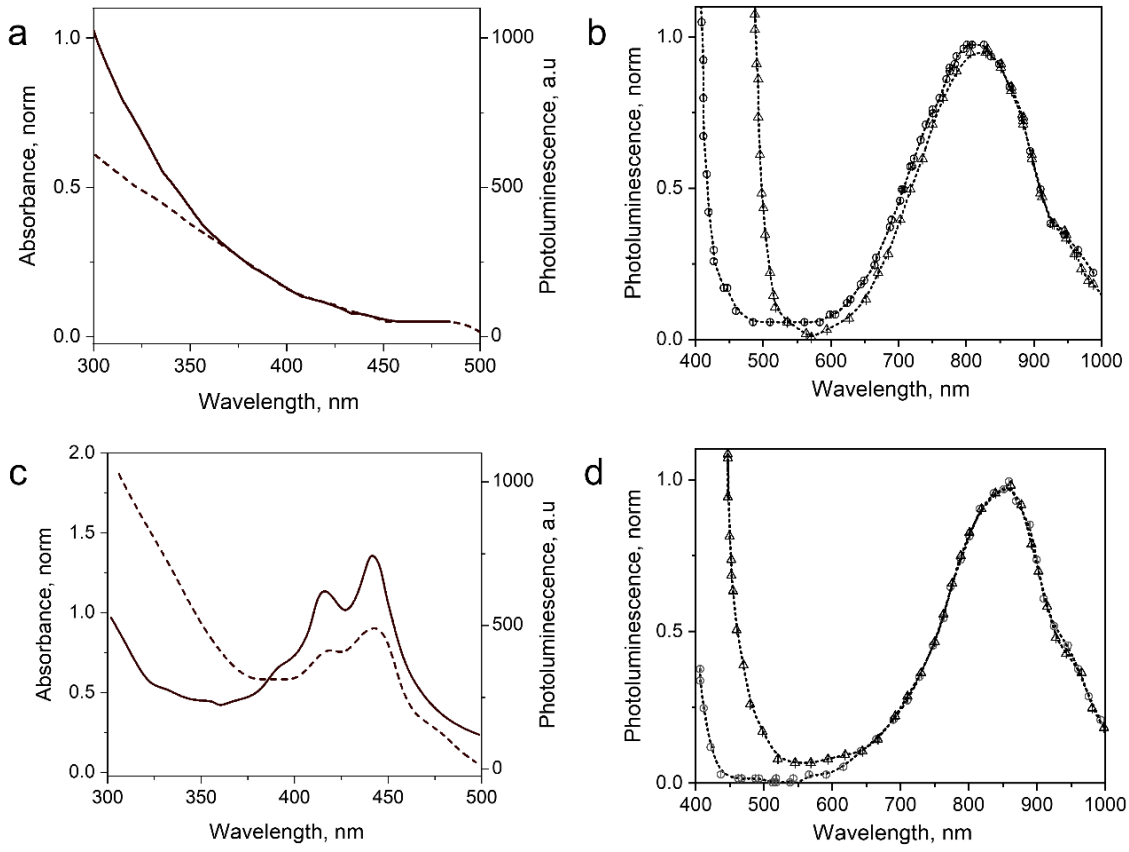

Figure 5-10. (a) Normalized UV/VIS absorption (solid line) and PLE spectra (dash line) of (C6)-SiNCs; (b) PL spectra of (C6)-SiNCs at 375nm (○) and 450nm (△) excitations; (c) Normalized UV/VIS absorption (solid line) and PLE (dash line) spectrums of (C6)-(p1)-SiNCs; (d) PL spectra of (C6)-(p1)-SiNCs at 375nm (○) and 450nm (△) excitations [236].

The PLQY values obtained at different excitation wavelengths were slightly different (as shown in Figure 5-11). The highest PLQY values of 33±6% were measured for the excitation wavelengths of 300 and 375 nm, whereas slightly lower values of 30±5% and 28±5% were found for excitation with wavelengths 405 and 440 nm, respectively. It should be mentioned that the error bars reflect the minimum and maximum values of PLQY for the synthesis repeated five times.

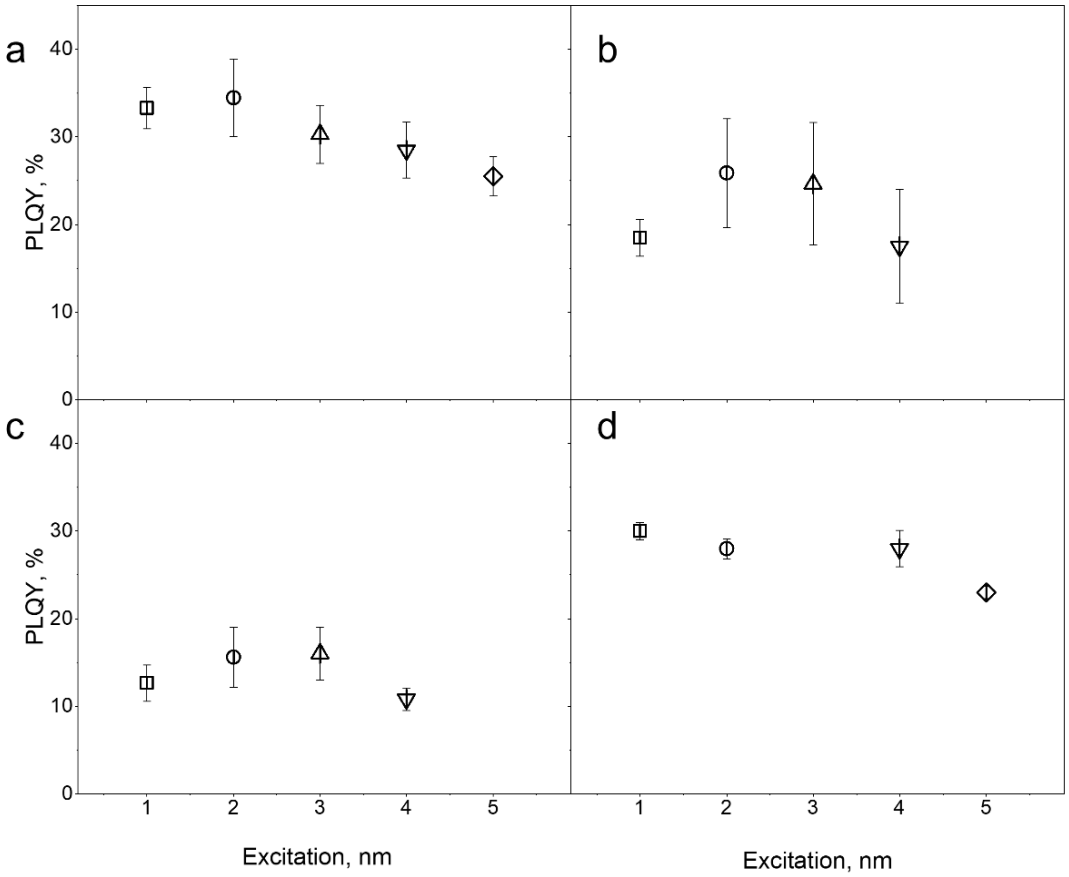

Figure 5-11. PLQY values of (a): (C6)-SiNCs, (b): (C6)-(1)-SiNCs, (c): (C6)-(2)-SiNCs and (d): (C6)-(3)-SiNCs measured at different excitation wavelengths 300 nm (□), 375 nm (○), 405 nm (△), 450 nm (▽), and 515 nm (◇) . The PLQY values are the result of averaging for five independent synthetic batches. The error bars indicate maximum and minimum values measured for five independent synthetic batches [236].

5.2 3-ethenyl perylene (dye-p1)

The absorption and PLE spectra of **(C6)-(1)**-SiNCs displayed absorption spectra that combined the SiNCs and the dye **(p1)** with a maximum of 442 nm. The absorption maximum exhibited the hypsochromic shift compared to the unreacted dye **(p1)** with an absorption maximum at 453 nm. This effect can be explained by reducing the double bond after the hydrosilylation reaction with **H**-SiNCs; thus, the conjugation of the perylene unit and the double bond vanished. The **(C6)-(p1)**-SiNCs demonstrated similar behaviour with the **(C6)**-SiNCs extinction coefficient λ_{300nm} and the enhanced extinction at longer

wavelengths (Table 1). For instance, a ~10-fold enhancement of the extinction coefficient was observed at 440 nm excitations.

Earlier, light with a wavelength 300 nm was envisioned to allow selective excitation of the SiNCs core without the dye's contribution to the absorption. Unexpectedly, the PLQY value of **(C6)-(1)**-SiNCs (14±5%) measured at 300 nm excitation was smaller than PLQY of the **(C6)-**SiNCs (33±6%) (Figure 5-11a, b). Firstly, more substantial surface oxidation of SiNCs after the reaction with the dyes were considered as the possible explanation for the decreased PLQY. The FTIR spectra indicated that the surface of both **(C6)**-SiNCs and **(C6)-(p1)**-SiNCs is slightly oxidized during the surface modification via the hydrosilylation reaction.

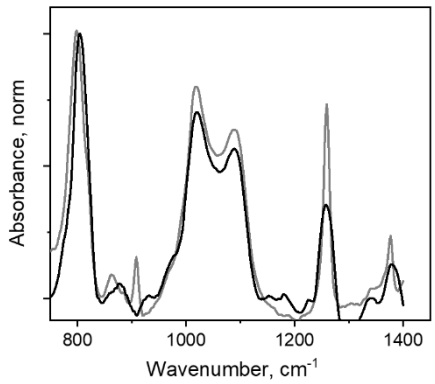

Figure 5-12. FTIR spectra of (C6)-SiNCs and (C6)-(p1)-SiNCs. The spectra were normalized using the Si-C peak at 800 cm^{-1} [236].

Infrared (IR) spectra of **(C6)**-SiNCs and SiNCs modified with the dye (p**1**) were measured to prove this hypothesis. Two feature peaks allowed for a comparison of the surface oxidation of SiNCs. The peak at 800 cm^{-1} is attributed to Si–C (stretching) vibration, whereas the broad peak at 960–1140 cm^{-1} to Si–O (stretching) vibration (Figure 5-12**)** [313-315]. One would expect more substantial surface oxidation (and a smaller PLQY) for a high *R*-value (Equation5.17):

$$R = \frac{A_{\bar{\nu}(Si-O)}}{A_{\bar{\nu}(Si-C)}} = \frac{\int_{960cm^{-1}}^{1140cm^{-1}} \bar{\nu}_{(1140-960cm^{-1})}\, d\bar{\nu}}{\int_{760cm^{-1}}^{830cm^{-1}} \bar{\nu}_{(830-760cm^{-1})}\, d\bar{\nu}} \tag{5.16}$$

where *R*-relative ratio of oxygen to hydrocarbon functionalized SiNCs, $A_{\bar{\nu}(Si-O)}$ -integrated absorbance area of the Si-O peak, $A_{\bar{\nu}(Si-C)}$ - integrated absorbance area of the Si-C peak, and $\bar{\nu}$ -vibration energy. In our measurement, the **(C6)**-SiNCs and **(C6)-(1)**-SiNCs samples exhibited a small difference in *R*-value. However, together with the unchanged PL spectra, it might indicate that the dye's reaction did not significantly increase the surface oxidation of the SiNCs. More substantial oxidation usually leads to a hypsochromic shift in the PL spectrum due to trap states' emission [52, 127].

To explain the decrease of PLQY measured at 300 nm excitation, it was assumed that the dye might quench the luminescence of SiNCs. More specifically, back-energy transfer (BET) was predicted from SiNCs (donor) to the triplet state of the dye (acceptor). The position of perylene triplet state (~800-850 nm)[127] coincides well with the broad SiNCs NIR emission (with PL maximum at 848 nm). Thus, the perylene triplet state might ultimately enable such an energy transfer that ultimately reduces the PLQY. Recently, the efficient energy transfer between QDs and the triplet state of dyes attached to its surface was described in the literature [246, 316-318]. For instance, Mongin *et al.* [245] reported a Dexter-like triplet-triplet energy transfer between CdSe nanocrystals and a surface-anchored polyaromatic dye. Recently, Xia *et al.* [247] described triplet-triplet annihilation up conversion utilizing energy transfer from SiNCs to the diphenyl anthracene's triplet state anchored with the SiNCs surface.

PL decays of SiNCs (Figure 5-13a, b) was measured to validate this idea. All investigated SiNCs exhibited PL decays with multi-exponential behaviour due to size polydispersity. Indeed, investigated narrow fractions of SiNCs demonstrated that PL lifetime rises significantly with nanocrystal size. For simplicity, the PL decays were fitted with double-exponential function, and the amplitude-averaged PL lifetime was assessed using Equation 5.18,

$$\tau_{av} = \frac{A_1\tau_1 + A_2\tau_2}{A_1 + A_2} \tag{5.17}$$

where τ_1 and τ_2 is the decay time of the first and second components, whereas A_1 and A_2 are amplitudes of first and second components.

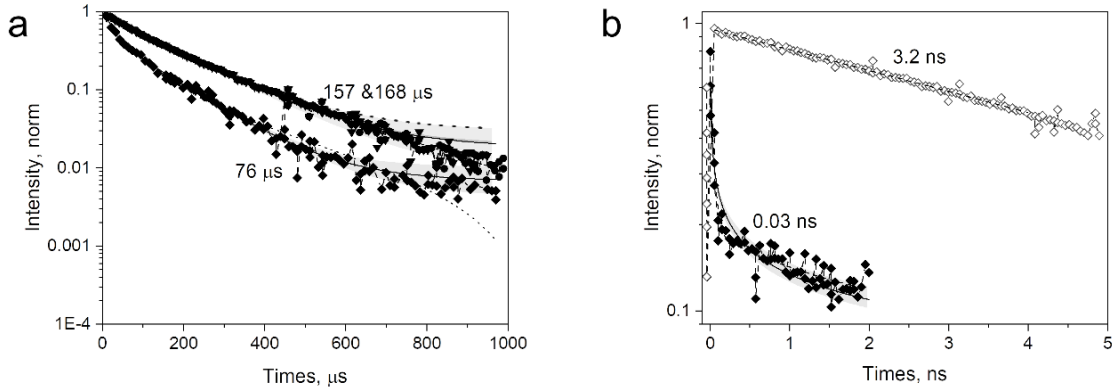

Figure 5-13. (a) Long-time (μs) PL decays for ligand functionalized SiNCs excited at 405 nm and measured at 810 nm. (C6)-SiNCs (●) (168 μs), (C6)-(pb)-SiNCs (▼) (157 μs), (C6)-(p1)-SiNCs (♦) (168 μs). (b) Short-time (ns) PL decays of dye-(p1) (◊) and (C6)-(p1)- SiNCs (♦); excited at 440 nm and measured at 450-550 nm. All presented lifetimes are average lifetimes estimated with Equation 5.18 after double-exponential fitting. The shaded area represents ~95% of the fitting confident band [236].

The **(C6)-**SiNCs demonstrated a relatively long PL lifetime of 168 μs. This value was in good agreement with previously reported PL lifetime values [319]. In contrast, **(C6)-(p1)-**SiNCs displayed a significantly shorter lifetime of 76 μs, which confirmed quenching of the SiNC NIR PL signal and resulted

in a PLQY decrease for **(C6)-(p1)-**SiNCs excited at 300 nm. The efficiency of BET was calculated as the ratio of $PLQY_{300nm}$ and $PLQY_{(0)300nm}$ calculated as in Equation 5.19,

$$\eta_{BET} = 1 - \frac{PLQY_{300nm}}{PLQY_{(0)300nm}} \tag{5.18}$$

or

$$\eta_{BET} = 1 - \frac{\tau_{av(C6)-SiNCs}}{\tau_{av(C6)-(p1)-SiNCs}} \tag{5.19}$$

where $PLQY_{300nm}$ and $PLQY_{(0)300nm}$ are values measured at 300 nm excitation for (**C6**)-(**p1**)-SiNCs and (**C6**)-SiNCs, respectively; and $\tau_{av(C6)\text{-}SiNCs}$ and $\tau_{av(C6)\text{-}(1)\text{-}SiNC}$ are lifetimes of NIR PL measured for (**C6**)-(**p1**)-SiNCs and (**C6**)-SiNCs, respectively. The value η_{BET} = 55% was calculated using Equation 5.19, whereas the value of η_{BET} calculated with Equation 5.20 was expected to be in the range of 30-75%, taking into account the reproducibility of the PLQY measurements.

Under excitation at 440 nm, an additional loss mechanism leading to reduced $PLQY_{400nm}$ value must be considered. If the efficiency of the direct energy transfer (DET) between the dye (donor) and the SiNCs (acceptor) is significantly less than 100%, the relationship $PLQY_{440nm} < PLQY_{300nm}$ should be observed as well. However, Figure 5-11b demonstrates that $PLQY_{440nm} \approx PLQY_{300nm.}$ To explain this result and assess the DET's value, the measurements were focused on ns-decays of dye **(p1)** before and after a reaction with **H**-SiNCs (Figure 5-13). The ns-decay exhibited a double-exponential behaviour with two distinguished lifetimes. It was assumed that the shorter component of 0.03 ns (and amplitude 81%) and a more extended component with a lifetime of 3 ns (and amplitude 19%) corresponded to quenched and unquenched dye **(p1)**, respectively. Unquenched dye observation might be due to the partial incorporation of dye molecules into thin hydrocarbon corona surrounding SiNCs [195, 320]. Considering the much longer distance between the dye and SiNCs surface, in this case, it was assumed the lack of DET for a small fraction of the dye attached to the surface of SiNCs. A DET efficiency of 99 % was calculated using Equation 5.21,

$$\eta_{DET} = 1 - \frac{\tau_{av(C6)-(p1)-SiNCs}}{\tau_0} \tag{5.20}$$

where $\tau_{av\ (C6)\text{-}(1)\text{-}SiNCs}$ = 0.03 ns is PL lifetime of dye **(p1)** after reaction with **H**-SiNCs, whereas τ_0 is the hypothetical PL lifetime of reacted dye **(p1)** without energy transfer.

To be exact, the last parameter can differ from the lifetime of the unreacted dye **(p1)**, considering the reduction of the double bond in the dye **(p1)** after the completion of the hydrosilylation reaction. The difference in the lifetime might be caused by the different withdrawing effects of ethyl and vinyl groups. Indeed, the examination of the PL lifetime of the dye **(p1)** dissolved in hexane displayed a lifetime of 3.2 ns, whereas the unsubstituted perylene or perylene with saturated alkyl substituents (for instance 2, 5, 8, 11-tetra-tert-butylperylene) usually demonstrated a longer lifetime of 4.3-4.5 ns [321-323]. Nevertheless, this difference in τ_0 led to only minor correction of η_{BET} = 99.3% (for τ_0 = 3.2 ns) instead of 99 % if τ_0 =

4.4 ns was considered. Thus, DET's high efficiency explained the reasons for the PLQY values obtained at 300 nm and 440 nm excitation being similar. PL decays of dye (**p1**) show a lifetime -3.2 ns, (**p2**) demonstrates a lifetime -4.1 ns, whereas the dye (**pb**) was– 7.1 ns, as depicted in Figure 5-14.

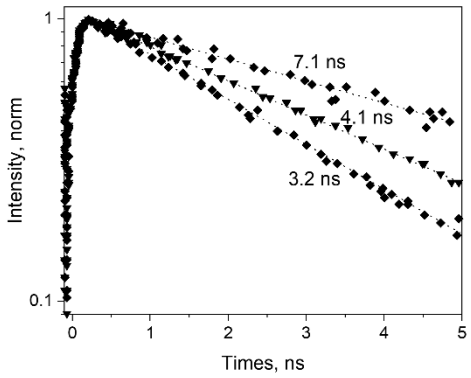

Figure 5-14. Short time (ns) decays of visible PL for dye (p1) (♦), (p2) (▲), and (pb) (▼), respectively, dissolved in hexane. All presented lifetimes were derived from mono-exponential fitting [236].

These results predicted the enhancement of ~300 % for NIR PL of SiNCs when excited with a blue light source (440 nm). The 300% value comprises a 10-fold enhancement due to absorption and ~50 % losses due to BET from SiNC to the dye triplet. Indeed, Figure 5-15 displays steady-state PL spectrums for solutions, **(C6)-**SiNCs and **(C6)-(p1)-**SiNCs, with equal absorbance at 300 nm and excited with LED (440 nm). In this experiment, the NIR PL's enchantment ~270 % was observed, which was in good agreement with the predicted value.

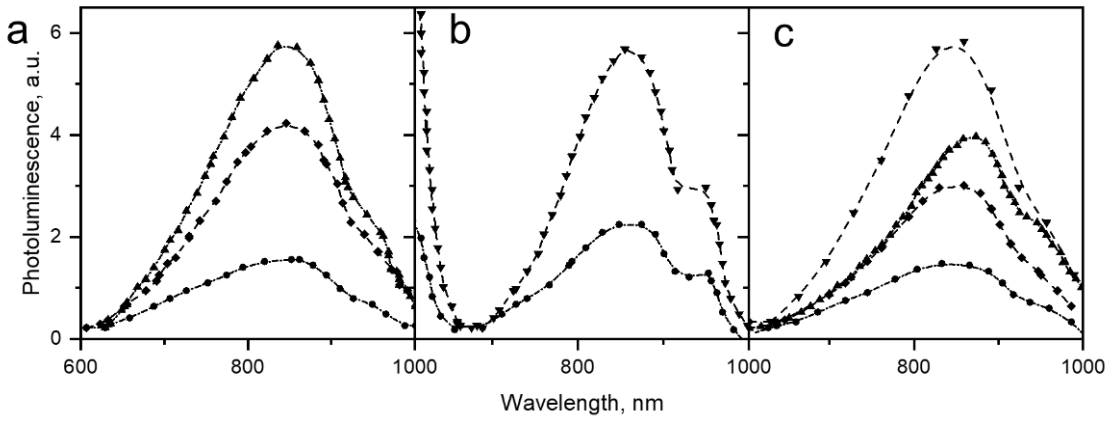

Figure 5-15. (a): PL under excitation with LED 440nm of (C6)-SiNCs (●), (C6)-(p1)-SiNCs (♦) and (C6)-(p2)-SiNCs (▲); (b): PL under excitation with LED 515nm of (C6)-SiNCs (●) and (C6)-(pb)-SiNCs (▼); (c): PL under broadband excitation (435-550 nm) of (C6)-SiNCs (●), (C6)-(p1)-SiNCs (♦), (C6)-(p2)-SiNCs(▲) and (C6)-(pb)-SiNCs (▼). All dispersions have similar absorbance of 0.3 at 300 nm (A300). The PL spectra were normalized to emission of (C6)-SiNCs (●) [236].

5.3 3-ethynyl perylene (dye-p2)

Next, the triple bonds' effect was examined on the dye's hydrosilylation reaction **(p2)**. The absorption and PLE spectra of **(C6)-(p2)**-SiNCs displayed the combination of absorption spectra of SiNCs and dye **(p2)** (Figure 5-17a) with a maximum at 441 nm. The extinction coefficient ε_{440nm} for **(C6)-(p2)**-SiNCs is a little bit higher then coefficient ε_{440nm} for **(C6)-(p1)**-SiNCs (Table 1). This difference might indicate that 3-ethynylperylene (perylene with triple bond) has slightly higher activities in the hydrosilylation reaction then ethenylperylene (perylene with double bond). The NIR PL of SiNCs exhibited similar spectra under excitation with different wavelengths, for example, a PL maximum of 832 nm and FWHM of 170 nm (Figure 5-17b). The PLQY value of 12 ± 4% was measured for **(C6)-(p2)**-SiNCs at 300 nm excitation. This value was comparable (though slightly lower) to the PLQY for SiNCs modified with ethenylperylene. The value of PLQY correlated with the shorter PL lifetime of 76 μs measured for NIR emission of **(C6)-(p2)**-SiNCs (Figure 5-16). This observation confirmed more efficient BET from SiNCs to the triplet state of the dye **(p2)**, due to a bathochromic shift of the dye triplet state (as compared with **(C6)-(p1)**-SiNCs), because of the conjugation of the perylene core with the double bond. The value η_{BET} = 57% was calculated using Equation 5.19, whereas the value of η_{BET} calculated with Equation 5.20 was expected to be in the range 52-75%.PL decays for NIR and visible emission for (**C6**)-(**p2**)-SiNCs dispersed in hexane demonstrate a lifetime of 72 μs and 3.8 ns, respectively.

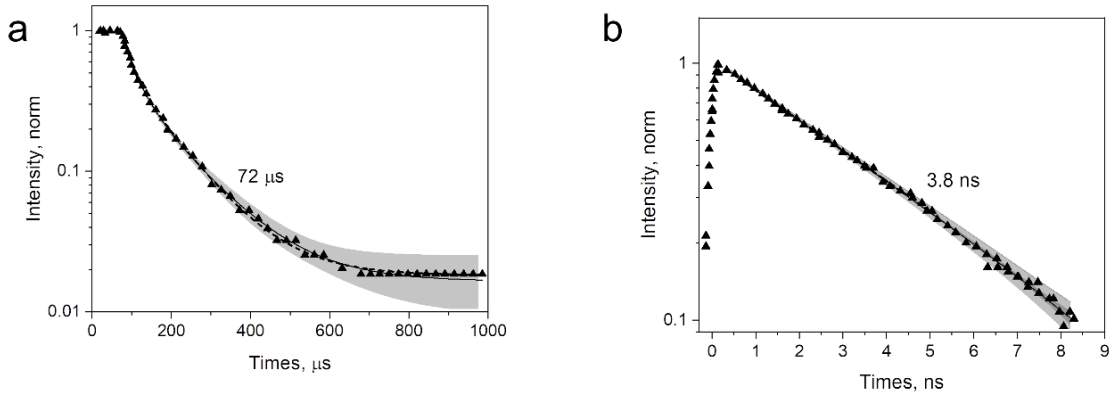

Figure 5-16. (a): long-time (μs) decay of NIR PL of (C6) -(p2)- SiNCs (▲); (b): short-time (ns) decay of visible PL for (C6)-(p2)- SiNCs. All presented lifetimes are average lifetimes estimated with Equation 5.18 after biexponential fitting. The shaded area represents ~95% of the fitting confident band [236].

The measurement results of ns-lifetime (for dye emission in the range 440-560 nm) displayed decay with a lifetime of 3.8 ns (Figure 5-18). This extended lifetime indicated that DET from the dye to SiNC is considerably less efficient than DET in the system **(C6)-(p1)**-SiNC. The precise calculation of η_{DET} was complicated in case of **(C6)-(p2)**-SiNCs, as the exact value of τ_0 was unknown (τ_0 and $\tau_{av(C6)-(p2)-SiNC}$ should have the same order of magnitude). The enhancement factor for the **(C6)-(p2)**-SiNCs system should

be logically lower than the enchantment in the case of **(C6)-(p1)**-SiNCs due to less efficient DET and the pronounced BET observed for the **(C6)-(p2)**-SiNCs conjugate. Indeed, Figure 5-18 demonstrates a 175 % enhancement of NIR PL achieved with excitation at 440 nm.

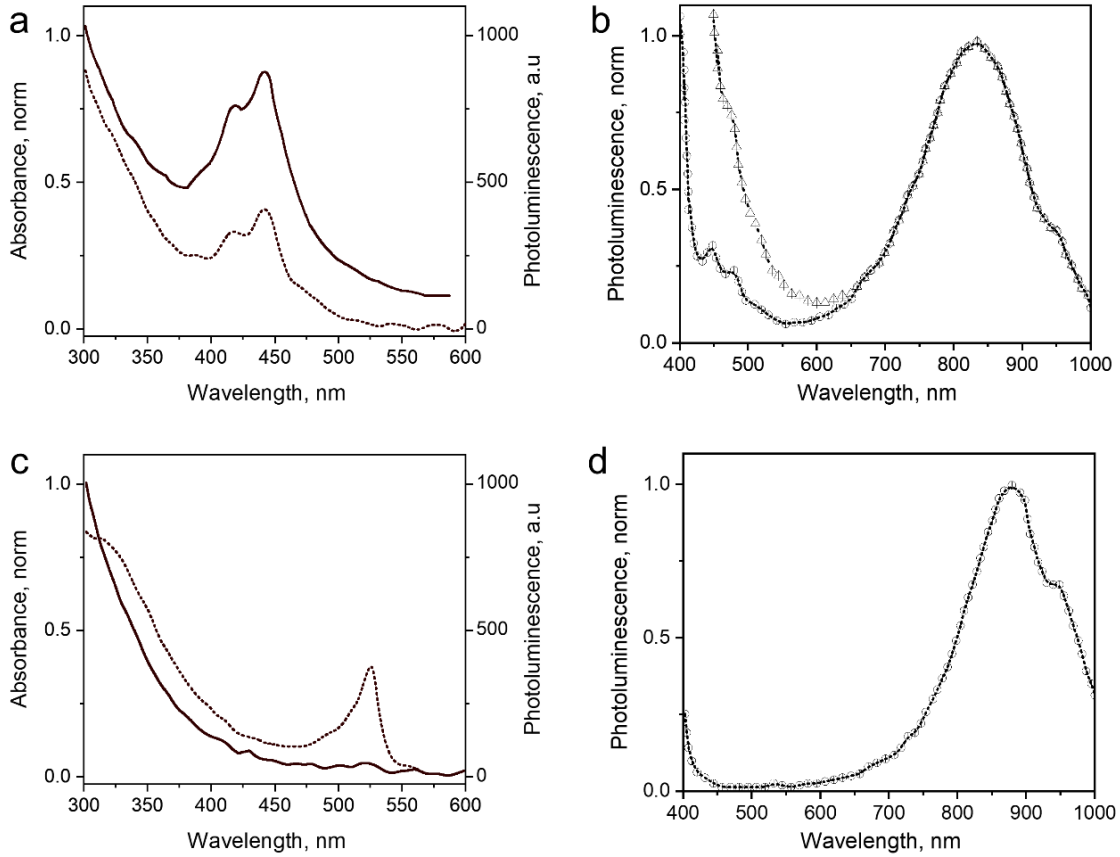

Figure 5-17. (a): Normalized absorption (solid line) and PLE (dash line) spectra of (C6)-(p2)-SiNCs. (b): PL-emission spectra of (C6)-(p2)-SiNCs at 375 nm (○) and 450 nm (△) excitations. (c): Normalized absorption (solid line) and PLE (dash line) spectra of (C6)-(pb)-SiNCs. (d): PL-emission spectra of (C6)-(pb)-SiNCs at 375 nm (○) and 450 nm (△) excitations [236].

5.4 Ethylene-m-phenyl BODIPY (dye-pb)

To examine the possibility of DET between a dye absorbing in the green range of the visible spectrum and SiNCs, a hydrosilylation reaction was performed to dye **(pb)**. The dye **(pb)** demonstrated an absorption maximum at 514 nm, which can be seen in the absorption and PLE spectra of **(C6)-(pb)**-SiNCs (Figure 5-15c). It should be noted that very efficient surface anchoring for the dye **(3)** were not able to provide using the synthetic conditions that were similar to ones for dyes (**p1**) and (**p2**). It only a 3-fold increase was observed on extinction coefficient at 515 nm. Thus, the synthetic procedure in the case of dye **(pb)** requires further optimization. However, even with such an amount of the attached dye, enhancing

~200 % for excitation at 515 nm was observed at NIR PL (Figure 5-15). Two effects can explain such a significant enhancement: Firstly, the PLQY of the SiNCs was high (28±5 % under 300 nm excitation). This observation correlated with the long lifetime of NIR PL (157 μs, as presented in Figure 5-13). Thus, the less pronounced BET with η_{BET} = 7 % (the result of calculation with Equation 5.20) and $\eta_{BET} \approx 0$ - 34 % (the result of calculation with Equation 5.19) was observed in the **(C6)-(pb)**-SiNCs system due to lower dye surface concentration and the higher energy of the BODIPY triplet (~ 750 nm).[324, 325] Overall, the phenomenon of BET requires additional investigation and will be described in our future publication. Additionally, the ns-decay measured for the range 550-600 nm indicated strong quenching of BODIPY luminescence with η_{DET} = 94 %. In contrast to the unreacted dye **(pb)** with a lifetime of 7.1 ns, the **(C6)-(pb)**-SiNCs demonstrates the average PL lifetime of BODIPY emission of 0.4 ns. As the double bond reduction after the hydrosilylation reaction might lead to the only minor change of the lifetime (due to weak conjugation between the BODIPY core and the double bond), it is assumed that the lifetime of 7.1 ns could be used in the calculation of DET efficiency. Therefore, by having only small losses due to the energy transfer processes, the absorption enhancement can be efficiently utilized in the case of **(C6)-(pb)**-SiNCs. PL decays for visible emission of (**C6**)-(**pb**)-SiNCs dispersed in hexane demonstrate a lifetime of 0.3 ns.

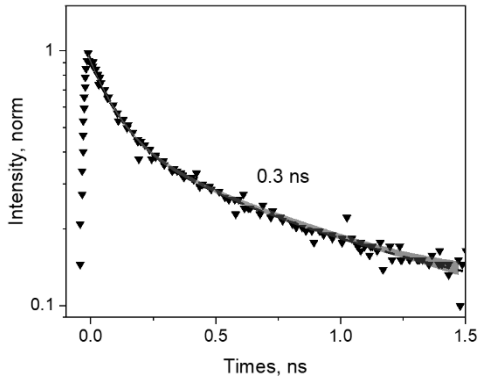

Figure 5-18. Short-time (ns) decay of visible PL for (C6)-(pb)-SiNC. The shaded area represents ~95% of the fitting confident band [236].

Last-but-not-least, the NIR PL of sensitized samples were investigated under a broad spectral excitation that can mimic, for instance, the excitation with solar radiation. To get comparable results, the concentration of all solutions was tuned to have similar absorbance at 300 nm. Figure 5-18 displays the PL spectra of four solutions under the broadband excitation (a white LED was used together with a 550 nm short-pass filter). The enhancement of 280 %, 100 %, and 160 % for the NIR PL of **(C6)-(1)**-SiNCs, **(C6)-(2)**-SiNCs, and **(C6)-(3)**-SiNCs samples were achieved, respectively.

6 Singlet oxygen generation

Some of the results present in Chapter 6 were published in Beri et al. [326]. The author did all the syntheses and performed all the characterization experiments in this chapter. Except for singlet oxygen yield measurements were performed by author and co-author Dr. Dmitry Busko, whereas co-author Marius Jakoby performed low-temperature PL-measurements. The original idea was brainstormed with co-authors Dr. Andrey Turshatov and Prof. Bryce S. Richards. This chapter's goal was developed based on the anomaly behaviour of perylene-SiNCs' PLQY at 300 nm. Indeed, the perylene molecule has limited absorption at 300 nm, so we foresee there must be back energy transfer from SiNCs to perylene that occurred in covalently anchored perylene-SiNCs. To reveal the quest, in ambient air, the populated triplet state in perylene-as resulting in back energy transfer-has a high chance to produce singlet oxygen via triplet-triplet energy transfer. Meanwhile, alkyl-SiNCs do not possess an intrinsic ability to generate singlet oxygen. We demonstrated that covalently anchored perylene-SiNCs generate quite a significant singlet oxygen. There are two methods used to determine singlet oxygen. Both methods are described in detail in this chapter. This research could benefit in bioimaging and theranostics, for example, to treat cancer cells.

6.1 Dye functionalized SiNCs as a photosensitizer

The molecular structures of phenalenone (**phen**), 9,10-Dimethylanthracene (**dma**), 5,6,11,12-Tetraphenylnaphthacen (**rubrene**), perylene derivatives dye-**p1** and dye-**p2**, as well as hexyl functionalized SiNCs (**C6**)-SiNCs), hexyl-dye functionalized SiNCs (**C6**)-(**p1**)-SiNCs and (**C6**)-(**p2**)-SiNCs) are shown in Figure 6-1. Reference photosensitizer molecule is **phen**, probe molecule are **dma** and **rubrene**, and photosensitizer samples are dye-**p1**, dye-**p2**, (**C6**)-SiNCs, (**C6**)-(**p1**)-SiNCs, and (**C6**)-(**p2**)-SiNCs.

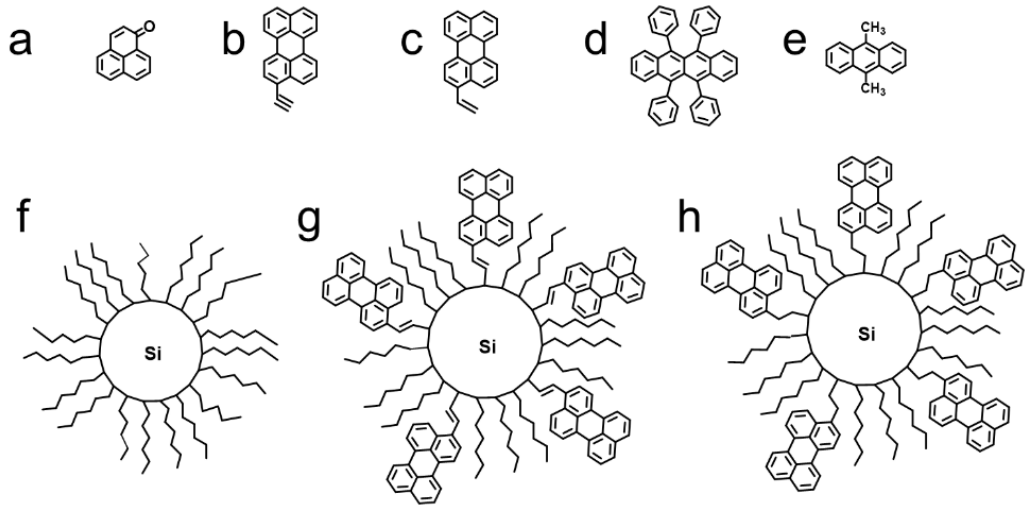

Figure 6-1. Molecular structures of (a) phenalenone (phen), (b) 3-ethenylperylene (dye-p1), (c) 3-ethynylperylene (dye-p2), (d) 5,6,11,12-Tetraphenylnaphthacen (rubrene), (e) 9,10-Dimethylanthracene (dma) (f) hexyl-functionalized SiNCs [(C6)-SiNCs], (g) 3-ethynylperylene/hexyl-functionalized SiNCs [(C6)-(p2)-SiNCs], and (h) 3-ethenylperylene/hexyl-functionalized SiNCs [(C6)-(p1)-SiNCs].

A reference, probes, and samples were illuminated with 300 nm LED excitations for 60 minutes to monitor the photostability as a preliminary study. The UV-Vis-NIR spectra depicted in Figure 6-2 demonstrate photodegradation of **phen, dma, rubrene**, **dye-p1**, **dye-p2**, and **(C6)-SiNCs** after 60 minutes of illumination using 300 nm LED excitation. Reference **phen** demonstrated 31% photodegradation (4.3% uncertainty of our result is coming from it). **Dma** and **rubrene** show 22% and 65% photodegradation, respectively; (22% of photodegradation contributes to another 3.3% uncertainty). In contrast, 65% of **rubrene** photodegradation is far above the expected degradation. Rubrene photodegradation has been observed previously by Ronzani *et al.* [327]. The authors proposed that the experiment should be performed at rubrene concentration below 1×10^{-5} M. Because at a concentration above 1×10^{-5} M, photodegradation was found exhibited 35% at 266 nm excitation wavelength. In my work, rubrene photodegradation was even higher because excitation was performed directly to the maximum peak (λ_{max}=300nm) of rubrene absorption. Due to the limitation, the rubrene molecule is skipped from being used as a probe molecule. Photodegradation of dye-**p1**, dye-**p2,** and (**C6**)-SiNCs show as much as 6%, 5%, and 9%, respectively, after 60 minutes of illumination using 300 nm LED excitation (see Figure 6-2).

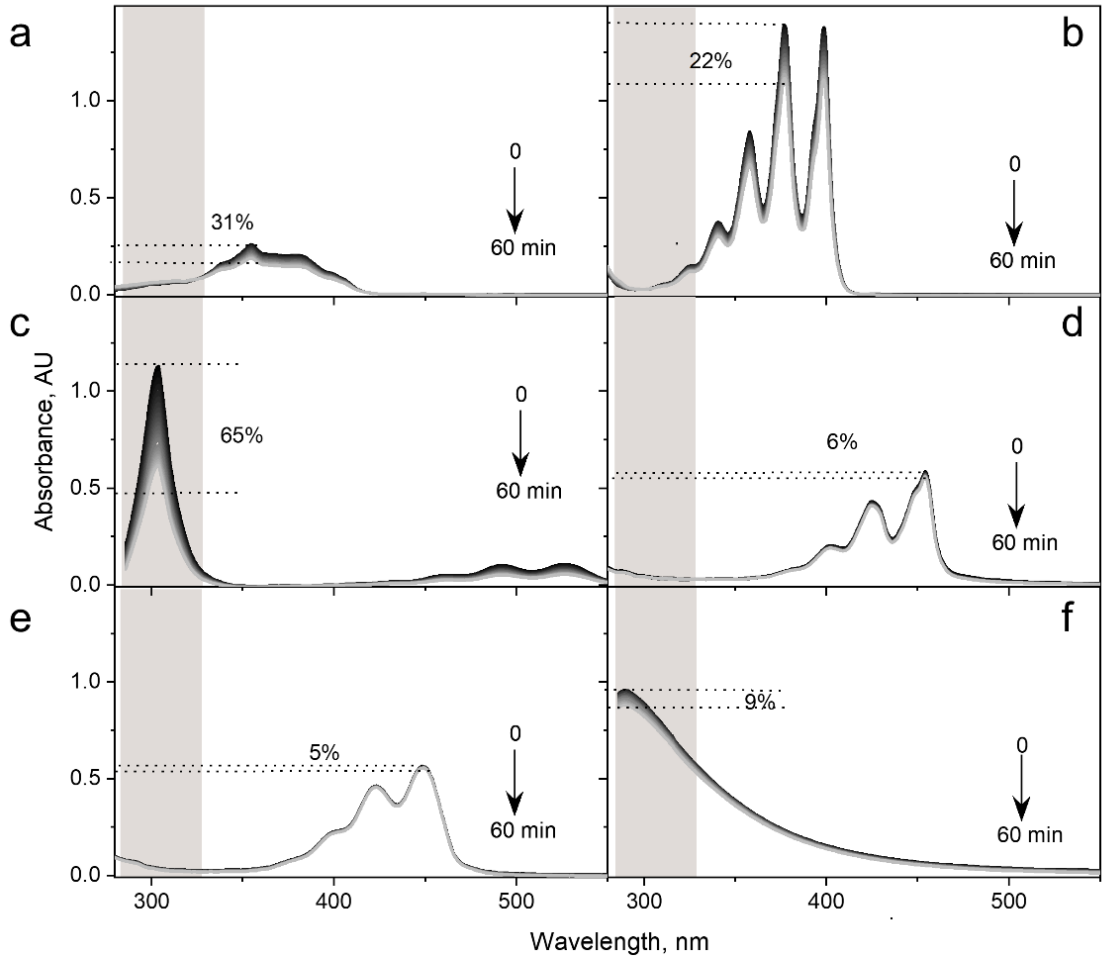

Figure 6-2. Evolution of UV-Vis-NIR-spectra upon illumination (a) phenalenone (phen), (b) 9,10-dimethylanthracene (dma), (c) 5,6,11,12-Tetraphenylnaphthacen (rubrene) (d) 3-

ethynylperylene (dye-p2), and (e) 3-ethenylperylene (dye-p1), and (f) hexyl-functionalized SiNCs [(C6)-SiNCs]. 300 nm excitation for 60 minutes.

To get an insight into a $^1O_2$ generation, a series of possible reaction processes could be described in chemical equations. Equations (6.21)-(6.31) summarize the possible reactions and corresponding rate constants of the photosensitization process to produce $^1O_2$ [327].

$$PS \xrightarrow{h\nu} PS^* \tag{6.21}$$

$$PS^* \xrightarrow{k_{ISC}} {}^3PS^* \tag{6.22}$$

$${}^3PS^* + {}^3O_2 \xrightarrow{k_{ET}} PS + {}^1O_2 \tag{6.23}$$

$${}^1O_2 \xrightarrow{k_{SD}} {}^3O_2 \tag{6.24}$$

$${}^1O_2 \xrightarrow{k_{em}} {}^3O_2 + h\nu' \tag{6.25}$$

$${}^1O_2 + Tr \xrightarrow{k_x^{Tr}} TrO_2 \tag{6.26}$$

In Equation (6.21)**,** a photosensitizer received a photon and excited it to the excited singlet state. Excited singlet state released the energy to the triplet state ($^3PS^*$) *via* intersystem crossing (k_{ISC}) (Equation (6.22)). The triplet state of a photosensitizer ($^3PS^*$) is transferred the energy to the triplet state of an ambient oxygen molecule ($^3O_2$) *via* energy transfer (k_{ET}) to form singlet oxygen ($^1O_2$) and relaxed back to the ground state (PS) (Equation (6.23)). Resulting in $^1O_2$ is diluted in the solvent (cyclohexane), and some energy might be transferred to the solvent *via* non-radiative relaxation/diffusion (k_{SD}) (Equation (6.24)). A small part of the energy is released *via* $^1O_2$ phosphorescence at 1270 nm (k_{em}) (Equation (6.25)). This phosphorescence could be observed at 1270 nm wavelength. In addition, $^1O_2$ could also be trapped using probe molecules (Tr), such as 9, 10-dimethylanthracene (**dma**) (6.26).

6.2 Determination of Φ_Δ using chemical methods

There are two well-established methods to determine the Φ_Δ. The first method uses particular probe compounds such as 9, 10-dimethylanthracene (**dma**) [328, 329]. Herein, Φ_Δ can be calculated by comparing the quenching rate of photosensitizer-x relative to photosensitizer reference molecule (phenalenone) using Equation 6.27. [327]

$$\Phi_\Delta^x = \Phi_\Delta^R \frac{k_x^{Tr}}{k_R^{Tr}} \frac{I_a^x}{I_a^R} \tag{6.27}$$

Where Φ_Δ^R is $^1O_2$ -quantum yield of reference (**phen**), k_x^{Tr} and k_R^{Tr} are quenching rate constants for probe-x and reference-**phen (**see Figure 6-3**)**. I_a^x, and $\boldsymbol{I_a^R}$ are photon flux absorbed by photosensitizer and reference.

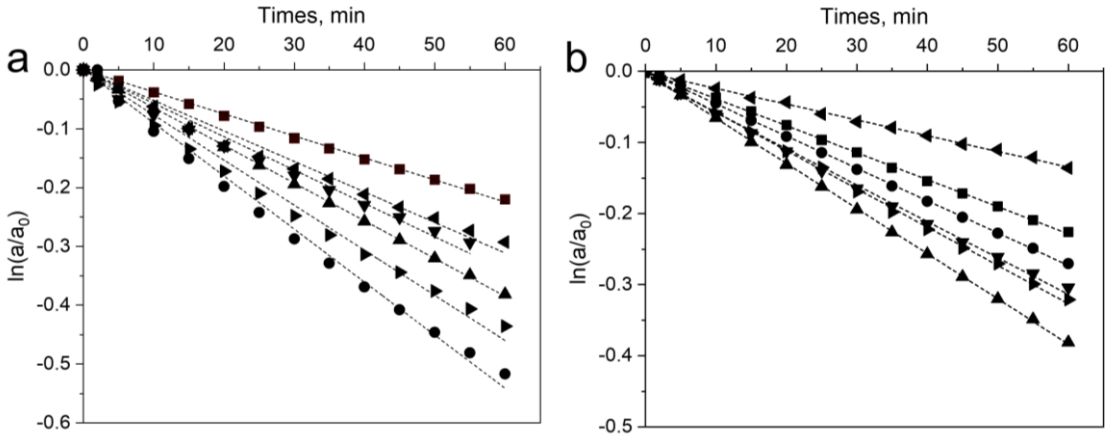

Figure 6-3. (a) Dma photodegradation due to illumination at 300nm LED excitation, (■) dma, (●) phenalenone, (▲) dye-p1, (▼) dye-p2, (◄) (C6)-(p1)-SiNCs, (►) (C6)-(p2)-SiNCs. (b) Dma photodegradation due to illumination at 405 nm LED excitation, (■) dma, (●) phenalenone, (▲) dye-p1, (▼) dye-p2, (◄) (C6)-(p1)-SiNCs, (►) (C6)-(p2)-SiNCs

The results of the calculated Φ_Δ determined by the chemical method are tabulated inTable 2.

Table 2. Singlet oxygen quantum yields (Φ_Δ) data measured using the chemical method.

PS	*a(300nm)* ($\times 10^{-2}$)	k_x^{dma} † ($\times 10^{-3}$)	*a(405nm)* ($\times 10^{-2}$)	k_x^{dma} ‡ ($\times 10^{-3}$)	*PLQY,%*	Φ_Δ,% †	Φ_Δ,%‡
phen	5	9.00	1.5	4.55	—	92 ± 10*	92 ± 10*
dye-**p1**	5	6.41	2.3	6.38	68 ± 1‡,§	65 ± 15	81 ± 7
dye-**p2**	4	5.21	2.3	5.28	52 ± 1‡,§	70 ± 15	70 ± 7
(**C6**)-SiNc	90	3.7	2.5	0.3	33 ± 1†,♦	0.02 ± 5	0.3 ± 5
(**C6**)-(**p1**)-SiNCs	19	5.67	2.9	2.26	22 ± 1†,♦	15 ± 6	23 ± 6
(**C6**)-(**p2**)-SiNCs	16	7.66	3.3	5.48	15 ± 1†,♦	24 ± 6	50 ± 6

†corresponds to the 300 nm excitation; ‡ corresponds to the 405 nm excitation; * reference Φ_Δ= 0.92±0.5 (Schmidt et al., 1994) § PLQY of dyes visible emission integrated with the range of 350-500 nm. ♦PLQY of SiNCs NIR emission integrated with the range of 650-1,000 nm. k_x^{dma} are quenching rate constant of **dma** as a function of 60-minute illumination using 300 and 405 nm LED excitation. The uncertainty of Φ_Δ was calculated in agreement with the procedure in Chapter 3. The uncertainties of PLQY measurements were earlier reported in [243].

6.3 The Φ_Δ determination using singlet oxygen phosphorescence

The second method is based on measurements of $^1O_2$ phosphorescence, as described in Equation 6.28. The radiative relaxation process from excited $^1O_2$ to the ground triplet state ($^1\Delta_g \rightarrow {}^3\Sigma_g$) yields an emission at 1,270 nm with a relatively long lifetime (ms-to-s, depending on solvent) [330]. The present study's primary goal is to compare Φ_Δ under the direct excitation of the attached dyes (with 405 nm laser) and SiNCs (with 317.5 nm laser), with the two chosen wavelengths enabling this selectivity.

$$\Phi_{\Delta}^{x} = \Phi_{\Delta}^{R} \frac{[S_{em}^{x}]}{[S_{em}^{R}]} \frac{[I_{abs}^{R}]}{[I_{abs}^{x}]} \tag{6.28}$$

The Φ_{Δ} as well as PLQY values of photosensitizers (were used in this work) are tabulated in Table 3. The calculation was based on the integrated emission of the known reference material (**phen**).

Table 3. Singlet oxygen quantum yields data measured using the Φ_{Δ} phosphorescence.

PS	*a(317.5nm)*	$I_{em}^{\dagger}$	*a(405nm)*	$I_{em}^{\ddagger}$	*PLQY,%*	Φ_{Δ},% †	Φ_{Δ},%‡
phen	0.576	1	0.760	1	—	92 ± 10*	92 ± 10*
dye-**p1**	0.081	0.090	0.760	0.382	52 ± 1‡,§	56 ± 25	34 ± 5
dye-**p2**	0.138	0.111	0.763	0.381	68 ± 1‡,§	45 ± 14	35 ± 5
(**C6**)-SiNCs	0.780	—	0.773	—	33 ± 1$^{\dagger,\blacklozenge}$	—	—
(**C6**)-(**p1**)-SiNCs	0.331	0.052	n/a	n/a	22 ± 1$^{\dagger,\blacklozenge}$	9 ± 6	n/a
(**C6**)-(**p2**)-SiNCs	0.576	0.213	0.693	0.264	15 ± 1$^{\dagger,\blacklozenge}$	20 ± 5	27 ± 5

†corresponds to the 317.5 nm excitation; ‡ corresponds to the 405 nm excitation; *reference Φ_{Δ}= 0.95±0.5 (Schmidt et al., 1994) § PLQY of dyes visible emission integrated in the range of 350-500 nm; $^{\blacklozenge}$PLQY of SiNCs NIR emission integrated in the range 650-1,000 nm; I_{em} was normalized using the emission of $^{1}O_2$ excited *via* **phen** (I_{em} = 1 for **phen**); The uncertainty of Φ_{Δ} was calculated in agreement with Equation 3.12. The uncertainty of PLQY measurements was reported earlier in [246]. The Φ_{Δ} for dye-2 under 317.5 excitation is not reported because luminescence of $^{1}O_2$ was too weak.

6.4 Singlet oxygen generation of *dye-p1* and *dye-p2*

The photodegradation of **phen** was found after long-time (1 hour) irradiation of the reference PS previously described in the first paragraph. Taking into account that the acquisition of $^{1}O_2$ luminescence (using 317.5 nm laser with an intensity of 45 mW) takes approximately 100 seconds, it was considered that the reference PS as photostable. After knowing that the **phen** was photostable, $^{1}O_2$ generation was investigated for dye-**p1** and dye-**p2**. Perylene by itself exhibits a very high PLQY of 94 % in cyclohexane [331] and is thus a very poor PS. However, perylene derivatives have demonstrated the ability to generate $^{1}O_2$ with a high quantum yield [242, 332, 333]. Figure 6-4b and Figure 6-4d demonstrate the phosphorescence of $^{1}O_2$ generated *via* photoexcitation of dye-**p1** and dye- **p2** solutions in cyclohexane via both 405 nm and 317.5 nm laser excitation. The concentration of solutions with dye-**p1**, dye-**p2,** and **phen** was adjusted to have similar absorption at the excitation wavelengths (Figure 6-4). The absorption of the samples $A_{\%}^{x}$ was estimated from absorbance a_x using Equation 6.29:

$$A_{\%}^{x} = 100\% - 10^{(2-a_x)} \tag{6.29}$$

where $A_{\%}^{x}$ is % of absorbed light and a_x is absorbance measured experimentally.

A calculation using Equation 6.34 gives the value of Φ_{Δ} = 34 ± 5 % for dye-**p1**, and Φ_{Δ} = 35 ± 5 % for dye-**p2** when excited with the 405 nm laser. The results are only about half of Φ_{Δ} results determined using chemical methods. For a possible explanation for this difference, review back to Equation 6.25 and Equation 6.26. There are some potential losses due to energy transfer from $^{1}O_2$ to the solvent cyclohexane. The $^{1}O_2$ releases energy to the solvent during excitation with a 405 nm laser. Our laser aperture

is 5 mm and directly hit the sample in the middle of 1 cm fluorescent cuvette, so the excess of solvent might absorb energy during diffusion of $^1O_2$ in the solution. Measurements with the other excitation wavelength (317.5 nm) result in very weak $^1O_2$ phosphorescence with very high uncertainty in Φ_Δ = 56±25% (for dye-**p1**) and Φ_Δ = 45 ± 14 % (for dye – **p2**) because of the weak dye absorption at 317.5 nm. The results are lower than the chemical method, and our hypothesis is due to an energy transfer from $^1O_2$ molecules to the excess of solvents, besides the considerable uncertainty due to the low absorption at ~300 nm.

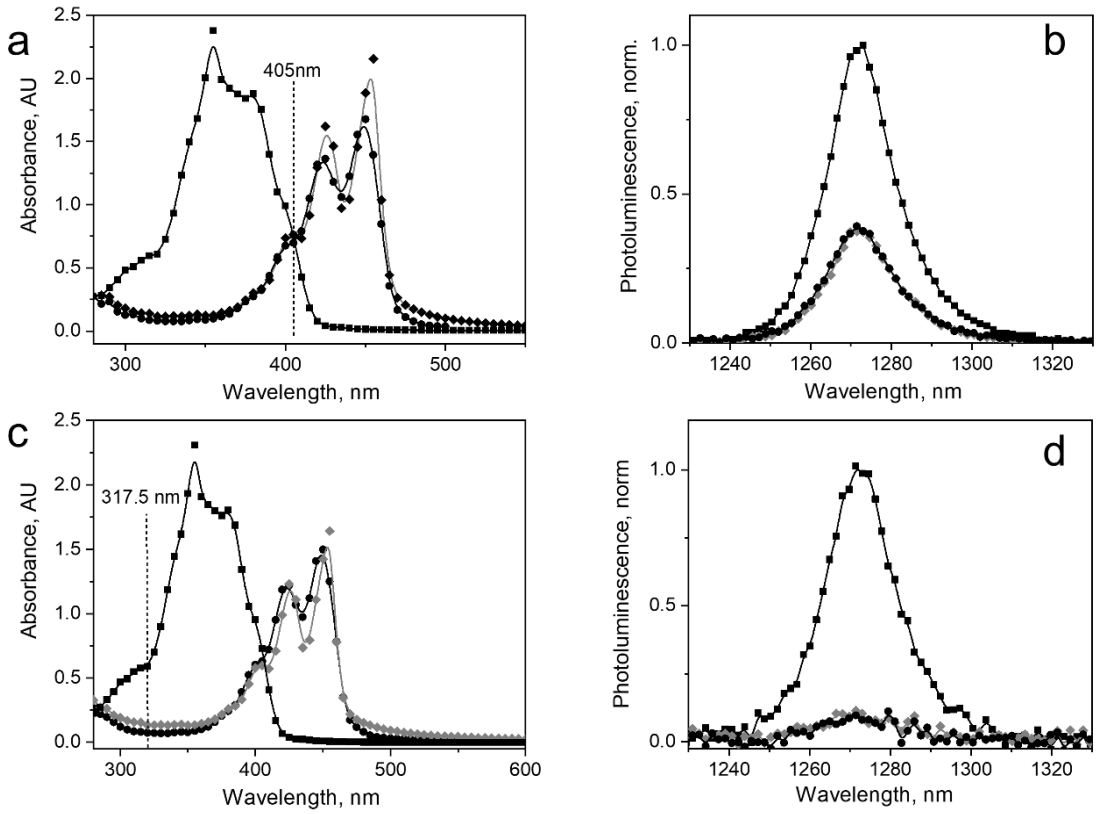

Figure 6-4. (a) UV-Vis absorption spectra of solutions of phen (■), dye-p1 (●) and dye-p2 (♦) in cyclohexane used for the generation of $^1O_2$ with 405 nm laser; (b) $^1O_2$ phosphorescence excited via irradiation of solutions of phen (■), dye-p1 (●) and dye-p2 (♦) with 405 nm laser (75 mW); (c) UV-Vis absorption spectra of solutions of phen (■), dye-p1 (●) and dye-p2 (♦) in cyclohexane used for the generation of $^1O_2$ with 317.5 nm laser; (d) $^1O_2$ phosphorescence excited via irradiation of solutions of phen (■), dye-p1 (●) and dye-p2 (♦) with 317.5 nm laser (excitation intensity of 15 mW). The dashed line is representing the excitation wavelength (317.5 and 405 nm)

The dyes demonstrate unusually large values of Φ_Δ together with large values of absolute PLQY of 52 ± 1% and 68 ± 1 % measured for dye-**p1** and dye-**p2**, respectively. Note that absolute PLQYs were estimated in the integrating sphere and have higher precision than Φ_Δ. To gain insight into $^1O_2$ photosensitization, PLQY for dye solutions prepared inside a glovebox was measured under oxygen-free conditions. Resulting in PLQY of 80 % for dye-**p1** and 98 % for dye- **p2,** and the obtained result indicates that photosensitization of $^1O_2$ occurs solely *via* the excited singlet state in dye-**p1** and dye-**p2**. For dye **p1**,

~50 % of the excitation energy was decaying *via* radiative relaxation, whereas the remainder (~30 %) transfers the energy to oxygen. It appears that around two-thirds of the excited singlet states relax *via* the radiative transition for dye-**p2**.

In contrast, around one-third of the excited singlets transfer the energy to oxygen molecules. Earlier, the highest Φ_Δ of 67 % for perylene-like molecules were reported for rather complicated perylene derivatives - di-(perylenebisimide) [332]. However, our measurements indicate that a moderate Φ_Δ of 35 ± 5 % can be achieved with the simple molecules, which can be produced without expensive and time-consuming multistep synthesis.

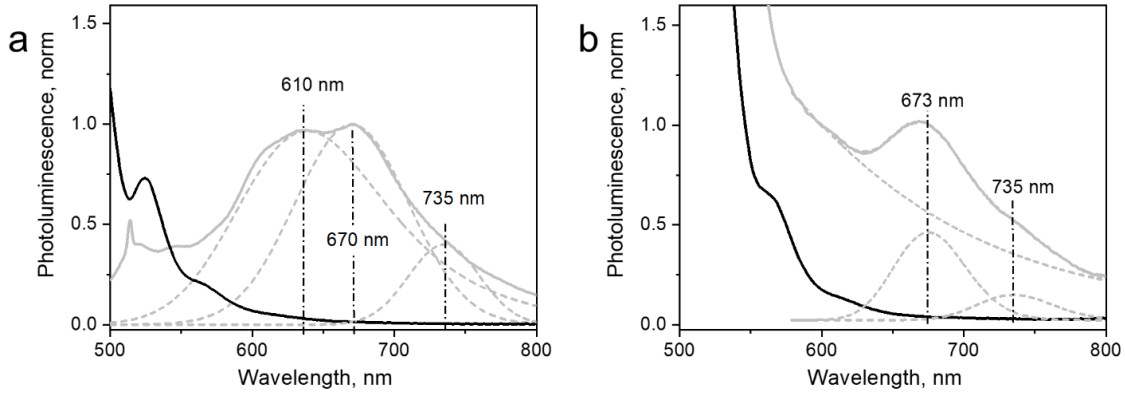

Figure 6-5. Photoluminescence of (a) dye-p1 and (b) dye-p2 at the temperature of 300 K (black line) and 20 K (grey line). Deconvolution of low-temperature photoluminescence using Gaussian peaks centred at 610 nm, 670 nm, and 735 nm for dye p1 and 673 nm and 735 nm for dye p2 (dash line).

To obtain additional information about triplet states of dye-**p1** and dye-**p2**, the emission spectra of their glassy solutions (in cyclohexane) were measured at low temperature (20 K). Assuming a small but non-zero probability of ISC, it was expected to detect phosphorescence of dye-**p1** and dye-**p2** at a low temperature. Figure 6-5 demonstrates a comparison of PL spectra collected at room temperature and 20 K. New emission bands appear in the low-temperature spectra with maxima at 670 nm and 735 nm for dye-**p1** and 674 nm and 735 nm for dye-**p2**. The appearance of these bands was attributed to the radiative $T_1 – S_0$ transition. These peaks' position is slightly blue-shifted compared with the position of T_1 state of 800 - 850 nm in the unsubstituted perylene molecule [250]. However, it is highly likely that the dye triplet with the T_1 energy of ~1.7 eV (740 nm) can be excited *via* the energy transfer process utilizing the energy of SiNCs with PL in the range 1.2 – 1.9 eV (650 – 1,000 nm).

6.5 Singlet oxygen generation by (C6)-(p1)-SiNCs and (C6)-(p2)-SiNCs

The dyes' chemical reaction with **H**- SiNCs yields a conjugation product that demonstrates both components' absorption. The PLE spectra of (**C6**)-(**p1**)-SiNCs (Figure 6-5) and (**C6**)-(**p2**)-SiNCs (Figure

6-4) confirm the dye attachment. The excitation of SiNCs becomes possible *via* dye excitation in the range of 400 – 450 nm, which indicates the very short distance between dyes and SiNCs. In contrast, the physical mixture of (**C6**)-SiNCs and the dyes do not demonstrate NIR luminescence when the sample is excited with blue light (400 – 450 nm).

It should be pointed out that the irradiation of (**C6**)-(**p1**)-SiNCs and (**C6**)-(**p2**)-SiNCs with 300 or 317.5, and 405 nm lasers excites different species. The 405 nm laser mainly excites the dye molecule anchored to the surface of SiNCs. In contrast, the 300 or 317.5 nm laser directly excites SiNCs as the dyes exhibit an absorption minimum at this wavelength. The results of the calculation with Equation 6.28 (using the data presented in Figure 6-6 and Table 3) indicate that (**C6**)-(**p2**)-SiNCs excited with 405 nm laser generate $^1O_2$ with $\Phi_\Delta = 27 \pm 5$ %. This quantum yield is lower than Φ_Δ of pure dye-**p2**. However, the experiment emphasizes that the (**C6**)-(**p2**)-SiNCs conjugate exhibits synergistic behaviour. Under blue light excitation at room temperature, the nanoparticles demonstrate NIR emission (originating from the SiNCs core) with PLQY of 15 ± 1 % and $^1O_2$ generation (originated from the anchored dye). Thus, this new conjugate can attract photomedicine's potential interest as a new chemical agent combining PS and NIR phosphor properties.

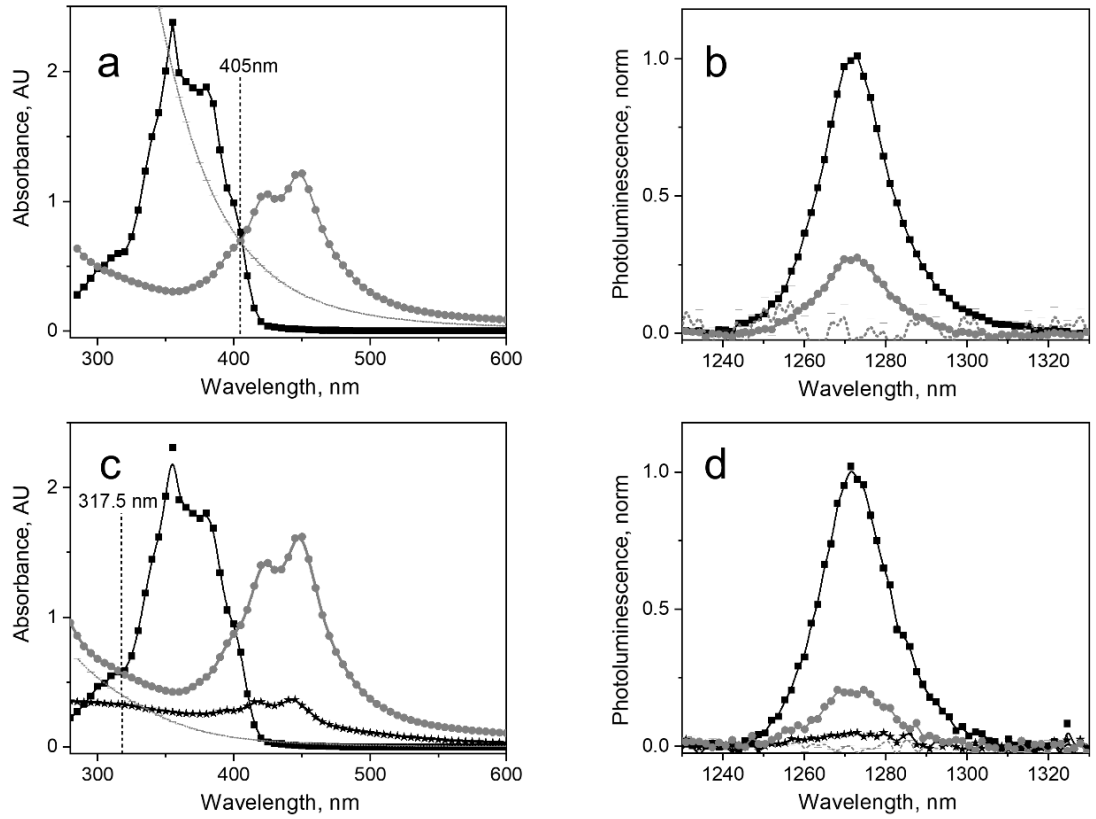

Figure 6-6. (a) UV-Vis absorption spectra of solutions of phen (■), (C6)-SiNCs (dash grey) and (C6)-(p2)-SiNCs (●) in cyclohexane used for the generation of $^1O_2$ with 405 nm laser; (b) $^1O_2$-phosphorescence via irradiation of solutions of phen (■), (C6)-SiNCs (dash grey) and (C6)-(p2)-SiNCs (●) with 405 nm laser (excitation intensity of 75 mW); (c) UV-Vis absorption spectra of solutions of phen (■), (C6)-SiNCs (dash grey), (C6)-(p1)-SiNCs (*)

and (C6)-(p2)-SiNCs (●) in cyclohexane used for the generation of 1O2 with 317.5 nm laser; (d) 1O2-phosphorescence excited via irradiation of solutions of phen, C6-SiNCs, C6-1-SiNCs and C6-2-SiNCs with 317.5 nm laser (excitation intensity of 45 mW).

The irradiation of (**C6**)-(**p2**)-SiNCs with the 317.5 nm laser should lead to selective excitation of SiNCs. To the best of our knowledge, the SiNCs synthesized from SiO_x are not able to generate $^1O_2$. Indeed, the excitation of (**C6**)-SiNCs with 317.5 and 405 nm lasers do not produce $^1O_2$ phosphorescence (Figure 6-6b and Figure 6-6d). However, the excitation of the (**C6**)-(**p2**)-SiNCs conjugate with the 317.5 nm laser results in $^1O_2$ phosphorescence with $\Phi_\Delta = 20 \pm 5$ %. The enhancement factor (F) of $^1O_2$ oxygen generation with UV light (317.5 nm) for (**C6**)-(**p2**)-SiNCs *vs.* dye-**p2** can be determined using Equation 6.30:

$$F = \frac{[\Phi_\Delta^{(C6)-1-SiNCs}]}{[\Phi_\Delta^{dye}]} \frac{[a_{(C6)-1-SiNCs}]}{[a_{dye}]} \quad (6.30)$$

Where it was assumed that two solutions (**C6**)-(**p2**)-SiNCs and dye-**p2**) were exhibiting similar absorbance at the 450 nm peak (the indication of similar perylene concentration); $\Phi_\Delta^{(C6)-(p2)-SiNCs}$ and Φ_Δ^{dye-p2} are quantum yields of $^1O_2$ generation measured at the 317.5 nm excitation for the (**C6**)-(**p2**)-SiNCs conjugate and dye-**p2**, respectively; $a_{(C6)-p2-SiNCs}$ and a_{dye-p2} are absorbance of the two solutions at 317.5 nm.

The enhancement factor $F = 2.3$ indicates that the solution with (**C6**)-(**p2**)-SiNCs is able to produce 2.3 times more $^1O_2$ then the solution with dye-**p2** with a similar concentration of perylene chromophore. The calculation of F was performed at 300 nm excitations. Furthermore, the results are enhancement factor F=2.1 for the solution of (**C6**)-(**p2**)-SiNCs and F=0.9 for the solution of (**C6**)-(**p1**)-SiNCs. From F-value, it can be seen that the enhancement factor for (**C6**)-(**p1**)-SiNCs was smaller compare with (**C6**)-(**p2**)-SiNCs. Thus, the (**C6**)-(**p2**)-SiNCs conjugate demonstrates the ability of efficient $^1O_2$ generation over an extensive spectral range utilizing the absorption of SiNCs (~300 – 350 nm) and the absorption of dye-**p2** (~350 – 460 nm)[293, 294, 334].

In the previous publication, energy transfer from SiNCs to the triplet state of dye-**p1** is found less efficient. This observation was also confirmed in the experiment with $^1O_2$ generation. The (**C6**)-(**p1**)-SiNCs conjugate exhibits significantly lower $\Phi_\Delta = 9 \pm 6$ % under excitation with UV light (317.5 nm) (Figure 6-7c, d**,** Table 3), and $\Phi_\Delta = 15 \pm 6$ % under UV excitation 300nm (Table 2).

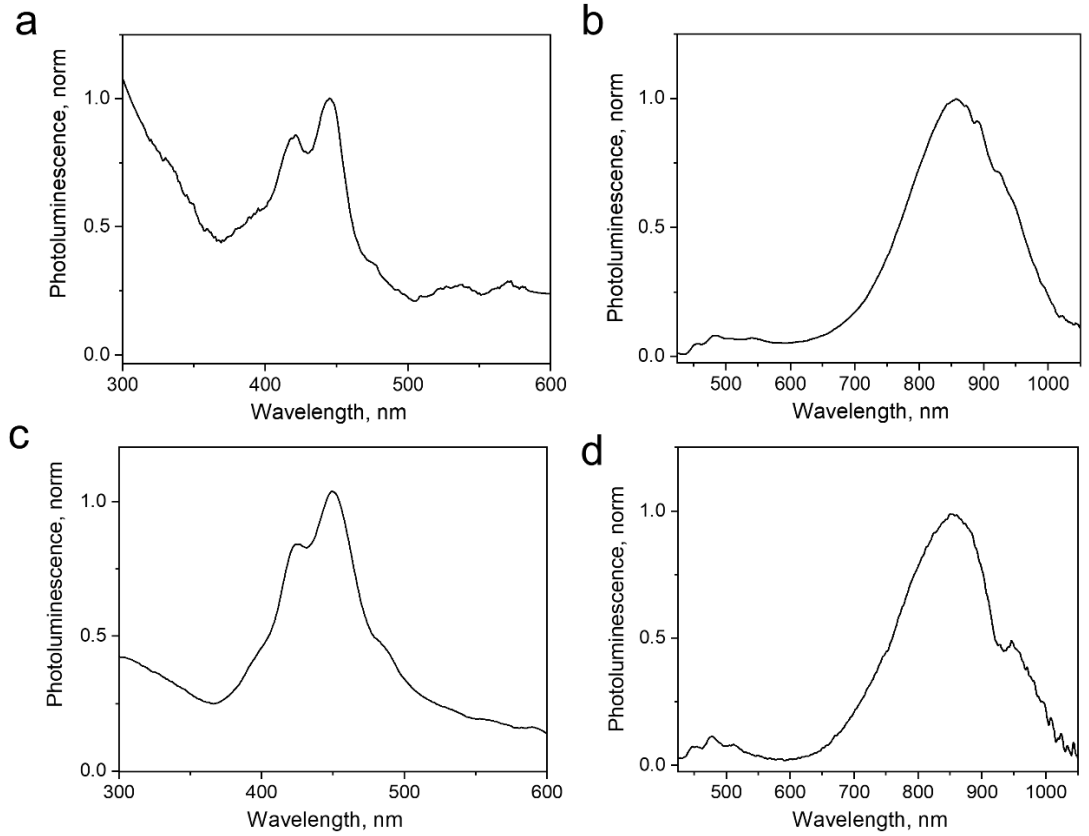

Figure 6-7. (a) The photoluminescence excitation spectrum of (C6)-(p1)-SiNCs conjugate. The intensity of photoluminescence at 800 nm was measured as a function of the excitation wavelength. The results indicate that NIR luminescence of SiNCs can be excited via the excitation of dye-p1. (b) Photoluminescence spectrum of (C6)-(p1)-SiNCs excited at 405 nm. The spectrum consists of weak luminescence of dye-p1 (420-500 nm) and strong luminescence of SiNCs (650 – 1,000 nm), (c) Photoluminescence excitation spectrum of (C6)-(p2)-SiNCs conjugate. The intensity of photoluminescence at 800 nm was measured as a function of the excitation wavelength. The results indicate that NIR luminescence of SiNCs can be excited via the excitation of dye-p2. (d) Photoluminescence spectrum of (C6)-(p2)-SiNCs excited at 405 nm. The spectrum consists of a weak luminescence of dye-p2 (420-500 nm) and a strong luminescence of SiNCs (650 – 1,000 nm).

6.6 Energy transfer from SiNCs to perylene chromophore

The schematic in Figure 6-8 displays a $^1O_2$ generation pathway under UV excitation of (**C6**)-(**p2**)-SiNCs. Under excitation with a 300 and 317.5 nm laser, the crystals emit NIR photons with 860 nm wavelength. At the same time, the excitation energy can be transferred to the triplet state of the dye. The triplet state interacts with molecular oxygen. The interaction produces $^1O_2$ that emits NIR photons with a wavelength of 1,270 nm with the overall quantum efficiency of $^1O_2$ production around 20-24%[326].

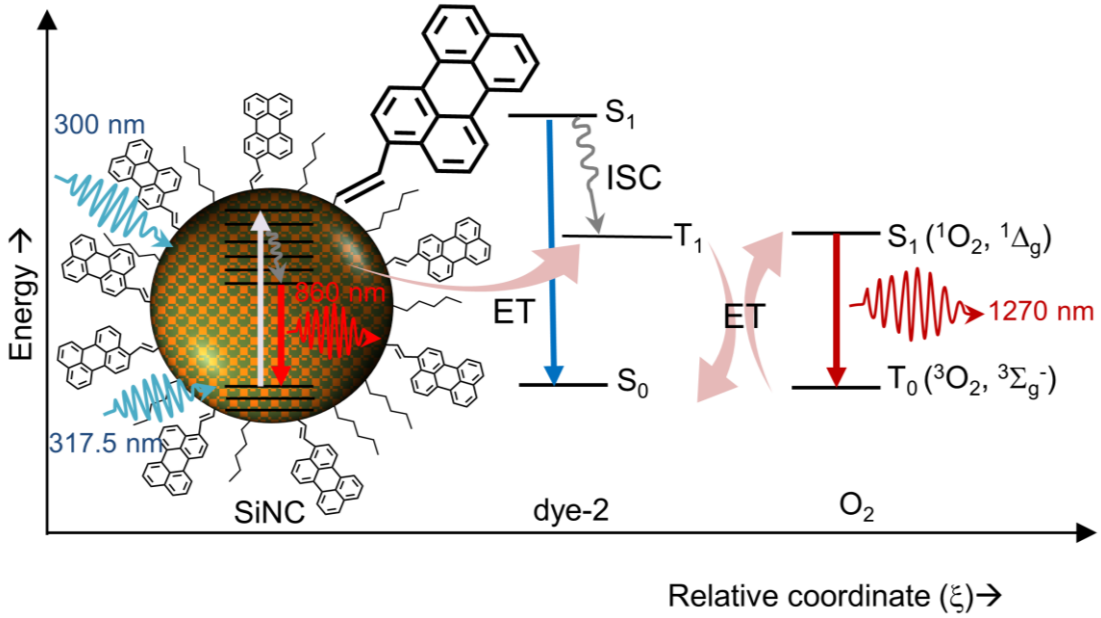

Figure 6-8. Schematic showing photosensitization of $^1O^2$ with SiNCs using the attached dye as a transmitter for the excitation energy.

Finally, the efficiency of energy transfer (η_{ET}) from the SiNC core to the perylene chromophore was able to evaluate using Φ_Δ calculations. At 300 and 317.5 nm excitations, the efficient energy transfer can be calculated using Equation 6.31, and the values contained in Table 2 and Table 3:

$$\eta_{ET} = \frac{\left[\Phi_\Delta^{300nm/317.5nm}\right] - \left[P_{dye}^{300nm/317.5nm}\right]\left[\Phi_\Delta^{405nm}\right]}{\left[P_{SiNCs}^{300/317.5nm}\right]\left[\Phi_\Delta^{405nm}\right]} \qquad (6.31)$$

where η_{ET} is energy transfer efficiency from SiNCs to attached dyes, $[\Phi_\Delta^{300nm}]$= 24 % and $\left[\Phi_\Delta^{317.5nm}\right]$= 20 % is the quantum yield of $^1O_2$ generation by (**C6**)-(**2p)**-SiNCs under 300 and 317.5 nm excitations; $\left[\Phi_\Delta^{405nm}\right]$= 27 % and 50% are the quantum yield of $^1O_2$ generation by (**C6**)-(**p2**)-SiNCs under 405 nm excitation; $\left[P_{dye}^{300nm}\right] = 15\%$ and $\left[P_{dye}^{317.5nm}\right]$= 24 %, are a part of the excitation light (with a wavelength of 300 and 317.5 nm) absorbed by the dye; $[P_{SiNCs}^{300nm}]$= 85 % and $\left[P_{SiNCs}^{317.5nm}\right]$= 76 % are part of the excitation light (with a wavelength of 300 and 317.5 nm) absorbed by the SiNC core.

The calculation of η_{ET} in Equation 6.26 gives a value of 39% and 66 % for (**C6**)-(**p2**)-SiNCs using chemical and phosphorescent methods. Whereas the value of 53% was calculated for (**C6**)-(**p1**)-SiNCs using a chemical method. This value is in agreement with the value of η_{ET} of 55 % calculated using PL lifetimes of the NIR emission of (**C6**)-SiNCs and (**C6**)-(**p2**)-SiNCs nanocrystals[326].

7 Conclusions and outlook

7.1 Conclusions

To conclude, the SiO_x precursor's thermal annealing shows the formation of SiNCs whose embedded in the silica matrices and can be observed by FTIR and XRD. The crystallite size of embedded SiNC was ~3.8-4.0 nm determined using the Scherrer method. The silica matrices had been removed by HF etching to produce H-SiNCs. Longer etching time tended to reduce the particle size of SiNCs. In addition, NH_4F etching at an equivalent fluoride ratio works at a similar rate with HF to etch SiNCs. At the same time, MeOH/KOH etching methods produce SiNCs whose photophysical properties resemble ethylene glycol functionalization SiNCs (EG-SiNCs). The photophysical properties of H-SiNCs are not stable and prone to oxidation. Alkyl functionalization is carried out to passivate the surface of SiNCs, improve PLQY and photophysical stability, and to prevent the reaction with oxygen molecules. Alkyl functionalization is performed using hydrosilylation reaction. To my experience, hydrosilylation reaction using CTH enables to produce (C10)-SiNCs with PLQY value maximum ~26% for one best ensemble of size separated sample. The size separation *via* selective precipitation has been used to separate particle size from ~2.0 nm to ~12.0 nm and monitored by DLS measurement and PL-maxima position. PL-emission of (C10) functionalized SiNCs locate in the red to near-infrared spectra of electromagnetic radiation (600-1000 nm wavelength range). The position of PL-maxima of (C10)-SiNCs could be varied and highly depends on the particle size of SiNCs. Hence, the emission of (C10)-SiNCs are size dependence and following quantum confinement theory. In the attempt to modify surface coverage in order to enhance PLQY and photophysical stability, different lengths of alkyl chain length have been anchored covalently to SiNCs. The reactions were performed using MWH hydrosilylation because it has some advantages compared with CTH. Hydrosilylation reaction using MWH works faster, and resulting in SiNCs have higher PLQY (PLQY~27% for batch sample) compare with hydrosilylation reaction using CTH (PLQY~5% for batch sample) of (C10)-SiNCs. MWH in a short time of 20 minutes allows getting Si-NCs with a high PLQY of ~41% for short alkyl-SiNCs at an emission maximum of ~850 nm. The highest PLQY is achieved through functionalization with allyl, methyl ether – the shortest ligand among investigated alkenes (**C3**). An increase of PLQY in capping with shortest ligands was attributed to reducing long-range electronic-to-vibrational energy transfer from NCs to matrix vibrational overtones. Furthermore, SiNCs prepared from silicon monoxide SiO_x bear a sufficient number of surface defects associated with deformed Si–O–Si bonds, which can intrinsically limit the values of PLQY prepared form this type of precursor. Meanwhile, MWH results in highly luminescent Si-NCs with long shelf-life (> 6 months) at the ambient conditions.

A two-step hydrosilylation reaction performed in an MW reactor allowed us to attach functional dyes (perylene and BODIPY) to the surface of SiNCs. A low amount of the functional dyes (2 mg) was used in the hydrosilylation reaction in order to achieve 13-fold absorption enhancement at 440 nm for (C6)-(p2)-SiNCs (perylene-SiNCs) and 3-fold absorption enchantment at 515 nm for (C6)-(bp)-SiNCs

(BODIPY-SiNCs). The efficient direct energy transfer from perylene (η_{DET} = 99 %) and BODIPY (η_{DET} = 99 %) chromophores to SiNC was measured. The overall PL enhancement of 280 % and 200 % demonstrated blue- and green-light excitation of the modified SiNCs, respectively. The synthesis of stable SiNCs with enhanced NIR PL excited with visible light paves the way for applications of this abundant and non-toxic material in the field of solar energy harvesting, optical sensing, and bioimaging.

The SiNC-dye conjugates were investigated for the first time within the context of singlet oxygen generation. The singlet oxygen yield was determined *via* chemical methods and measurements of singlet oxygen phosphorescence (at 1,270 nm) in cyclohexane solutions using the comparison with the singlet oxygen phosphorescence produced by the reference PS – **phen**. In the chemical method, the Φ_Δ values were estimated for two excitation wavelengths: 300 nm and 405 nm excitations, whereas in the singlet oxygen phosphorescence method, the Φ_Δ values were estimated for two excitation wavelengths: 317.5 nm at 405 nm. The calculation of Φ_Δ for the (**C6**)-(**p1**)-SiNCs *via* chemical method exhibits $\Phi_\Delta = 15 \pm 6\%$ and $\Phi_\Delta = 23 \pm 6\%$ for 300 and 405 nm excitations. Whereas calculation of Φ_Δ for (**C6**)-(**p2**)-SiNCs exhibits $\Phi_\Delta = 24 \pm 6\%$ and $\Phi_\Delta = 50 \pm 6\%$ for the same excitations wavelength. Meanwhile, the calculation of (**C6**)-(**p2**)-SiNCs *via* phosphorescent method exhibits $\Phi_\Delta = 27 \pm 5\%$ and $\Phi_\Delta = 20 \pm 5\%$ for 405 nm and 317.5 nm excitations, respectively. Whereas the dye – **p1** is a less efficient acceptor for SiNCs. As a result, the Φ_Δ value of the (**C6**)-(**p1**)-SiNCs conjugates is smaller (Φ_Δ=9 ± 6 %) than (**C6**)-(**p2**)-SiNCs. Thus, this finding indicates an enormous potential of the dye modified SiNCs for the production of singlet oxygen.

7.2 Outlook

Finally, many works need to be done in the field of SiNCs research. So far, in our experiences, some weaknesses could be improved in future work:

1. The commercial silicon monoxide precursor is far from ideal for synthesis because some left-over internal oxide is embedded inside the structure. From FTIR spectra, it can be observed that the peaks Si-O at 1,000-1,200 cm^{-1} and the characteristics peak Si-O at 1,250 cm^{-1} always appeared in the product. This embedded oxide was confined in the crystalline structure, so prolonging the etching time does not work well to remove it. So far, we are not successful in removing it entirely. We proposed that our PLQY results were below the highest reported value (60%) due to this embedded oxide. It is an opportunity to look for another precursor or another method to improve the process.
2. High concentration hydrogen fluoride worked fine but working with high concentration HF is very risky. It is an excellent opportunity to find similar etching chemicals that work as well as HF, but are safe to handle. We had initiated working with NH_4F and KOH, and it is a breakthrough invention to develop another etching agent.
3. Alkyl functionalized SiNCs with different lengths of carbon atom had worked perfectly in passivating SiNCs. However, the disadvantage of alkyl-SiNCs is solubility in the polar solvent and water. There are some reports on micellar embedded alkyl-SiNCs in the protein/water, but the dispersions' PL-emissions

and stability remain in question. It is an excellent opportunity to have conjugate water-soluble ligands-SiNCs with high PLQY values and having long-time stability in water. Because in the future, one of the advancements of SiNCs is in the medical fields. Hence, SiNCs must be soluble/dispersible in water for medical applications.

4. Thus far, the fabrication of SiNCs is mainly on a laboratory scale. It is an excellent opportunity to scale up the synthesis in order to accommodate industrial demands. One opportunity is by using ball-mill synthesis from the element of silicon.
5. Optimized functionalization of dye-SiNCs could be another research field in the future. There are some reports on the light-harvesting method using dye functionalized SiNCs, the SiNCs based on upconverting and downconverting materials, and SiNCs based photosensitizers.

References

1. Ekimov, A.I. and A.A. Onushchenko, *Quantum Size Effect in 3-Dimensional Microscopic Semiconductor Crystals.* JETP Letters, 1981. **34**(6): p. 345-349.
2. Ekimov, A.I. and A.A. Onushchenko, *Size Quantization of the Electron-Energy Spectrum in a Microscopic Semiconductor Crystal.* JETP Letters, 1984. **40**(8): p. 1136-1139.
3. Smith, A.M. and S.M. Nie, *Semiconductor Nanocrystals: Structure, Properties, and Band Gap Engineering.* Accounts of Chemical Research, 2010. **43**(2): p. 190-200.
4. Efros, A.L., *Quantum dots realize their potential.* Nature, 2019. **575**(7784): p. 604-605.
5. Skryshevsky, V.A., T. Serdiuk, Y.E. Zakharko, S.A. Alekseev, A. Géloën, and V. Lysenko, *Preparation, Luminescent Properties and Bioimaging Application of Quantum Dots Based on Si and SiC*, in *Functional Nanomaterials and Devices for Electronics, Sensors and Energy Harvesting*, A. Nazarov, F. Balestra, V. Kilchytska, and D. Flandre, Editors. 2014, Springer International Publishing: Cham. p. 323-348.
6. Shaikh, J.S., N.S. Shaikh, S.S. Mali, J.V. Patil, S.A. Beknalkar, A.P. Patil, N.L. Tarwal, P. Kanjanaboos, C.K. Hong, and P.S. Patil, *Quantum Dot Based Solar Cells: Role of Nanoarchitectures, Perovskite Quantum Dots, and Charge-Transporting Layers.* ChemSusChem, 2019. **12**(21): p. 4724-4753.
7. Rühle, S., *Tabulated values of the Shockley–Queisser limit for single junction solar cells.* Solar Energy, 2016. **130**: p. 139-147.
8. Semonin, O.E., J.M. Luther, S. Choi, H.-Y. Chen, J. Gao, A.J. Nozik, and M.C. Beard, *Peak External Photocurrent Quantum Efficiency Exceeding 100% via MEG in a Quantum Dot Solar Cell.* Science, 2011. **334**(6062): p. 1530-1533.
9. Kamat, P.V., *Quantum Dot Solar Cells. Semiconductor Nanocrystals as Light Harvesters.* The Journal of Physical Chemistry C, 2008. **112**(48): p. 18737-18753.
10. Lan, X., O. Voznyy, A. Kiani, F.P. García de Arquer, A.S. Abbas, G.-H. Kim, M. Liu, Z. Yang, G. Walters, J. Xu, M. Yuan, Z. Ning, F. Fan, P. Kanjanaboos, I. Kramer, D. Zhitomirsky, P. Lee, A. Perelgut, S. Hoogland, and E.H. Sargent, *Passivation Using Molecular Halides Increases Quantum Dot Solar Cell Performance.* Advanced Materials, 2016. **28**(2): p. 299-304.
11. Xu, J., O. Voznyy, M. Liu, A.R. Kirmani, G. Walters, R. Munir, M. Abdelsamie, A.H. Proppe, A. Sarkar, F.P. García de Arquer, M. Wei, B. Sun, M. Liu, O. Ouellette, R. Quintero-Bermudez, J. Li, J. Fan, L. Quan, P. Todorovic, H. Tan, S. Hoogland, S.O. Kelley, M. Stefik, A. Amassian, and E.H. Sargent, *2D matrix engineering for homogeneous quantum dot coupling in photovoltaic solids.* Nature Nanotechnology, 2018. **13**(6): p. 456-462.
12. Hu, L., C. Zhang, G. Zeng, G. Chen, J. Wan, Z. Guo, H. Wu, Z. Yu, Y. Zhou, and J. Liu, *Metal-based quantum dots: synthesis, surface modification, transport and fate in aquatic environments and toxicity to microorganisms.* RSC Advances, 2016. **6**(82): p. 78595-78610.
13. Wood, V., M.J. Panzer, J.E. Halpert, J.M. Caruge, M.G. Bawendi, and V. Bulović, *Selection of Metal Oxide Charge Transport Layers for Colloidal Quantum Dot LEDs.* ACS Nano, 2009. **3**(11): p. 3581-3586.
14. Bozyigit, D., O. Yarema, and V. Wood, *Origins of Low Quantum Efficiencies in Quantum Dot LEDs.* Advanced Functional Materials, 2013. **23**(24): p. 3024-3029.
15. Zhu, X., L. Bian, H. Fu, L. Wang, B. Zou, Q. Dai, J. Zhang, and H. Zhong, *Broadband perovskite quantum dot spectrometer beyond human visual resolution.* Light: Science & Applications, 2020. **9**(1): p. 73.
16. Chen, X., Y. Liu, and Q. Ma, *Recent advances in quantum dot-based electrochemiluminescence sensors.* Journal of Materials Chemistry C, 2018. **6**(5): p. 942-959.
17. Cui, L., X.P. He, and G.R. Chen, *Recent progress in quantum dot based sensors.* RSC Advances, 2015. **5**(34): p. 26644-26653.
18. Biju, V., Y. Makita, A. Sonoda, H. Yokoyama, Y. Baba, and M. Ishikawa, *Temperature-Sensitive Photoluminescence of CdSe Quantum Dot Clusters.* The Journal of Physical Chemistry B, 2005. **109**(29): p. 13899-13905.
19. Chen, Y., W. Luan, S. Zhang, and F. Yang, *Quantum-dots based materials for temperature sensing: effect of cyclic heating-cooling on fluorescence.* Journal of Nanoparticle Research, 2019. **21**(8): p. 185.

20. Hajjaji, H., S. Alekseev, G. Guillot, N.P. Blanchard, V. Monnier, Y. Chevolot, G. Brémond, M. Querry, D. Philippon, P. Vergne, and J.M. Bluet, *Luminescence nanothermometry with alkyl-capped silicon nanoparticles dispersed in nonpolar liquids.* Nanoscale Research Letters, 2014. **9**(1): p. 94.
21. Bueno, A., I. Suarez, R. Abargues, S. Sales, and J.P.M. Pastor, *Temperature Sensor Based on Colloidal Quantum Dots–PMMA Nanocomposite Waveguides.* IEEE Sensors Journal, 2012. **12**(10): p. 3069-3074.
22. Li, Q., Y.P. Zheng, X.M. Hou, T. Yang, T.X. Liang, and J.J. Zheng, *A wide range photoluminescence intensity-based temperature sensor developed with BN quantum dots and the photoluminescence mechanism.* Sensors and Actuators B-Chemical, 2020. **304**: p. 127353.
23. Guo, M.R., W.C. Law, X. Liu, H.X. Cai, L.W. Liu, M. Swihart, X.H. Zhang, and P.N. Prasad, *Plasmonic Semiconductor Nanocrystals as Chemical Sensors: Pb2+ Quantitation via Aggregation-Induced Plasmon Resonance Shift.* Plasmonics, 2014. **9**(4): p. 893-898.
24. Frasco, M.F. and N. Chaniotakis, *Semiconductor quantum dots in chemical sensors and biosensors.* Sensors (Basel), 2009. **9**(9): p. 7266-86.
25. Moon, H., C. Lee, W. Lee, J. Kim, and H. Chae, *Stability of Quantum Dots, Quantum Dot Films, and Quantum Dot Light-Emitting Diodes for Display Applications.* Advanced Materials, 2019. **31**(34): p. 1804294.
26. Xia, H., J. Hu, J. Tang, K. Xu, X. Hou, and P. Wu, *A RGB-Type Quantum Dot-based Sensor Array for Sensitive Visual Detection of Trace Formaldehyde in Air.* Scientific Reports, 2016. **6**(1): p. 36794.
27. Tajarrod, N., M.K. Rofouei, M. Masteri-Farahani, and R. Zadmard, *A quantum dot-based fluorescence sensor for sensitive and enzymeless detection of creatinine.* Analytical Methods, 2016. **8**(30): p. 5911-5920.
28. Molaei, M.J., *Principles, mechanisms, and application of carbon quantum dots in sensors: a review.* Analytical Methods, 2020. **12**(10): p. 1266-1287.
29. Matea, C.T., T. Mocan, F. Tabaran, T. Pop, O. Mosteanu, C. Puia, C. Iancu, and L. Mocan, *Quantum dots in imaging, drug delivery and sensor applications.* International Journal of Nanomedicine, 2017. **12**: p. 5421-5431.
30. Medintz, I.L., H.T. Uyeda, E.R. Goldman, and H. Mattoussi, *Quantum dot bioconjugates for imaging, labelling and sensing.* Nature Materials, 2005. **4**(6): p. 435-446.
31. Lesiak, A., K. Drzozga, J. Cabaj, M. Bański, K. Malecha, and A. Podhorodecki, *Optical Sensors Based on II-VI Quantum Dots.* Nanomaterials (Basel, Switzerland), 2019. **9**(2): p. 192.
32. Tsolekile, N., S. Parani, M.C. Matoetoe, S.P. Songca, and O.S. Oluwafemi, *Evolution of ternary I–III–VI QDs: Synthesis, characterization and application.* Nano-Structures & Nano-Objects, 2017. **12**: p. 46-56.
33. Fitzmorris, R.C., R.P. Oleksak, Z. Zhou, B.D. Mangum, J.N. Kurtin, and G.S. Herman, *Structural and optical characterization of CuInS2 quantum dots synthesized by microwave-assisted continuous flow methods.* Journal of Nanoparticle Research, 2015. **17**(7): p. 319.
34. Chang, J.-Y., G.-R. Chen, and J.-D. Li, *Synthesis of magnetofluorescence Gd-doped CuInS2/ZnS quantum dots with enhanced longitudinal relaxivity.* Physical Chemistry Chemical Physics, 2016. **18**(10): p. 7132-7140.
35. Shao, L.J., Y.F. Gao, and F. Yan, *Semiconductor Quantum Dots for Biomedicial Applications.* Sensors, 2011. **11**(12): p. 11736-11751.
36. Reiss, P., M. Protiere, and L. Li, *Core/Shell Semiconductor Nanocrystals.* Small, 2009. **5**(2): p. 154-168.
37. Priolo, F., T. Gregorkiewicz, M. Galli, and T.F. Krauss, *Silicon nanostructures for photonics and photovoltaics.* Nature Nanotechnology, 2014. **9**(1): p. 19-32.
38. Hardman, R., *A toxicologic review of quantum dots: toxicity depends on physicochemical and environmental factors.* Environ Health Perspect, 2006. **114**(2): p. 165-72.
39. Godt, J., F. Scheidig, C. Grosse-Siestrup, V. Esche, P. Brandenburg, A. Reich, and D.A. Groneberg, *The toxicity of cadmium and resulting hazards for human health.* J Occup Med Toxicol, 2006. **1**: p. 22.
40. Filali, S., F. Pirot, and P. Miossec, *Biological Applications and Toxicity Minimization of Semiconductor Quantum Dots.* Trends in Biotechnology, 2020. **38**(2): p. 163-177.
41. Hardman, R., *A toxicologic review of quantum dots: toxicity depends on physicochemical and environmental factors.* Environmental health perspectives, 2006. **114**(2): p. 165-172.

42. Valizadeh, A., H. Mikaeili, M. Samiei, S.M. Farkhani, N. Zarghami, M. kouhi, A. Akbarzadeh, and S. Davaran, *Quantum dots: synthesis, bioapplications, and toxicity.* Nanoscale Research Letters, 2012. **7**(1): p. 480.
43. Liu, J., F. Erogbogbo, K.-T. Yong, L. Ye, J. Liu, R. Hu, H. Chen, Y. Hu, Y. Yang, J. Yang, I. Roy, N.A. Karker, M.T. Swihart, and P.N. Prasad, *Assessing Clinical Prospects of Silicon Quantum Dots: Studies in Mice and Monkeys.* ACS Nano, 2013. **7**(8): p. 7303-7310.
44. Erogbogbo, F., K.-T. Yong, I. Roy, G. Xu, P.N. Prasad, and M.T. Swihart, *Biocompatible luminescent silicon quantum dots for imaging of cancer cells.* ACS nano, 2008. **2**(5): p. 873-878.
45. Canham, L.T., *Silicon quantum wire array fabrication by electrochemical and chemical dissolution of wafers.* Applied Physics Letters, 1990. **57**(10): p. 1046-1048.
46. Canham, L., *Introductory lecture: origins and applications of efficient visible photoluminescence from silicon-based nanostructures.* Faraday Discussions, 2020. **222**(0): p. 10-81.
47. Shu, Y. and B.G. Levine, *First-Principles Study of Nonradiative Recombination in Silicon Nanocrystals: The Role of Surface Silanol.* The Journal of Physical Chemistry C, 2016. **120**(40): p. 23246-23253.
48. Pavesi, L., L. Dal Negro, C. Mazzoleni, G. Franzò, and F. Priolo, *Optical gain in silicon nanocrystals.* Nature, 2000. **408**(6811): p. 440-444.
49. Berends, A.C., F.T. Rabouw, F.C.M. Spoor, E. Bladt, F.C. Grozema, A.J. Houtepen, L.D.A. Siebbeles, and C. de Mello Donegá, *Radiative and Nonradiative Recombination in CuInS2 Nanocrystals and CuInS2-Based Core/Shell Nanocrystals.* The Journal of Physical Chemistry Letters, 2016. **7**(17): p. 3503-3509.
50. Canham, L., *Silicon Optoelectronics at the End of the Rainbow.* Physics World, 1992. **5**(3): p. 41-44.
51. Hannah, D.C., J. Yang, P. Podsiadlo, M.K.Y. Chan, A. Demortière, D.J. Gosztola, V.B. Prakapenka, G.C. Schatz, U. Kortshagen, and R.D. Schaller, *On the Origin of Photoluminescence in Silicon Nanocrystals: Pressure-Dependent Structural and Optical Studies.* Nano Letters, 2012. **12**(8): p. 4200-4205.
52. Sinelnikov, R., M. Dasog, J. Beamish, A. Meldrum, and J.G.C. Veinot, *Revisiting an Ongoing Debate: What Role Do Surface Groups Play in Silicon Nanocrystal Photoluminescence?* ACS Photonics, 2017. **4**(8): p. 1920-1929.
53. Heitmann, J., F. Müller, M. Zacharias, and U. Gösele, *Silicon Nanocrystals: Size Matters.* Advanced Materials, 2005. **17**(7): p. 795-803.
54. Şahin, M. and M. Tomak, *Electronic structure of a many-electron spherical quantum dot with an impurity.* Physical Review B, 2005. **72**(12): p. 125323.
55. Reimann, S.M. and M. Manninen, *Electronic structure of quantum dots.* Reviews of Modern Physics, 2002. **74**(4): p. 1283-1342.
56. Kůsová, K., *Silicon Nanocrystals: From Indirect to Direct Bandgap.* physica status solidi (a), 2018. **215**(7): p. 1700718.
57. Fernée, M.J., P. Tamarat, and B. Lounis, *Cryogenic Single-Nanocrystal Spectroscopy: Reading the Spectral Fingerprint of Individual CdSe Quantum Dots.* The Journal of Physical Chemistry Letters, 2013. **4**(4): p. 609-618.
58. Sychugov, I., A. Fucikova, F. Pevere, Z. Yang, J.G.C. Veinot, and J. Linnros, *Ultranarrow Luminescence Linewidth of Silicon Nanocrystals and Influence of Matrix.* ACS Photonics, 2014. **1**(10): p. 998-1005.
59. Fu, H., L.-W. Wang, and A. Zunger, *Applicability of the $\mathbf{k}\ensuremath{\cdot}\mathbf{p}$ method to the electronic structure of quantum dots.* Physical Review B, 1998. **57**(16): p. 9971-9987.
60. Belyakov, V.A., V.A. Burdov, R. Lockwood, and A. Meldrum, *Silicon Nanocrystals: Fundamental Theory and Implications for Stimulated Emission.* Advances in Optical Technologies, 2008. **2008**.
61. Malyutenko, V.K., V.V. Bogatyrenko, and O.Y. Malyutenko, *Radiative cooling of bulk Si by optical down-conversion.* Journal of Applied Physics, 2010. **108**(7): p. 073104.
62. Rabouw, F.T., R. Vaxenburg, A.A. Bakulin, R.J.A. van Dijk-Moes, H.J. Bakker, A. Rodina, E. Lifshitz, A.L. Efros, A.F. Koenderink, and D. Vanmaekelbergh, *Dynamics of Intraband and Interband Auger Processes in Colloidal Core–Shell Quantum Dots.* ACS Nano, 2015. **9**(10): p. 10366-10376.

63. Hintermayr, V.A., L. Polavarapu, A.S. Urban, and J. Feldmann, *Accelerated Carrier Relaxation through Reduced Coulomb Screening in Two-Dimensional Halide Perovskite Nanoplatelets.* ACS Nano, 2018. **12**(10): p. 10151-10158.
64. Delerue, C., G. Allan, and M. Lannoo, *Theoretical aspects of the luminescence of porous silicon.* Physical Review B, 1993. **48**(15): p. 11024-11036.
65. Haken, H., *On the theory of excitons in solids.* Journal of Physics and Chemistry of Solids, 1959. **8**: p. 166-171.
66. Ray, S.K., S. Maikap, W. Banerjee, and S. Das, *Nanocrystals for silicon-based light-emitting and memory devices.* Journal of Physics D: Applied Physics, 2013. **46**(15): p. 153001.
67. Rontani, M., F. Rossi, F. Manghi, and E. Molinari, *Coulomb correlation effects in semiconductor quantum dots: The role of dimensionality.* Physical Review B, 1999. **59**(15): p. 10165-10175.
68. Pejova, B. and I. Grozdanov, *Three-dimensional confinement effects in semiconducting zinc selenide quantum dots deposited in thin-film form.* Materials Chemistry and Physics, 2005. **90**(1): p. 35-46.
69. Wang, L.W. and A. Zunger, *Solving Schrödinger's equation around a desired energy: Application to silicon quantum dots.* The Journal of Chemical Physics, 1994. **100**(3): p. 2394-2397.
70. Brus, L., *Luminescence of Silicon Materials: Chains, Sheets, Nanocrystals, Nanowires, Microcrystals, and Porous Silicon.* The Journal of Physical Chemistry, 1994. **98**(14): p. 3575-3581.
71. Liu, X., Y. Zhang, T. Yu, X. Qiao, R. Gresback, X. Pi, and D. Yang, *Optimum Quantum Yield of the Light Emission from 2 to 10 nm Hydrosilylated Silicon Quantum Dots.* Particle & Particle Systems Characterization, 2016. **33**(1): p. 44-52.
72. Hessel, C.M., D. Reid, M.G. Panthani, M.R. Rasch, B.W. Goodfellow, J. Wei, H. Fujii, V. Akhavan, and B.A. Korgel, *Synthesis of Ligand-Stabilized Silicon Nanocrystals with Size-Dependent Photoluminescence Spanning Visible to Near-Infrared Wavelengths.* Chemistry of Materials, 2012. **24**(2): p. 393-401.
73. Yu, Y., G. Fan, A. Fermi, R. Mazzaro, V. Morandi, P. Ceroni, D.-M. Smilgies, and B.A. Korgel, *Size-Dependent Photoluminescence Efficiency of Silicon Nanocrystal Quantum Dots.* The Journal of Physical Chemistry C, 2017. **121**(41): p. 23240-23248.
74. Öğüt, S., J.R. Chelikowsky, and S.G. Louie, *Quantum Confinement and Optical Gaps in Si Nanocrystals.* Physical Review Letters, 1997. **79**(9): p. 1770-1773.
75. Green, M.A., J. Zhao, A. Wang, P.J. Reece, and M. Gal, *Efficient silicon light-emitting diodes.* Nature, 2001. **412**(6849): p. 805-808.
76. Proot, J.P., C. Delerue, and G. Allan, *Electronic structure and optical properties of silicon crystallites: Application to porous silicon.* Applied Physics Letters, 1992. **61**(16): p. 1948-1950.
77. Ledoux, G., J. Gong, F. Huisken, O. Guillois, and C. Reynaud, *Photoluminescence of size-separated silicon nanocrystals: Confirmation of quantum confinement.* Applied Physics Letters, 2002. **80**(25): p. 4834-4836.
78. Ledoux, G., O. Guillois, D. Porterat, C. Reynaud, F. Huisken, B. Kohn, and V. Paillard, *Photoluminescence properties of silicon nanocrystals as a function of their size.* Physical Review B, 2000. **62**(23): p. 15942-15951.
79. Hill, N.A. and K.B. Whaley, *Size Dependence of Excitons in Silicon Nanocrystals.* Physical Review Letters, 1995. **75**(6): p. 1130-1133.
80. Hill, N.A. and K.B. Whaley, *A theoretical study of light emission from nanoscale silicon.* Journal of Electronic Materials, 1996. **25**(2): p. 269-285.
81. Thiessen, A.N., L. Zhang, A.O. Oliynyk, H. Yu, K.M. O'Connor, A. Meldrum, and J.G.C. Veinot, *A Tale of Seemingly "Identical" Silicon Quantum Dot Families: Structural Insight into Silicon Quantum Dot Photoluminescence.* Chemistry of Materials, 2020. **32**(16): p. 6838-6846.
82. Furukawa, S. and T. Miyasato, *Quantum size effects on the optical band gap of microcrystalline Si:H.* Physical Review B, 1988. **38**(8): p. 5726-5729.
83. Mastronardi, M.L., F. Maier-Flaig, D. Faulkner, E.J. Henderson, C. Kübel, U. Lemmer, and G.A. Ozin, *Size-Dependent Absolute Quantum Yields for Size-Separated Colloidally-Stable Silicon Nanocrystals.* Nano Letters, 2012. **12**(1): p. 337-342.
84. Hessel, C.M., E.J. Henderson, and J.G.C. Veinot, *An Investigation of the Formation and Growth of Oxide-Embedded Silicon Nanocrystals in Hydrogen Silsesquioxane-Derived Nanocomposites.* The Journal of Physical Chemistry C, 2007. **111**(19): p. 6956-6961.

85. Beri, D., D. Busko, A. Mazilkin, I.A. Howard, B.S. Richards, and A. Turshatov, *Highly photoluminescent and stable silicon nanocrystals functionalized via microwave-assisted hydrosilylation.* RSC Advances, 2018. **8**(18): p. 9979-9984.
86. Sun, W., C.X. Qian, L.W. Wang, M. Wei, M.L. Mastronardi, G. Casillas, J. Breu, and G.A. Ozin, *Switching-On Quantum Size Effects in Silicon Nanocrystals.* Advanced Materials, 2015. **27**(4): p. 746-749.
87. Sun, W., C. Qian, K.K. Chen, and G.A. Ozin, *Silicon Nanocrystals: It's Simply a Matter of Size.* ChemNanoMat, 2016. **2**(9): p. 847-855.
88. Sun, W., C. Qian, X.S. Cui, L. Wang, M. Wei, G. Casillas, A.S. Helmy, and G.A. Ozin, *Silicon monoxide--a convenient precursor for large scale synthesis of near infrared emitting monodisperse silicon nanocrystals.* Nanoscale, 2016. **8**(6): p. 3678-84.
89. Sun, W., C. Qian, L. Wang, M. Wei, M.L. Mastronardi, G. Casillas, J. Breu, and G.A. Ozin, *Switching-On Quantum Size Effects in Silicon Nanocrystals.* Advanced Materials, 2015. **27**(4): p. 746-749.
90. Mastronardi, M.L., F. Maier-Flaig, D. Faulkner, E.J. Henderson, C. Kubel, U. Lemmer, and G.A. Ozin, *Size-Dependent Absolute Quantum Yields for Size-Separated Colloidally-Stable Silicon Nanocrystals.* Nano Letters, 2012. **12**(1): p. 337-342.
91. Poddubny, A.N. and K. Dohnalová, *Direct band gap silicon quantum dots achieved via electronegative capping.* Physical Review B, 2014. **90**(24).
92. Chung, N.X., R. Limpens, and T. Gregorkiewicz, *Photoluminescence Quantum Yield in Ensembles of Si Nanocrystals.* Advanced Optical Materials, 2017. **5**(4): p. 1600709.
93. Limpens, R., S.L. Luxembourg, A.W. Weeber, and T. Gregorkiewicz, *Emission efficiency limit of Si nanocrystals.* Scientific Reports, 2016. **6**(1): p. 19566.
94. Hori, Y., S. Kano, H. Sugimoto, K. Imakita, and M. Fujii, *Size-Dependence of Acceptor and Donor Levels of Boron and Phosphorus Codoped Colloidal Silicon Nanocrystals.* Nano Letters, 2016. **16**(4): p. 2615-2620.
95. Weissker, H.C., J. Furthmüller, and F. Bechstedt, *Structure- and spin-dependent excitation energies and lifetimes of Si and Ge nanocrystals from ab initio calculations.* Physical Review B, 2004. **69**(11): p. 115310.
96. Leung, K. and K.B. Whaley, *Electron-hole interactions in silicon nanocrystals.* Physical Review B, 1997. **56**(12): p. 7455-7468.
97. Lippens, P.E. and M. Lannoo, *Calculation of the band gap for small CdS and ZnS crystallites.* Physical Review B, 1989. **39**(15): p. 10935-10942.
98. Wilson, W.L., P.F. Szajowski, and L.E. Brus, *Quantum confinement in size-selected, surface-oxidized silicon nanocrystals.* Science, 1993. **262**(5137): p. 1242-4.
99. Dohnalová, K., T. Gregorkiewicz, and K. Kůsová, *Silicon quantum dots: surface matters.* Journal of Physics: Condensed Matter, 2014. **26**(17): p. 173201.
100. Dohnalová, K., P. Hapala, K. Kůsová, and I. Infante, *Electronic Structure Engineering Achieved via Organic Ligands in Silicon Nanocrystals.* Chemistry of Materials, 2020. **32**(15): p. 6326-6337.
101. Dohnalová, K., A.N. Poddubny, A.A. Prokofiev, W.D.A.M. de Boer, C.P. Umesh, J.M.J. Paulusse, H. Zuilhof, and T. Gregorkiewicz, *Surface brightens up Si quantum dots: direct bandgap-like size-tunable emission.* Light: Science & Applications, 2013. **2**(1): p. e47-e47.
102. Islam, M.A., M.H. Mobarok, R. Sinelnikov, T.K. Purkait, and J.G.C. Veinot, *Phosphorus Pentachloride Initiated Functionalization of Silicon Nanocrystals.* Langmuir, 2017. **33**(35): p. 8766-8773.
103. Mangolini, L., E. Thimsen, and U. Kortshagen, *High-Yield Plasma Synthesis of Luminescent Silicon Nanocrystals.* Nano Letters, 2005. **5**(4): p. 655-659.
104. Sarkar, A., R. Bar, S. Singh, R.K. Chowdhury, S. Bhattacharya, A.K. Das, and S.K. Ray, *Size-tunable electroluminescence characteristics of quantum confined Si nanocrystals embedded in Si-rich oxide matrix.* Applied Physics Letters, 2020. **116**(23): p. 231105.
105. Wang, Y. and Y. Xia, *Bottom-Up and Top-Down Approaches to the Synthesis of Monodispersed Spherical Colloids of Low Melting-Point Metals.* Nano Letters, 2004. **4**(10): p. 2047-2050.
106. Cao, G. and Y. Wang, *Nanostructures and Nanomaterials*. World Scientific Series in Nanoscience and Nanotechnology. Vol. Volume 2. 2011, Singapore: World Scientific Publishing Co. Pte. Ltd. 596.

107. Liang, J., C. Huang, and X. Gong, *Silicon Nanocrystals and Their Composites: Syntheses, Fluorescence Mechanisms, and Biological Applications.* ACS Sustainable Chemistry & Engineering, 2019. **7**(22): p. 18213-18227.
108. Jurbergs, D., E. Rogojina, L. Mangolini, and U. Kortshagen, *Silicon nanocrystals with ensemble quantum yields exceeding 60%.* Applied Physics Letters, 2006. **88**(23): p. 233116.
109. Sankaran, R.M., D. Holunga, R.C. Flagan, and K.P. Giapis, *Synthesis of Blue Luminescent Si Nanoparticles Using Atmospheric-Pressure Microdischarges.* Nano Letters, 2005. **5**(3): p. 537-541.
110. Shen, X.-B., B. Song, B. Fang, X. Yuan, Y.-Y. Li, S.-Y. Wang, S.-J. Ji, and Y. He, *Solvent polarity-induced photoluminescence enhancement (SPIPE): A method enables several-fold increase in quantum yield of silicon nanoparticles.* Nano Research, 2019. **12**(2): p. 315-322.
111. Anthony, R.J., D.J. Rowe, M. Stein, J. Yang, and U. Kortshagen, *Routes to Achieving High Quantum Yield Luminescence from Gas-Phase-Produced Silicon Nanocrystals.* Advanced Functional Materials, 2011. **21**(21): p. 4042-4046.
112. Linares, J., A. López-Suárez, C. Ramos, M. Picquart, M.F. García-Sánchez, A. Dutt, and G. Santana, *Very low-temperature growth of silicon thin films using chlorinated precursors and optical properties.* Materials Science in Semiconductor Processing, 2020. **108**: p. 104859.
113. Longeaud, C., J.P. Kleider, P. Roca i Cabarrocas, S. Hamma, R. Meaudre, and M. Meaudre, *Properties of a new a-Si:H-like material: hydrogenated polymorphous silicon.* Journal of Non-Crystalline Solids, 1998. **227-230**: p. 96-99.
114. Stuckelberger, M., R. Biron, N. Wyrsch, F.-J. Haug, and C. Ballif, *Review: Progress in solar cells from hydrogenated amorphous silicon.* Renewable and Sustainable Energy Reviews, 2017. **76**: p. 1497-1523.
115. Waman, V.S., M.M. Kamble, S.S. Ghosh, R.R. Hawaldar, D.P. Amalnerkar, V.G. Sathe, S.W. Gosavi, and S.R. Jadkar, *Influence of helium dilution of silane on microstructure and opto-electrical properties of hydrogenated nanocrystalline silicon (nc-Si:H) thin films deposited by HW-CVD.* Materials Research Bulletin, 2012. **47**(11): p. 3445-3451.
116. Mangolini, L. and U. kortshagen, *Nonthermal Plasma Synthesis of Silicon Nanocrystals*, in *Silicon Nanocrystals*, L. Pavesi and R. Turan, Editors. 2010, Willey-VCH: Winheim. p. 309-348.
117. Kortshagen, U.R., R.M. Sankaran, R.N. Pereira, S.L. Girshick, J.J. Wu, and E.S. Aydil, *Nonthermal Plasma Synthesis of Nanocrystals: Fundamental Principles, Materials, and Applications.* Chemical Reviews, 2016. **116**(18): p. 11061-11127.
118. Mangolini, L., *Synthesis, properties, and applications of silicon nanocrystals.* Journal of Vacuum Science & Technology B, 2013. **31**(2): p. 020801.
119. Atkins, T.M., A.Y. Louie, and S.M. Kauzlarich, *An efficient microwave-assisted synthesis method for the production of water soluble amine-terminated Si nanoparticles.* Nanotechnology, 2012. **23**(29): p. 294006.
120. Beekman, M., S.M. Kauzlarich, L. Doherty, and G.S. Nolas, *Zintl Phases as Reactive Precursors for Synthesis of Novel Silicon and Germanium-Based Materials.* Materials (Basel, Switzerland), 2019. **12**(7): p. 1139.
121. Dasog, M., Z. Yang, S. Regli, T.M. Atkins, A. Faramus, M.P. Singh, E. Muthuswamy, S.M. Kauzlarich, R.D. Tilley, and J.G.C. Veinot, *Chemical Insight into the Origin of Red and Blue Photoluminescence Arising from Freestanding Silicon Nanocrystals.* ACS Nano, 2013. **7**(3): p. 2676-2685.
122. Neiner, D., H.W. Chiu, and S.M. Kauzlarich, *Low-Temperature Solution Route to Macroscopic Amounts of Hydrogen Terminated Silicon Nanoparticles.* Journal of the American Chemical Society, 2006. **128**(34): p. 11016-11017.
123. Yang, C.-S., S.M. Kauzlarich, and Y.C. Wang, *Synthesis and Characterization of Germanium/Si−Alkyl and Germanium/Silica Core−Shell Quantum Dots.* Chemistry of Materials, 1999. **11**(12): p. 3666-3670.
124. Zou, J., R.K. Baldwin, K.A. Pettigrew, and S.M. Kauzlarich, *Solution Synthesis of Ultrastable Luminescent Siloxane-Coated Silicon Nanoparticles.* Nano Letters, 2004. **4**(7): p. 1181-1186.
125. English, D.S., L.E. Pell, Z. Yu, P.F. Barbara, and B.A. Korgel, *Size Tunable Visible Luminescence from Individual Organic Monolayer Stabilized Silicon Nanocrystal Quantum Dots.* Nano Letters, 2002. **2**(7): p. 681-685.

126. Holmes, J.D., K.J. Ziegler, R.C. Doty, L.E. Pell, K.P. Johnston, and B.A. Korgel, *Highly Luminescent Silicon Nanocrystals with Discrete Optical Transitions.* Journal of the American Chemical Society, 2001. **123**(16): p. 3743-3748.
127. Yu, Y. and B.A. Korgel, *Controlled Styrene Monolayer Capping of Silicon Nanocrystals by Room Temperature Hydrosilylation.* Langmuir, 2015. **31**(23): p. 6532-6537.
128. Ddungu, John L.Z., S. Silvestrini, A. Tassoni, and L. De Cola, *Shedding light on the aqueous synthesis of silicon nanoparticles by reduction of silanes with citrates.* Faraday Discussions, 2020. **222**(0): p. 350-361.
129. Zhong, Y., F. Peng, F. Bao, S. Wang, X. Ji, L. Yang, Y. Su, S.-T. Lee, and Y. He, *Large-Scale Aqueous Synthesis of Fluorescent and Biocompatible Silicon Nanoparticles and Their Use as Highly Photostable Biological Probes.* Journal of the American Chemical Society, 2013. **135**(22): p. 8350-8356.
130. Shen, P., N. Uesawa, S. Inasawa, and Y. Yamaguchi, *Stable and color-tunable fluorescence from silicon nanoparticles formed by single-step plasma assisted decomposition of SiBr4.* Journal of Materials Chemistry, 2010. **20**(9): p. 1669-1675.
131. Ding, L., T.P. Chen, Y. Liu, C.Y. Ng, Y.C. Liu, and S. Fung, *Thermal annealing effect on the band gap and dielectric functions of silicon nanocrystals embedded in SiO2 matrix.* Applied Physics Letters, 2005. **87**(12): p. 121903.
132. Gribov, B.G., K.V. Zinov'ev, O.N. Kalashnik, N.N. Gerasimenko, D.I. Smirnov, V.N. Sukhanov, N.N. Kononov, and S.G. Dorofeev, *Production of Silicon Nanoparticles for Use in Solar Cells.* Semiconductors, 2018. **51**(13): p. 1675-1680.
133. Kapaklis, V., C. Politis, P. Poulopoulos, and P. Schweiss, *Photoluminescence from silicon nanoparticles prepared from bulk amorphous silicon monoxide by the disproportionation reaction.* Applied Physics Letters, 2005. **87**(12): p. 123114.
134. Kapaklis, V., C. Politis, P. Poulopoulos, and P. Schweiss, *Photoluminescent Si nanoparticles embedded in silicon oxide matrix.* Materials Science and Engineering: B, 2005. **124-125**: p. 475-478.
135. Ke, W., X. Feng, and Y. Huang, *Annealing effects on the size of Si-nanocrystals embedded in bulk SiO.* Journal of Crystal Growth, 2011. **316**(1): p. 191-195.
136. Mamiya, M., H. Takei, M. Kikuchi, and C. Uyeda, *Preparation of fine silicon particles from amorphous silicon monoxide by the disproportionation reaction.* Journal of Crystal Growth, 2001. **229**(1): p. 457-461.
137. Park, N.-M., C.-J. Choi, T.-Y. Seong, and S.-J. Park, *Quantum Confinement in Amorphous Silicon Quantum Dots Embedded in Silicon Nitride.* Physical Review Letters, 2001. **86**(7): p. 1355-1357.
138. Kim, T.-W., C.-H. Cho, B.-H. Kim, and S.-J. Park, *Quantum confinement effect in crystalline silicon quantum dots in silicon nitride grown using SiH4 and NH3.* Applied Physics Letters, 2006. **88**(12): p. 123102.
139. Kirkey, W.D., A.N. Cartwright, X. Li, Y. He, M.T. Swihart, Y. Sahoo, and P.N. Prasad, *Optical Properties of Polymer-Embedded Silicon Nanoparticles.* MRS Proceedings, 2011. **789**: p. N15.30.
140. Li, X., Y. He, S.S. Talukdar, and M.T. Swihart, *Process for Preparing Macroscopic Quantities of Brightly Photoluminescent Silicon Nanoparticles with Emission Spanning the Visible Spectrum.* Langmuir, 2003. **19**(20): p. 8490-8496.
141. Talukdar, S.S. and M.T. Swihart, *Aerosol dynamics modeling of silicon nanoparticle formation during silane pyrolysis: a comparison of three solution methods.* Journal of Aerosol Science, 2004. **35**(7): p. 889-908.
142. Heinrich, J.L., C.L. Curtis, G.M. Credo, M.J. Sailor, and K.L. Kavanagh, *Luminescent Colloidal Silicon Suspensions from Porous Silicon.* Science, 1992. **255**(5040): p. 66-68.
143. Abderrafi, K., R. García Calzada, M.B. Gongalsky, I. Suárez, R. Abarques, V.S. Chirvony, V.Y. Timoshenko, R. Ibáñez, and J.P. Martínez-Pastor, *Silicon Nanocrystals Produced by Nanosecond Laser Ablation in an Organic Liquid.* The Journal of Physical Chemistry C, 2011. **115**(12): p. 5147-5151.
144. Alkis, S., A.K. Okyay, and B. Ortaç, *Post-Treatment of Silicon Nanocrystals Produced by Ultra-Short Pulsed Laser Ablation in Liquid: Toward Blue Luminescent Nanocrystal Generation.* The Journal of Physical Chemistry C, 2012. **116**(5): p. 3432-3436.
145. Krivonosov, A., D. Zuev, S. Kaputkina, V. Mikhailovskii, E. Egorova, E. Ageev, and G. Odintsova, *Evolution of size distribution of Si nanoparticles produced by pulsed laser ablation in water.* Optical and Quantum Electronics, 2020. **52**(3): p. 158.

146. Morozov, M.O., I.N. Zavestovskaya, A.V. Kabashin, and V.Y. Timoshenko, *Photoluminescence properties of silicon nanocrystals grown by nanosecond laser ablation of solid-state targets in an inert gas atmosphere.* Bulletin of the Lebedev Physics Institute, 2017. **44**(12): p. 353-356.
147. Rasouli, H.R., A. Ghobadi, T.G.U. Ghobadi, H. Ates, K. Topalli, and A.K. Okyay, *Nanosecond pulsed laser ablated sub-10 nm silicon nanoparticles for improving photovoltaic conversion efficiency of commercial solar cells.* Journal of Optics, 2017. **19**(10): p. 105902.
148. Vendamani, V.S., S. Hamad, V. Saikiran, A.P. Pathak, S. Venugopal Rao, V.V. Ravi Kanth Kumar, and S.V.S. Nageswara Rao, *Synthesis of ultra-small silicon nanoparticles by femtosecond laser ablation of porous silicon.* Journal of Materials Science, 2015. **50**(4): p. 1666-1672.
149. Zhang, X., Y. Duan, X. Dai, T. Li, Y. Xia, P. Zheng, H. Li, and Y. Jiang, *Atomistic origin of amorphous-structure-promoted oxidation of silicon.* Applied Surface Science, 2020. **504**: p. 144437.
150. Kharin, A.Y., A. Fronya, S. Antonenko, N. Karpov, S. Derzhavin, Y. Dombrovska, A. Garmash, N. Kargin, S. Klimentov, V.Y. Timoshenko, and A. Kabashin. *Photoluminescent Si-based nanocrystals prepared by pulsed laser ablation in low-pressure helium-nitrogen mixtures for biomedical applications*. in *Synthesis and Photonics of Nanoscale Materials XVII*. 2020. SPIE.DOI: https://doi.org/10.1117/12.2551482.
151. Lasemi, N., C. Rentenberger, G. Liedl, and D. Eder *The influence of the fluid nature on femtosecond laser ablation properties of a SiO2/Si target and synthesis of ultrafine-grained Si nanoparticles*. Nanoscale Advances, 2020. DOI: 10.1039/D0NA00317D.
152. Taheri, M. and N. Mansour, *Silicon Nanoparticles Produced by Two-Step Nanosecond Pulsed Laser Ablation in Ethanol for Enhanced Blue Emission Properties.* Silicon, 2020. **12**(4): p. 789-797.
153. Lam, C., Y.F. Zhang, Y.H. Tang, C.S. Lee, I. Bello, and S.T. Lee, *Large-scale synthesis of ultrafine Si nanoparticles by ball milling.* Journal of Crystal Growth, 2000. **220**(4): p. 466-470.
154. Kuang, L., B.S. Mitchell, and M.J. Fink, *Silicon nanoparticles synthesised through reactive high-energy ball milling: enhancement of optical properties from the removal of iron impurities.* Journal of Experimental Nanoscience, 2015. **10**(16): p. 1214-1222.
155. Goyal, A., M. Demmenie, C.-C. Huang, P. Schall, and K. Dohnalova, *Photophysical properties of ball milled silicon nanostructures.* Faraday Discussions, 2020.
156. Nilssen, B.E. and R.A. Kleiv, *Silicon Powder Properties Produced in a Planetary Ball Mill as a Function of Grinding Time, Grinding Bead Size and Rotational Speed.* Silicon, 2020. **12**(10): p. 2413-2423.
157. Borouni, M., B. Niroumand, and A. Maleki, *A study on crystallization of amorphous nano silica particles by mechanical activation at the presence of pure aluminum.* Journal of Solid State Chemistry, 2018. **263**: p. 208-215.
158. Elangovan, H., A. Maske, R. Narayanan, P.C. Ramamurthy, and K. Chattopadhyay, *Green synthesis of germanium nano ink and inkjet printing of Si/Ge heterostructure.* Materials Research Bulletin, 2020. **132**: p. 110984.
159. Gonzalez, C.M. and J.G.C. Veinot, *Silicon nanocrystals for the development of sensing platforms.* Journal of Materials Chemistry C, 2016. **4**(22): p. 4836-4846.
160. Kamrani, S., D. Penther, A. Ghasemi, R. Riedel, and C. Fleck, *Microstructural characterization of Mg-SiC nanocomposite synthesized by high energy ball milling.* Advanced Powder Technology, 2018. **29**(7): p. 1742-1748.
161. Odo, E.A., D.T. Britton, and M. Harting, *Sub-oxide passivation of silicon nanoparticles through rapid mechanical attrition.* Powder Technology, 2017. **317**: p. 230-235.
162. Stanciu, C.D., T.F. Marinca, I. Chicinaş, and O. Isnard, *Characterisation of the Fe-10wt% Si nanocrystalline powder obtained by mechanical alloying and annealing.* Journal of Magnetism and Magnetic Materials, 2017. **441**: p. 455-464.
163. Zhang, J., C. Zhang, Z. Liu, J. Zheng, Y. Zuo, C. Xue, C. Li, and B. Cheng, *High-performance ball-milled SiOx anodes for lithium ion batteries.* Journal of Power Sources, 2017. **339**: p. 86-92.
164. van Sebille, M., J. Allebrandi, J. Quik, R.A.C.M.M. van Swaaij, F.D. Tichelaar, and M. Zeman, *Optimizing Silicon Oxide Embedded Silicon Nanocrystal Inter-particle Distances.* Nanoscale Research Letters, 2016. **11**(1): p. 355-355.
165. Higashi, G.S., Y.J. Chabal, G.W. Trucks, and K. Raghavachari, *Ideal hydrogen termination of the Si (111) surface.* Applied Physics Letters, 1990. **56**(7): p. 656-658.

166. Dittrich, T., S. Rauscher, V.Y. Timoshenko, J. Rappich, I. Sieber, H. Flietner, and H.J. Lewerenz, *Ultrathin luminescent nanoporous silicon on n-Si: pH dependent preparation in aqueous NH4F solutions.* Applied Physics Letters, 1995. **67**(8): p. 1134-1136.
167. Hsiao, R. and J. Carr, *Si/SiO2 etching in high density SF6/CHF3/O2 plasma.* Materials Science and Engineering: B, 1998. **52**(1): p. 63-77.
168. Ikeda, M., S. Iwamoto, and N. Nagashima, *Behavior of fluorine on silicon (100) surfaces etched with NH4F aqueous solutions.* Electronics and Communications in Japan (Part II: Electronics), 2000. **83**(7): p. 41-47.
169. Oehrlein, G.S., Y. Zhang, D. Vender, and O. Joubert, *Fluorocarbon high-density plasmas. II. Silicon dioxide and silicon etching using CF4 and CHF3.* Journal of Vacuum Science & Technology A, 1994. **12**(2): p. 333-344.
170. Higgins, E.A., V. Fiorca, A.A. Thomas, and H.V. Davis, *Acute toxicity of brief exposures to HF, HCl, NO2 and HCN with and without CO.* Fire Technology, 1972. **8**(2): p. 120-130.
171. Zuo, H., L. Chen, M. Kong, L. Qiu, P. Lü, P. Wu, Y. Yang, and K. Chen, *Toxic effects of fluoride on organisms.* Life Sciences, 2018. **198**: p. 18-24.
172. Johnston, N.R. and S.A. Strobel, *Principles of fluoride toxicity and the cellular response: a review.* Archives of Toxicology, 2020. **94**(4): p. 1051-1069.
173. Kabir, H., A.K. Gupta, and S. Tripathy, *Fluoride and human health: Systematic appraisal of sources, exposures, metabolism, and toxicity.* Critical Reviews in Environmental Science and Technology, 2020. **50**(11): p. 1116-1193.
174. Wimalawansa, S.J., *Molecular and cellular toxicity of fluoride in mystery, tubulointerstitial chronic kidney disease: a systematic review.* Reviews in Environmental Science and Bio/Technology, 2020. **19**(1): p. 117-147.
175. Sato, K., H. Tsuji, K. Hirakuri, N. Fukata, and Y. Yamauchi, *Controlled chemical etching for silicon nanocrystals with wavelength-tunable photoluminescence.* Chemical Communications, 2009(25): p. 3759-3761.
176. Miyano, M., S. Endo, H. Takenouchi, S. Nakamura, Y. Iwabuti, O. Shiino, T. Nakanishi, and Y. Hasegawa, *Novel Synthesis and Effective Surface Protection of Air-Stable Luminescent Silicon Nanoparticles.* The Journal of Physical Chemistry C, 2014. **118**(34): p. 19778-19784.
177. Xin, Y., R. Wakimoto, and K.-i. Saitow, *Synthesis of Size-controlled Luminescent Si Nanocrystals from (HSiO1.5)n Polymers.* Chemistry Letters, 2017. **46**(5): p. 699-702.
178. Tay, F.E.H., C. Iliescu, J. Jing, and J. Miao, *Defect-free wet etching through pyrex glass using Cr/Au mask.* Microsystem Technologies, 2006. **12**(10): p. 935-939.
179. Knotter, D.M., *Etching Mechanism of Vitreous Silicon Dioxide in HF-Based Solutions.* Journal of the American Chemical Society, 2000. **122**(18): p. 4345-4351.
180. Marinins, A., Z. Yang, H. Chen, J. Linnros, J.G.C. Veinot, S. Popov, and I. Sychugov, *Photostable Polymer/Si Nanocrystal Bulk Hybrids with Tunable Photoluminescence.* ACS Photonics, 2016. **3**(9): p. 1575-1580.
181. Falcão, B.P., J.P. Leitão, M.R. Soares, L. Ricardo, H. Águas, R. Martins, and R.N. Pereira, *Oxidation and Strain in Free-standing Silicon Nanocrystals.* Physical Review Applied, 2019. **11**(2): p. 024054.
182. Popelensky, V.M., S.G. Dorofeev, N.N. Kononov, S.S. Bubenov, and A.A. Vinokurov, *Room temperature oxidation of Si nanocrystals at dry and wet air.* Journal of Nanoparticle Research, 2020. **22**(3): p. 54.
183. Plaza-Castillo, J., A. García-Barrientos, M. Moreno-Moreno, M.J. Arellano-Jiménez, K.Y. Vizcaíno, and J.L. Bernal, *Analysis of H 2 and SiH 4 in the Deposition of pm-Si:H Thin Films by PECVD Process for Solar Cell Applications.* Microscopy and Microanalysis, 2016. **22**(S3): p. 1874-1875.
184. Rinck, J., D. Schray, C. Kübel, A.K. Powell, and G.A. Ozin, *Size-Dependent Oxidation of Monodisperse Silicon Nanocrystals with Allylphenylsulfide Surfaces.* Small, 2015. **11**(3): p. 335-340.
185. Gupta, A. and H. Wiggers, *Freestanding silicon quantum dots: origin of red and blue luminescence.* Nanotechnology, 2010. **22**(5): p. 055707.
186. de Boer, W.D.A.M., D. Timmerman, K. Dohnalová, I.N. Yassievich, H. Zhang, W.J. Buma, and T. Gregorkiewicz, *Red spectral shift and enhanced quantum efficiency in phonon-free photoluminescence from silicon nanocrystals.* Nature Nanotechnology, 2010. **5**(12): p. 878-884.

187. Ghosh, B. and N. Shirahata, *Colloidal silicon quantum dots: synthesis and luminescence tuning from the near-UV to the near-IR range.* Science and Technology of Advanced Materials, 2014. **15**(1): p. 014207.
188. Prokofiev, A.A., A.S. Moskalenko, I.N. Yassievich, W.D.A.M. de Boer, D. Timmerman, H. Zhang, W.J. Buma, and T. Gregorkiewicz, *Direct bandgap optical transitions in Si nanocrystals.* JETP Letters, 2010. **90**(12): p. 758-762.
189. Valenta, J., A. Fucikova, I. Pelant, K. Kůsová, K. Dohnalová, A. Aleknavičius, O. Cibulka, A. Fojtík, and G. Kada, *On the origin of the fast photoluminescence band in small silicon nanoparticles.* New Journal of Physics, 2008. **10**(7): p. 073022.
190. Ulusoy Ghobadi, T.G., A. Ghobadi, T. Okyay, K. Topalli, and A.K. Okyay, *Controlling luminescent silicon nanoparticle emission produced by nanosecond pulsed laser ablation: role of interface defect states and crystallinity phase.* RSC Advances, 2016. **6**(113): p. 112520-112526.
191. Bruhn, B., B.J.M. Brenny, S. Dekker, I. Doğan, P. Schall, and K. Dohnalová, *Multi-chromatic silicon nanocrystals.* Light: Science & Applications, 2017. **6**(6): p. e17007-e17007.
192. Galář, P., T. Popelář, J. Khun, I. Matulková, I. Němec, K.D. Newell, A. Michalcová, V. Scholtz, and K. Kůsová, *The red and blue luminescence in silicon nanocrystals with an oxidized, nitrogen-containing shell.* Faraday Discussions, 2020. **222**(0): p. 240-257.
193. Dung, M.X., D.D. Tung, S. Jeong, and H.-D. Jeong, *Tuning Optical Properties of Si Quantum Dots by π-Conjugated Capping Molecules.* Chemistry – An Asian Journal, 2013. **8**(3): p. 653-664.
194. Carroll, G.M., R. Limpens, and N.R. Neale, *Tuning Confinement in Colloidal Silicon Nanocrystals with Saturated Surface Ligands.* Nano Letters, 2018. **18**(5): p. 3118-3124.
195. Yang, Z., G.B. De los Reyes, L.V. Titova, I. Sychugov, M. Dasog, J. Linnros, F.A. Hegmann, and J.G.C. Veinot, *Evolution of the Ultrafast Photoluminescence of Colloidal Silicon Nanocrystals with Changing Surface Chemistry.* ACS Photonics, 2015. **2**(5): p. 595-605.
196. Li, Q., Y. He, J. Chang, L. Wang, H. Chen, Y.-W. Tan, H. Wang, and Z. Shao, *Surface-Modified Silicon Nanoparticles with Ultrabright Photoluminescence and Single-Exponential Decay for Nanoscale Fluorescence Lifetime Imaging of Temperature.* Journal of the American Chemical Society, 2013. **135**(40): p. 14924-14927.
197. Hirata, A., S. Kohara, T. Asada, M. Arao, C. Yogi, H. Imai, Y. Tan, T. Fujita, and M. Chen, *Atomic-scale disproportionation in amorphous silicon monoxide.* Nature Communications, 2016. **7**(1): p. 11591.
198. Brown, S.L., J.B. Miller, R.J. Anthony, U.R. Kortshagen, A. Kryjevski, and E.K. Hobbie, *Abrupt Size Partitioning of Multimodal Photoluminescence Relaxation in Monodisperse Silicon Nanocrystals.* ACS Nano, 2017. **11**(2): p. 1597-1603.
199. Brown, S.L., D.J. Vogel, J.B. Miller, T.M. Inerbaev, R.J. Anthony, U.R. Kortshagen, D.S. Kilin, and E.K. Hobbie, *Enhancing Silicon Nanocrystal Photoluminescence through Temperature and Microstructure.* The Journal of Physical Chemistry C, 2016. **120**(33): p. 18909-18916.
200. Mangolini, L., D. Jurbergs, E. Rogojina, and U. Kortshagen, *Plasma synthesis and liquid-phase surface passivation of brightly luminescent Si nanocrystals.* Journal of Luminescence, 2006. **121**(2): p. 327-334.
201. Meinardi, F., S. Ehrenberg, L. Dhamo, F. Carulli, M. Mauri, F. Bruni, R. Simonutti, U. Kortshagen, and S. Brovelli, *Highly efficient luminescent solar concentrators based on earth-abundant indirect-bandgap silicon quantum dots.* Nature Photonics, 2017. **11**(3): p. 177-185.
202. Pringle, T.A., K.I. Hunter, A. Brumberg, K.J. Anderson, J.A. Fagan, S.A. Thomas, R.J. Petersen, M. Sefannaser, Y. Han, S.L. Brown, D.S. Kilin, R.D. Schaller, U.R. Kortshagen, P.R. Boudjouk, and E.K. Hobbie, *Bright Silicon Nanocrystals from a Liquid Precursor: Quasi-Direct Recombination with High Quantum Yield.* ACS Nano, 2020. **14**(4): p. 3858-3867.
203. Wu, J.J. and U.R. Kortshagen, *Photostability of thermally-hydrosilylated silicon quantum dots.* RSC Advances, 2015. **5**(126): p. 103822-103828.
204. Qian, C., W. Sun, L. Wang, C. Chen, K. Liao, W. Wang, J. Jia, B.D. Hatton, G. Casillas, M. Kurylowicz, C.M. Yip, M.L. Mastronardi, and G.A. Ozin, *Non-wettable, Oxidation-Stable, Brightly Luminescent, Perfluorodecyl-Capped Silicon Nanocrystal Film.* Journal of the American Chemical Society, 2014. **136**(45): p. 15849-15852.
205. Mazzaro, R., A. Gradone, S. Angeloni, G. Morselli, P.G. Cozzi, F. Romano, A. Vomiero, and P. Ceroni, *Hybrid Silicon Nanocrystals for Color-Neutral and Transparent Luminescent Solar Concentrators.* ACS Photonics, 2019. **6**(9): p. 2303-2311.

206. Romano, F., S. Angeloni, G. Morselli, R. Mazzaro, V. Morandi, J.R. Shell, X. Cao, B.W. Pogue, and P. Ceroni, *Water-soluble silicon nanocrystals as NIR luminescent probes for time-gated biomedical imaging.* Nanoscale, 2020. **12**(14): p. 7921-7926.
207. Marinins, A., R. Zandi Shafagh, W. van der Wijngaart, T. Haraldsson, J. Linnros, J.G.C. Veinot, S. Popov, and I. Sychugov, *Light-Converting Polymer/Si Nanocrystal Composites with Stable 60-70% Quantum Efficiency and Their Glass Laminates.* ACS Appl Mater Interfaces, 2017. **9**(36): p. 30267-30272.
208. Sangghaleh, F., I. Sychugov, Z. Yang, J.G.C. Veinot, and J. Linnros, *Near-Unity Internal Quantum Efficiency of Luminescent Silicon Nanocrystals with Ligand Passivation.* ACS Nano, 2015. **9**(7): p. 7097-7104.
209. van Dam, B., C.I. Osorio, M.A. Hink, R. Muller, A.F. Koenderink, and K. Dohnalova, *High Internal Emission Efficiency of Silicon Nanoparticles Emitting in the Visible Range.* ACS Photonics, 2018. **5**(6): p. 2129-2136.
210. Sieval, A.B., R. Linke, H. Zuilhof, and E.J.R. Sudhölter, *High-Quality Alkyl Monolayers on Silicon Surfaces.* Advanced Materials, 2000. **12**(19): p. 1457-1460.
211. Bhairamadgi, N.S., S.P. Pujari, F.G. Trovela, A. Debrassi, A.A. Khamis, J.M. Alonso, A.A. Al Zahrani, T. Wennekes, H.A. Al-Turaif, C. van Rijn, Y.A. Alhamed, and H. Zuilhof, *Hydrolytic and Thermal Stability of Organic Monolayers on Various Inorganic Substrates.* Langmuir, 2014. **30**(20): p. 5829-5839.
212. Du, X. and Z. Huang, *Advances in Base-Metal-Catalyzed Alkene Hydrosilylation.* ACS Catalysis, 2017. **7**(2): p. 1227-1243.
213. Chatgilialoglu, C., C. Ferreri, Y. Landais, and V.I. Timokhin, *Thirty Years of (TMS)3SiH: A Milestone in Radical-Based Synthetic Chemistry.* Chemical Reviews, 2018. **118**(14): p. 6516-6572.
214. McVey, B.F.P. and R.D. Tilley, *Solution Synthesis, Optical Properties, and Bioimaging Applications of Silicon Nanocrystals.* Accounts of Chemical Research, 2014. **47**(10): p. 3045-3051.
215. Pujari, S.P., H. Driss, F. Bannani, B. van Lagen, and H. Zuilhof, *One-Pot Gram-Scale Synthesis of Hydrogen-Terminated Silicon Nanoparticles.* Chemistry of Materials, 2018. **30**(18): p. 6503-6512.
216. Wang, J., Y. Liu, F. Peng, C. Chen, Y. He, H. Ma, L. Cao, and S. Sun, *A General Route to Efficient Functionalization of Silicon Quantum Dots for High-Performance Fluorescent Probes.* Small, 2012. **8**(15): p. 2430-2435.
217. Linford, M.R. and C.E.D. Chidsey, *Alkyl monolayers covalently bonded to silicon surfaces.* Journal of the American Chemical Society, 1993. **115**(26): p. 12631-12632.
218. Buriak, J.M., *Organometallic Chemistry on Silicon and Germanium Surfaces.* Chemical Reviews, 2002. **102**(5): p. 1271-1308.
219. Coletti, C., A. Marrone, G. Giorgi, A. Sgamellotti, G. Cerofolini, and N. Re, *Nonradical Mechanisms for the Uncatalyzed Thermal Functionalization of Silicon Surfaces by Alkenes and Alkynes: A Density Functional Study.* Langmuir, 2006. **22**(24): p. 9949-9956.
220. Clark, R.J., M. Aghajamali, C.M. Gonzalez, L. Hadidi, M.A. Islam, M. Javadi, M.H. Mobarok, T.K. Purkait, C.J.T. Robidillo, R. Sinelnikov, A.N. Thiessen, J. Washington, H. Yu, and J.G.C. Veinot, *From Hydrogen Silsesquioxane to Functionalized Silicon Nanocrystals.* Chemistry of Materials, 2017. **29**(1): p. 80-89.
221. Kelly, J.A., A.M. Shukaliak, M.D. Fleischauer, and J.G.C. Veinot, *Size-Dependent Reactivity in Hydrosilylation of Silicon Nanocrystals.* Journal of the American Chemical Society, 2011. **133**(24): p. 9564-9571.
222. Kelly, J.A. and J.G.C. Veinot, *An Investigation into Near-UV Hydrosilylation of Freestanding Silicon Nanocrystals.* ACS Nano, 2010. **4**(8): p. 4645-4656.
223. Zai, H., Y. Zhao, S. Chen, L. Ge, C. Chen, Q. Chen, and Y. Li, *Heterogeneously supported pseudo-single atom Pt as sustainable hydrosilylation catalyst.* Nano Research, 2018. **11**(5): p. 2544-2552.
224. Kantam, M.L., S. Laha, J. Yadav, P.R. Likhar, B. Sreedhar, and B.M. Choudary, *Asymmetric Hydrosilylation of Prochiral Ketones Catalyzed by Nanocrystalline Copper(II) Oxide.* Advanced Synthesis & Catalysis, 2007. **349**(10): p. 1797-1802.
225. Purkait, T.K., M. Iqbal, M.H. Wahl, K. Gottschling, C.M. Gonzalez, M.A. Islam, and J.G.C. Veinot, *Borane-Catalyzed Room-Temperature Hydrosilylation of Alkenes/Alkynes on Silicon Nanocrystal Surfaces.* Journal of the American Chemical Society, 2014. **136**(52): p. 17914-17917.

226. Chen, D., W. Sun, C. Qian, L.M. Reyes, A.P.Y. Wong, Y. Dong, J. Jia, K.K. Chen, and G.A. Ozin, *Porous NIR Photoluminescent Silicon Nanocrystals-POSS Composites.* Advanced Functional Materials, 2016. **26**(28): p. 5102-5110.
227. Dasog, M., J. Kehrle, B. Rieger, and J.G.C. Veinot, *Silicon Nanocrystals and Silicon-Polymer Hybrids: Synthesis, Surface Engineering, and Applications.* Angewandte Chemie International Edition, 2016. **55**(7): p. 2322-2339.
228. Hofmann, R.J., M. Vlatković, and F. Wiesbrock, *Fifty Years of Hydrosilylation in Polymer Science: A Review of Current Trends of Low-Cost Transition-Metal and Metal-Free Catalysts, Non-Thermally Triggered Hydrosilylation Reactions, and Industrial Applications.* Polymers, 2017. **9**(10): p. 534.
229. Moran, I.W. and K.R. Carter, *Direct Passivation of Hydride-Terminated Silicon (100) Surfaces by Free-Radically Tethered Polymer Brushes.* Langmuir, 2009. **25**(16): p. 9232-9239.
230. Yang, Z., C.M. Gonzalez, T.K. Purkait, M. Iqbal, A. Meldrum, and J.G.C. Veinot, *Radical Initiated Hydrosilylation on Silicon Nanocrystal Surfaces: An Evaluation of Functional Group Tolerance and Mechanistic Study.* Langmuir, 2015. **31**(38): p. 10540-10548.
231. Kappe, C.O. and D. Dallinger, *The impact of microwave synthesis on drug discovery.* Nature Reviews Drug Discovery, 2006. **5**(1): p. 51-63.
232. Baghbanzadeh, M., L. Carbone, P.D. Cozzoli, and C.O. Kappe, *Microwave-Assisted Synthesis of Colloidal Inorganic Nanocrystals.* Angewandte Chemie International Edition, 2011. **50**(48): p. 11312-11359.
233. Boukherroub, R., A. Petit, A. Loupy, J.-N. Chazalviel, and F. Ozanam, *Microwave-Assisted Chemical Functionalization of Hydrogen-Terminated Porous Silicon Surfaces.* The Journal of Physical Chemistry B, 2003. **107**(48): p. 13459-13462.
234. Sun, W., C. Qian, M.L. Mastronardi, M. Wei, and G.A. Ozin, *Hydrosilylation kinetics of silicon nanocrystals.* Chemical Communications, 2013. **49**(97): p. 11361-11363.
235. Sun, W., C. Qian, M.L. Mastronardi, M. Wei, and G.A. Ozin, *Hydrosilylation kinetics of silicon nanocrystals.* Chem Commun (Camb), 2013. **49**(97): p. 11361-3.
236. Beri, D., M. Jakoby, I.A. Howard, D. Busko, B.S. Richards, and A. Turshatov, *Improved photon absorption in dye-functionalized silicon nanocrystals synthesized via microwave-assisted hydrosilylation.* Dalton Transactions, 2020. **49**(7): p. 2290-2299.
237. Ravotto, L., Q. Chen, Y. Ma, S.A. Vinogradov, M. Locritani, G. Bergamini, F. Negri, Y. Yu, B.A. Korgel, and P. Ceroni, *Bright Long-Lived Luminescence of Silicon Nanocrystals Sensitized by Two-Photon Absorbing Antenna.* Chem, 2017. **2**(4): p. 550-560.
238. Abdelhameed, M., D.R. Martir, S. Chen, W.Z. Xu, O.O. Oyeneye, S. Chakrabarti, E. Zysman-Colman, and P.A. Charpentier, *Tuning the Optical Properties of Silicon Quantum Dots via Surface Functionalization with Conjugated Aromatic Fluorophores.* Scientific Reports, 2018. **8**(1): p. 3050.
239. Binetti, E., M. Striccoli, T. Sibillano, C. Giannini, R. Brescia, A. Falqui, R. Comparelli, M. Corricelli, R. Tommasi, A. Agostiano, and M.L. Curri, *Tuning light emission of PbS nanocrystals from infrared to visible range by cation exchange.* Science and Technology of Advanced Materials, 2015. **16**(5): p. 055007.
240. Ghosh, B., M. Takeguchi, J. Nakamura, Y. Nemoto, T. Hamaoka, S. Chandra, and N. Shirahata, *Origin of the Photoluminescence Quantum Yields Enhanced by Alkane-Termination of Freestanding Silicon Nanocrystals: Temperature-Dependence of Optical Properties.* Scientific Reports, 2016. **6**(1): p. 36951.
241. Qi, L. and J. Rongchao, *Photoluminescence from colloidal silicon nanoparticles: significant effect of surface.* Nanotechnology Reviews, 2017. **6**(6): p. 601-612.
242. Locritani, M., Y. Yu, G. Bergamini, M. Baroncini, J.K. Molloy, B.A. Korgel, and P. Ceroni, *Silicon Nanocrystals Functionalized with Pyrene Units: Efficient Light-Harvesting Antennae with Bright Near-Infrared Emission.* The Journal of Physical Chemistry Letters, 2014. **5**(19): p. 3325-3329.
243. Fermi, A., M. Locritani, G. Di Carlo, M. Pizzotti, S. Caramori, Y. Yu, B.A. Korgel, G. Bergamini, and P. Ceroni, *Light-harvesting antennae based on photoactive silicon nanocrystals functionalized with porphyrin chromophores.* Faraday Discussions, 2015. **185**(0): p. 481-495.
244. Abdelhameed, M., S. Aly, J.T. Lant, X. Zhang, and P. Charpentier, *Energy/Electron Transfer Switch for Controlling Optical Properties of Silicon Quantum Dots.* Scientific Reports, 2018. **8**(1): p. 17068.

245. Mongin, C., S. Garakyaraghi, N. Razgoniaeva, M. Zamkov, and F.N. Castellano, *Direct observation of triplet energy transfer from semiconductor nanocrystals.* Science, 2016. **351**(6271): p. 369-372.
246. Mongin, C., P. Moroz, M. Zamkov, and F.N. Castellano, *Thermally activated delayed photoluminescence from pyrenyl-functionalized CdSe quantum dots.* Nature Chemistry, 2018. **10**(2): p. 225-230.
247. Xia, P., E.K. Raulerson, D. Coleman, C.S. Gerke, L. Mangolini, M.L. Tang, and S.T. Roberts, *Achieving spin-triplet exciton transfer between silicon and molecular acceptors for photon upconversion.* Nature Chemistry, 2020. **12**(2): p. 137-144.
248. Roy, D., C. Fouzder, A. Mukhuty, S. Pal, M.K. Mondal, R. Kundu, and P. Chowdhury, *Designed Synthesis of Dual Emitting Silicon Quantum Dot for Cell Imaging: Direct Labeling of Alpha 2-HS-Glycoprotein.* Bioconjugate Chemistry, 2019. **30**(5): p. 1575-1583.
249. Romano, F., Y. Yu, B.A. Korgel, G. Bergamini, and P. Ceroni, *Light-Harvesting Antennae Based on Silicon Nanocrystals.* Topics in Current Chemistry, 2016. **374**(4): p. 53.
250. Soujon, D., K. Becker, A.L. Rogach, J. Feldmann, H. Weller, D.V. Talapin, and J.M. Lupton, *Time-Resolved Förster Energy Transfer from Individual Semiconductor Nanoantennae to Single Dye Molecules.* The Journal of Physical Chemistry C, 2007. **111**(31): p. 11511-11515.
251. Morselli, G., F. Romano, and P. Ceroni, *Amine functionalised silicon nanocrystals with bright red and long-lived emission.* Faraday Discussions, 2020. **222**(0): p. 108-121.
252. Nakahara, Y., K. Machiya, T. Sato, N.T. Nwe, T. Furuike, H. Tamura, and K. Kimura, *Synthesis of Silicon Quantum Dots Functionalized Chemically with Monosaccharides and Their Use in Biological Fluorescence Imaging.* Chemistry Letters, 2013. **42**(5): p. 498-500.
253. Mazzaro, R. and A. Vomiero, *The Renaissance of Luminescent Solar Concentrators: The Role of Inorganic Nanomaterials.* Advanced Energy Materials, 2018. **8**(33): p. 1801903.
254. Xu, L., Y.-N. Zhang, X.-H. Ji, and Z.-K. He, *The ratiometric fluorescent detection of anthrax spore biomarker based on functionalized silicon nanodots.* Chemical Papers, 2019. **73**(7): p. 1753-1759.
255. Huang, Z., X. Li, M. Mahboub, K.M. Hanson, V.M. Nichols, H. Le, M.L. Tang, and C.J. Bardeen, *Hybrid Molecule–Nanocrystal Photon Upconversion Across the Visible and Near-Infrared.* Nano Letters, 2015. **15**(8): p. 5552-5557.
256. Piland, G.B., Z. Huang, M. Lee Tang, and C.J. Bardeen, *Dynamics of Energy Transfer from CdSe Nanocrystals to Triplet States of Anthracene Ligand Molecules.* The Journal of Physical Chemistry C, 2016. **120**(11): p. 5883-5889.
257. Beery, D., J.P. Wheeler, A. Arcidiacono, and K. Hanson, *CdSe Quantum Dot Sensitized Molecular Photon Upconversion Solar Cells.* ACS Applied Energy Materials, 2020. **3**(1): p. 29-37.
258. De Roo, J., Z. Huang, N.J. Schuster, L.S. Hamachi, D.N. Congreve, Z. Xu, P. Xia, D.A. Fishman, T. Lian, J.S. Owen, and M.L. Tang, *Anthracene Diphosphate Ligands for CdSe Quantum Dots; Molecular Design for Efficient Upconversion.* Chemistry of Materials, 2020. **32**(4): p. 1461-1466.
259. Li, X., Z. Huang, R. Zavala, and M.L. Tang, *Distance-Dependent Triplet Energy Transfer between CdSe Nanocrystals and Surface Bound Anthracene.* The Journal of Physical Chemistry Letters, 2016. **7**(11): p. 1955-1959.
260. Ronchi, A., P. Brazzo, M. Sassi, L. Beverina, J. Pedrini, F. Meinardi, and A. Monguzzi, *Triplet–triplet annihilation based photon up-conversion in hybrid molecule–semiconductor nanocrystal systems.* Physical Chemistry Chemical Physics, 2019. **21**(23): p. 12353-12359.
261. Zhou, Y., F.N. Castellano, T.W. Schmidt, and K. Hanson, *On the Quantum Yield of Photon Upconversion via Triplet–Triplet Annihilation.* ACS Energy Letters, 2020. **5**(7): p. 2322-2326.
262. Bakalova, R., H. Ohba, Z. Zhelev, T. Nagase, R. Jose, M. Ishikawa, and Y. Baba, *Quantum Dot anti-CD Conjugates: Are They Potential Photosensitizers or Potentiators of Classical Photosensitizing Agents in Photodynamic Therapy of Cancer?* Nano Letters, 2004. **4**(9): p. 1567-1573.
263. Cheng, L., C. Wang, L. Feng, K. Yang, and Z. Liu, *Functional Nanomaterials for Phototherapies of Cancer.* Chemical Reviews, 2014. **114**(21): p. 10869-10939.
264. Wang, L., D. Xu, J. Gao, X. Chen, Y. Duo, and H. Zhang, *Semiconducting quantum dots: Modification and applications in biomedical science.* Science China Materials, 2020. **63**(9): p. 1631-1650.

265. Wong, X.Y., A. Sena-Torralba, R. Álvarez-Diduk, K. Muthoosamy, and A. Merkoçi, *Nanomaterials for Nanotheranostics: Tuning Their Properties According to Disease Needs.* ACS Nano, 2020. **14**(3): p. 2585-2627.
266. Samia, A.C.S., X. Chen, and C. Burda, *Semiconductor Quantum Dots for Photodynamic Therapy.* Journal of the American Chemical Society, 2003. **125**(51): p. 15736-15737.
267. Kalem, S., *Synthesis of ammonium silicon fluoride cryptocrystals on silicon by dry etching.* Applied Surface Science, 2004. **236**(1): p. 336-341.
268. Simonov, Y.A., A.A. Kritskii, V.N. Rychkov, and V.A. Tomashov, *Investigation of the treatment process of associated dioxides of zirconium and silicon by an aqueous solution of ammonium fluoride.* Russian Journal of Non-Ferrous Metals, 2010. **51**(4): p. 320-323.
269. Husáková, L., I. Urbanová, T. Šídová, T. Cahová, T. Faltys, and J. Šrámková, *Evaluation of ammonium fluoride for quantitative microwave-assisted extraction of silicon and boron from different solid samples.* International Journal of Environmental Analytical Chemistry, 2015. **95**(10): p. 922-935.
270. Clark, R.J., M. Aghajamali, C.M. Gonzalez, L. Hadidi, M.A. Islam, M. Javadi, M.H. Mobarok, T.K. Purkait, C.J.T. Robidillo, R. Sinelnikov, A.N. Thiessen, J. Washington, H. Yu, and J.G.C. Veinot, *From Hydrogen Silsesquioxane to Functionalized Silicon Nanocrystals.* Chemistry of Materials, 2016. **29**(1): p. 80-89.
271. Veinot, J.G., *Synthesis, surface functionalization, and properties of freestanding silicon nanocrystals.* Chem Commun (Camb), 2006(40): p. 4160-8.
272. N. Mansour, A. Momeni, R. Karimzadeh, and M. Amini, *Blue-green luminescent silicon nanocrystals fabricated by nanosecond pulsed laser ablation in dimethyl sulfoxide.* Opt. Mater. Express, 2012. **2**: p. 740-748.
273. Yang, S., W. Li, B. Cao, H. Zeng, and W. Cai, *Origin of Blue Emission from Silicon Nanoparticles: Direct Transition and Interface Recombination.* The Journal of Physical Chemistry C, 2011. **115**(43): p. 21056-21062.
274. Jung, D.E., J.S. Han, and B.R. Yoo, *Thermal hydrosilylation of olefin with hydrosilane. Preparative and mechanistic aspects.* Journal of Organometallic Chemistry, 2011. **696**(23): p. 3687-3692.
275. Maier-Flaig, F., E.J. Henderson, S. Valouch, S. Klinkhammer, C. Kübel, G.A. Ozin, and U. Lemmer, *Photophysics of organically-capped silicon nanocrystals – A closer look into silicon nanocrystal luminescence using low temperature transient spectroscopy.* Chemical Physics, 2012. **405**: p. 175-180.
276. Mastronardi, M.L., F. Hennrich, E.J. Henderson, F. Maier-Flaig, C. Blum, J. Reichenbach, U. Lemmer, C. Kubel, D. Wang, M.M. Kappes, and G.A. Ozin, *Preparation of Monodisperse Silicon Nanocrystals Using Density Gradient Ultracentrifugation.* Journal of the American Chemical Society, 2011. **133**(31): p. 11928-11931.
277. Chen, K.K., M.L. Mastronardi, C. Kübel, and G.A. Ozin, *Size-Selective Separation and Purification of "Water-Soluble" Organically Capped Brightly Photoluminescent Silicon Nanocrystals.* Particle & Particle Systems Characterization, 2015. **32**(3): p. 301-306.
278. Faulkner, D.O., J.J. McDowell, A.J. Price, D.D. Perovic, N.P. Kherani, and G.A. Ozin, *Measurement of absolute photoluminescence quantum yields using integrating spheres - Which way to go?* Laser & Photonics Reviews, 2012. **6**(6): p. 802-806.
279. Henderson, E.J., A.J. Shuhendler, P. Prasad, V. Baumann, F. Maier-Flaig, D.O. Faulkner, U. Lemmer, X.Y. Wu, and G.A. Ozin, *Colloidally stable silicon nanocrystals with near-infrared photoluminescence for biological fluorescence imaging.* Small, 2011. **7**(17): p. 2507-16.
280. Mastronardi, M.L., K.K. Chen, K. Liao, G. Casillas, and G.A. Ozin, *Size-Dependent Chemical Reactivity of Silicon Nanocrystals with Water and Oxygen.* The Journal of Physical Chemistry C, 2014. **119**(1): p. 826-834.
281. Mastronardi, M.L., E.J. Henderson, D.P. Puzzo, Y. Chang, Z.B. Wang, M.G. Helander, J. Jeong, N.P. Kherani, Z. Lu, and G.A. Ozin, *Silicon nanocrystal OLEDs: effect of organic capping group on performance.* Small, 2012. **8**(23): p. 3647-54.
282. Mastronardi, M.L., E.J. Henderson, D.P. Puzzo, and G.A. Ozin, *Small silicon, big opportunities: the development and future of colloidally-stable monodisperse silicon nanocrystals.* Adv Mater, 2012. **24**(43): p. 5890-8.
283. Rabenau, A., *The Role of Hydrothermal Synthesis in Preparative Chemistry.* Angewandte Chemie International Edition in English, 1985. **24**(12): p. 1026-1040.

284. Stein, A., S.W. Keller, and T.E. Mallouk, *Turning Down the Heat: Design and Mechanism in Solid-State Synthesis.* Science, 1993. **259**(5101): p. 1558-1564.
285. de Mello, J.C., H.F. Wittmann, and R.H. Friend, *An improved experimental determination of external photoluminescence quantum efficiency.* Advanced Materials, 1997. **9**(3): p. 230-232.
286. Marsico, F., A. Turshatov, K. Weber, and F.R. Wurm, *A Metathesis Route for BODIPY Labeled Polyolefins.* Organic Letters, 2013. **15**(15): p. 3844-3847.
287. Schmidt, R., C. Tanielian, R. Dunsbach, and C. Wolff, *Phenalenone, a Universal Reference Compound for the Determination of Quantum Yields of Singlet Oxygen O2(1-Delta-G) Sensitization.* Journal of Photochemistry and Photobiology a-Chemistry, 1994. **79**(1-2): p. 11-17.
288. Fitzgerald, E.A., *Engineered substrates and their future role in microelectronics.* Materials Science and Engineering: B, 2005. **124-125**: p. 8-15.
289. Chen, X.Y., Y.F. Lu, L.J. Tang, Y.H. Wu, B.J. Cho, X.J. Xu, J.R. Dong, and W.D. Song, *Annealing and oxidation of silicon oxide films prepared by plasma-enhanced chemical vapor deposition.* Journal of Applied Physics, 2005. **97**(1): p. 014913.
290. Klevenz, M., S. Wetzel, M. Möller, and A. Pucci, *Evaporation and Condensation of SiO and SiO2 Studied by Infrared Spectroscopy.* Applied Spectroscopy, 2010. **64**(3): p. 298-303.
291. Klevenz, M., S. Wetzel, M. Trieloff, H.-P. Gail, and A. Pucci, *Vibrational spectroscopy of SiO on Si(111).* Physica Status Solidi (b), 2010. **247**(9): p. 2179-2184.
292. Cheng, X., S.B. Lowe, P.J. Reece, and J.J. Gooding, *Colloidal silicon quantum dots: from preparation to the modification of self-assembled monolayers (SAMs) for bio-applications.* Chemical Society Reviews, 2014. **43**(8): p. 2680-2700.
293. Dasog, M., G.B. De los Reyes, L.V. Titova, F.A. Hegmann, and J.G.C. Veinot, *Size vs Surface: Tuning the Photoluminescence of Freestanding Silicon Nanocrystals Across the Visible Spectrum via Surface Groups.* ACS Nano, 2014. **8**(9): p. 9636-9648.
294. De los Reyes, G.B., M. Dasog, M. Na, L.V. Titova, J.G.C. Veinot, and F.A. Hegmann, *Charge transfer state emission dynamics in blue-emitting functionalized silicon nanocrystals.* Physical Chemistry Chemical Physics, 2015. **17**(44): p. 30125-30133.
295. DeBenedetti, W.J.I., S.-K. Chiu, C.M. Radlinger, R.J. Ellison, B.A. Manhat, J.Z. Zhang, J. Shi, and A.M. Goforth, *Conversion from Red to Blue Photoluminescence in Alcohol Dispersions of Alkyl-Capped Silicon Nanoparticles: Insight into the Origins of Visible Photoluminescence in Colloidal Nanocrystalline Silicon.* The Journal of Physical Chemistry C, 2015. **119**(17): p. 9595-9608.
296. Dewan, S., J.H. Odhner, K.M. Tibbetts, S. Afsari, R.J. Levis, and E. Borguet, *Resolving the source of blue luminescence from alkyl-capped silicon nanoparticles synthesized by laser pulse ablation.* Journal of Materials Chemistry C, 2016. **4**(28): p. 6894-6899.
297. Taheri, M. and N. Mansour, *Silicon Nanoparticles Produced by Two-Step Nanosecond Pulsed Laser Ablation in Ethanol for Enhanced Blue Emission Properties.* Silicon, 2019.
298. Tsybeskov, L., J.V. Vandyshev, and P.M. Fauchet, *Blue emission in porous silicon: Oxygen-related photoluminescence.* Phys Rev B Condens Matter, 1994. **49**(11): p. 7821-7824.
299. Wang, Y., H. Wang, J. Guo, J. Wu, L.J. Gao, Y.H. Sun, J. Zhao, and G.F. Zou, *Water-Soluble Silicon Quantum Dots with Quasi-Blue Emission.* Nanoscale Res Lett, 2015. **10**(1): p. 1012.
300. Laine, R.M., K.Y. Blohowiak, T.R. Robinson, M.L. Hoppe, P. Nardi, J. Kampf, and J. Uhm, *Synthesis of pentacoordinate silicon complexes from SiO2.* Nature, 1991. **353**(6345): p. 642-644.
301. Blohowiak, K.Y., D.R. Treadwell, B.L. Mueller, M.L. Hoppe, S. Jouppi, P. Kansal, K.W. Chew, C.L.S. Scotto, and F. Babonneau, *SiO2 as a Starting Material for the Synthesis of Pentacoordinate Silicon Complexes. 1.* Chemistry of Materials, 1994. **6**(11): p. 2177-2192.
302. Donhärl, W., I. Elhofer, P. Wiede, and U. Schubert, *Elemental silicon and solid SiO give the same products as SiO2 upon reaction with alkali-metal glycolates.* Journal of the Chemical Society, Dalton Transactions, 1998(15): p. 2445-2446.
303. Serezhkin, V.N. and V.S. Urusov, *Stereochemistry of silicon in oxygen-containing compounds.* Crystallography Reports, 2017. **62**(1): p. 50-59.
304. Ogunsipe, A., D. Maree, and T. Nyokong, *Solvent effects on the photochemical and fluorescence properties of zinc phthalocyanine derivatives.* Journal of Molecular Structure, 2003. **650**(1): p. 131-140.
305. Limpens, R., A. Lesage, M. Fujii, and T. Gregorkiewicz, *Size confinement of Si nanocrystals in multinanolayer structures.* Scientific Reports, 2015. **5**(1): p. 17289.

306. Sugimoto, H., M. Yamamura, R. Fujii, and M. Fujii, *Donor–Acceptor Pair Recombination in Size-Purified Silicon Quantum Dots.* Nano Letters, 2018. **18**(11): p. 7282-7288.
307. Abid, S.B.H., Sarra; Richy, Nicolas; Camerel, Franck; Jamoussi, Bassem; Blanchard-Desce, Mireille; Mongin, Olivier; Paul, Frédéric; Paul-Roth, Christine O., *Phthalocyanine-Cored Fluorophores with Fluorene-Containing Peripheral Two-Photon Antennae as Photosensitizers for Singlet Oxygen Generation.* Molecules, 2020. **25**(2): p. 239.
308. Hessel, C.M., D. Reid, M.G. Panthani, M.R. Rasch, B.W. Goodfellow, J.W. Wei, H. Fujii, V. Akhavan, and B.A. Korgel, *Synthesis of Ligand-Stabilized Silicon Nanocrystals with Size-Dependent Photoluminescence Spanning Visible to Near-Infrared Wavelengths.* Chemistry of Materials, 2012. **24**(2): p. 393-401.
309. Yang, Z., M. Iqbal, A.R. Dobbie, and J.G. Veinot, *Surface-induced alkene oligomerization: does thermal hydrosilylation really lead to monolayer protected silicon nanocrystals?* J Am Chem Soc, 2013. **135**(46): p. 17595-601.
310. Kehrle, J., S. Kaiser, T.K. Purkait, M. Winnacker, T. Helbich, S. Vagin, J.G.C. Veinot, and B. Rieger, *In situ IR-spectroscopy as a tool for monitoring the radical hydrosilylation process on silicon nanocrystal surfaces.* Nanoscale, 2017. **9**(24): p. 8489-8495.
311. Aharoni, A., D. Oron, U. Banin, E. Rabani, and J. Jortner, *Long-Range Electronic-to-Vibrational Energy Transfer from Nanocrystals to Their Surrounding Matrix Environment.* Physical Review Letters, 2008. **100**(5): p. 057404.
312. Mazzaro, R., M. Locritani, J.K. Molloy, M. Montalti, Y. Yu, B.A. Korgel, G. Bergamini, V. Morandi, and P. Ceroni, *Photoinduced Processes between Pyrene-Functionalized Silicon Nanocrystals and Carbon Allotropes.* Chemistry of Materials, 2015. **27**(12): p. 4390-4397.
313. Erogbogbo, F., C.-W. Chang, J. May, P.N. Prasad, and M.T. Swihart, *Energy transfer from a dye donor to enhance the luminescence of silicon quantum dots.* Nanoscale, 2012. **4**(16): p. 5163-5168.
314. Hara, K., T. Sato, R. Katoh, A. Furube, T. Yoshihara, M. Murai, M. Kurashige, S. Ito, A. Shinpo, S. Suga, and H. Arakawa, *Novel Conjugated Organic Dyes for Efficient Dye-Sensitized Solar Cells.* Advanced Functional Materials, 2005. **15**(2): p. 246-252.
315. Tahir, M., Muddusir, D.N. Khan, S. Gul, F. Wahab, and S.M. Said, *Photovoltaic effect on the microelectronic properties of perylene/p-Si heterojunction devices.* Journal of Materials Science: Materials in Electronics, 2019. **30**(21): p. 19463-19470.
316. Huang, Z., X. Li, M. Mahboub, K.M. Hanson, V.M. Nichols, H. Le, M.L. Tang, and C.J. Bardeen, *Hybrid Molecule-Nanocrystal Photon Upconversion Across the Visible and Near-Infrared.* Nano Letters, 2015. **15**(8): p. 5552-7.
317. Okumura, K., K. Mase, N. Yanai, and N. Kimizuka, *Employing Core-Shell Quantum Dots as Triplet Sensitizers for Photon Upconversion.* Chemistry – A European Journal, 2016. **22**(23): p. 7721-7726.
318. Yao, D., X. Zhang, O. Mongin, F. Paul, and C.O. Paul-Roth, *Synthesis and Characterization of New Conjugated Fluorenyl-Porphyrin Dendrimers for Optics.* Chemistry, 2016. **22**(16): p. 5583-97.
319. Erogbogbo, F., C.W. Chang, J. May, P.N. Prasad, and M.T. Swihart, *Energy transfer from a dye donor to enhance the luminescence of silicon quantum dots.* Nanoscale, 2012. **4**(16): p. 5163-8.
320. Cheng, X., E. Hinde, D.M. Owen, S.B. Lowe, P.J. Reece, K. Gaus, and J.J. Gooding, *Enhancing Quantum Dots for Bioimaging using Advanced Surface Chemistry and Advanced Optical Microscopy: Application to Silicon Quantum Dots (SiQDs).* Advanced Materials, 2015. **27**(40): p. 6144-6150.
321. Turshatov, A., D. Busko, Y. Avlasevich, T. Miteva, K. Landfester, and S. Baluschev, *Synergetic Effect in Triplet–Triplet Annihilation Upconversion: Highly Efficient Multi-Chromophore Emitter*. ChemPhysChem, 2012. **13**(13): p. 3112-3115.
322. Turshatov, A., D. Busko, S. Baluschev, T. Miteva, and K. Landfester, *Micellar carrier for triplet–triplet annihilation-assisted photon energy upconversion in a water environment.* New Journal of Physics, 2011. **13**(8): p. 083035.
323. Verhagen, J.C.D., M.A.M.J. van Zandvoort, J.M. Vroom, L.B.Å. Johansson, and G. van Ginkel, *Spectroscopic Properties of 2,5,8,11-Tetra-tert-butylperylene in Polymer Films.* The Journal of Physical Chemistry B, 1997. **101**(49): p. 10568-10575.
324. Patalag, L.J., L.P. Ho, P.G. Jones, and D.B. Werz, *Ethylene-Bridged Oligo-BODIPYs: Access to Intramolecular J-Aggregates and Superfluorophores.* Journal of the American Chemical Society, 2017. **139**(42): p. 15104-15113.

325. Zhang, C., J. Zhao, S. Wu, Z. Wang, W. Wu, J. Ma, S. Guo, and L. Huang, *Intramolecular RET Enhanced Visible Light-Absorbing Bodipy Organic Triplet Photosensitizers and Application in Photooxidation and Triplet–Triplet Annihilation Upconversion.* Journal of the American Chemical Society, 2013. **135**(28): p. 10566-10578.
326. Beri, D., M. Jakoby, D. Busko, B.S. Richards, and A. Turshatov *Enhancing Singlet Oxygen Generation in Conjugates of Silicon Nanocrystals and Organic Photosensitizers*. Frontiers in Chemistry, 2020. **8**, DOI: 10.3389/fchem.2020.00567.
327. Ronzani, F., E. Arzoumanian, S. Blanc, P. Bordat, T. Pigot, C. Cugnet, E. Oliveros, M. Sarakha, C. Richard, and S. Lacombe, *Efficient cyanoaromatic photosensitizers for singlet oxygen production: synthesis and characterization of the transient reactive species.* Phys Chem Chem Phys, 2013. **15**(40): p. 17219-32.
328. You, Y., *Chemical tools for the generation and detection of singlet oxygen.* Org Biomol Chem, 2018. **16**(22): p. 4044-4060.
329. Nathan, R.A. and A.H. Adelman, *Photosensitized generation of singlet molecular oxygen with near-infrared radiation.* Journal of the Chemical Society, Chemical Communications, 1974(16): p. 674-675.
330. Khan, A.U. and M. Kasha, *Direct spectroscopic observation of singlet oxygen emission at 1268 nm excited by sensitizing dyes of biological interest in liquid solution.* Proceedings of the National Academy of Sciences, 1979. **76**(12): p. 6047-6049.
331. Taniguchi, M., H. Du, and J.S. Lindsey, *PhotochemCAD 3: Diverse Modules for Photophysical Calculations with Multiple Spectral Databases.* Photochem Photobiol, 2018. **94**(2): p. 277-289.
332. Wu, Y., Y. Zhen, Y. Ma, R. Zheng, Z. Wang, and H. Fu, *Exceptional Intersystem Crossing in Di(perylene bisimide)s: A Structural Platform toward Photosensitizers for Singlet Oxygen Generation.* The Journal of Physical Chemistry Letters, 2010. **1**(17): p. 2499-2502.
333. Filatov, M.A., S. Karuthedath, P.M. Polestshuk, S. Callaghan, K.J. Flanagan, T. Wiesner, F. Laquai, and M.O. Senge, *BODIPY-Pyrene and Perylene Dyads as Heavy-Atom-Free Singlet Oxygen Sensitizers.* ChemPhotoChem, 2018. **2**(7): p. 606-615.
334. Dasog, M. and J.G.C. Veinot, *Tuning silicon quantum dot luminescence via surface groups.* Physica Status Solidi (b), 2014. **251**(11): p. 2216-2220.